Synthesis and Characterization of Cobalt-containing Perovskite-type Oxides

by

Hany Zakaria Ibrahim El Shinawi

A thesis Submitted to the

University of Birmingham

For the Degree of

Doctor of Philosophy

School of Chemistry
The University of Birmingham
Birmingham
B15 2TT, UK

January 2010

Abstract

A number of cobalt-containing perovskite-type oxides were synthesized and characterized in this study. All materials were half-doped with cobalt in their B-sites, *i.e.* contain the $Co_{0.5}M_{0.5}$ B-site state where M = Fe, Mn, Cr, Ni; the materials adopted single-layered, double-layered and simple perovskite-type structures. The materials $La_{2-x}Sr_xCo_{0.5}M_{0.5}O_4$ (M = Fe, Cr) have shown enhanced stability to structural breakdown under reducing conditions (10% H_2/N_2, up to 1000 ºC) with the formation of oxygen-deficient compounds, while no evidence for oxygen hyperstoichiometry was observed under oxidizing conditions. Materials such as $La_{1.2}Sr_{0.8}Co_{0.5}Mn_{0.5}O_{4.1}$ and $La_{1.7}Sr_{0.3}Co_{0.5}Ni_{0.5}O_{4.08}$, however, exhibit oxygen hyperstoichiometry under oxidizing conditions and also withstand reducing conditions *via* formation of oxygen deficiency. Oxygen vacancies were disordered and confined to the equatorial planes of the single-layered structure in all materials, while oxygen hyperstoichiometry was accommodated in the interstitial (0, 0.5, 0.25) sites of the tetragonal K_2NiF_4-type structure. In the double-layered materials $La_{1+x}Sr_{2-x}CoMnO_{7-\delta}$, oxygen vacancies were confined to the common apex of the double-layered structure. Ordered and disordered oxygen vacancies were observed in the perovskite system $LaSrCoFeO_{6-\delta}$. The new brownmillerite phase $LaSrCoFeO_5$ was synthesized and fluorination produced the new oxyfluoride $LaSrCoFeO_5F$. Magnetic interactions between $Co^{2+(3+)}$ ions and ions such as Fe^{3+}, Mn^{3+}, Cr^{3+}, Ni^{2+} in different perovskite-type structures were also studied and a range of magnetically ordered materials, at low and room temperatures, were investigated.

Acknowledgements

I am really grateful to my supervisor Professor Colin Greaves for all his support and encouragement. His ideas and suggestions were extremely useful to get this thesis to its final shape. One feels scientifically "covered" when he works with him, and I feel lucky to work for him.

I would also like to thank Professor Frank J. Berry and Dr Jose F. Marco for provision and interpretation of Mössbauer and X-ray absorption spectra. Thanks also to Professor Frank J. Berry for his support and encouragement. I would also like to thank Professor Joke Hadermann for provision and interpretation of electron microscopy and Professor C. F. McConville for provision of the XPS data. Thanks to all the instrument scientists for assistance with the collection of NPD data, particularly Dr Emma Suard and Dr Vladimir Pomjakushin. I am also grateful to the Egyptian Education Bureau (London) for financial support.

I would also like to thank everyone in the fifth floor for their support, encouragement and friendship. The fifth floor was really good place to work.

Thanks to my family -mother, sisters and my wife- for their support and continuous encouragement. The support I get from my mother is very special! Thanks to Hisham who helped me to be here in Birmingham. My wife was very patient and supportive during my PhD helping me studying and taking care of my small family- thank you!

TABLE OF CONTENTS

Chapter 1 - Introduction

Chapter 2 - Experimental techniques

Abbreviations

AFM	Antiferromagnetic
ED	Electron diffraction
EDTA	Ethylene diamine tetraacetic acid
FM	Ferromagnetic
FC	Field-cooled
GDC	Gadolinia-doped ceria
HRTEM	High resolution transmission electron microscopy
LSM	Lanthanum-strontium-manganese oxides
LSCF	Lanthanum-strontium-cobalt-iron oxides
LSGM	Lanthanum-strontium-magnesium-gallium oxides
NPD	Neutron powder diffraction
RP	Ruddlesden-Popper
SOFC	Solid oxide fuel cell
SDC	Samaria-doped ceria
TGA	Thermogravimetric analysis
TG	Thermogravimetric
XRD	X-ray powder diffraction
XPS	X-ray photoelectron spectroscopy
YSZ	Yttria-stabilized zirconia
ZFC	Zero-field-cooled

CHAPTER 1

Introduction

1.1 Perovskites: structural diversity

In addition to being the name for the specific mineral of composition $CaTiO_3$, perovskite is the name for a structural family with the general formula ABX_3. The A cations are generally alkaline earth or lanthanide ions, the B cations are usually transition metal ions and the X anions are either oxygen or halide ions; however, the majority of the periodic table elements can be found in some variant of perovskite-structured compound. The perovskite structure can be described as a framework of corner-sharing BX_6 octahedra (similar to that of ReO_3), with the A cations located in interstices surrounded by eight octahedra (*Figure 1.1 (a)*). Another way of representing the perovskite structure, which is useful in describing layered derivatives of perovskites, is shown in *Figure 1.1 (b)* where the perovskite is formed by alternate stacking of rock salt AX and BX_2 layers.

The perovskite structure ABX_3 is one of the highest multifunctional structures that, with structural manipulation, can produce an incredibly wide array of phases with totally different functions (*Figure 1.1 (c)*).

One dimension of the compositional and structural diversity of perovskites arises from the extreme flexibility of the structure with regard to cationic and anionic replacements, and tolerance to distortion and cation order. It is the degree of mismatch between AX and BX_2 layers (as determined by ionic sizes) which determines whether or not the ions will be “tolerated” by the perovskite or perovskite-related structure. A perfect match between these layers, which gives the so-called “ideal perovskite structure”, is geometrically expected if:

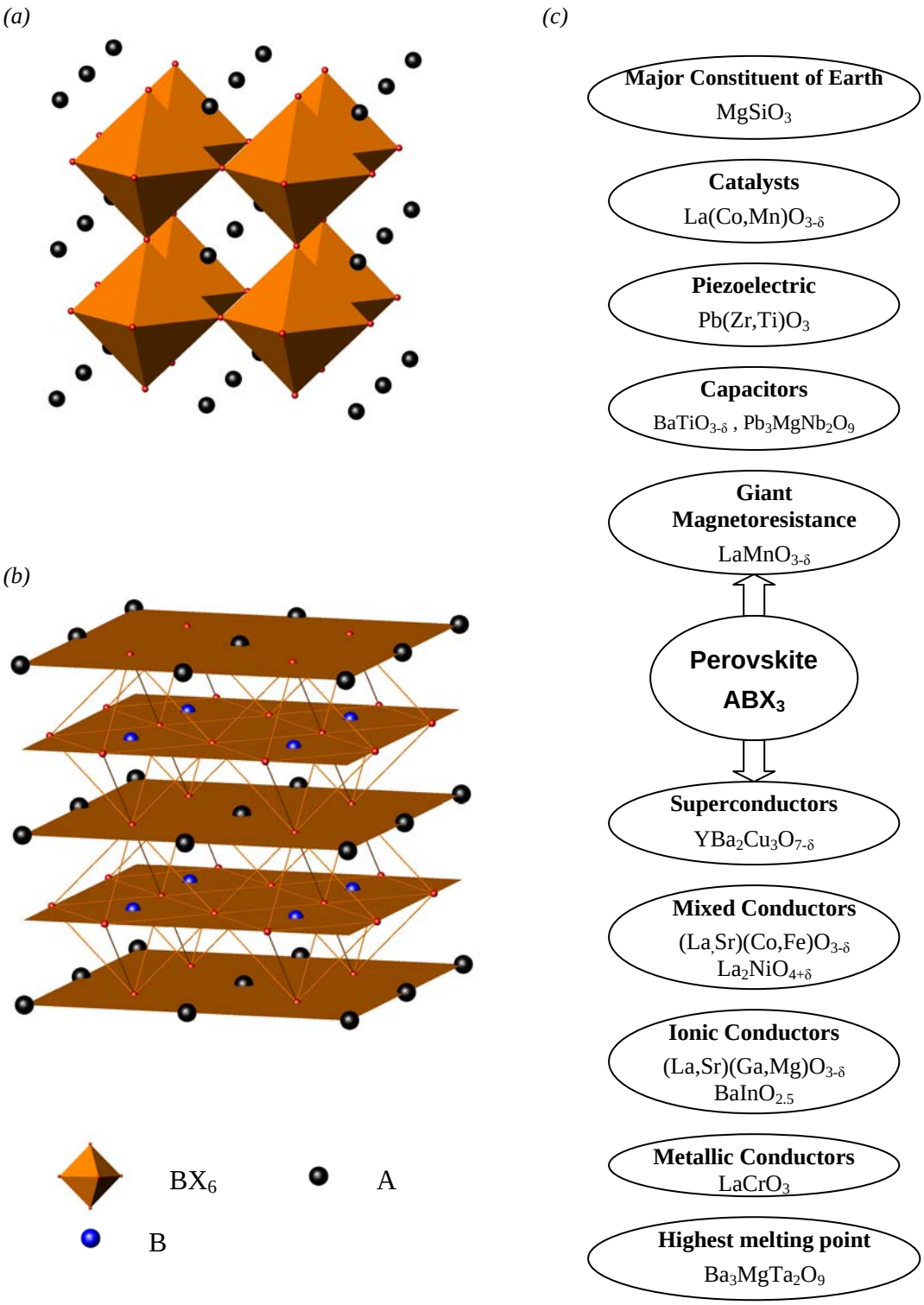

Figure 1.1 The perovskite structure: (a) polyhedral structure, (b) layer structure and (c) multifunctional property.

$$r(A-X) = \sqrt{2}\ r(B-X) \qquad (1.1)$$

where $r(A-X)$ and $r(B-X)$ are the distances obtained from ionic radii. This structural requirement is usually expressed in terms of the "tolerance factor" *t*; a concept first introduced by Goldschmidt [1],

$$t = r(A-X)/\sqrt{2}\ r(B-X) \qquad (1.2)$$

For the ideal perovskite structure, *t* is unity and the symmetry group is the cubic space group $Pm\bar{3}m$. $SrTiO_3$ adopts the $Pm\bar{3}m$ space group and its structure approaches that of the ideal perovskite ($t = 1.002$) [1]. However, diverse perovskite structures of lower symmetry can exist for values of *t* as low as 0.8. Perovskites with $t < 1$ would have A–X bonds under tension and B–X bonds under compression; to reduce this effect the corner shared BX_6 octahedra usually tilt or rotate about pseudocubic axes to accommodate such small A cations in the interstices between them. Tilting of octahedra reduces the $Pm\bar{3}m$ symmetry of the perovskite structure to lower symmetric sub-groups, and, using crystallographic principles, a particular tilt can be associated to a specific space group or symmetry [2,3]. In addition to rotation of octahedra a distortion associated with changes in the B-X bond lengths may occur due to the presence of Jahn-Teller active B cations such as Mn^{3+}, Fe^{4+}, Ni^{3+} and Cu^{2+}. When $t > 1$, A cations are too large to fit in the 12-fold site within the BX_6 polyhedral framework and a hexagonal polytype structure may be formed. Of particular interest is the stability of the cubic phase in $BaTiO_3$ with $t \approx 1.04$ where such high tolerance factor induces cooperative ferroelectric displacement of the Ti^{4+} cations [4]. Cations with ns^2 core electrons may also induce special structural effects associated with their lone pair of electrons. The stereochemical lone pair effect of Pb on the oxygen framework in $PbTiO_3$ is known to result in strong displacements of Pb^{2+} and Ti^{4+} ions from

their polyhedral centres [4]. Cation order either in the A- or B- sites provides another variant of structural diversity in stoichiometric perovskites. The commonest type of cation order is the 1:1 B-site ordering with the general formula $AB_{0.5}B'_{0.5}X_3$. The ideal 1:1 B-site ordered perovskite crystallizes in the space group $Fm\bar{3}m$, although a diversity of lower symmetry space groups have also been assigned to possible distortions in these materials.

A second dimension of the structural diversity of perovskites is the high tolerance of the perovskite structure to low dimensionality. In terms of the layered representation of the perovskite structure (*Figure 1.1 (b)*) the parent structure is formed by alternate stacking of AX and BX_2 layers. The diversity of how this stack can be interrupted by intergrowth entities, and how flexible the layers are (in terms of being off-set in position and sequence) to accommodate different types of intergrowths, is really interesting and results in several homologous series and structural families, which are collectively referred to as layered perovskites. Ruddlesden-Popper, Dion-Jacobson, Aurivillius phases and the huge family of high-temperature superconducting cuprates [5] are examples of layered perovskites. The Ruddlesden-Popper (RP) series is an important and basic example of layered perovskites in which the alternate stacking of AX and BX_2 is interrupted by additional AX layers. If the layer structure of the perovskite is represented as $(AX\text{-}BX_2)_\infty$, the RP compounds are simply represented as $AX(AX\text{-}BX_2)_n$ where the perovskite stacks $(AX\text{-}BX_2)_n$ are separated by a single additional AX layer. The n = 1 and n = 2 members of this series are shown in *Figure 1.2 (a,b)*. As a result, the perovskite stacks $(AX\text{-}BX_2)_n$ become off-set due to a displacement of ½ (*a* + *b)* along [110] within the interlayer plane (*Figure 1.2 (c)*). The n = 1 member of the RP series has the general formula of A_2BX_4 and its structure is well known as the K_2NiF_4-type structure. Intergrowths with cations other than A may occur in perovskites; Dion-Jacobson and Aurivillius phases [5] are examples of these materials

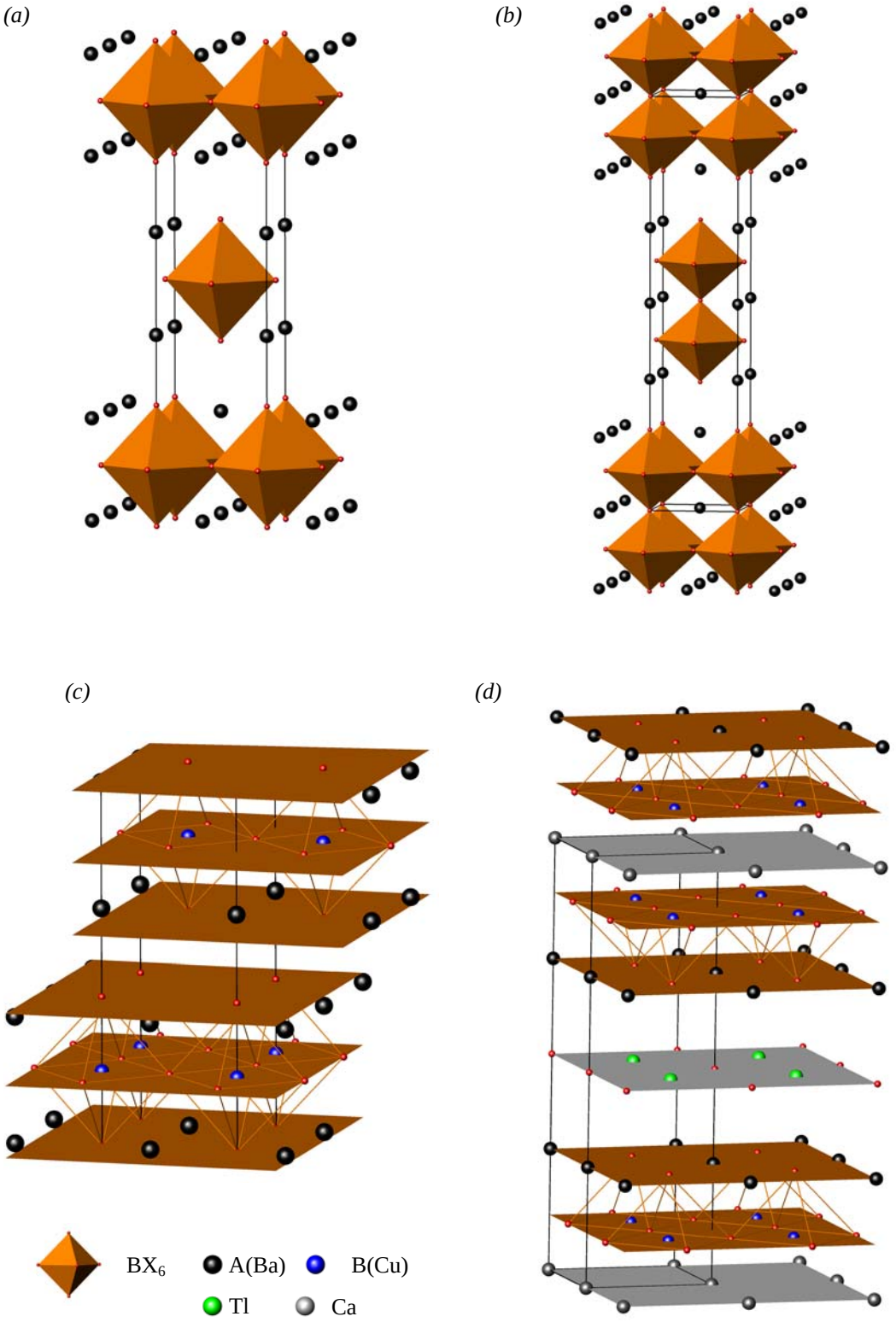

Figure 1.2 (a) The n = 1 Ruddlesden-Popper structure; (b) the n = 2 Ruddlesden-Popper structure; (c) perovskite layer shift in Ruddlesden-Popper phases; (d) representation of the layer structure of superconducting cuprates (the example illustrates the structure of $TlCaBa_2Cu_2O_7$).

where the perovskite layer stack is interrupted by intergrowths containing M^{1+} (usually alkali metal) and Bi^{3+} ions, respectively. Layered cuprates [5], however, show greater flexibility of the AX and BX_2 (CuO_2) layers to accommodate more than one type of intergrowth layers (see *Figure 1.2 (d)*). Three types of intergrowth layers often occur in layered cuprates: M (*e.g.* Y and Ca), MO (*e.g.* TlO, BaO, BiO) and CuO. The sequence, number and composition of these layers are versatile giving this family of compounds special impact in structural diversity in addition to their potential impact in industrial applications.

A third dimension of the structural diversity of perovskites arises from the high susceptibility of the perovskite materials (including layered perovskites) to nonstoichiometry. Bronzes of the type A_xBO_3 (B = W, Re, Mo) form a large family of compounds which are usually considered as A-site deficient perovskites [5]. Anion nonstoichiometry is also very common in perovskite and perovskite-related compounds [5]. Low concentrations of oxide ion vacancies or interstitials in perovskite-type oxides are often disordered and result in potential applications of the materials as ionic or mixed electronic-ionic conductors. Higher degrees of oxygen deficiency, however, usually result in ordered structures which exhibit interesting structural, magnetic and electronic properties. The present work focuses on oxygen nonstoichiometry in perovskite-type oxides; the structural, magnetic and electronic properties associated with this oxygen nonstoichiometry are investigated. A range of defect structures are discussed in this thesis, and are described in section 1.2.

1.2 Related oxygen-nonstoichiometric phases

1.2.1 Oxygen-deficient $A_2B_2O_5$ phases

$A_2B_2O_5$ is the general formula of a large number of materials which exhibit an ordered oxygen-deficiency in the $ABO_{3-\delta}$ system. Different schemes of vacancy ordering have been observed in this system. The $Ca_2Mn_2O_5$ structure and the brownmillerite structure are two examples of these ordered structures, although the latter is more common.

Adopting the layered representation of the perovskite structure, the $Ca_2Mn_2O_5$ structure is formed by removal of oxygen from every BO_2 plane of the perovskite structure where one-half of the anions in alternate $[110]_c$ rows are removed (*Figure 1.3 (a,b)*). This type of vacancy order results in doubling a pseudotetragonal $\sqrt{2}\ a_c$ axis ($b \approx 2\sqrt{2}\ a_c$) and gives sheets of five-coordinate cations with square pyramidal coordination (*Figure 1.3 (b)*). The vacancies are superimposed in adjacent sheets and the *c* axis is therefore not multiplied. $A_2B_2O_5$ compounds such as $Ca_2Mn_2O_5$ [6] and $Sr_2Mn_2O_5$ [7] crystallize in this structure.

The brownmillerite structure, on the other hand, is formed by removal of anions in alternate $[110]_c$ rows from alternate BO_2 layers giving rise to alternating layers of octahedral and tetrahedral metal centres (*Figure 1.3 (a,c)*). Tetrahedral metal centres in a given layer are corner linked to form chains running along a $[110]_c$ direction. This type of vacancy ordering does not double a pseudotetragonal $\sqrt{2}\ a_c$ axis, but ordering of vacancies between the BO_2 layers increases the *b* axis such that $b \approx 4\ a_c$ (*Figure 1.3 (c)*). Removal of oxygen from alternate BO_2 layers in the brownmillerite structure leads to significant atomic displacements within these layers to achieve optimum metal-oxygen bond-length criteria. Two opposite sets of displacements are possible in a given BO_2 layer, which correspond to cooperative rotation of the BO_4 tetrahedra in opposite directions (*Figure 1.4*)

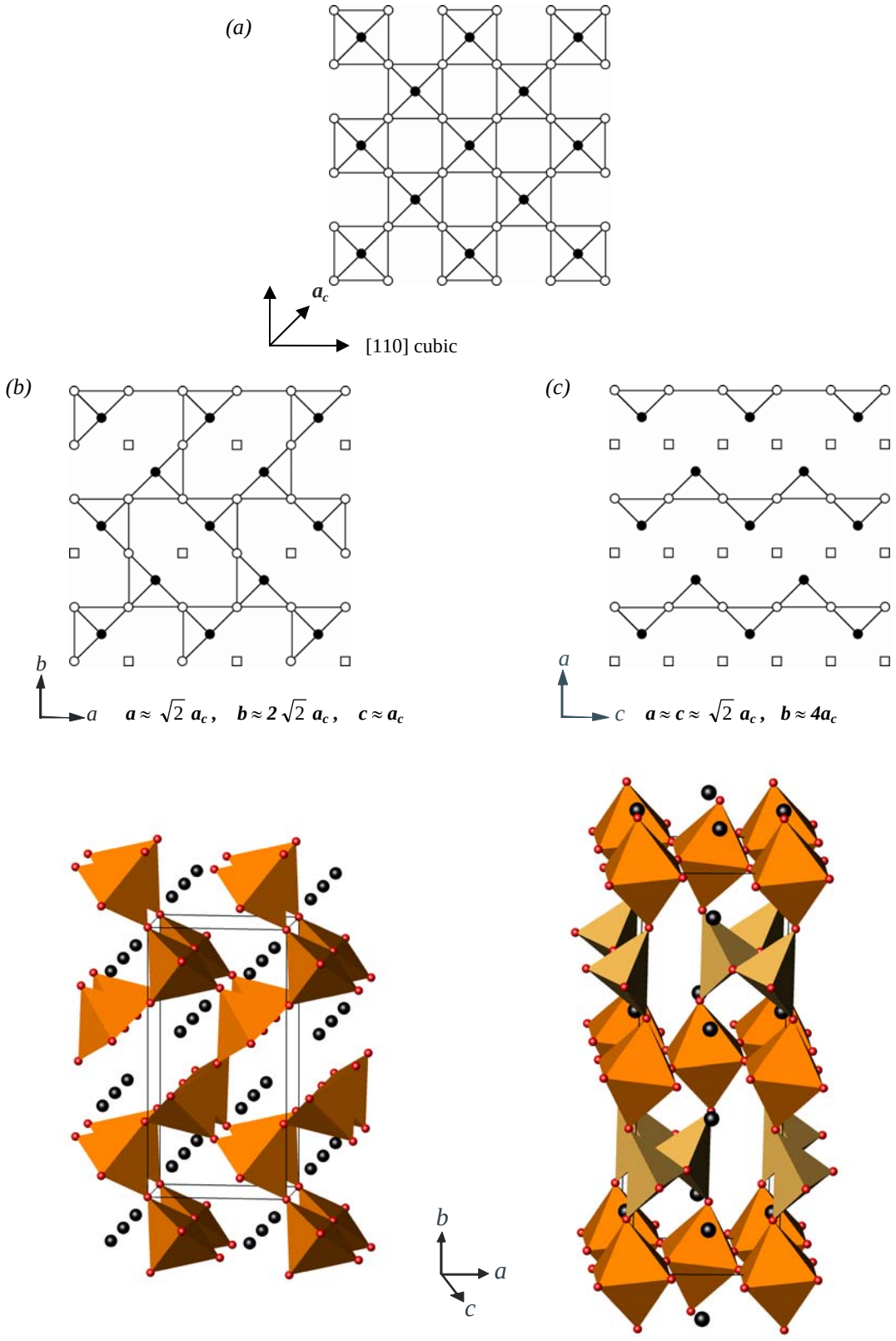

Figure 1.3 (a) A BO_2 layer of a stoichiometric perovskite ABO_3; (b) BO_2 vacancy scheme and structure of $Ca_2Mn_2O_5$; (c) BO_2 vacancy scheme and structure of a brownmillerite $A_2B_2O_5$ (the oxygen-deficient BO_2 layers alternate along *b*; *Ibm2* symmetry was used to aid clarity).

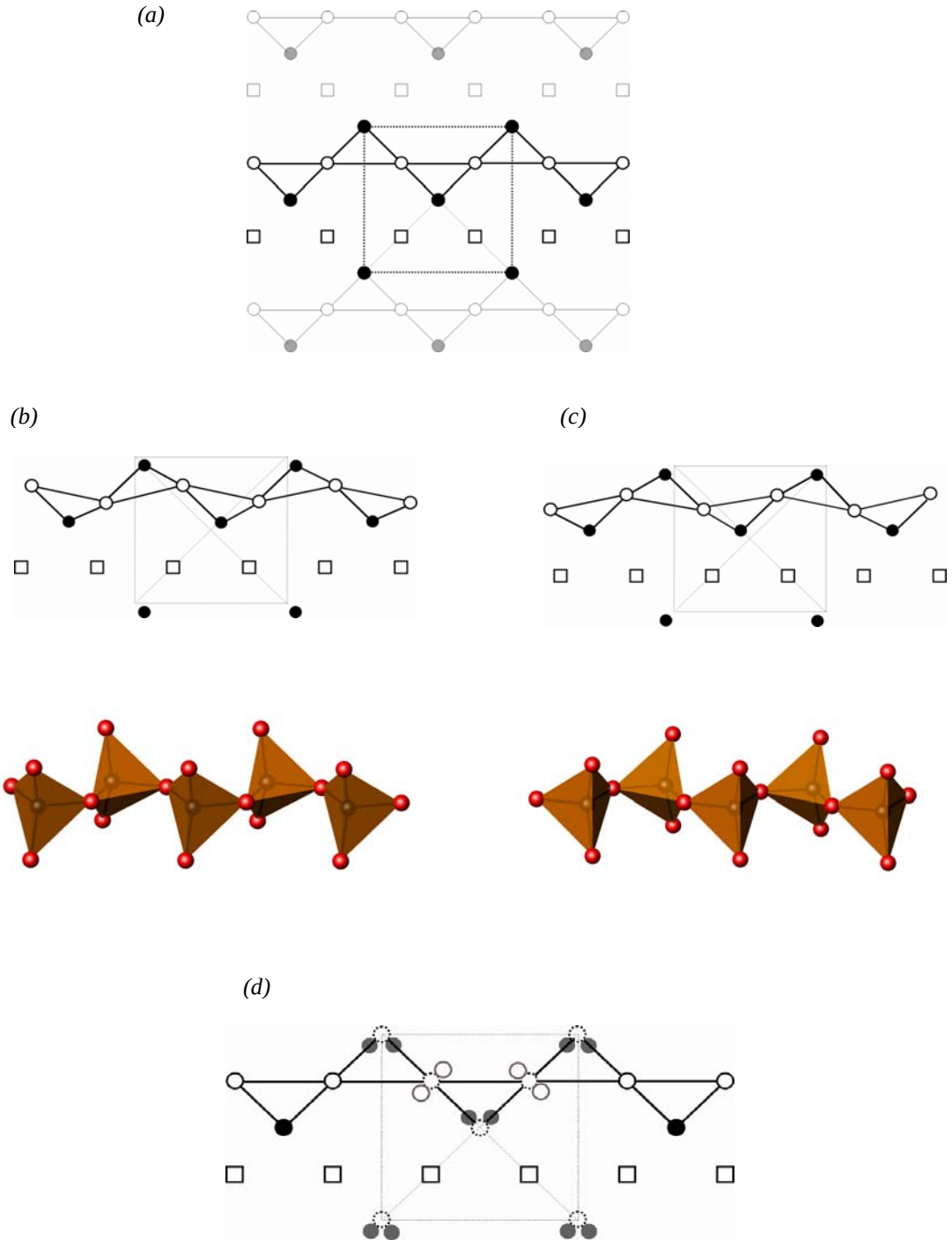

Figure 1.4 A schematic presentation of atomic displacements within a layer of tetrahedra in the brownmillerite structure, showing the ideal structure (a), and two types of displacements resulting in two different orientations of BO_4 tetrahedral chains (b and c). The split of B and O sites in the *Icmm* space group allows the two types of displacements (d).

These displacements result in two possible orientations of the tetrahedral chains in a given layer (see *Figure 1.4 (b,c)*). Although only one type of displacement normally occur in a given layer, the two types of displacements may order or disorder between adjacent layers giving rise to different symmetries of the brownmillerite structure, namely *Ibm2*, *Pcmn* and *Icmm*. In the *Ibm2* symmetry only one set of displacements exits in all the BO_2 layers; in the *Pcmn* symmetry the two sets of displacements order between layers; in the *Icmm* symmetry the two sets are disordered between layers. The latter disorder is allowed in the *Icmm* space group through splitting of B and O sites and half-occupation of these ions to the *8i* sites where they distribute randomly between two equivalent sites (*Figure 1.4 (d)*). Many $A_2B_2O_5$ compounds adopt the brownmillerite structure, *e.g.* Ca_2MnAlO_5 (*Ibm2*) [8], $Ca_2Fe_2O_5$ (*Pcmn*) [9] and $Sr_2Fe_2O_5$ (*Icmm*) [10].

1.2.2 Oxygen-deficient Ruddlesden-Popper phases

The Ruddlesden-Popper-type oxides have shown a special aptitude for oxygen deficiency which alters the transition metal oxidation states and interestingly modifies the magnetic and transport properties of these phases. Oxygen deficiency can be produced in these materials through synthesis in air/inert-atmosphere in order to achieve lower oxidation states of the B-site cations (*e.g.* $Sr_3M_2O_{7-\delta}$, M = Co, Fe [11-15]). Oxygen deficiency can also be induced by controlled reduction of near-stoichiometric phases in hydrogen. Examples include many K_2NiF_4-type phases such as $La_{2-x}Sr_xNiO_{4-\delta}$ [16,17] and $LaSrCoO_{4-\delta}$ [18]. Powerful reducing agents such as CaH_2 have recently been used to produce highly oxygen-deficient phases in which unusual two-dimensional coordination geometries of transition metal ions such as cobalt and iron have been achieved [19,20].

1.2.2.1 $A_2BO_{4-\delta}$ phases

Oxygen deficiency is usually produced in these materials by reduction of the stoichiometric A_2BO_4 phases. Regarding the two oxygen sites in this system (O1 and O2 in *Figure 1.5*), oxygen deficiency is often produced within the equatorial BO_2 planes of the structure (O1 sites). However, a distribution of oxygen vacancy between apical and equatorial sites has been reported for $NdSrCuO_{4-\delta}$ [21]. On the other hand, oxygen vacancies may order or disorder within the equatorial planes of the structure. A scheme of vacancy order within the BO_2 planes, similar to that of $Ca_2Mn_2O_5$ (see section 1.2.1), has been suggested for $Ca_2MnO_{3.5}$ [22]. The material is therefore formed of sheets of five-coordinate cations with square pyramidal coordination. A different pattern of MnO_5 square pyramids interconnection in these sheets has been suggested by Greaves *et al.* for $Sr_2MnO_{3.5}$ [23]. Reduction studies on $La_{2-x}Sr_xNiO_{4-\delta}$ phases showed that the vacancy in the Ni^{1+}-containing materials $La_{1.6}Sr_{0.4}NiO_{3.47}$ and $LaSrNiO_{3.1}$ is confined to the equatorial planes with strong preference to occur along one of the tetragonal axes of the K_2NiF_4 structure [16,17]. More recent studies on the reduction of $LaSrCoO_4$ using hydrogen and sodium hydride allowed the isolation of reduced phases with the composition $LaSrCoO_{3.5-x}$ [18]. Oxygen vacancies in these materials were disordered and confined to the equatorial BO_2 planes of the structure. This type of vacancy does not lead to symmetry lowering and the tetragonal symmetry of the parent compound (*I4/mmm* space group) was retained.

1.2.2.2 $A_3B_2O_{7-\delta}$ phases

Unlike the n = 1 RP phases $A_2BO_{4-\delta}$, oxygen deficiency is more common in the n = 2 phases $A_3B_2O_{7-\delta}$. In addition to the equatorial BO_2 oxygen (O1), two types of AO oxygens can be distinguished in this system: the one linking the BO_6 octahedra in the

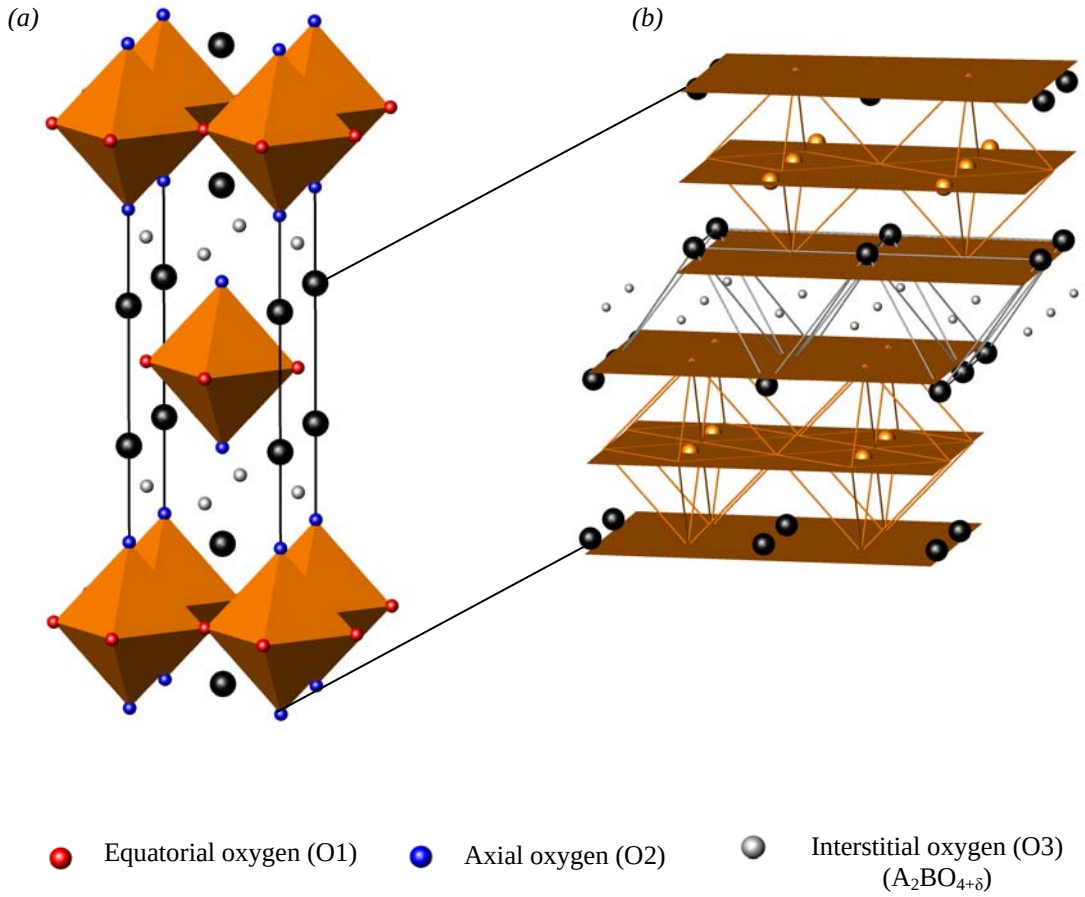

Figure 1.5 The n=1 Ruddlesden-Popper $A_2BO_{4\pm\delta}$ phases: (a) polyhedral structure and (b) layer structure.

perovskite region (O3) and the AO oxygen in the intergrowth region (O2) (*Figure 1.6 (a)*). High degrees of oxygen deficiency could be achieved in this system with the oxygen vacancy usually accommodated in O1 or O3 positions. A simple random distribution of oxygen vacancy within the BO_2 planes (similar to that observed in the n = 1 phases) is reported for $Sr_3Mn_2O_{6.55}$ [24]. Further reduction of this phase to the O6-type phase ($Sr_3Mn_2O_6$) resulted in ordering of the vacancy within the BO_2 planes in a manner similar to that observed in the single-layered $Sr_2MnO_{3.5}$ [25]. Apart from manganese-containing phases, oxygen deficient $A_3B_2O_{7-\delta}$ phases are usually formed by removal of oxygen from the apical O3 sites. $La_3Ni_2O_{6.35}$ [26], for example, is formed by loss of 65% of the apical

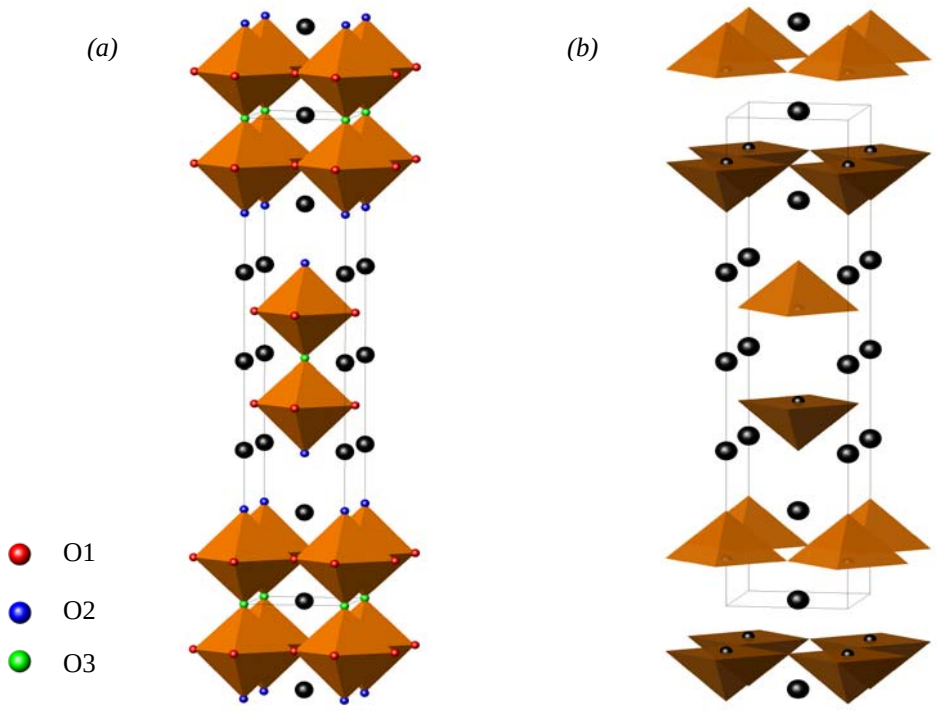

Figure 1.6 (a) The $A_3B_2O_7$ n = 2 RP structure; (b) a reduced $A_3B_2O_6$ phase with apical oxygen vacancies giving BO_5 square pyramids.

(O3) oxygen. The O6-type phases containing cobalt and iron are also formed by the complete elimination of oxygen from O3 sites giving rise to a square pyramidal coordination around transition metal ions [11,12] (*Figure 1.6 (b)*). This structure is first reported for $La_{2-x}Sr_{1+x}Cu_2O_6$ [27]. Materials of this type retain the crystal symmetry of the parent O7 compounds (*I4/mmm* space group). Further reduction of these materials may locate oxygen vacancies within the equatorial BO_2 planes as well as the apical O3 sites. Oxygen vacancies in $Sr_3CoFeO_{5.45}$ [15] are located in O3 sites and in the BO_2 planes leading to cobalt and iron in tetrahedral and pyramidal coordinations. Studies on $Sr_3Co_2O_{5+\delta}$ [13] showed that oxygen vacancies are found both in O1 and O3 sites with the majority being along one crystallographic axis in the BO_2 plane which induced an orthorhombic distortion in these materials. $Sr_3Co_2O_{5.78}$ [11], however, has a different

defect structure where oxygen vacancies are ordered along the *b* axis resulting in a 3x supercell in this direction. The compound therefore crystallizes in the orthorhombic space group *Immm* with the coordination around cobalt being both octahedral and square pyramidal [11].

1.2.3 Oxygen-excess $A_2BO_{4+\delta}$ phases

The n = 1 RP A_2BO_4 phases consist of alternate perovskite ($AO\text{-}BO_2$) and rock salt (AO) layers and exhibit a tetragonal symmetry (*I4/mmm* space group) when *t* is close to unity (*Figure 1.5*). Orthorhombic and even monoclinic distortions are observed in this system when $t < 1$ [28]. An important feature of this structure is the ability to accommodate excess oxygen between adjacent rock salt layers, whereby excess ions are tetrahedrally coordinated by A ions *(Figure 1.5 (b))*. The excess negative charge introduced by excess oxygen is neutralized by oxidation of B ions. This effect has been regarded as a way to relieve the internal lattice stresses associated with $t < 1$ [29] (in addition to rotation of BO_6 octahedra). La_2CoO_4, La_2NiO_4 and La_2CuO_4 have $t < 1$ at room temperature [28]. In the absence of interstitial oxygen these compounds are orthorhombic at room temperature as a result of cooperative rotation of MO_6 polyhedra. Interstitial oxygen is introduced in La_2NiO_4 on sintering in air [30] while a pressure of 3 kbar is required to incorporate oxygen in La_2CuO_4 [31,32]. La_2CoO_4, on the other hand, is spontaneously oxidized in air to oxygen-excess phases, *e.g.* $La_2CoO_{4.16}$ [33]. A tetragonal symmetry has been suggested for oxygen-excess $La_2NiO_{4+\delta}$ phases such as single crystal $La_2NiO_{4.13}$ [34] and polycrystalline $La_2NiO_{4+\delta}$ ($\delta > 0.14$) [35]. Considering the fact that the thermal expansion coefficient of A–O is generally larger than that of B–O, *t* will increase with temperature and $t \approx 1$ is expected for $A_2BO_{4(+\delta)}$ compounds at sintering temperature

[29]. For $La_2NiO_{4+\delta}$, the compound is expected to adopt a tetragonal symmetry irrespective of oxygen stoichiometry [36] and a transition from orthorhombic to tetragonal symmetry is reported for stoichiometric La_2NiO_4 at 500 °C [35]. Thermogravimetric studies on $La_2NiO_{4+\delta}$ have shown that excess oxygen starts to leave the oxide at about 350 ºC and the process is reversible [37,38]. Different degrees of oxygen hyperstoichiometry have been assigned for $La_2NiO_{4+\delta}$, [36,39] which are generally reduced under strontium doping where the tetragonal symmetry is retained [40,41].

Excess oxygen in $A_2BO_{4+\delta}$ is accommodated between the rock salt layers (*Figure 1.5*). According to Jorgensen *et al.* [30], interstitial oxygen in $La_2NiO_{4+\delta}$ is located at (0.25, 0.25, ~ 0.23) site in the orthorhombic *Fmmm* lattice which allows interstitial oxygen to be tetrahedrally coordinated by four La atoms, but requires four neighbouring (apical) oxygen atoms to be displaced ~ 0.5 Å form their normal lattice sites. Heaney *et al.* [42], however, modelled the incorporation of the excess oxygen as substitution of a nonbonded O-O for an apical oxygen.

1.3 Related magnetic structures

Cooperative magnetic effects, which often occur in perovskite oxides, are ferro- and antiferro- magnetism. These effects have been explained in terms of indirect spin coupling of the magnetic B cations *via* intervening nonmagnetic oxide ions. This is often referred to as exchange interactions. Two types of exchange interactions namely double- and super- exchange have been used to explain ferro- and antiferro- magnetism [43]. In the ferromagnetic (FM) mixed-valence compound $La_{1-x}Ca_xMn^{III/IV}O_3$, the double-exchange mechanism considers an electron on Mn^{3+} to be mobile and to transfer to an intervening oxygen which in turn transfers an electron of same spin to the neighbouring Mn^{4+} (*Figure 1.7 (a)*). The net result is parallel spins on the manganese ions, an increase in the conductivity and destruction of the MnO_6 distortion associated with the Jahn-Teller active Mn^{3+} ions. In antiferromagnetism the unpaired d electrons of pairs of B ions will couple through covalent bonding with the p orbitals of the intervening O^{2-} ions (*Figure 1.7 (b)*) resulting in antiparallel alignment of spins and lowering the overall energy of the system. Super-exchange may result in FM or antiferromagnetic (AFM) order depending on a number of factors such as the electron configuration of the magnetic ions, the angle of interaction and the type of B-O-B bonding. The outcome of magnetic coupling in perovskite systems can often be predicted from Goodenough-Kanamori rules of magnetic exchange [44,45]. The possible AFM ordering schemes in perovskite oxides have been shown by Wollan and Koehler [46] to be three types, namely A-type, C-type and G-type (Figure *1.7 (c)*). At least one of the perovskite subcell axes will be doubled in the magnetic structure due to the antiparallel alignment of the spins. In the A-type structure atoms in adjacent layers have opposite spins; in the C-type structure neighbouring atoms in a given layer have opposite spins; in the G-type structure the spin on a B-atom is antiparallel to the

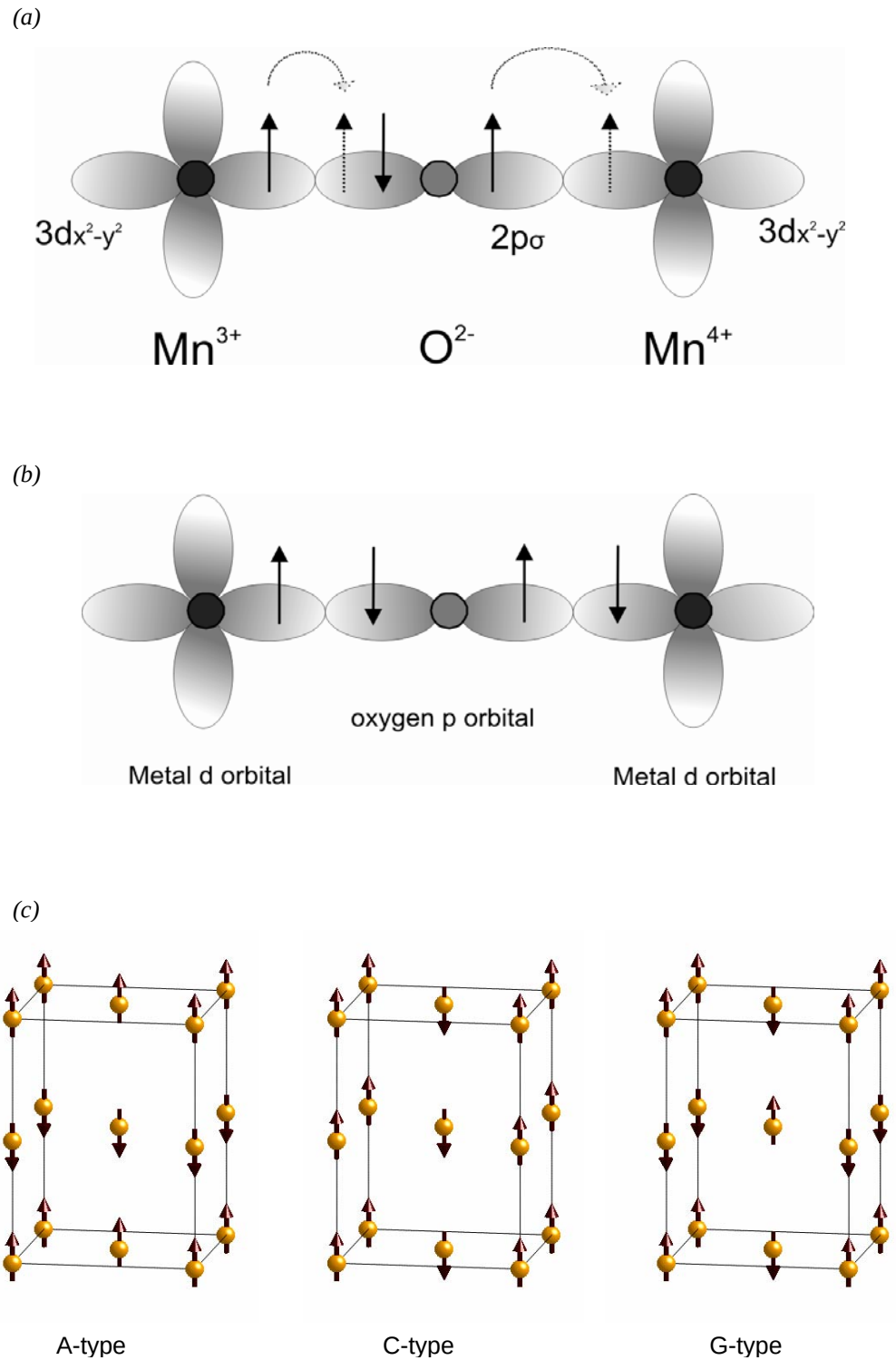

Figure 1.7 (a) Ferromagnetic and (b) antiferromagnetic exchange interactions between two metal ions coupled via an oxygen p orbital; (c) antiferromagnetic ordering schemes in perovskite-type compounds.

spin at all six neighbours. The perovskite B-lattice, and consequently the magnetic order, are not strongly affected by structural modifications such as distortion and anion nonstoichiometry. However, the three-dimensional nature of the magnetic order may be affected in layered compounds where the BO_2 layers are further separated by intergrowth layers and/or displaced to accommodate the intergrowths. If A cations are nonmagnetic and B cations are magnetic, the A_2BO_4 phases, for example, may have strong intralayer coupling and weak interlayer coupling. This often results in the so-called two-dimensional magnetic ordering. This type of magnetic ordering has been observed in Sr_2FeO_4, La_2CuO_4 and La_2NiO_4 phases [47-49]. However, a change from two-dimensional to three-dimensional ordering may occur with decreasing temperature as a result of increasing interlayer magnetic interactions. It has been suggested that the change from two-dimensional to three-dimensional correlations depends on the electron configuration of B cations and the extent of covalency of the A–O bond [50]. When A_2BO_4 materials exhibit three-dimensional magnetic ordering, the moments can point along the *z* axis, as found in Ca_2MnO_4, or can be confined to the *xy* plane (*xy*-antiferromagnetism) as in most cuprate oxides and La_2NiO_4. A doubling of the unit cell along the *c* axis is observed in Ca_2MnO_4 [51,52] (*Figure 1.8 (a)*). Two types of collinear models related to La_2CuO_4 and $La_2NiO_{4+\delta}$ [49,53-55] often occur in *xy*-antiferromagnets; both models consist of alternate (100) ferromagnetic sheets coupled antiferromagnetically, with the moments aligned either parallel (La_2CuO_4-type model) or perpendicular ($La_2NiO_{4+\delta}$-type model) to the ferromagnetic planes (*Figure 1.8 (b,c)*). These collinear structures clearly have orthorhombic symmetry and can not be applied for tetragonal A_2BO_4 phases. Whenever no evidence of symmetry reduction from tetragonal to orthorhombic is observed in the A_2BO_4 phases, alternative noncollinear magnetic structures with tetragonal symmetry should be

considered. Based on magnetic symmetry arguments, these noncollinear structures can be derived and viewed as coherent supervisions of each structure and its 90° counterpart [56] (*Figure 1.9 (a,b)*). Tetragonal noncollinear structures of this type have been used to account for the magnetic coupling in compounds such as Pr_2CuO_4 [54] and $LaSrCoO_{4-\delta}$ [18]; however, a magnetic component parallel to the *z* axis is considered in the latter compound.

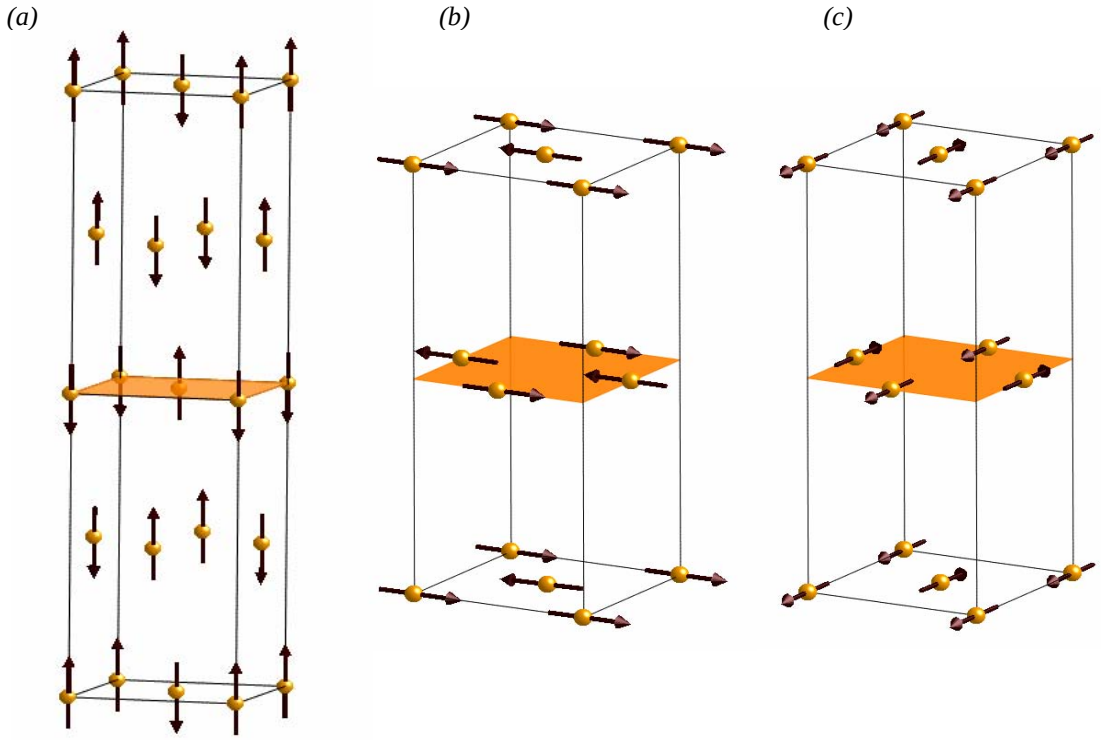

Figure 1.8 Antiferromagnetic ordering schemes in (a) Ca_2MnO_4, (b) La_2CuO_4-type and (c) $La_2NiO_{4+\delta}$-type compounds.

1.9a)

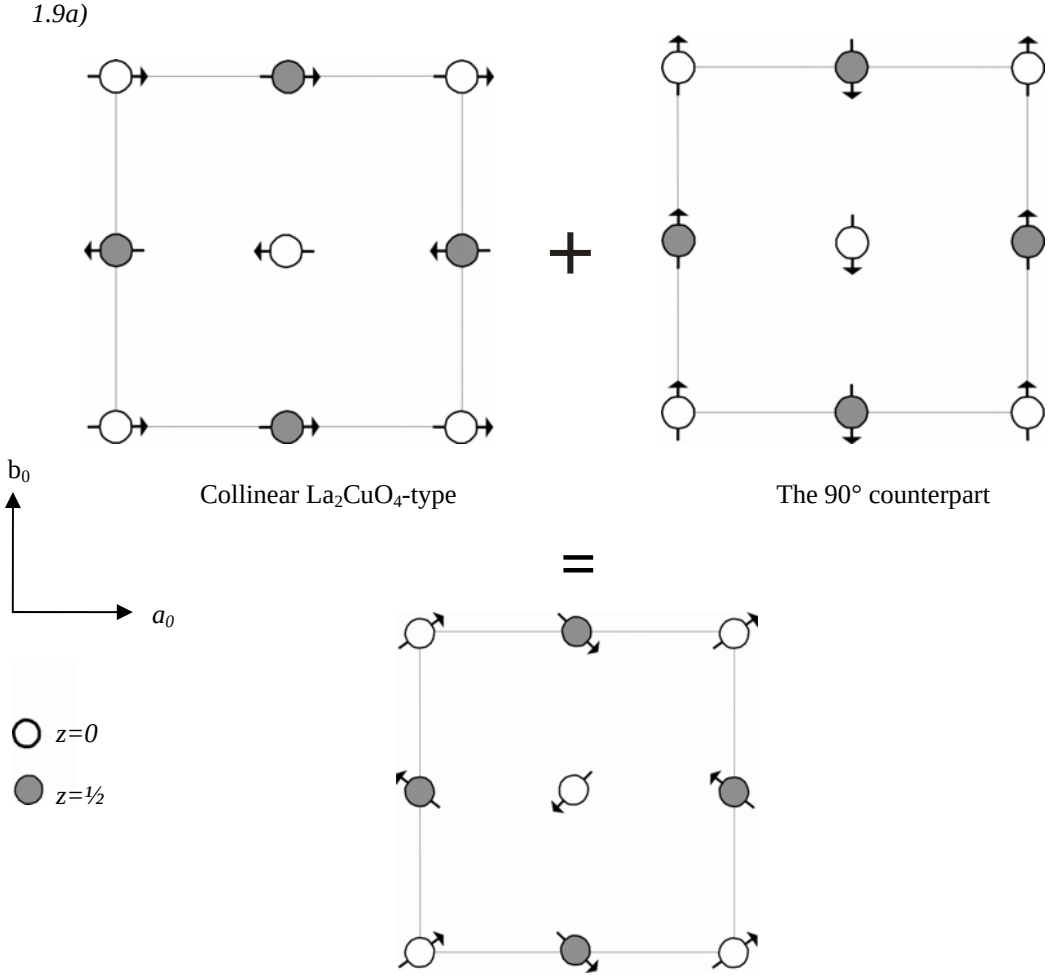

Collinear La_2CuO_4-type

The 90° counterpart

Noncollinear La_2CuO_4-type

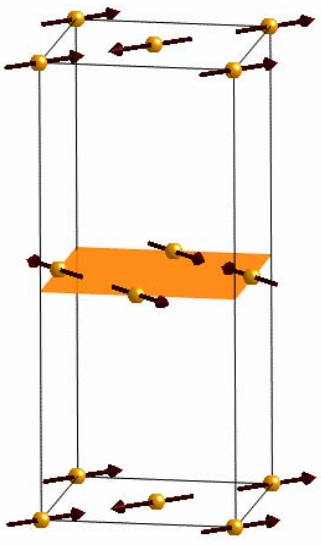

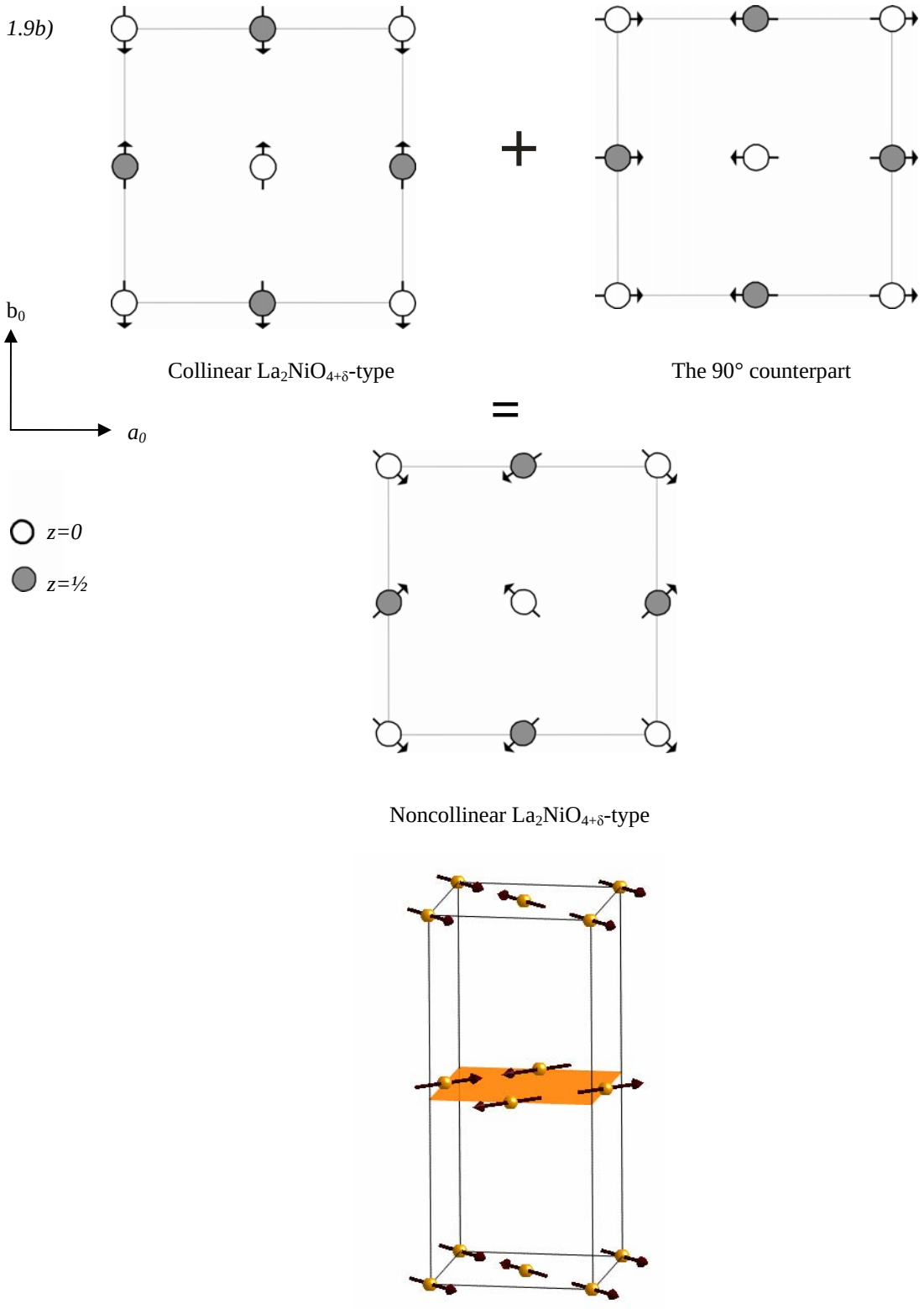

Figure 1.9 Relation between the orthorhombic collinear and tetragonal noncollinear magnetic models for (a) La_2CuO_4-type and (b) $La_2NiO_{4+\delta}$-type compounds.

1.4 Transport properties of $A_2BO_{4+\delta}$

$A_2BO_{4+\delta}$ phases have attracted a renewed interest in the literature since the observation of high oxygen transport properties in $La_2NiO_{4+\delta}$. The low-temperature electronic properties of $A_2BO_{4+\delta}$ phases have been subjected to earlier extensive studies since the discovery of superconductivity in $La_2CuO_{4+\delta}$. Recently, more attention has been focused on the high temperature electronic and oxygen-transport properties of these materials. $La_2NiO_{4+\delta}$-based materials are more widely studied because of their high transport properties and relative phase stability; however, comparisons with the data available for $La_2CuO_{4+\delta}$ are frequently established. At oxygen partial pressures of 3 kbar, $La_2CuO_{4+\delta}$ exhibits oxygen hyperstoichiometry but the δ values are lower than that observed for $La_2NiO_{4+\delta}$ [31,32]. Electrical conductivity of $La_2CuO_{4+\delta}$ at 25-1000 ºC was established to be temperature independent (10 Ω^{-1} cm^{-1}), while other rare-earth derivatives of the general formula Ln_2CuO_4 are semiconductors [57-59]. $La_2NiO_{4+\delta}$, on the other hand, exhibits a semiconductor to metal-like transition at about 350 ºC [58-60]. The semiconductor-metal transition also occurs in strontium-doped nickelates with the transition temperature decreasing with increasing x in $La_{2-x}Sr_xNiO_{4+\delta}$, and $LaSrNiO_4$ is metallic at room temperature [29,61]. The transition also occurs in $La_2Ni_{1-x}Co_xO_{4+\delta}$ phases with small x values [62]. The heat capacity measurements performed on $La_2NiO_{4+\delta}$ in air at 300-400 ºC revealed a sharp exothermic peak near $T_{transition}$ preceded at a slightly lower temperature by a sharp endothermic peak [63]. In the low temperature range, $T < T_{transition}$, the conductivity of $La_2NiO_{4+\delta}$ was described by the relation

$$\sigma(T) = \sigma_0 \exp(-E_g / k_B T) \qquad (1.3)$$

with E_g = 0.053 eV [58]. The relation represents simple thermally activated electrical conductivity in which an electron or hole (as the charge carrier) hops between localized

states; in this equation, σ_0 is the electrical conductivity at extremely high temperatures, E_g is the thermal activation energy of the electron or hole and k_B is the Boltzmann constant. Goodenough *et al.* suggested a localized-electron to itinerant-electron transition among the antibonding σ* electrons to account for the semiconductor-metal transition observed in $La_2NiO_{4+\delta}$ [29,64,65]. Localized-electron behaviour is characterized by localized magnetic moments on the cations and small polaron conduction, and the itinerant-electron behaviour is characterized by metallic conduction and possibly Pauli paramagnetism. They showed that the thermal activation energy E_g = 53 meV ≈ $k\mathrm{T}_{\mathrm{Transition}}$ found for the conductivity of $La_2NiO_{4+\delta}$ phases is characteristic of the localized-electron to itinerant-electron transition. At lower temperatures, the electron hopping is reduced further by small polaron formation; at higher temperatures, a kT greater than E_g puts the mobile electrons or holes in the threshold of itinerant character. According to the Goodenough model, the transition from localized to itinerant electronic behaviour will be accompanied by a lattice contraction and will also be endothermic as a result of the loss of the entropy associated with disordered localized-electron spins [29]. He suggested that an associated orthorhombic-tetragonal transition at $\mathrm{T}_{\mathrm{transition}}$ presumably provides the exothermic component of the complex transition at $\mathrm{T}_{\mathrm{transition}}$. Bassat *et al.* [37,38] have shown that $La_2NiO_{4+\delta}$ does not maintain constant composition at T > 350 ºC which should be considered in the interpretation of the origin of the semiconductor-metal transition. The study revealed that oxygen starts to leave the oxide at $\mathrm{T} \approx \mathrm{T}_{\mathrm{transition}}$. They suggested that the endothermic variation in the heat capacity curve may correspond to the oxygen departure while the exothermic part corresponds to an associated structural reorganization following the oxygen loss [37]. The following equilibrium (expressed using Kröger-Vink notation)

$$\frac{1}{2}\,O_2 \leftrightarrow O_i'' + 2h^{\bullet} \qquad (1.4)$$

is established for $La_2NiO_{4+\delta}$ at high temperatures in oxidizing conditions. In this equilibrium O_i'' is an interstitial O^{2-} and $h^{\bullet}$ is a hole which may be located on a lattice oxygen or Ni cation. Bassat *et al.* [37] have expressed the conductivity in terms of the concentration of the holes ($h^{\bullet}$), assuming that the holes are the main charge carrier. They showed that below 350 ºC the oxide may be considered as having constant composition. In the high temperature range the hole-content is subject to variations caused by oxygen loss through reactions such as

$$O_i'' + 2O_o^{\bullet} \leftrightarrow \frac{1}{2}O_2 + 2O_o^{\times} \qquad (1.5)$$

$$2O_o^{\bullet} \leftrightarrow \frac{1}{2}O_2 + V_o^{\bullet\bullet} + O_o^{\times} \qquad (1.6)$$

where holes are assumed to be located on lattice oxygen. In these equilibria $O_o^{\bullet}$ is a lattice O^{1-} (lattice oxygen carrying a hole), $O_o^{\times}$ is a lattice O^{2-} and $V_o^{\bullet\bullet}$ is an oxygen vacancy. Based on the defect model in equation 1.4, the conductivity of the related $La_2Ni_{0.9}Co_{0.1}O_{4+\delta}$ phases at high temperature was shown to be predominately *p*-type electronic with small-polaron conduction mechanism [66].

$La_2NiO_{4+\delta}$ exhibits maximum electronic conductivity of about 100 Ω^{-1} cm^{-1} which is not very high compared with mixed conducting perovskites; however, the material is found to exhibit significant and high oxide ion conductivity at intermediate temperatures. Kilner *et al.* have shown that the oxygen diffusivity of $La_2NiO_{4+\delta}$ is higher than that of $La_{0.6}Sr_{0.4}Co_{0.2}Fe_{0.8}O_3$ (LSCF) and one order of magnitude lower than the best perovskite oxide ion conductor $La_{0.3}Sr_{0.7}CoO_3$ [67]. These observations have stimulated an interest in $A_2BO_{4+\delta}$ phases as possible candidates for use in ceramic oxygen generators and solid

oxide fuel cells (SOFCs). Oxygen diffusivity of $La_2NiO_{4+\delta}$ is shown to be two or three order of magnitude higher than that of the oxygen-deficient $La_{2-x}Sr_xCuO_{4-\delta}$ [68]. An important feature of oxygen diffusion in these materials is the anisotropic nature of the diffusivity. It has been shown that the oxygen diffusivity along the perovskite layers of $La_2CuO_{4+\delta}$ (*ab* plane) was considerably higher than along the *c* direction [68]. Oxygen diffusion in $La_2CuO_{4+\delta}$ and $La_{2-x}Sr_xCuO_{4\pm\delta}$ solid solutions was generally assumed to occur *via* a vacancy mechanism. The oxygen diffusivity in $La_{2-x}Sr_xCuO_{4\pm\delta}$ solid solutions increases slightly with strontium content (x = 0-0.07) and then decreases for x = 0.07-0.20. This behaviour is explained by ordering of the oxygen sublattice or by immobilization of oxygen vacancies due to formation of defect clusters [68,69]. Kharton *et al.* have shown that both oxygen hyperstoichiometry and oxygen ionic conductivity in $La_2Cu_{1-x}Co_xO_{4+\delta}$ increase with partial substitution of copper with cobalt indicating participation of interstitial oxygen in the oxygen transport process [70]. With the higher degree of interstitial oxygen in $La_2NiO_{4+\delta}$, the oxygen diffusion is expected to occur *via* interstitial oxygen. However, it has been assumed from oxygen permeability studies that both oxygen interstitial migration and vacancy diffusion mechanisms may contribute to the total ionic conductivity of iron-doped $La_2NiO_{4+\delta}$ phases [71]. An atomistic study of oxygen migration in $La_2NiO_{4+\delta}$ [72] indicated that diffusion occurs *via* an interstitialcy mechanism. The study indicated that the migration within the *ab* plane occurs with far lower activation energy than migration in the *c* direction which suggests anisotropic oxygen diffusivity in the compound.

1.5 Aims of project

There are few reports in the literature where perovskite-type oxides contain pure Co^{2+} in their B-sites. These phases are often prepared under oxygen-free or reducing conditions due to their susceptibility to oxidation by atmospheric air. Apart from La_2CoO_4, the presence of Co^{2+} in perovskite-type oxides is often linked to oxide ion vacancies; $La_2Co_2O_5$, $La_4Co_3O_9$ and $LaSrCoO_{3.5-x}$ [73,74,18] are examples of such materials where oxide ion vacancies are either ordered or disordered. Octahedral, tetrahedral, pyramidal and even square planar or trigonal planar coordinations were assigned to cobalt ions in these materials, which indicate the flexibility of cobalt ions to accommodate a wide range of coordination environments. These phases, however, are unstable in air and also have a limited stability under reducing conditions.

On the other hand, stoichiometric K_2NiF_4-type phases containing Co^{2+} or Co^{2+}/Co^{3+} may be converted to oxygen hyperstoichiometric phases *via* oxidation of some Co^{2+} to Co^{3+}. This effect has been observed in $La_2Co(M)O_{4+\delta}$ phases [75-77] where the excess oxygen is incorporated between the rock-salt layers as described in section 1.2.3. Oxygen hyperstoichiometry has also been suggested for strontium-doped phases containing Co^{2+}/Co^{3+}, *i.e.* $(La,Sr)_2Co^{II/III}O_4$ [78,79], but these materials have not been fully characterized.

This study aimed to utilize the variety of oxidation states and coordination flexibility of cobalt in layered perovskites to achieve oxygen nonstoichiometry (and mixed valency) that is stable in different oxygen partial pressure and temperature environments. Such materials may be of great interest in applications such as SOFCs and oxygen separation membranes. It has been suggested that perovskite-type oxides with a mixed B-site state such as $Co^{II/III}_{0.5}$-$M_{0.5}$, where M is a relatively stable metal ion (with respect to

changing oxygen partial pressure), may exhibit an improved phase-stability under different oxygen partial pressures, allowing reduction to oxygen-deficient phases under reducing conditions (due to reduction of Co^{3+} to Co^{2+}) and oxidation to oxygen-excess phases under oxidizing conditions (due to oxidation of Co^{2+} to Co^{3+}).

The study also aimed to investigate the type of oxygen vacancy which can be produced under reduction of Co^{3+} to Co^{2+} in different perovskite-type oxides, and to investigate magnetic interactions between Co^{2+} and cations such as Fe^{3+}, Mn^{3+}, Cr^{3+} and Ni^{2+}. Perovskite-type materials with the elemental composition A = La, Sr, B = $Co_{0.5}M_{0.5}$, X = O were therefore suggested in this study, where M = Fe, Mn, Cr and Ni, and the structure is single-layered, double-layered or simple perovskite; the focus of attention was on single-layered materials.

The synthesis and characterization of the n = 1 RP phases $La_{2-x}Sr_xCo_{0.5}M_{0.5}O_{4\pm\delta}$ (M = Fe, Mn, Cr, Ni) are described in chapters 3, 4 and 5. Chapter 6 describes the structural and magnetic properties of the n = 2 RP phases $La_{1+x}Sr_{2-x}CoMnO_{7-\delta}$. The new perovskite-related materials $LaSrCoFeO_5$, $LaSrCoFeO_5F$ and $LaSrCoFeO_{5.5}$ were also synthesized and characterized (chapter 7).

1.6 References

[1] V. M. Goldschmidt, Geochemische Verteilungsgesetze der Elementer V11. Skrifter Norske Videnskaps Akademi Klasse 1. Matematisk, Naturvidenskaplig Klasse, Oslo, 1926.

[2] A. M. Glazer, *Acta Cryst*. **B28** (1972) 3384.

[3] A. M. Glazer, *Acta Cryst*. **A31** (1975) 756.

[4] J. B. Goodenough, *Prog. Solid State Chem*. **5** (1971) 145.

[5] R.H. Mitchell, Perovskites**:** Modern and Ancient**,** Almaz Press, Ontario, Canada, 2002.

[6] K. R. Poeppelmeier, M. E. Leonowicz, J. M. Longo, *J. Solid State Chem.* **44** (1982) 89.

[7] V. Caignaert, N. Nguyen, M. Hervieu, B. Raveau, *Mat. Res. Bull.* **20** (1985) 479.

[8] A. J. Wright, H. M. Palmer, P. A. Anderson, C. Greaves, *J. Mater. Chem.* **12** (2002) 978.

[9] P. Berastegui, S. -G. Eriksson, S. Hull, *Mat. Res. Bull.* **34** (1999) 303.

[10] C. Greaves, A. J. Jacobson, B. C. Tofield, B. E. F. Fender, *Acta Cryst. B* **31** (1975) 641.

[11] S. E. Dann, M. T. Weller, *J. Solid State Chem.* **115** (1995) 499.

[12] S. E. Dann, M. T. Weller, D. B. Currie, *J. Solid State Chem.* **97** (1992) 179.

[13] J. M. Hill, B. Dabrowski, J. F. Mitchell, J. D. Jorgensen, *Phys. Rev. B* **74** (2006) 174417.

[14] L. Viciu, H. W. Zandbergen, Q. Xu, Q. Huang, M. Lee, R.J. Cava, *J. Solid State Chem.* **179** (2006) 500.

[15] Y. Bréard, C. Michel, M. Hervieu, F. Studer, A. Maignan, B. B. Raveau, *Chem. Mater.* **14** (2002) 3128.

[16] M. Crespin, J. M. Bassat, P. Odier, P. Mouron, J. Choisnet, *J. Solid State Chem.* **84** (1990) 165.

[17] M. Crespin, C. Landron, P. Odier, J. M. Bassat, P. Mouron, J. Choisnet, *J. Solid State Chem.* **100** (1992) 281.

[18] M. A. Hayward, M. J. Rosseinsky, *Chem. Mater.* **12** (2000) 2182.

[19] A. Bowman, M. Allix, D. Pelloquin, M. J. Rosseinsky, *J. Am. Chem. Soc.* **128** (2006) 12606.

[20] H. Kageyama, T. Watanabe, Y. Tsujimoto, A. Kitada, Y. Sumida, K. Kanamori, K. Yoshimura, N. Hayashi, S. Muranaka, M. Takano, M. Ceretti, W. Paulus, C. Ritter, G. André, *Angew. Chem. Int. Ed.* **47** (2008) 5740.

[21] P. H. Labbe, M. Ledesert, V. Caignaert, B. Raveau, *J. Solid State Chem.* **91** (1991) 362.

[22] M. E. Leonowicz, K. R. Poeppelmeier, J. M. Longo, *J. Solid State Chem.* **59** (1985) 71.

[23] L. J. Gillie, A. J. Wright, J. Hadermann, G. Van Tendeloo, C. Greaves. *J. Solid State Chem.* **167** (2002) 145.

[24] J. F. Mitchell, J. E. Millburn, M. Medarde, S. Short, J. D. Jorgensen, *J. Solid State Chem.* **141** (1998) 599.

[25] L. J. Gillie, A. J. Wright, J. Hadermann, G. Van Tendeloo, C. Greaves, *J. Solid State Chem.* **175** (2003) 188.

[26] Z. Zhang, M. Greenblatt, J. B. Goodenough, *J. Solid State Chem.* **108** (1994) 402.

[27] N. Nguyen, L. Er-Rakho, C. Michel, J. Choisnet, B. Raveau, *Mater. Res. Bull.* **15** (1980) 891.

[28] P. Ganguly, C. N. R. Rao, *J. Solid State Chem.* **53** (1984) 193.

[29] Y. Takeda, R. Kanno, M. Sakano, O. Yamamoto, M. Takano, Y. Bando, H. Akinaga, K. Takita, J. B. Goodenough, *Mat. Res. Bull.* **25** (1990) 293.

[30] J. D. Jorgensen, B. Dabrowski, Shiyou Pei, D. R. Richards, D. G. Hinks, *Phys. Rev. B* **40** (1989) 2187.

[31] J. Beille, B. Chevalier, G. Demazeau, F. Deslandes, J. Etourneau, O. Laborde, C. Michel, P. Lejay, J. Provost, B. Raveau, A. Sulpice, J. L. Tholence, R. Tournier, *Physica B* **146** (1987) 307.

[32] J. D. Schirber, B. Morosin, R. M. Merrill, P. F. Hlava, E. L. Venturini, J. F. Kwak, P. J. Nigrey, R. J. Baughman, D. S. Ginley, *Physica C* **152** (1988) 121.

[33] A. Nemudry, P. Rudolf, R. Schollhorn, *Solid State Ionics* **109** (1998) 213.

[34] W. Paulus, A. Cousson, G. Heger, A. Revcolevschi, G. Dhalenne, S. Hosoya, *Physica B* **234-236** (1997) 20.

[35] J. Rodriguez-Carvajal, M. T. Fernandez-Diaz, J. L. Martinez, *J. Phys.:Condens. Matter* **3** (1991) 3215.

[36] D. E. Rice, D. J. Buttrey, *J. Solid State Chem.* **105** (1993) 197.

[37] P. Odier, J. M. Bassat, J. C. Rifflet, J. P. Loup, *Solid State Commun.* **85** (1993) 561.

[38] J. M. Bassat, P. Odier, J. P. Loup, *J. Solid State Chem.* **110** (1994) 124.

[39] H. Tamura, A. Hayashi, Y. Ueda, *Physica C* **216** (1993) 83.

[40] V. V. Vashook, S. P. Tolochko, I. I. Yushkevich, L. V. Makhnach, I. F. Kononyuk, H. Altenburg, J. Hauck, H. Ullmann, *Solid State Ionics* **110** (1998) 245.

[41] A. Aguadero, M. J. Escudero, M. Perez, J. A. Alonso, V. Pomjakushim, L. Daza, *Dalton Trans.* **36** (2006) 4377.

[42] A. Mehta, P. J. Heaney, *Phys. Rev. B* **49** (1994) 563

[43] P. A. Cox, Transition metal oxides, Oxford Science Publications, Oxford, 1991.

[44] J. B. Goodenough, Magnetism and the Chemical Bond, Interscience, New York, 1963.

[45] J. Kanamori, *J. Phys. Chem. Solids* **10** (1959) 87.

[46] E. O. Wollan, W. C. Koehler, *Phys. Rev.* **100** (1955) 545.

[47] S. E. Dann, M. T. Weller, D. B. Currie, M. F. Thomas, A. D. Al-Rawwas, *J. Mater. Chem.* **3**, (1993) 1231.

[48] G. Shirane, Y. Endoh, R. J. Birgeneau, M. A. Kastner, Y. Hidaka, M. Oda, M. Suzuki, T. Murakami, *Phys. Rev. Lett*. **59** (1987) 1613.

[49] G. Aeppli, D. J. Buttrey, *Phys. Rev. Lett*. **61** (1988) 203.

[50] G. Le Flem, G. Demazeau, P. Hagenmuller, *J. Solid State Chem.* **44** (1982) 82.

[51] D. E. Cox, G. Shirane, R. J. Birgeneau, J. B. MacChesney, *Phys. Rev.* **188** (1969) 930.

[52] K. Tezuka, M. Inamura, Y. Hinatsu, Y. Shimojo, Y. Morii, *J. Solid State Chem.* **145** (1999) 705.

[53] G. Aeppli, D. R. Harshman, D. Buttrey, E. Ansaldo, G. P. Espinosa, A. S. Cooper, J. P. Remeika, T. Treltoft, T. M. Riseman, D. R. Noakes, B. Ellman, T. F. Rosenbaum, D. L. Williams, *Physica C* **153-155** (1988) 1111.

[54] D. E. Cox, A. I. Goldman, M. A. Subramanian, J. Gopalakrishnan, A. W. Sleight, *Phys. Rev. B* **40** (1989) 6998.

[55] A. L. Hector, C. S. Knee, A. I. MacDonald, D. J. Price, M. T. Weller, *J. Mater Chem.* **15**, (2005) 3093.

[56] W. Opechowski and R. Guccione, Magnetism, edited by G. T. Rado and H. Suhl (Academic, New York, 1965), Vol. 2A, p. 105.

[57] K. K. Singh, P. Ganguly, C. N. R. Rao. *Mater. Res. Bull.* **17** (1982) 493.

[58] P. Ganguly, C. N. R. Rao. *Mater. Res. Bull.* **8** (1973) 405.

[59] K. K. Singh, P. Ganguly, J. B. Goodenough. *J. Solid State Chem.* **52** (1984) 254.

[60] C. N. R. Rao, D. J. Buttrey, N. Otsuka, P. Ganguly, H. R. Harrison, C. J. Sandberg, J. M. Honig, *J. Solid State Chem.* **51** (1984) 266.

[61] K. Sreedhar, J. M. Honig, *J. Solid State Chem*. **111** (1994) 147.

[62] S. Nishiyama, D. Sakaguchi, T. Hattori, *Solid State Commun*. **94** (1995) 279.

[63] C. P. Tavares, *Mat. Res. Bull.* **20** (1985) 979.

[64] J. B. Goodenough, S. Ramasesha, *Mater. Res. Bull*. **17** (1982) 383.

[65] J. B. Goodenough, *J. Less-common Met.* **116** (1986) 83.

[66] A. A. Yaremchenko, V. V. Kharton, M. V. Patrakeev, J. R. Frade, *J. Mater. Chem.* **13** (2003) 1136.

[67] S. J. Skinner, J. A. Kilner, *Solid State Ionics* **135** (2000) 709.

[68] E. J. Opila, H. L. Tuller, B. J. Wuensch, J. Maier. *J. Am. Ceram. Soc.* **76** (1993) 2363.

[69] J. L. Routbort, S. J. Rothman, B. K. Flandenneyer, L. J. Nowicki, J. E. Baker. *J. Mater. Res.* **3** (1988) 116.

[70] D. M. Bochkov, V. V. Kharton, A. V. Kovalevsky, A. P. Viskup, E. N. Naumovich, *Solid State Ionics* **120** (1999) 281.

[71] V. V. Kharton, A. P. Viskup, E. N. Naumovich, F. M. B. Marques, *J. Mater. Chem.* **9** (1999) 2623.

[72] L. Minervini, R. W. Grimes, J. Kilner, K. E. Sickafus, *J. Mater. Chem.* **10** (2000) 2349.

[73] O. H. Hansteen, H. Fjellvag, B. C. Hauback, *J. Solid State Chem.* **141** (1998) 411.

[74] O. H. Hansteen, H. Fjellvag, B. C. Hauback, *J. Mater Chem.* **8** (1998) 2089.

[75] R. Le Toquin, W. Paulus, A. Cousson, G. Dhalenne, A. Revcolevschi, *Physica B: Condensed Matter* **350** (2004) E269.

[76] A. Lappas, K. Prassides, *J. Solid State Chem.* **108** (1994) 59.

[77] G. Amow, P. S. Whitfield, I. J. Davidson, R. P. Hammond, C. N. Munnings, S. J. Skinner, *Ceramics International* **30** (2004) 1635.

[78] V. V. Vashook, H. Ullmann, O. P. Olshevskaya, V. P. Kulik, V. E. Lukashevich, L. V. Kokhanovskij, *Solid State Ionics* **138** (2000) 99.

[79] M. James, A. Tedesco, D. Cassidy, M. Colella, P. J. Smythe, *J. Alloys Compd.* **419** (2006) 201.

CHAPTER 2

Experimental techniques

2.1 Synthetic techniques

2.1.1 Solid state reactions

The increasing interest in developing new materials with interesting properties has stimulated the development of several synthetic techniques in solid state chemistry. Developing a new synthetic route may make the synthesis process achievable and/or help manipulate the properties of a material for a specific application. One of the most basic, and most commonly used, synthetic methods in solid state chemistry is the solid state reaction (ceramic) method. In the ceramic method, solid precursors of the different constituents are mixed to obtain the desired product. A high temperature is therefore required to overcome the slow diffusion rates of the solid materials. The technique is simple and can be used to obtain highly pure product materials; however, a very high temperature may be required to achieve complete reaction, which often results in coarse polycrystalline products. The ceramic method was used to synthesize materials such as $LaSrCo_{0.5}M_{0.5}O_4$ (M = Fe, Mn, Cr) and $LaSrCoFeO_6$ in this thesis. Although a B-site average oxidation state of 3.5+ could be achieved in the latter perovskite material, it was not possible to achieve B-site oxidation state higher than 3+ in single-layered materials, employing similar synthetic conditions. A modified sol-gel method was therefore used to synthesize materials such as $La_{0.8}Sr_{1.2}Co_{0.5}M_{0.5}O_4$ (M = Fe, Mn).

2.1.2 Sol-gel method

Mixing precursors in the liquid phase allows the ions to be mixed at the atomic scale and reduces the problems of lack of homogeneity and slow diffusion rates associated with mixing solid precursors. The ions in solution can then be co-precipitated or converted into a gel (sol-gel method), dried and calcined to obtain the final product. This lowers the sintering temperature and produces small-particle-size materials. The sol-gel method has extensively been used in the synthesis of functional oxides. The pyrolysis of a complex gel seems to be the easiest and the most common variation of the sol-gel methods, which is usually called modified Pechini method as first developed by Pechini [1]. Acetic acid/acetate mixtures were used in the sol-gel synthesis of $La_{0.8}Sr_{1.2}Co_{0.5}M_{0.5}O_4$ (M = Fe, Mn) in this study (chapters 3 and 4).

The microstructure of oxide materials greatly affects their performance in applications such as catalysis and electrochemical devices (*e.g.* SOFCs, batteries, sensors). Reduction of the particle size (increasing the surface area) usually results in improved mechanical, electrical and catalytic properties [2,3]. Methods developed to produce small-particle-size materials are many [4] and some of them are complicated and compositional selective or sensitive. However, the Pechini method represents a simple, powerful and less selective method which is also suitable for large scale syntheses. Shao *et al.* have recently suggested a mixed EDTA-citrate-metal complexing process to produce nano-crystalline materials for SOFCs and oxygen membrane applications [5,6]. In this method a stoichiometric mixture of the metal ions is mixed with EDTA (dissolved in NH_3) followed by addition of solid citric acid (mole ratio of total metal ions to EDTA and to citrate = 1 : 1 : 2) with a suitable control of the pH. This method was used to synthesize

$La_{1.7}Sr_{0.3}Co_{0.5}Ni_{0.5}O_{4+\delta}$ in this study (chapter 5) in an attempt to improve its microstructure for use in SOFC applications.

2.2 Characterization techniques

2.2.1. Diffraction techniques

2.2.1.1 Neutron diffraction

Neutron powder diffraction (NPD) was extensively used throughout this thesis to study the crystallographic and magnetic structures of the studied materials. In addition to determining the magnetic structure, the technique was very useful in characterizing structural effects such as oxygen nonstoichiometry and crystallographic-site mixed-occupancy which were poorly resolved by X-ray powder diffraction (XRD). The basic concepts of neutron diffraction are discussed in this section (see ref. 7 and 8 for more details). The basic event of scattering is shown in *Figure 2.1*. $\mathbf{K_i}$ and $\mathbf{K_s}$ are the incident

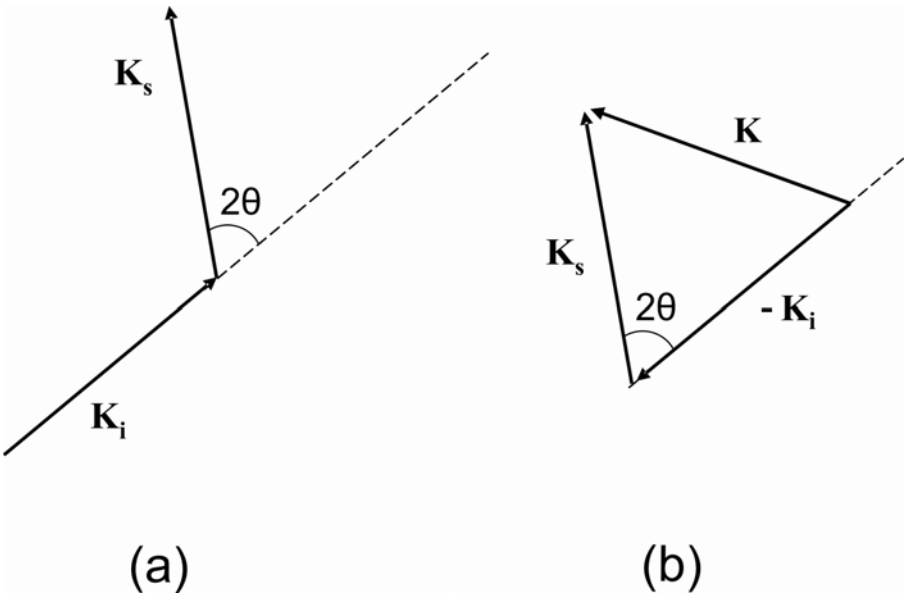

Figure 2.1 (a) Scattering event; (b) scattering triangle.

and scattered neutron wave vectors. **K** is the wave transfer vector or "scattering vector" where $\mathbf{K} = \mathbf{K}_s - \mathbf{K}_i$ and 2θ is the scattering angle. Then, $K^2 = K_i^2 + K_s^2 - 2K_iK_s\cos 2\theta$; in case of elastic scattering $\mathbf{K}_i = \mathbf{K}_s$ and $K = 2K_i \sin\theta = 4\pi\sin\theta/\lambda$ where $K_i = 2\pi/\lambda$. Neutrons are scattered by nuclei, and by atomic magnetic moments due to unpaired electrons. Considering only the nuclear scattering and neglecting complicating effects, such as extinction, absorption, inelastic scattering and multiple scattering, the scattered intensity in a neutron diffraction experiment is proportional to the structure factor S(**K**) given by

$$S(\mathbf{K}) = \frac{1}{N}\left| \sum_i^N b_i \exp(i\mathbf{K}\cdot\mathbf{r}_i) \right|^2 \qquad (2.1)$$

where N is the number of nuclei in the crystallite under investigation, $\mathbf{r}_i$ is the position of atom *i*, and b_i is the scattering length for atom *i*. The scattering length *b* is a measure of the strength of the interaction between the incident radiation and the atom. The periodicity of the lattice implies that S(**K**) is zero except at specific values of **K**, such that the phase factors $\exp(i\mathbf{K}\cdot\mathbf{r}_i)$ constructively interfere. These values of **K** construct the reciprocal lattice, and a nonzero S(**K**) is obtained when

$$\mathbf{K} = \mathbf{K}_{hkl} = ha^* + kb^* + lc^* \qquad (2.2)$$

where $\mathbf{K}_{hkl}$ is a reciprocal lattice vector characterizing a reflection with *hkl* indices. Hence, scattering occurs when $K = K_{hkl} = 4\pi\sin\theta/\lambda$,

$$i.e.\ \ \lambda = 2d_{hkl}\sin\theta \qquad (2.3)$$

which is the Bragg equation (where $d_{hkl} = 2\pi/K_{hkl}$ is the distance between the diffracting planes). For polycrystalline material, providing that crystallites are randomly oriented to give collectively all possible orientations, the scattering factor in equation 2.1 should be

integrated over all angles in space. For an orthogonal lattice the structure factor of the unit cell for an *hkl* reflection (F_{hkl}) is usually defined as

$$F_{hkl}^2 = \left| \sum b \exp\{2\pi i(hx/a_0 + ky/b_0 + lz/c_0)\} \right|^2 \qquad (2.4)$$

where the expression $\exp\{2\pi i(hx/a_0 + ky/b_0 + lz/c_0)\}$ is equivalent to $\exp(i\mathbf{K}_{hkl} \cdot \mathbf{r}_i)$ and summation is over all atoms in the unit cell; *x*, *y*, *z* and a_0, b_0, c_0 are the Cartesian coordinates and the dimensions of the unit cell, respectively.

2.2.1.1.1 Effect of isotopes

Nuclei of the same element may differ due to the presence of different isotopes of the element with different abundances. These isotopes will be randomly distributed among the atomic sites in the crystal and will each have their own characteristic scattering length *b*. In this case the expression for the structure factor S(**K**) must be modified. Fore example equation 2.1 becomes

$$S(\mathbf{K}) = \frac{1}{N}\left\{ \left| \sum_i^N \overline{b_i} \exp(i\mathbf{K} \cdot \mathbf{r}_i) \right|^2 + \sum_i^N \left(\overline{b_i^2} - \overline{b_i}^2 \right) \right\} \qquad (2.5)$$

where $\overline{b_i}$ is the average value of scattering lengths. The first term in this expression will be the same for all atomic sites and will contribute coherently to the scattered intensity. On the other hand, the second term (which is independent on **K**) will vary randomly over the sites and there will be no phase correlation between their contributions from it (incoherent scattering). In the case of isotopes possessing spin, there will be two abundance factors for each isotope (contributing to the average in $\overline{b_i}$) corresponding to different interactions with the neutron spin. The quantities $\sigma_c = 4\pi\overline{b}^2$ and $\sigma_I = 4\pi\left(\overline{b^2} - \overline{b}^2 \right)$ are called coherent and incoherent scattering cross sections, respectively. Most elements scatter

predominately coherently; two important exceptions are hydrogen and vanadium. Due to its very small coherent scattering cross section, vanadium is often used to make sample containers in neutron diffraction experiments.

2.2.1.1.2 Effect of thermal vibrations

The thermal displacement of atoms from their equilibrium positions leads to a reduction of the coherent Bragg reflections due to an increase in the diffuse reflection of the neutrons or X-rays. The effect is often called “thermal diffuse scattering”. In case of isotropic thermal motion, Bragg intensities are modified by replacing b_i by

$$b_i \exp\left(-\frac{1}{2}\mathrm{K}^2\overline{U_i^2}\right) \qquad (2.6)$$

where the exponential term is “the temperature factor” or “Debye-Waller factor” for an atom *i*; $\overline{U_i^2}$ is the atom’s mean square displacement. If the thermal motion is anisotropic the expression of the temperature factor is considerably more complicated.

2.2.1.1.3 Magnetic scattering

Neutrons possess spin, s = 1/2, and so have magnetic moment and interact with magnetic moments on atoms with unpaired electrons. When the material exhibits long-range magnetic order, neutrons will be scattered coherently from the electrons just as they scatter from nuclei. If the beam is unpolarized the total structure factor $\mathrm{S}_{tot}(\mathbf{K})$ may be written as

$$\mathrm{S}_{tot}(\mathbf{K}) = \mathrm{S}(\mathbf{K}) + \mathrm{S}_M(\mathbf{K})\sin 2\alpha \qquad (2.7)$$

where α is the angle between the magnetization vector **M** and the scattering vector **K**. The expression for $S_M(\mathbf{K})$ is similar to equation 2.1, except that b_i is replaced with a quantity $A_i f_i^M(\mathrm{K})$, where A_i depends on the magnet moment and $f_i^M(\mathrm{K})$ is the magnetic form factor.

2.2.1.2 Neutron diffraction vs. X-ray diffraction

Although the basic theory of diffraction is similar for X-rays and neutrons, there are significant differences between the two techniques. In the case of neutron scattering, and in the absence of magnetic scattering, the fundamental scattering body is the nucleus not the electron. Since X-rays interact with the electrons, the interaction is dependent on the number of electrons, *i.e.* atomic number, and X-ray form factors increase rapidly with the atomic number of elements. The intensity of X-ray scattering from lighter atoms is therefore relatively low and can be concealed by that from heavier elements. In neutron scattering, on the other hand, the scattering length *b* varies somewhat irregularly with the atomic number; however, typically within a factor of 2 or 3, most atoms scatter neutrons equally well in contrast to the rapid increase of the X-ray form factors with atomic number. Neutron diffraction is therefore very useful to locate light elements in compounds containing heavy elements. In the present study, XRD was found to be insensitive to oxygen nonstoichiometry in most of the studied materials. This is expected because of the low cross-section of oxygen for X-rays and that the materials contain heavy scatters such as lanthanum. NPD was therefore used to determine the oxygen content and to locate oxygen vacancies/interstitials in the majority of studied materials. Due to differences in the scattering lengths, NPD can also differentiate elements that are close to one another in the periodic table and therefore barely distinguishable in X-ray experiments. This is useful in

characterizing mixed occupancy of crystallographic sites in materials such as mixed B-site perovskites. In the present study, NPD has been used to confirm a B-site disorder in mixed B-site materials such as $La_{2-x}Sr_xCo_{0.5}Mn_{0.5}O_{4\pm\delta}$ and $La_{1+x}Sr_{2-x}CoMnO_{7-\delta}$ (chapters 4 and 6). A NPD study of the brownmillerite phase $LaSrCoFeO_5$ (chapter 7) also revealed that iron and cobalt are disordered between the octahedral and tetrahedral sites of the structure.

Another important distinction between X-ray diffraction and neutron diffraction is the fact that the neutron-nucleus interaction is of very short range compared with interatomic distance, so that scattering lengths are essentially independent of $\sin\theta/\lambda$. On the other hand X-rays interact with the electron cloud surrounding a nucleus which is comparable with interatomic distances and the X-ray form factors decrease quickly with increasing $\sin\theta/\lambda$. Neutrons therefore more readily provide information at larger scattering angles.

Another advantage of NPD is that it can be used to study the magnetic interactions in materials containing magnetic ions (with unpaired electrons). When the ions have their magnetic moments oriented in a random manner, as in a paramagnetic material, the magnetic scattering will be entirely incoherent and will contribute to the background of a powder pattern. However, when the material exhibits a three-dimensional ordering of magnetic moments, the magnetic scattering will contribute coherently to the scattered intensity according to equation 2.7. The technique is therefore useful to determine magnetic structures as well as crystal structures. However, the electrons which determine the magnetic moment will be distributed over a volume of space having dimensions comparable with the neutron wavelength; the magnetic form factor will therefore decrease with $\sin\theta/\lambda$ similar to X-rays scattering, although form factors are different since X-rays scatter from the whole electron cloud around the nucleus while neutrons scatter from

valence electrons. NPD experiments at low temperatures were used in this study to determine the magnetic structure of materials such as $La_{2-x}Sr_xCo_{0.5}Fe_{0.5}O_{4-\delta}$ and $LaSrCoFeO_5$.

Neutrons are generally less absorbed by materials than X-rays. The ability of neutrons to penetrate deeply within materials is an advantage in studying materials with compositional gradient such as thin layers, where neutron diffraction will give information representing the bulk structure whereas X-rays will provide less information. However, neutron scattering from materials containing elements with large neutron absorption cross sections (*e.g.* Cd, Gd, Sm) is greatly reduced and a significant absorption correction may be necessary. In addition, γ radiation is produced which requires special safety concerns.

X-ray diffraction, with the advantage of being a laboratory-based technique, is a strongly powerful technique which is frequently preferable to neutron diffraction. However, it can be seen that neutron diffraction is superior/complementary in some situations when specific types of information are required. XRD was used in the present study to check the phase purity and to determine the unit cell parameters of the synthesized materials. Room temperature NPD data, however, were used to study more reliably the oxygen nonstoichiometry and crystal structure. Low temperature NPD data were used to determine the magnetic structure of magnetically ordered materials.

XRD data were collected using a Siemens D5000 and Bruker D8 diffractometer, both in transmission mode and employing $CuK\alpha_1$ radiation from a germanium monochromator. The computer programs INDEX [9] and DSPACE [10] were used for indexing and initial selection of space groups. Variable temperature X-ray powder diffraction (VT-XRD) under reducing conditions (10% H_2/N_2) was used to study the reduction behaviour of $LaSrCoFeO_6$. VT-XRD data were collected under a 10% H_2/N_2

atmosphere using a Bruker Axs D5005 diffractometer operating in reflection mode and fitted with a scintillation detector and an Anton-Parr HTK 1200 °C furnace.

NPD data were collected at room temperature and low temperatures (1.5 and 5 K) on the D2B diffractometer at the Institute Laue Langevin, Grenoble (ILL), using a wavelength of 1.594 Å, and on the HRPT diffractometer at SINQ, PSI, using wavelengths of 1.8852 Å and 1.4942 Å. Structural refinements based on XRD and NPD data were performed using the GSAS suite of programs [11].

2.2.1.3 Rietveld analysis

The standard method of analyzing powder diffraction data (XRD and NPD data) is known as "Rietveld profile refinement" and named after Hugo Rietveld [12]. The method involves fitting the parameters of a model to the measured "whole-profile", which is the intensity measured as a function of scattering angle. The model parameters in Rietveld refinement describe different aspects of the profile and can be divided into three general categories. First, the set of parameters which determine crystal symmetry (space group), unit cell parameters, atomic positions, site occupancy and displacements; these parameters describe the extinction (systematic absence), positions and integrated intensities of Bragg reflections. Second, there are the parameters which describe the background. Inelastic and/or incoherent scattering from the sample and its environment, air scattering, electronic noise, and other unwanted sources may contribute to the background. The Bragg peaks can usually be separated from the background because variation of the background scattering with scattering angle is relatively slow. A third set of parameters describe the shapes of Bragg peaks. Peak broadening is in part due to the resolution of the instrument itself, however crystallite size and strain effects may also contribute to the broadening.

The Rietveld refinement is guided numerically using agreement indices, or *R* values. The quantity minimized in the refinement is the residual S_y

$$S_y = \sum_i w_i \left[y_i(obs) - y_i(calc) \right]^2 \qquad (2.8)$$

where $y_i(obs)$ is the observed intensity at step *i*, $y_i(calc)$ is the calculated intensity and w_i is the weight. This quantity is included in the weighted-profile *R* value, R_{wp}, which is defined as

$$R_{wp} = \left\{ \frac{\sum_i w_i \left[y_i(obs) - y_i(calc) \right]^2}{\sum_i w_i \left[y_i(obs) \right]^2} \right\}^{1/2} \qquad (2.9)$$

Ideally R_{wp} should approach the statistically expected *R* value, R_{exp},

$$R_{\exp} = \left[\frac{(N-P)}{\sum_i^N w_i y_i(obs)^2} \right]^{1/2} \qquad (2.10)$$

where *N* is the number of observations and *P* the number of parameters. The goodness of fit is

$$\chi^2 = \left(\frac{R_{wp}}{R_{\exp}} \right)^2 \qquad (2.11)$$

Rietveld profile refinements in this study were performed on the XRD and NPD data using the GSAS suite of programs [11]. Peak shapes were typically described by a linear combination of Lorentzian and Gaussian functions, modelled by pseudo-Voigt functions. A combination of pseudo-Voigt and Finger-Cox-Jephcoat functions were used in the refinements of the reduced samples $La_{2-x}Sr_xCo_{0.5}Fe_{0.5}O_{4-\delta}$ indicating anisotropic strain in these materials (chapter 3). Refinements employed a 16-term cosine Fourier series background function.

Different approaches can be used in GSAS to model magnetically ordered systems. In one approach a single structural phase can be used for nuclear and magnetic scattering components. This requires an expansion of the nuclear structure to fulfil symmetry requirements of the magnetic structure. In a second approach a crystallographic phase that provides only nuclear scattering is modelled separately; the magnetic phase then can be modelled using either "color" space group symmetry or no symmetry (*P1* space group). The latter approach was used in this study. The concept of "color" or "Shubmikov" space groups has extended the traditional crystallographic space group theory for treatment of the symmetry of magnetic systems [13-15]. In the "color" space group theory, magnetic symmetry operations are given an additional attribute which is a "color" -either red or black- where a "black" operation applies the symmetry operation conventionally to the magnetic vector, while a "red" operation applies the symmetry operation and, in addition, a spin inversion. The red symmetry operations are usually marked with an apostrophe (') in the standard name of the space group. The color space group *Pm'mm*, for example, has the same symmetry operations as the standard *Pmmm* space group except that the mirror plane perpendicular to *a* is red. In the present study, the color space group $P4_2/nn'm$ is used to model the magnetic structure of $La_{2-x}Sr_xCo_{0.5}Fe_{0.5}O_{4-\delta}$ (chapter 3), while *P1* symmetry is used in refining the magnetic structure of $LaSrCoFeO_{6-\delta}$-related phases such as $LaSrCoFeO_5$, $LaSrCoFeO_5F$ and $LaSrCoFeO_{5.5}$ (chapter 7). An average of the magnetic form factors of the B-site cations was used in all refinements.

2.2.2 Thermogravimetric analysis (TGA)

The reduction behaviour of the studied materials was tested by thermogravimetric (TG) measurements in which a few milligrams of the sample were heated in reducing atmosphere (10% H_2/N_2) and the mass loss was monitored as a function of temperature. The measurements were performed in the temperature range 100-1000 °C at a rate of 10 °C min^{-1}. TG measurements were performed using a Rheometric Scientific STA 1500 thermal analyzer.

2.2.3 Magnetic measurements

Magnetic data were collected using a Quantum Design MPMS SQUID and PPMS magnetometers in the temperature range 5-300 K. Zero-field-cooled (ZFC) and field-cooled (FC) measurements were carried out using the DC extraction or induction method. The data were collected on warming using applied fields of 0.3 and 0.5 T.

The AC susceptibility measurements were performed by varying the frequency from 30 Hz to 1 kHz with root mean squared field amplitude of 3 x 10^{-4} T. No additional external field was applied during the measurements. These measurements were used to characterize the spin glass state in materials such as $La_{0.8}Sr_{1.2}Co_{0.5}M_{0.5}O_4$ (M = Fe, Mn).

2.2.4 Mössbauer spectroscopy

The ^{57}Fe Mössbauer spectra were recorded at 298 and 16 K with a constant acceleration transmission mode Mössbauer spectrometer. A 25 mCi ^{57}Co/Rh source was used. Data at low temperature were recorded with a helium closed-cycle cryorefrigerator. The spectrometer velocity was calibrated with the source and metallic iron foil. All the spectra were computer-fitted and the chemical isomer shift data are quoted relative to

metallic iron at room temperature. The correlation of chemical isomer shift data with oxidation states of iron was achieved by reference to the literature (*e.g.* ref. 16 and 17). All the Mössbauer data in this thesis were provided and interpreted by Professor Frank J. Berry and Dr Jose F. Marco.

2.2.5 X-ray photoelectron spectroscopy

X-ray photoelectron spectroscopy (XPS) has frequently been used to distinguish the different oxidation states of cobalt [18-20]. As shown in *Figure 2.2*, the high-spin Co^{2+} state results in intense satellite structures at the higher energy side of the Co $2p_{3/2}$ and Co $2p_{1/2}$ transitions in the Co 2p XPS spectrum. In contrast to the Co^{2+} state, the low-spin Co^{3+} state shows very weak satellite structures. The Co 2p XPS spectra were therefore used in this study to differentiate the two states (chapters 4 and 5).

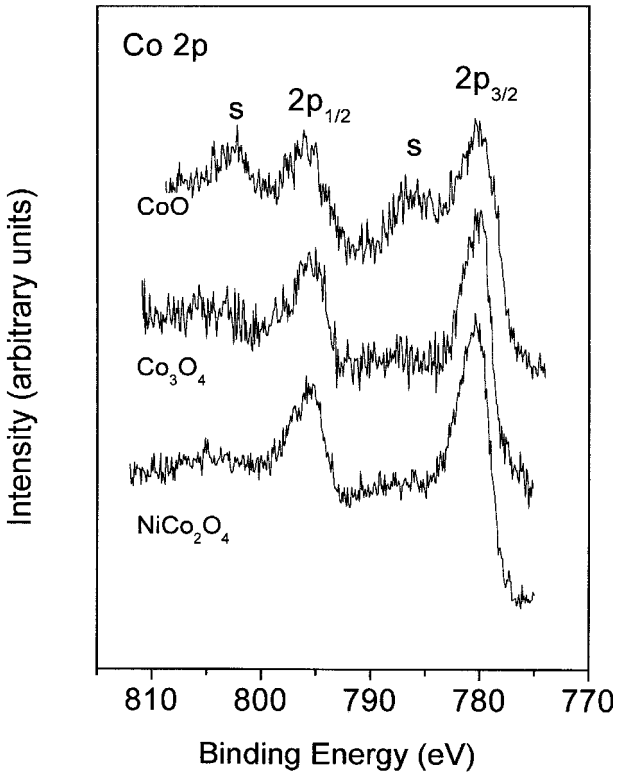

Figure 2.2 Cobalt XPS data for CoO, Co_3O_4 and $NiCo_2O_4$, showing the $2p_{1/2}$, $2p_{3/2}$ and satellite (s) peaks (ref. 20).

XPS data (Mg anode, 13 kV) were collected on a VSW TA10 using the hemispherical analyser VSW HA100. The samples were sprinkled onto carbon conductive tape mounted on a molybdenum sample plate. XPS data were provided by Professor C. F. McConville.

2.2.6 Electron microscopy and X-ray absorption spectroscopy

Electron diffraction (ED) and high resolution transmission electron microscopy (HRTEM) studies were performed on a JEOL 4000 EX and a Phillips CM 20 (ED) instrument. Samples for transmission electron microscopy were made by suspending the powder in ethanol and deposition onto a copper grid with a holey carbon layer. Calculated images for comparison with the experimental HRTEM images were made using the MacTempas software. ED and HRTEM data were provided and interpreted by Professor Joke Hadermann.

X-ray absorption spectra at the Co K- and Mn K- edges were recorded in fluorescence mode at the European Synchrotron Radiation Facility ESRF in Grenoble, France, on Beamline 25 at 298 K. The raw data were background subtracted and normalized using the program Athena [21]. The position of the Co- and Mn- edges was deduced from the most intense maximum of the first derivative of the corresponding X-ray absorption near-edge structure (XANES). The data were provided and interpreted by Professor Frank J. Berry and Dr Jose F. Marco.

2.2.7 Resistivity measurements

DC resistivity measurements were used in this study to determine the overall conductivity of some phases such as the oxygen-rich phases $La_{1.2}Sr_{0.8}Co_{0.5}Mn_{0.5}O_{4.1}$ and $La_{1.7}Sr_{0.3}Co_{0.5}Ni_{0.5}O_{4.08}$ (chapters 4 and 5). In order to obtain dense ceramic pellets for resistivity measurements, powder samples of the materials were first ball milled (in ethanol) and rod samples (8 mm in diameter and ~ 10 mm length) were then prepared by uniaxial pressing (2 tons). They were then sintered at 1350 °C for 2 h to give densities higher than 90% of their theoretical densities. Resistivity measurements were carried out using a standard four-probe DC method. The ends of the rod sample were coated with platinum paste (Heraeus) and platinum wires were used as current and voltage leads. Measurements were carried out in the temperature range 100-900 °C. In case of the nickel-containing materials (chapter 5), due to the relative sensitivity of resistivity toward annealing, the samples were first annealed at 950 °C for 12 h, cooled down slowly to room temperature (1 °C min^{-1}) and then measurements were made on heating.

2.3 References

[1] M. P. Pechini, U.S. Patent 3,330,697, 1967.

[2] Y. L. Zhang, S. W. Zha, M. L. Liu, *Adv. Mater.* **17** (2005) 487.

[3] G. Y. Zhang, J. Chen, *J. Electrochem. Soc.* **152** (2005) A2069.

[4] B. L. Cushing, V. L. Kolesnichenko, C. J. O'Connor, *Chem. Rev.* **104** (2004) 3893.

[5] Z. P. Shao, W. S. Yang, Y. Cong, H. Dong, J. H. Tong, G. X. J. Xiong, *Membr. Sci.* **172** (2000) 177.

[6] W. Zhou, Z. Shao, W. Jin, *J. Alloys and Compd.* **426** (2006) 368.

[7] G. E. Bacon, Neutron Diffraction, 3rd Ed, Oxford University Press, Oxford, 1975.

[8] S. W. Lovesey, Theory of Neutron Scattering from Condensed Matter, Oxford University Press, Oxford, 1987.

[9] D. Louer, M. Louer, *J. Appl. Cryst*. **5** (1972) 271.

[10] C. Greaves, University of Birmingham, 1982.

[11] A. C. Larson and R. B. von Dreele, General Structural Analysis System, Los Alamos National Laboratory, Los Alamos, NM, 1994.

[12] H. Rietveld, *J. Appl. Cryst*. **2** (1969) 65.

[13] H. Heesch, *Z. Kristallogr*. **73** (1930) 325.

[14] A. V. Shubnikov and N. V. Belov, Colored Symmetry, Oxford Pergamon, New York, 1964.

[15] B. K. Vainshtein, Fundamentals of Crystals, Symmetry, and Methods of Structural Crystallography, Springer, New York.

[16] N. N. Greenwood and T. C. Gibb, Mössbauer Spectroscopy, Chapman and Hall, London, 1971.

[17] D. P. E. Dichoon and F. J. Berry, Mössbauer Spectroscopy, Cambridge University Press, Cambridge, 1986.

[18] K. Takubo, T. Mizokawa, S. Hirata, J. Y. Son, A. Fujimori, D. Topwal, D. D. Sarma, S. Rayaprol, E. V. Sampathkumaran, *Phys. Rev. B* **71** (2005) 73406.

[19] I. Alvarez-Serrano, G. J. Cuello, M. L. Lopez, A. Jimenez-Lopez, C. Pico, E. Rodrıguez-Castellon, E. Rodrıguez, M. L. Veiga, *J. Phys. D: Appl. Phys.* **41** (2008) 195001.

[20] J. G. Kim, D. L. Pugmire, D. Battaglia, M. A. Langell, *Appl. Surf. Sci*. **165** (2000) 70.

[21] B. Ravel, M. Newville, *J. Synchrotron Rad.* **12** (2005) 537.

CHAPTER 3

Synthesis and characterization of $La_{2-x}Sr_xCo_{0.5}Fe_{0.5}O_{4-\delta}$ (x = 0.8, 1, 1.2)

3.1 Background

The mixed conducting perovskites $La_{1-x}Sr_xCo_{1-y}Fe_yO_{3-\delta}$ have been widely investigated [1-3]. Recently, some interest has been focused on the related RP phases $(La,Sr)_{n+1}(Co,Fe)_nO_{3n+1}$ which exhibit variable oxygen nonstoichiometry along with structural stability at high temperatures in reducing conditions; this has been linked to the flexibility of the cations in these materials to accommodate a range of transition metal coordination environments. Of these systems, the parent material $Sr_3Fe_2O_{7-\delta}$ has a tetragonal structure (space group *I4/mmm*) and exhibits oxygen deficiency $\delta \leq 1$. The sample with $\delta = 1$ was prepared in 5% H_2/N_2 atmosphere at 700 °C and showed no variation in the crystal structure symmetry [4]. Manthiram *et al*. [5] have studied the structural stability and oxygen permeation properties of $Sr_{3-x}La_xFe_{2-y}Co_yO_{7-\delta}$ which retain tetragonal symmetry at temperatures up to 1000 °C in the oxygen partial pressure range 10^{-5}-0.21 atm. Other related systems which have shown substantial ability to sustain low oxygen contents without change in crystal structure symmetry are $Sr_3FeCoO_{7-\delta}$ and $Sr_3LaFe_{1.5}Co_{1.5}O_{10-\delta}$ [6,7]. Regarding the n = 1 RP phases, the stoichiometric materials $LaSrCo_{1-x}Fe_xO_4$ have been synthesized by Tabuchi *et al*. [8]. The study involved detailed structural and magnetic characterization, although the half-doped member $LaSrCo_{0.5}Fe_{0.5}O_4$ has not been characterized. The synthesis and characterization of the n = 1 RP phases $La_{2-x}Sr_xCo_{0.5}Fe_{0.5}O_{4-\delta}$ are considered in this chapter. Particular attention has been devoted to the phases $La_{1.2}Sr_{0.8}Co_{0.5}Fe_{0.5}O_4$, $LaSrCo_{0.5}Fe_{0.5}O_4$ and $La_{0.8}Sr_{1.2}Co_{0.5}Fe_{0.5}O_4$ and their reduced forms $La_{1.2}Sr_{0.8}Co_{0.5}Fe_{0.5}O_{3.85}$, $LaSrCo_{0.5}Fe_{0.5}O_{3.75}$

and $La_{0.8}Sr_{1.2}Co_{0.5}Fe_{0.5}O_{3.65}$. Reduction was achieved in 10% H_2/N_2 at 700-800 °C and no variation in the crystal structure symmetry was observed; the TG data indicate structural stability of these materials in this atmosphere up to 1000 °C. The present study involves structural and magnetic characterization of these materials.

3.2 Synthesis

The materials $La_{1.2}Sr_{0.8}Co_{0.5}Fe_{0.5}O_4$ and $LaSrCo_{0.5}Fe_{0.5}O_4$ were synthesized by conventional solid state reactions using La_2O_3 (previously dried at 800 °C in air), $SrCO_3$, Co_3O_4 and Fe_2O_3 as starting materials. Commencing the reactions in air proved unsuccessful (due to formation of some perovskite impurities) and a two-step synthesis procedure was therefore adopted. Stoichiometric amounts of starting materials were intimately mixed, pressed into pellets and calcined at 1350 °C for 30 h under a N_2 atmosphere. After grinding, the samples were subsequently heated in air at 800 °C for 12 h in order to obtain oxygenated materials.

Attempts to synthesize $La_{0.8}Sr_{1.2}Co_{0.5}Fe_{0.5}O_4$ by solid state reactions were unsuccessful; a sol-gel approach was therefore employed. Stoichiometric amounts of La_2O_3, $SrCO_3$, $Co(CH_3COO)_2.4H_2O$ and $Fe(CH_3COO)_2$ were dissolved in acetic acid and boiled under reflux for 3 h. Small amounts of hydrogen peroxide and water were added and the mixture was further refluxed overnight to obtain a clear solution. This solution was evaporated to a dark red gel. The gel was dried and decomposed in air at 400 °C and the resulting powder pressed into pellets and calcined in flowing oxygen at 1350 °C for 18 h.

3.3 XRD and TG study

XRD patterns indicated that the synthesized materials (oxygenated materials) were single-phase with no evidence of product impurities or starting materials. The patterns were readily indexed on a body-centred tetragonal unit cell, consistent with a structure related to that of K_2NiF_4. Structural refinements based on XRD data confirmed the structure (*I4/mmm* space group) and the oxide ion sites could be fixed at full occupancy in all refinements. The reduction behaviour of these materials was followed by TG measurements in which the materials were heated (10 °C min^{-1}) in flowing 10% H_2/N_2 (*Figure 3.1*).

3.1a)

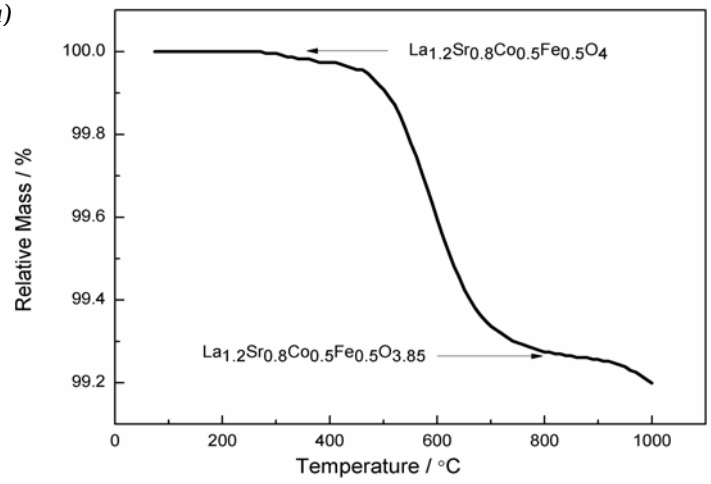

3.1b)

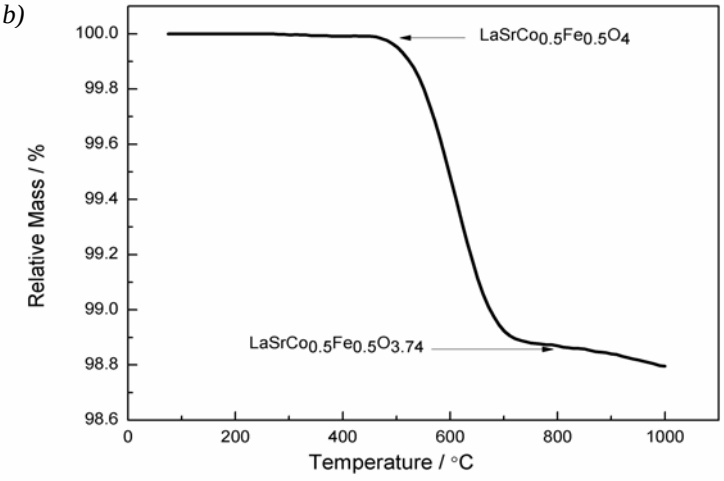

3.1c)

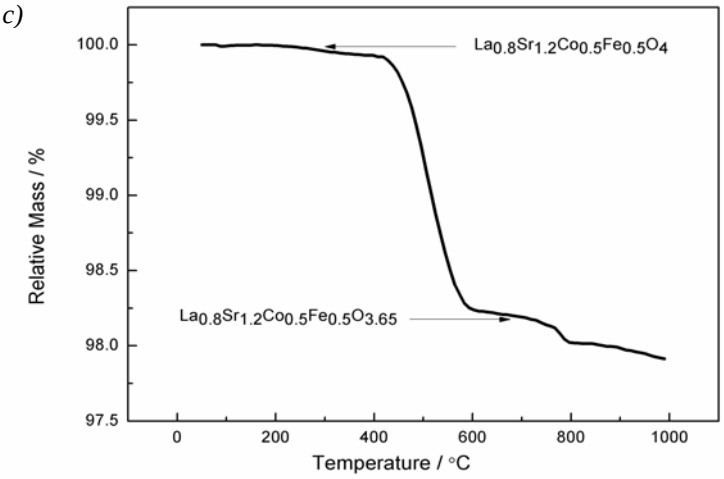

Figure 3.1 TG data for the reduction of different materials using 10% H_2 in N_2.

The TG plots show a significant mass loss at 500-600 °C in all samples. XRD analysis of the reduction products (in the temperature range 700-1000 °C) indicated that the K_2NiF_4-type structure is retained in all samples with slight decomposition in the case of $La_{0.8}Sr_{1.2}Co_{0.5}Fe_{0.5}O_4$ at T > 800 °C. In an attempt to repeat the reduction process on a larger scale, the materials were heated in flowing 10% H_2/N_2 at 800 °C (in the case of $La_{1.2}Sr_{0.8}Co_{0.5}Fe_{0.5}O_4$ and $LaSrCo_{0.5}Fe_{0.5}O_4$) and 700 °C (in the case of $La_{0.8}Sr_{1.2}Co_{0.5}Fe_{0.5}O_4$) for 12 h. XRD analysis indicated that the obtained materials were single-phase with the K_2NiF_4-type structure. However, the refinements were insensitive to oxygen nonstoichiometry and the oxide ion sites were therefore fixed at full occupancy. The data revealed an expansion in the *c* parameter and a slight contraction in the *a* parameter in all samples under reduction (*Figure 3.2*). Assuming that the oxygenated materials are stoichiometric in oxygen, the reduced materials are oxygen-deficient with the overall stoichiometries indicated in *Figure 3.1*.

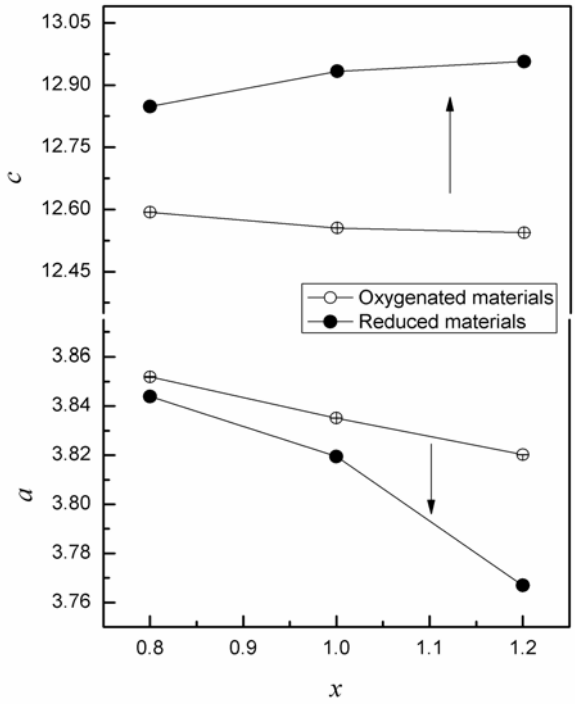

Figure 3.2 Variation of the XRD refined unit cell parameters with x in $La_{2-x}Sr_xCo_{0.5}Fe_{0.5}O_{4-\delta}$ (e.s.d. values are less than symbol size).

3.4 Room temperature NPD analysis

NPD data collected from different samples at room temperature were used to probe more reliably the oxygen content and defect structure of these phases. Rietveld profile refinements were performed employing the *I4/mmm* space group; a pseudo-Voigt peak shape (for the oxygenated materials) and a combination of pseudo-Voigt and Finger-Cox-Jephcoat functions (for the reduced materials) were used in refinements. The use of the latter function was necessary to obtain a good fit to the experimental data and indicates significant anisotropic peak broadening in the reduced phases. The profile fits and difference patterns of the Rietveld analysis of different samples are shown in *Figures 3.3* and *3.4*; structural data and some selected bond lengths are given in *Tables 3.1* and *3.2*, respectively. The oxygen contents of the reduced materials are based on formal oxidation states of Co^{2+} and Fe^{3+} (see section 3.5), which are in good agreement with refined data.

No evidence of oxygen nonstoichiometry could be observed through the refinement of the oxide ion site occupancies in the oxygenated materials. Oxide ion sites were therefore fixed at full occupancy throughout the refinements. Introduction of interstitial oxygen in these materials proved also unstable. The refinement of the oxide ion site occupancies in the reduced materials located the vacancies on the O1 equatorial sites and showed that the O2 apical sites were fully occupied. Variable and full occupancies of O1 and O2 sites, respectively, were therefore maintained throughout the refinements (*Table 3.1*). The O2 sites (0, 0, *z*) were allowed to vibrate anisotropically and most of the samples had higher displacements perpendicular to the (Co/Fe)–O bond (*Table 3.1*). Oxide ion vacancies in the reduced samples are therefore disordered and confined to the MO_2 planes of the K_2NiF_4-type structure; an associated twisting of the $(Co/Fe)O_6$ octahedra around the *z* axis was also observed in these materials; this transforms the oxide ion at (0.5, 0, 0) to the split position (0.5, *y*, 0), where *y* appears to increase with the concentration of oxygen vacancies (*Table 3.1*). The retention of the tetragonal symmetry under reduction with an equatorial distribution of oxide ion vacancies has been observed in $LaSrCoO_{3.5-x}$ [9]. Split oxide ion sites have been invoked in the analysis of these phases. Models of equatorial vacancy order (e.g. $Ca_2MnO_{3.5}$ [10] and $La_{1.6}Sr_{0.4}NiO_{3.47}$ [11]) or vacancy distribution between axial and equatorial sites (e.g. $NdSrCuO_{3.56}$ [12]) proved also unsuccessful for the studied materials. The NPD data are in good agreement with the TG results showing the overall stoichiometries of the studied materials as $La_{1.2}Sr_{0.8}Co_{0.5}Fe_{0.5}O_4$, $LaSrCo_{0.5}Fe_{0.5}O_4$, $La_{1.2}Sr_{0.8}Co_{0.5}Fe_{0.5}O_{3.88(1)}$, $LaSrCo_{0.5}Fe_{0.5}O_{3.73(1)}$ and $La_{0.8}Sr_{1.2}Co_{0.5}Fe_{0.5}O_{3.67(1)}$. The results therefore confirm that the oxygenated materials are stoichiometric in oxygen, and the oxygen-deficient materials are, within experimental error, $La_{1.2}Sr_{0.8}Co_{0.5}Fe_{0.5}O_{3.85}$, $LaSrCo_{0.5}Fe_{0.5}O_{3.75}$ and $La_{0.8}Sr_{1.2}Co_{0.5}Fe_{0.5}O_{3.65}$. The latter stoichiometries correspond to a B-site average oxidation state of 2.5+ (*i.e.* Co^{2+}/Fe^{3+}) (see section 3.5).

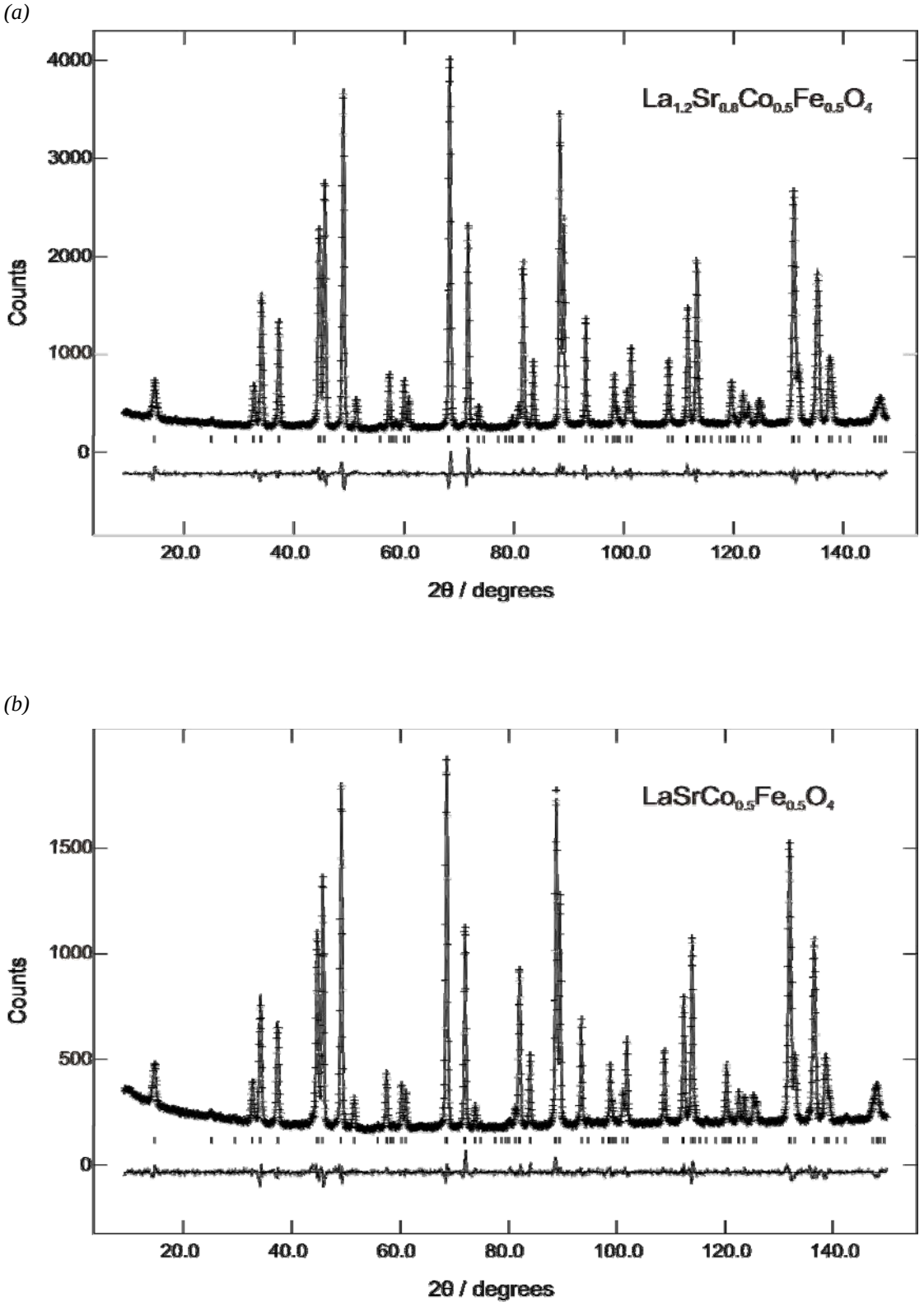

Figure 3.3 Observed, calculated and difference profiles for NPD data collected from (a) $La_{1.2}Sr_{0.8}Co_{0.5}Fe_{0.5}O_4$ and (b) $LaSrCo_{0.5}Fe_{0.5}O_4$ at room temperature.

3.4a)

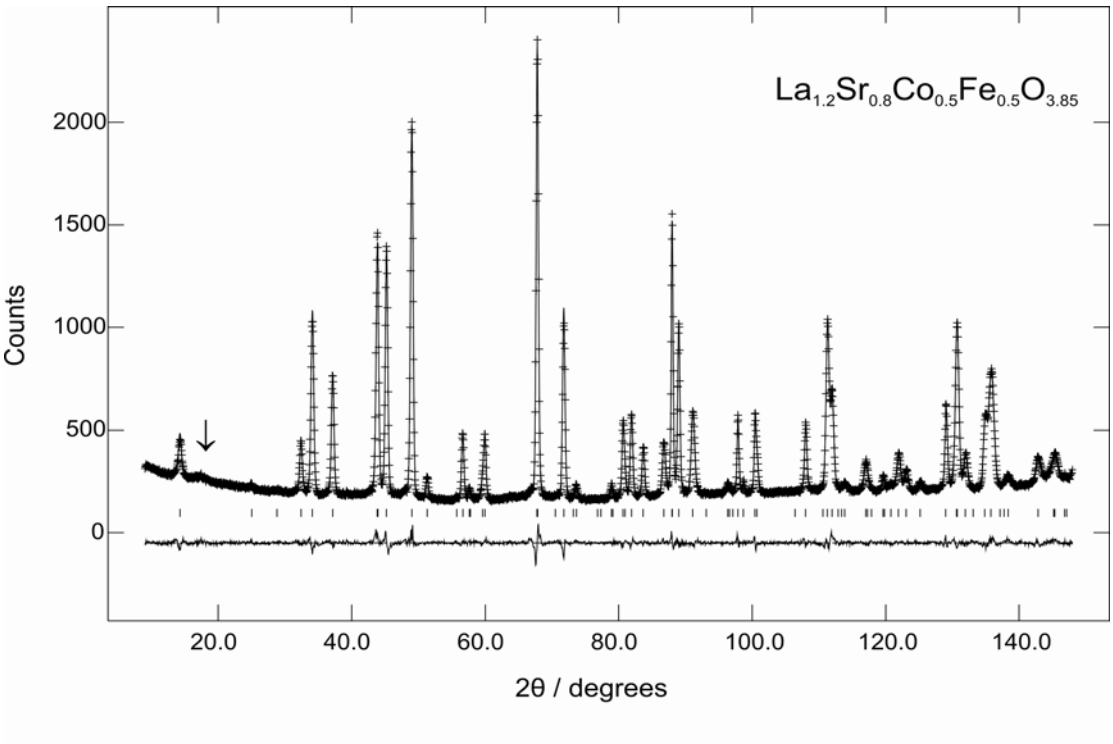
La1.2Sr0.8Co0.5Fe0.5O3.85
Counts
2000
1500
1000
500
0
20.0
40.0
60.0
80.0
100.0
120.0
140.0
2θ / degrees

3.4b)

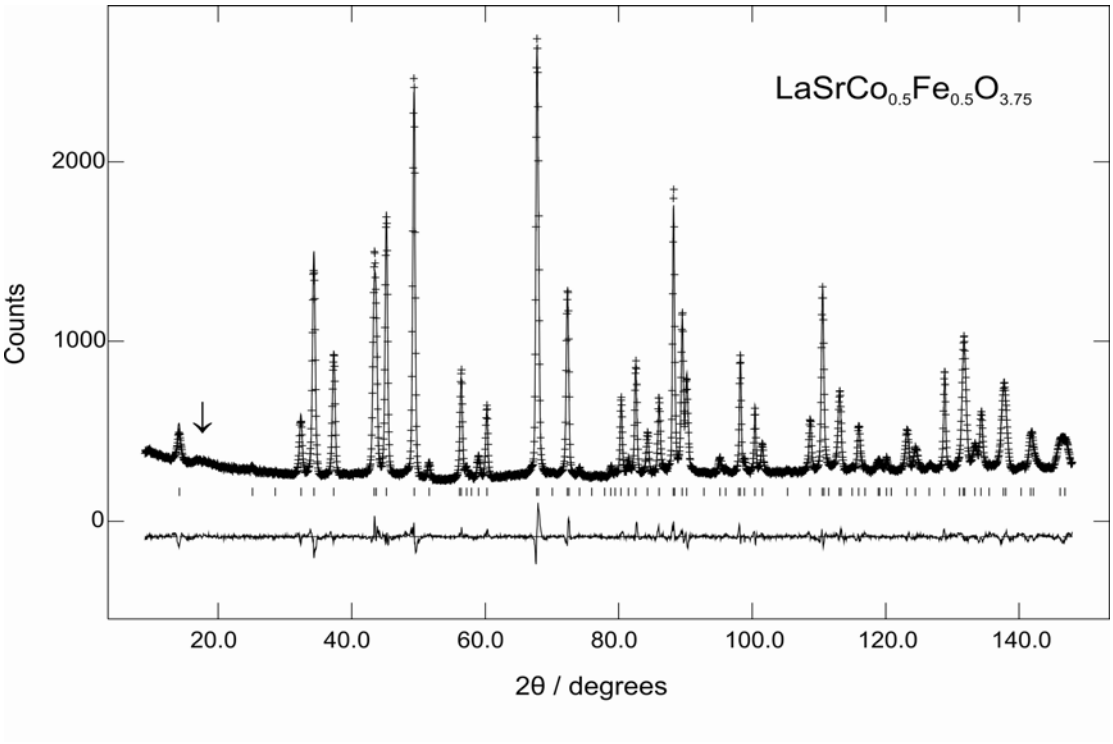
LaSrCo0.5Fe0.5O3.75
Counts
2000
1000
0
20.0
40.0
60.0
80.0
100.0
120.0
140.0
2θ / degrees

3.4c)

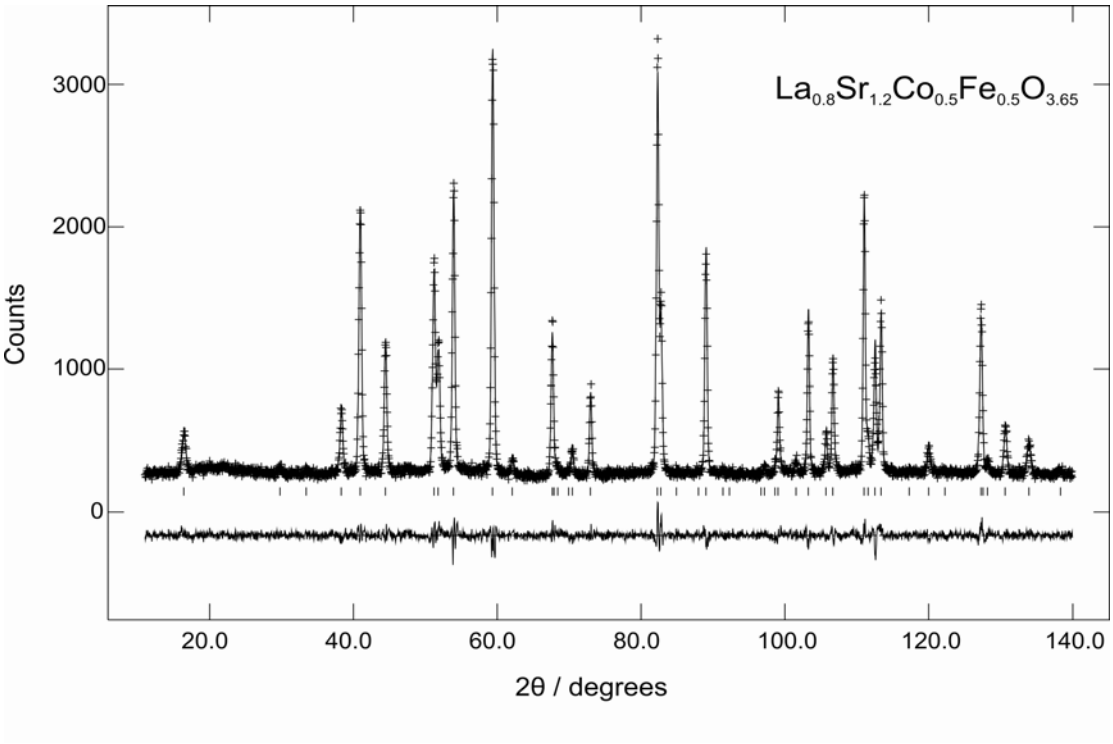

Figure 3.4 Observed, calculated and difference profiles for NPD data collected from different reduced samples at room temperature. The arrows in a) and b) show diffuse peaks that may indicate short-rang magnetic ordering.

Table 3.1 Structural results for the refinement of the NPD data collected from different samples at room temperature.

Atom	*x*	*y*	*z*	100 x Uiso (Å^2)	Occupancy	Site Symmetry
			$La_{1.2}Sr_{0.8}Co_{0.5}Fe_{0.5}O_4$, *a* = 3.85523(6) Å; *c* = 12.6071(2) Å wRp = 0.0352; Rp = 0.0261; $\chi 2$ = 3.226			
Co/Fe	0	0	0	0.30(3)	0.5/0.5	2a
La/Sr	0	0	0.3600(3)	0.36(2)	0.6/0.4	4e
O1	0.5	0	0	0.62(2)	1	4c
O2	0	0	0.1678(1)	1.62*	1	4e
*U_{11}=1.84(4) Å^2; U_{22}=1.84(4) Å^2; U_{33}=1.18(8) Å^2						
			$LaSrCo_{0.5}Fe_{0.5}O_4$, *a* = 3.83900(6) Å; *c* = 12.5676(2) Å wRp = 0.0314; Rp = 0.0237; $\chi 2$ = 2.423			
Co/Fe	0	0	0	0.11(3)	0.5/0.5	2a
La/Sr	0	0	0.3596(8)	0.17(2)	0.5/0.5	4e
O1	0.5	0	0	0.33(2)	1	4c
O2	0	0	0.1659(5)	1.09*	1	4e
*U_{11}=1.25(3) Å^2; U_{22}=1.25(3) Å^2; U_{33}=0.77(9) Å^2						
			$La_{1.2}Sr_{0.8}Co_{0.5}Fe_{0.5}O_{3.85}$, *a* = 3.84893(8) Å; *c* = 12.8406(3) Å wRp = 0.0303; Rp = 0.0234; $\chi 2$ = 2.294			
Co/Fe	0	0	0	0.31(2)	0.5/0.5	2a
La/Sr	0	0	0.3593(0)	0.36(2)	0.6/0.4	4e
O1	0.5	0.0333(7)	0	0.50(4)	0.470(2)	8j
O2	0	0	0.1710(2)	1.55*	1	4e
*U_{11}=1.95(3) Å^2; U_{22}=1.95(3) Å^2; U_{33}=0.74(8) Å^2						
			$LaSrCo_{0.5}Fe_{0.5}O_{3.75}$, *a* = 3.82375(4) Å; *c* = 12.9635(2) Å wRp = 0.0345; Rp = 0.0256; $\chi 2$ = 3.971			
Co/Fe	0	0	0	0.75(4)	0.5/0.5	2a
La/Sr	0	0	0.3571(5)	0.87(2)	0.5/0.5	4e
O1	0.5	0.0509(6)	0	0.70(5)	0.433(2)	8j
O2	0	0	0.1697(1)	1.81*	1	4e
*U_{11}=2.21(4) Å^2; U_{22}=2.21(4) Å^2; U_{33}=1.03(7) Å^2						
			$La_{0.8}Sr_{1.2}Co_{0.5}Fe_{0.5}O_{3.65}$, *a* = 3.7981(1) Å; *c* = 13.0515(5) Å wRp = 0.059; Rp = 0.0467; $\chi 2$ = 1.401			
Co/Fe	0	0	0	0.81(7)	0.5/0.5	2a
La/Sr	0	0	0.3551(1)	0.95(5)	0.4/0.6	4e
O1	0.5	0.061(1)	0	1.2(1)	0.417(3)	8j
O2	0	0	0.1675(2)	2.14*	1	4e
*U_{11}=2.14(8) Å^2; U_{22}=2.14(8) Å^2; U_{33}=2.1(2) Å^2						

Table 3.2 Selected bond lengths (Å) for the refined phases.

Bond	**$La_{1.2}Sr_{0.8}Co_{0.5}Fe_{0.5}O_4$**	**$LaSrCo_{0.5}Fe_{0.5}O_4$**	
Co/Fe–O1	1.92762(3)	1.91950(3)	
Co/Fe–O2	2.1153(1)	2.086(1)	
La/Sr–O1	2.6134(6)	2.6066(7)	
La/Sr–O2	2.7485(2)	2.7336(2)	
	2.424(2)	2.435(2)	
	$La_{1.2}Sr_{0.8}Co_{0.5}Fe_{0.5}O_{3.85}$	**$LaSrCo_{0.5}Fe_{0.5}O_{3.75}$**	**$La_{0.8}Sr_{1.2}Co_{0.5}Fe_{0.5}O_{3.65}$**
Co/Fe–O1*	1.9287(2)	1.9218(2)	1.9132(5)
Co/Fe–O2	2.196(1)	2.200(1)	2.187(2)
La/Sr–O1*	2.735(2)	2.805(2)	2.850(3)
	2.548(2)	2.526(2)	2.520(3)
La/Sr–O2	2.7493(2)	2.7261(2)	2.7019(3)
	2.418(2)	2.430(2)	2.448(3)

*Splitting of O1 sites gives twice the number of bonds compared with the ideal site

3.5 Mössbauer spectroscopy

The ^{57}Fe Mössbauer spectra recorded from different samples at room temperature confirmed that iron is present in all samples (except $La_{0.8}Sr_{1.2}Co_{0.5}Fe_{0.5}O_4$) as only the trivalent state (Fe^{3+}). *Figure 3.5* shows, for example, the Mössbauer spectra of $La_{1.2}Sr_{0.8}Co_{0.5}Fe_{0.5}O_4$ and $La_{1.2}Sr_{0.8}Co_{0.5}Fe_{0.5}O_{3.85}$ at room temperature. The data were best fitted to single doublets with a chemical isomer shift $\delta = 0.32$ mm s^{-1} for both samples and quadrupole splittings 1.09 and 1.49 mm s^{-1} for oxygenated and reduced samples, respectively. The observed isomer shift and quadrupole splitting values are characteristic of Fe^{3+} in distorted octahedral oxygen coordination [13,14]. For $La_{1.2}Sr_{0.8}Co_{0.5}Fe_{0.5}O_4$, the relatively high quadrupole splitting may be related to a slight distortion (M–O2/M–O1 is 1.10) and/or covalency effects. The higher quadrupole splitting of the reduced sample ($\Delta = 1.49$ mm s^{-1}) reflects an enhanced distortion which is consistent with an increased elongation along *c* (M–O2/M–O1 is 1.14) and the presence of oxygen vacancies.

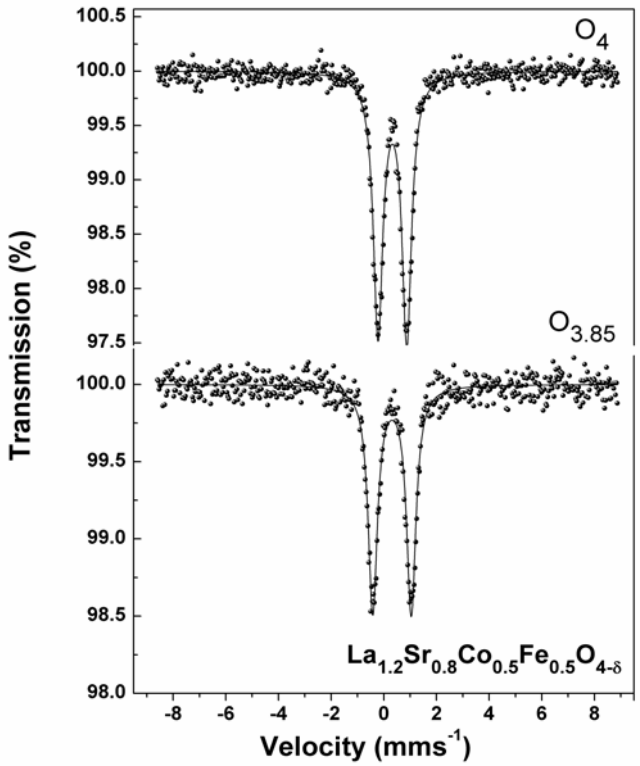

Figure 3.5 ^{57}Fe Mössbauer spectra recorded from $La_{1.2}Sr_{0.8}Co_{0.5}Fe_{0.5}O_4$ and $La_{1.2}Sr_{0.8}Co_{0.5}Fe_{0.5}O_{3.85}$ at 298 K.

Another example is the Mössbauer spectra recorded from $La_{0.8}Sr_{1.2}Co_{0.5}Fe_{0.5}O_{3.65}$ at 298 and 16 K (*Figure 3.6 (a)*, with parameters in *Table 3.3*). The spectrum recorded at 298 K was composed of a single doublet with chemical isomer shift $\delta = 0.31$ mm s^{-1} characteristic of Fe^{3+}. The large quadrupole splitting ($\Delta = 1.43$ mm s^{-1}) is also indicative of the Fe^{3+} ion being located in less than six-fold coordination. The spectrum recorded at 16 K showed a single magnetic hyperfine pattern with parameters (*Table 3.3*) compatible with this situation.

The ^{57}Fe Mössbauer spectra recorded from $La_{0.8}Sr_{1.2}Co_{0.5}Fe_{0.5}O_4$ are shown in *Figure 3.6 (b)*. The parameters are collected in *Table 3.3*. The spectrum recorded at 298 K was best fitted to two quadrupole split absorptions. The doublet with chemical isomer shift

δ = 0.30 mm s^{-1} is characteristic of Fe^{3+}. The magnitude of the quadrupole splitting, Δ = 0.83 mm s^{-1}, would indicate a distortion of the octahedral array of oxygen ions around iron. The chemical isomer shift of the other doublet, δ = 0.28 mm s^{-1}, is intermediate between that characteristic of Fe^{3+} and Fe^{4+} and, given the oxygen stoichiometry, we associate this with charge sharing between neighbouring Fe^{3+} and Fe^{4+} ions with a timescale smaller than 10^{-8} s. The spectrum recorded at 16 K was characterised by a complex broad lined magnetic hyperfine pattern which was best fitted to two discrete sextets (H = 45.4 and 41.1 T) and a distribution of magnetic hyperfine fields (H = 33.9 T). The large quadrupole interactions associated with the discrete sextets are indicative of a distorted octahedral array of oxygen around iron and is consistent with the large quadrupole splitting observed at 298 K for the Fe^{3+} component. We associate the overall complexity of the spectrum with the occurrence of complex magnetic interactions between Fe^{3+}, Fe^{4+}, Co^{3+} and Co^{4+}.

Mössbauer data suggest that the iron exists as Fe^{3+}/Fe^{4+} in $La_{0.8}Sr_{1.2}Co_{0.5}Fe_{0.5}O_4$ and only as Fe^{3+} in all other samples. Considering that the oxygenated materials are stoichiometric in oxygen, as evidenced by NPD and TG analyses, the B-site oxidation states $Co^{2+/3+}/Fe^{3+}$, Co^{3+}/Fe^{3+} and $(Co/Fe)^{3+/4+}$ are assigned for $La_{1.2}Sr_{0.8}Co_{0.5}Fe_{0.5}O_4$, $LaSrCo_{0.5}Fe_{0.5}O_4$ and $La_{0.8}Sr_{1.2}Co_{0.5}Fe_{0.5}O_4$, respectively. Given the presence of Fe^{3+} in the reduced samples, the oxygen contents are, within experimental error, consistent with phases containing pure Co^{2+} and Fe^{3+} ions. It is interesting to note that similar K_2NiF_4 phases containing Co mainly in the divalent state, such as La_2CoO_4 and $LaSrCoO_{3.5-x}$, undergo room temperature topotactic oxidation in air and are stable only under inert atmospheres [9,15]. In contrast, the Co^{2+}-containing phases studied here ($La_{1.2}Sr_{0.8}Co_{0.5}Fe_{0.5}O_{3.85}$, $LaSrCo_{0.5}Fe_{0.5}O_{3.75}$ and $La_{0.8}Sr_{1.2}Co_{0.5}Fe_{0.5}O_{3.65}$) do not show such reactivity toward atmospheric oxygen at ambient temperatures.

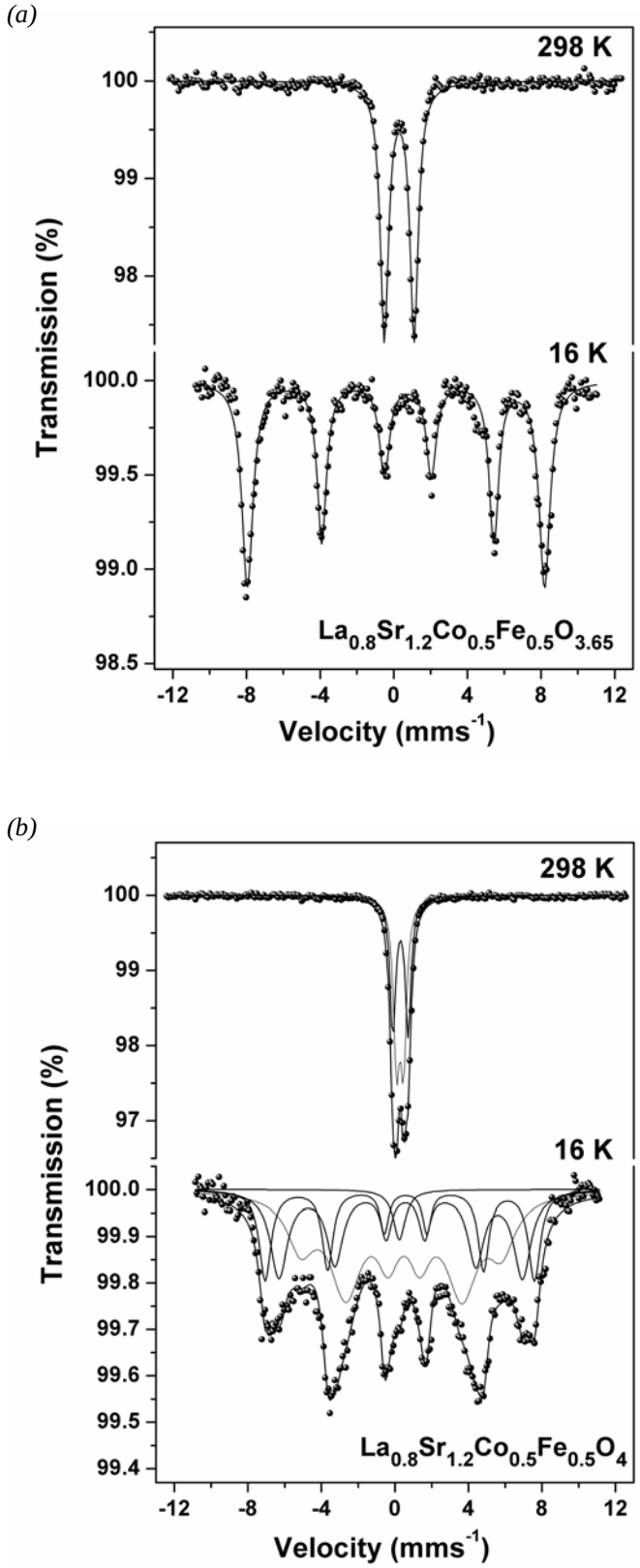

Figure 3.6 ^{57}Fe Mössbauer spectra recorded from (a) $La_{0.8}Sr_{1.2}Co_{0.5}Fe_{0.5}O_{3.65}$, and (b) $La_{0.8}Sr_{1.2}Co_{0.5}Fe_{0.5}O_4$ at 298 and 16 K.

Table 3.3 ^{57}Fe Mössbauer parameters (isomer shift, δ; quadrupole splitting, Δ; hyperfine field, H) for $La_{0.8}Sr_{1.2}Co_{0.5}Fe_{0.5}O_4$ and $La_{0.8}Sr_{1.2}Co_{0.5}Fe_{0.5}O_{3.65}$.

Material	Temperature	δ ± 0.04 (mm s^{-1})	Δ or $e^2Q_q/2$ ± 0.04 (mm s^{-1})	H ± 0.05 (T)	Area ±3%
$La_{0.8}Sr_{1.2}Co_{0.5}Fe_{0.5}O_4$	298	0.30	0.83		45
		0.28	0.38		55
	16	0.42	-0.32	45.4	22
		0.44	-0.26	41.1	28
		0.41	-0.14	33.9	50
$La_{0.8}Sr_{1.2}Co_{0.5}Fe_{0.5}O_{3.65}$	298	0.31	1.43		100
	16	0.44	-0.64	50.1	100

3.6 Magnetic susceptibility and low temperature NPD

Figure 3.7 shows the temperature dependence of the magnetic susceptibility of different samples. The oxygenated materials generally show higher magnetization than the reduced ones, with a paramagnetic enhancement of susceptibility at low temperatures. A distinct divergence between ZFC and FC susceptibilities for the oxygenated materials is suggestive of spin glass behaviour. As shown in the insets of *Figure 3.7*, susceptibilities of the reduced materials show antiferromagnetic-like peaks at $T \geq 200$ K indicating AFM ordering in these materials. Again, divergence between ZFC and FC data is seen, and may indicate a small FM component due to canting of the moments. The diffuse peaks which can be seen around $2\theta = 17°$ in the room temperature NPD patterns of $La_{1.2}Sr_{0.8}Co_{0.5}Fe_{0.5}O_{3.85}$ and $LaSrCo_{0.5}Fe_{0.5}O_{3.75}$ (see arrows in *Figure 3.4*) are consistent with the existence of short-range magnetic order; although no magnetic splitting is observed in the Mössbauer data of $La_{1.2}Sr_{0.8}Co_{0.5}Fe_{0.5}O_{3.85}$, probably because the Néel temperature of this material is very close to room temperature.

3.7a)

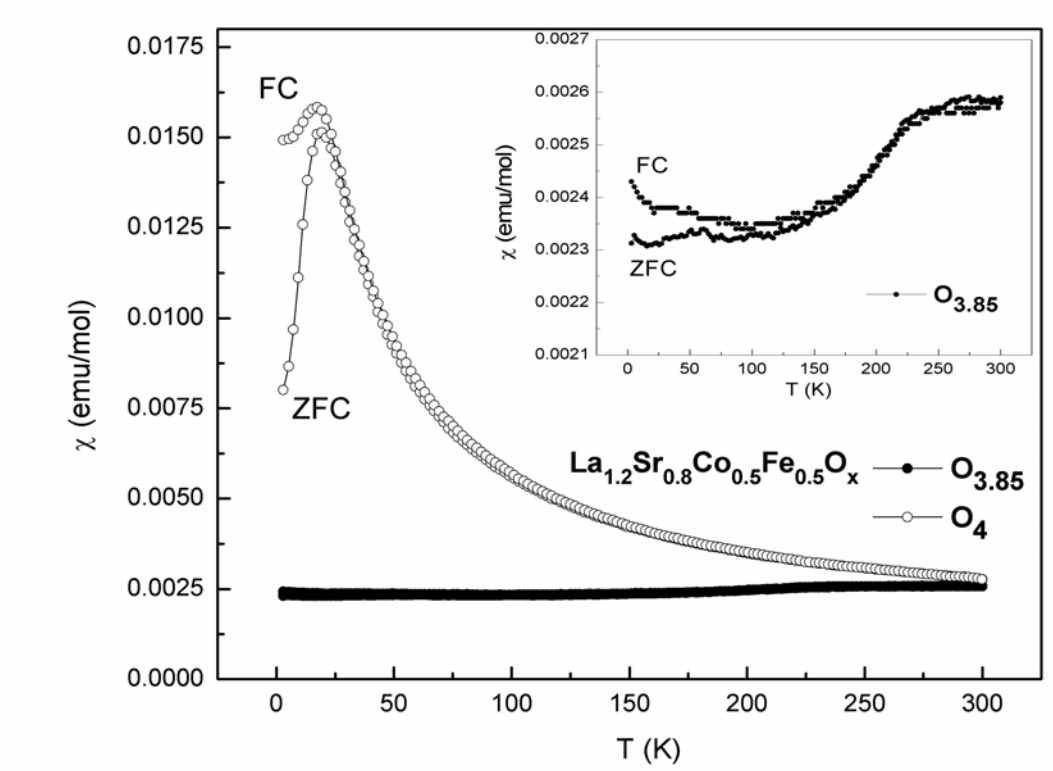
FC
ZFC
χ (emu/mol)
T (K)
La1.2Sr0.8Co0.5Fe0.5Ox
O3.85
O4
O3.85

3.7b)

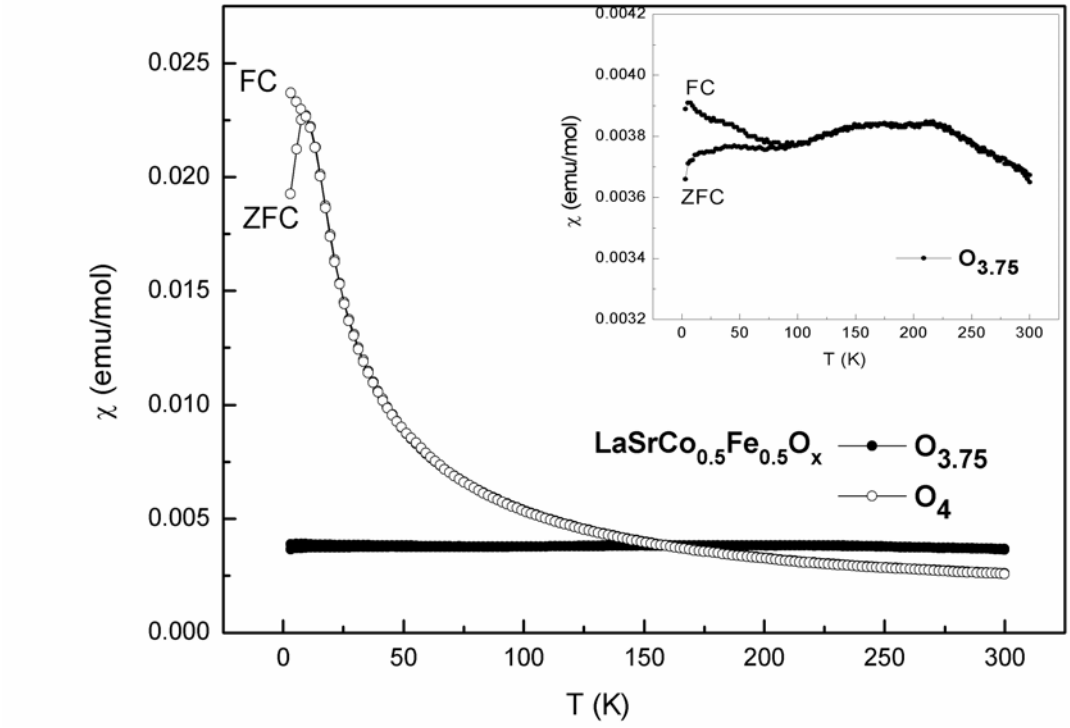
FC
ZFC
χ (emu/mol)
T (K)
LaSrCo0.5Fe0.5Ox
O3.75
O4
O3.75

3.7c)

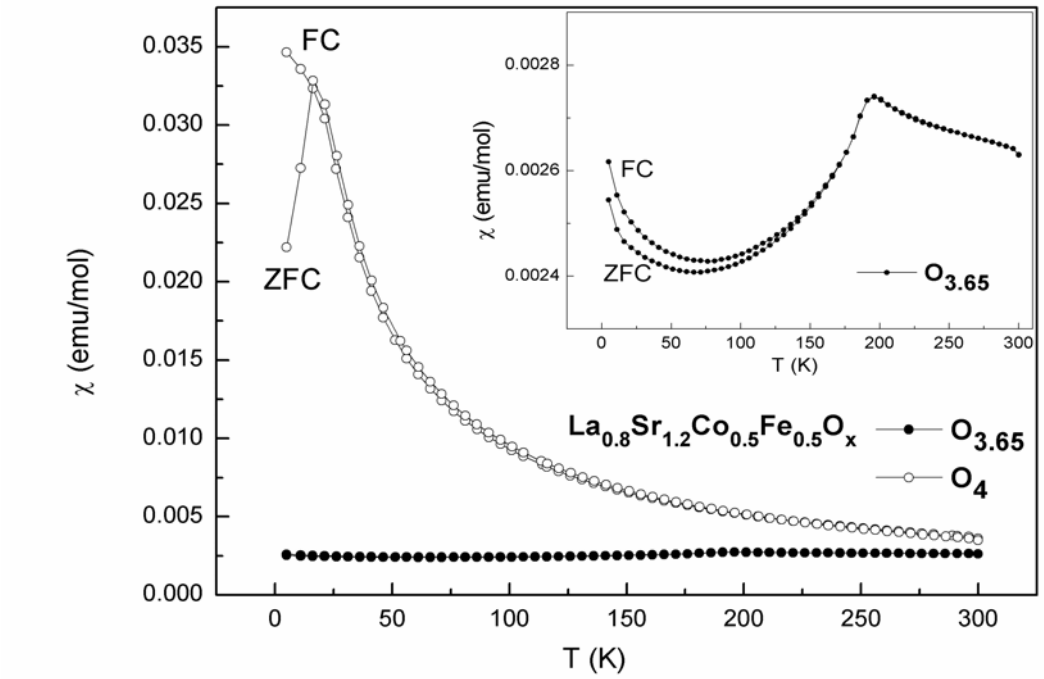

Figure 3.7 Variation of magnetic susceptibility (ZFC and FC) with temperature for (a) $La_{1.2}Sr_{0.8}Co_{0.5}Fe_{0.5}O_{4-\delta}$ (b) $LaSrCo_{0.5}Fe_{0.5}O_{4-\delta}$ and (c) $La_{0.8}Sr_{1.2}Co_{0.5}Fe_{0.5}O_{4-\delta}$.

NPD data collected at 5 K have confirmed that the reduced samples are magnetically ordered at this temperature. Compared with data sets collected at room temperature, a series of additional Bragg reflections were clearly observed for $La_{1.2}Sr_{0.8}Co_{0.5}Fe_{0.5}O_{3.85}$, $LaSrCo_{0.5}Fe_{0.5}O_{3.75}$ and $La_{0.8}Sr_{1.2}Co_{0.5}Fe_{0.5}O_{3.65}$ data at 5 K (see *Figure 3.8*). These additional Bragg reflections could be indexed with a primitive tetragonal cell with lattice parameters $a_{magnetic} = \sqrt{2}\ a_{nuclear}$ and $c_{magnetic} = c_{nuclear}$. Several models of AFM order were examined including alignments of moments parallel to the *z* axis and those with moments confined to the *xy* plane. Two collinear in-plane models related to La_2CuO_4 and $La_2NiO_{4+\delta}$ magnetic structures, frequently occur in ordered K_2NiF_4-type antiferromagnets [16-19]; both models consist of alternate FM sheets coupled antiferromagnetically, with the moments aligned either parallel (La_2CuO_4-type) or

perpendicular ($La_2NiO_{4+\delta}$-type) to the ferromagnetic planes (see section 1.3). As shown in *Figure 3.8*, NPD patterns of different samples show strong magnetic peaks corresponding to the (100) reflection of the magnetic supercell (*e.g.* peaks at $2\theta \approx 17°$ for $La_{1.2}Sr_{0.8}Co_{0.5}Fe_{0.5}O_{3.85}$ and $LaSrCo_{0.5}Fe_{0.5}O_{3.75}$; $\lambda = 1.5943$ Å). This observation requires a major FM component of the moments to be perpendicular to <100> directions, and is therefore consistent with a collinear La_2CuO_4-type magnetic order previously reported, for example, for $LaAFeO_4$ (A = Ca, Sr) [20,21]. However, there was no evidence in the low temperature diffraction data to suggest a lowering of the cell symmetry from tetragonal to orthorhombic. A noncollinear model consistent with the tetragonal symmetry should be therefore considered (see section 1.3). Based on arguments previously discussed in detail for this order [18,19], a noncollinear La_2CuO_4-type model ($P4_2/nn'm$ symmetry) has been adopted and the magnetic order is shown in *Figure 3.9*. In contrast to the magnetic structure reported for $LaSrCoO_{3.5-x}$ [9], no evidence was found for a magnetic component parallel to the *z* axis. The fits to the low temperature NPD data are shown in *Figure 3.8* with refined structural parameters given in *Table 3.4*; an average of Fe^{3+} and Co^{2+} form factors was used in the refinement. The ordered moments refined from the proposed model are 3.46(7), 3.38(3) and 3.34(5) μ_B for $La_{1.2}Sr_{0.8}Co_{0.5}Fe_{0.5}O_{3.85}$, $LaSrCo_{0.5}Fe_{0.5}O_{3.75}$ and $La_{0.8}Sr_{1.2}Co_{0.5}Fe_{0.5}O_{3.65}$, respectively. No evidence of AFM ordering has been observed in the low temperature NPD data of the oxygenated materials $La_{1.2}Sr_{0.8}Co_{0.5}Fe_{0.5}O_4$, $LaSrCo_{0.5}Fe_{0.5}O_4$ and $La_{0.8}Sr_{1.2}Co_{0.5}Fe_{0.5}O_4$. The spin glass behaviour in these materials has been confirmed by AC magnetic susceptibility measurements. The frequency dependence of the AC magnetic susceptibility of $La_{0.8}Sr_{1.2}Co_{0.5}Fe_{0.5}O_4$, for example, is shown in *Figure 3.10*. It is clearly seen that the location of the cusp at the freezing temperature is dependent of the frequency of the AC susceptibility measurement which is a characteristic feature of spin glasses.

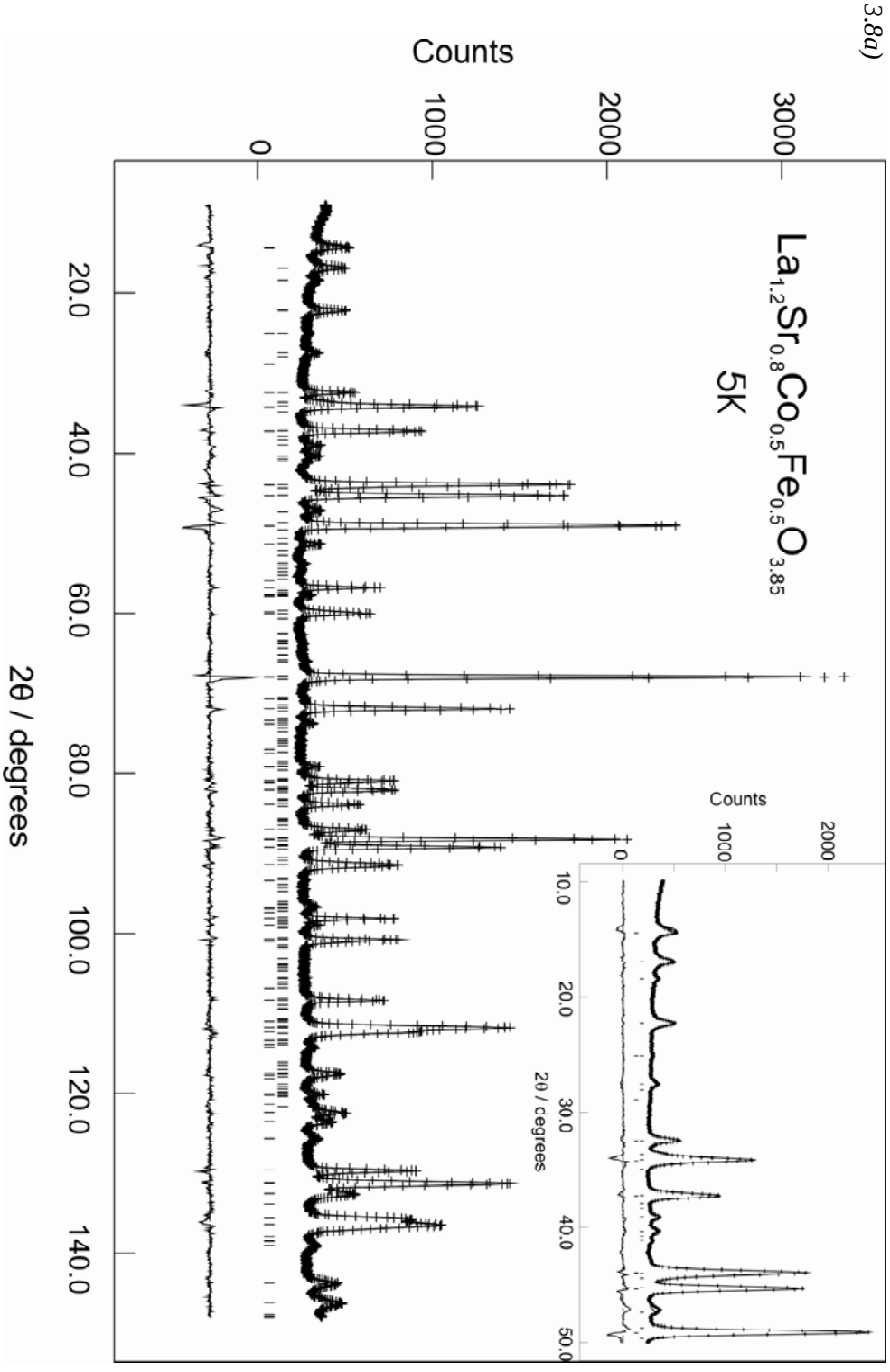
Counts
3000
2000
1000
0
$La_{1.2}Sr_{0.8}Co_{0.5}Fe_{0.5}O_{3.85}$
5K
20.0
40.0
60.0
80.0
100.0
120.0
140.0
2θ / degrees
Counts
2000
1000
0
10.0
20.0
30.0
40.0
50.0
2θ / degrees

3.8a)

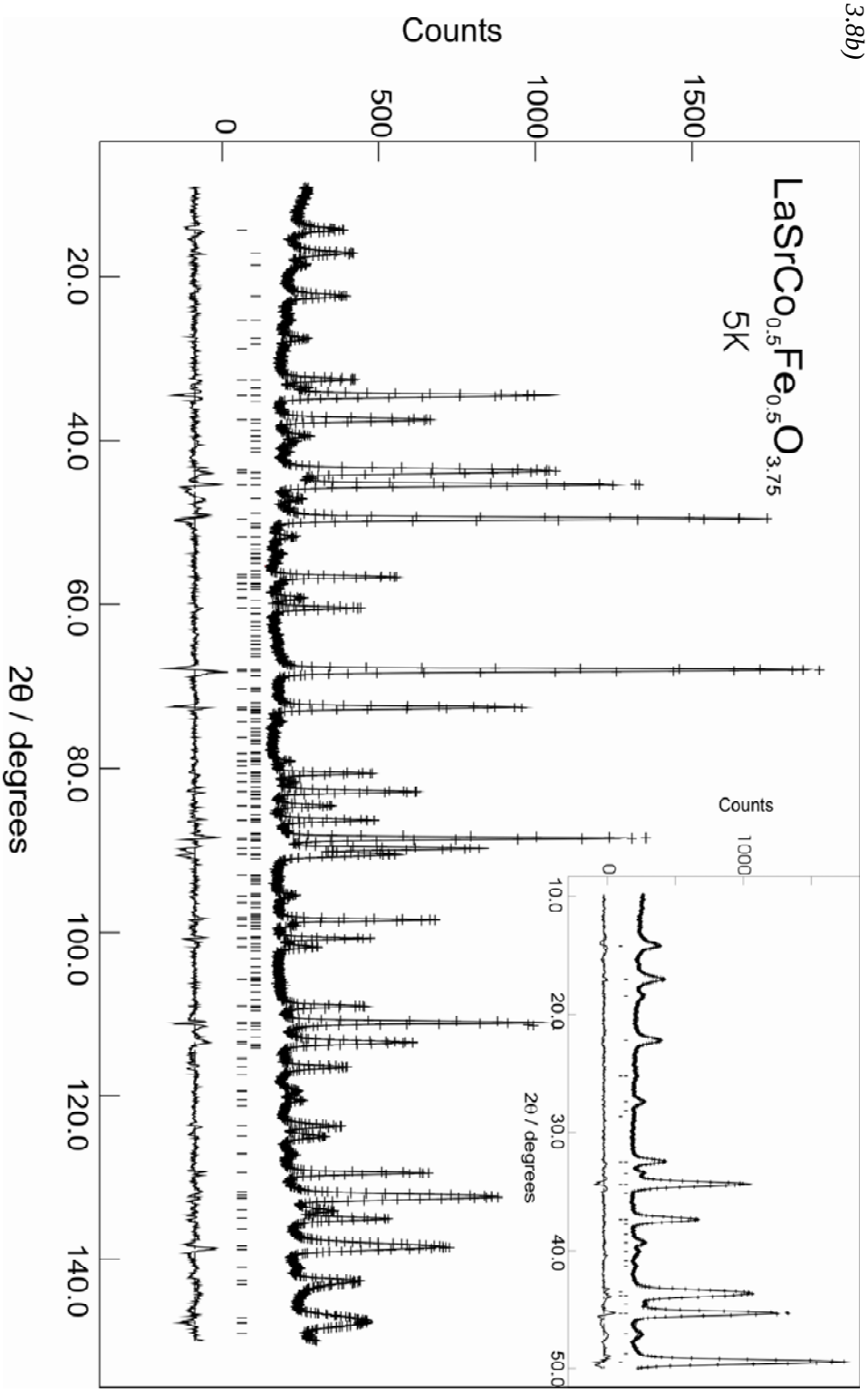
Counts
1500
1000
500
0
LaSrCo0.5Fe0.5O3.75
5K
20.0
40.0
60.0
80.0
100.0
120.0
140.0
2θ / degrees
Counts
1000
0
10.0
20.0
30.0
40.0
50.0
2θ / degrees

3.8b)

3.8c)

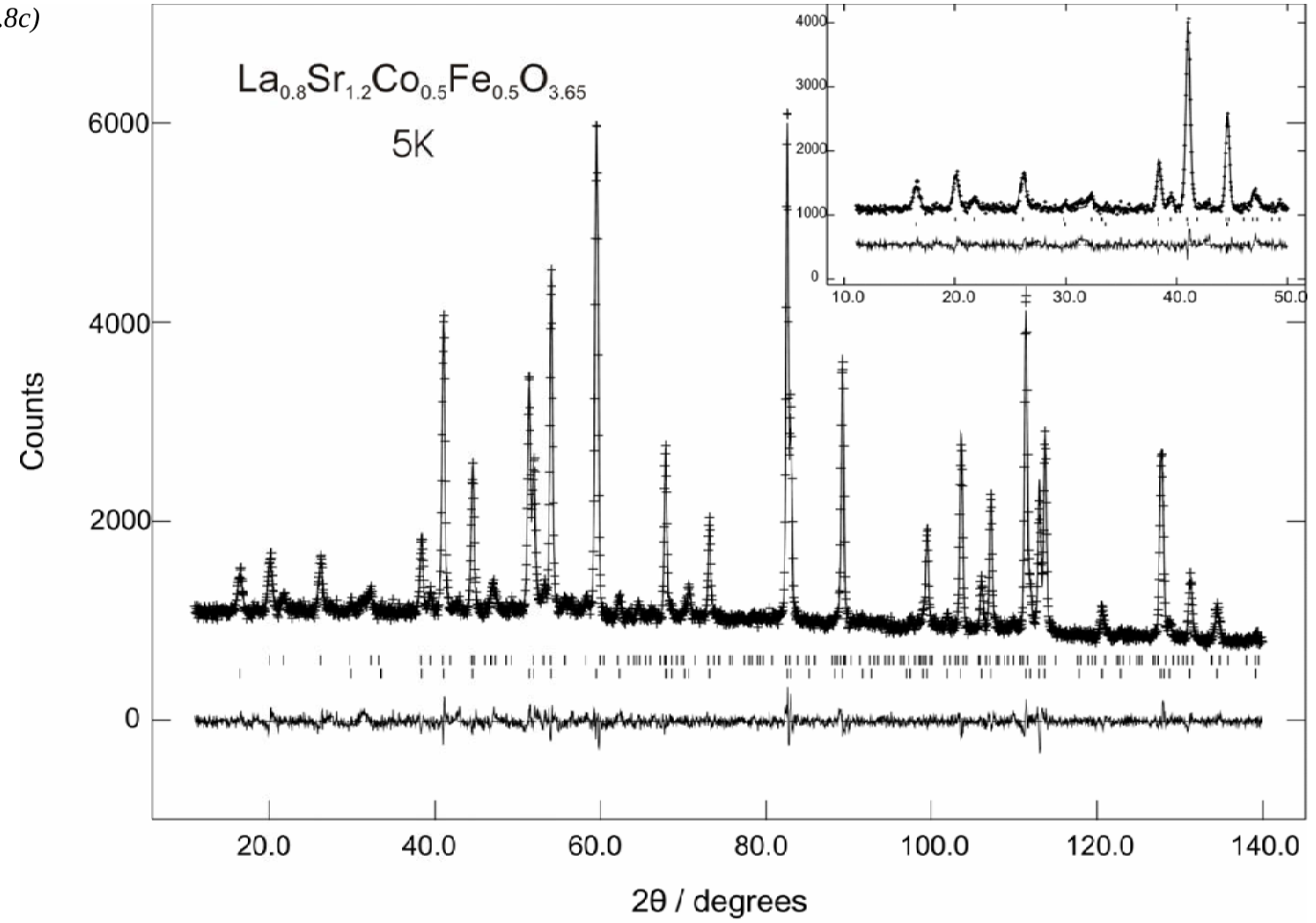

Figure 3.8 Observed, calculated and difference profiles for NPD data collected at 5 K for (a) $La_{1.2}Sr_{0.8}Co_{0.5}Fe_{0.5}O_{3.85}$, (b) $LaSrCo0_{.5}Fe_{0.5}O_{3.75}$ and (c) $La_{0.8}Sr_{1.2}Co_{0.5}Fe_{0.5}O_{3.65}$, showing nuclear (lower tick marks) and magnetic (upper tick marks) reflections.

Table 3.4 Structural results for the refinement of the NPD data collected from the reduced samples at 5 K.

Atom	*x*	*y*	*z*	100 x Uiso (Å^2)	Occupancy	Site Symmetry
$La_{1.2}Sr_{0.8}Co_{0.5}Fe_{0.5}O_{3.85}$: Space Groups *I4/mmm* (Nuclear) and *$P4_2/nn'm$* (Magnetic)						
Co/Fe	0	0	0	0**	0.5/0.5	2a
La/Sr	0	0	0.35895(8)	0.02(2)	0.6/0.4	4e
O1	0.5	0.0344(8)	0	0.01(5)	0.465(2)	8j
O2	0	0	0.1711(1)	1.12*	1	4e

*U_{11}=1.18(4) Å^2; U_{22}=1.18(4) Å^2; U_{33}=1.01(1) Å^2

**negative U_{iso} constrained to zero.

a = 3.84140(7) Å; *c* = 12.8063(3) Å

	x	*y*	*z*	M_x/μ_B	M_y/μ_B	M_z/μ_B	$\|M\|/\mu_B$
Co/Fe	0	0	0	2.45(5)	2.45(5)	0	3.46(7)

wRp = 0.0340; Rp = 0.0248; χ^2 = 4.019

$LaSrCo_{0.5}Fe_{0.5}O_{3.75}$: Space Groups *I4/mmm* (Nuclear) and *$P4_2/nn'm$* (Magnetic)							
Co/Fe	0	0	0	0.37(3)	0.5/0.5		2a
La/Sr	0	0	0.35745(9)	0.46(2)	0.5/0.5		4e
O1	0.5	0.0471(7)	0	0.66(5)	0.441(2)		8j
O2	0	0	0.1691(1)	1.32*	1		4e

*U_{11}=1.61(4) Å^2; U_{22}=1.61(4) Å^2; U_{33}=0.74(8) Å^2

a = 3.81538(8) Å; *c* = 12.9264(3) Å

	x	*y*	*z*	M_x/μ_B	M_y/μ_B	M_z/μ_B	$\|M\|/\mu_B$
Co/Fe	0	0	0	2.39(2)	2.39(2)	0	3.38(3)

wRp = 0.0395; Rp = 0.0305; χ^2 = 3.741

$La_{0.8}Sr_{1.2}Co_{0.5}Fe_{0.5}O_{3.65}$: Space Groups *I4/mmm* (Nuclear) and *$P4_2/nn'm$* (Magnetic)							
Co/Fe	0	0	0	0.85(9)	0.5		2a
La/Sr	0	0	0.3555(1)	0.89(7)	0.6		4e
O1	0.5	0.064(1)	0	1.0(1)	0.415(4)		8j
O2	0	0	0.1669(2)	1.91*	1		4e

*U_{11}=1.84(8) Å^2; U_{22}=1.84(8) Å^2; U_{33}=2.1(2) Å^2

a = 3.79067(5) Å; *c* = 13.0133(2) Å

	x	*y*	*z*	M_x/μ_B	M_y/μ_B	M_z/μ_B	$\|M\|/\mu_B$
Co/Fe	0	0	0	2.36(4)	2.36(4)	0	3.34(5)

wRp = 0.0366; Rp = 0.0289; χ^2 = 1.715

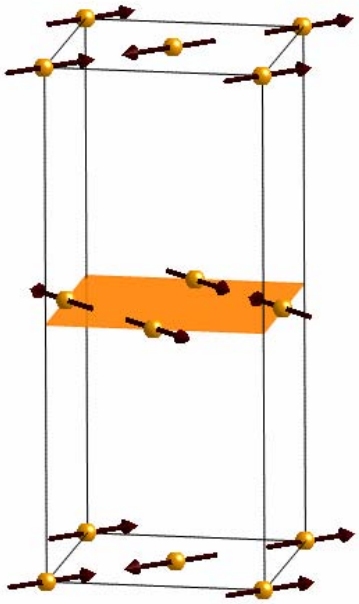

Figure 3.9 Magnetic structure of the reduced samples. The arrows indicate the direction of Co/Fe magnetic moments.

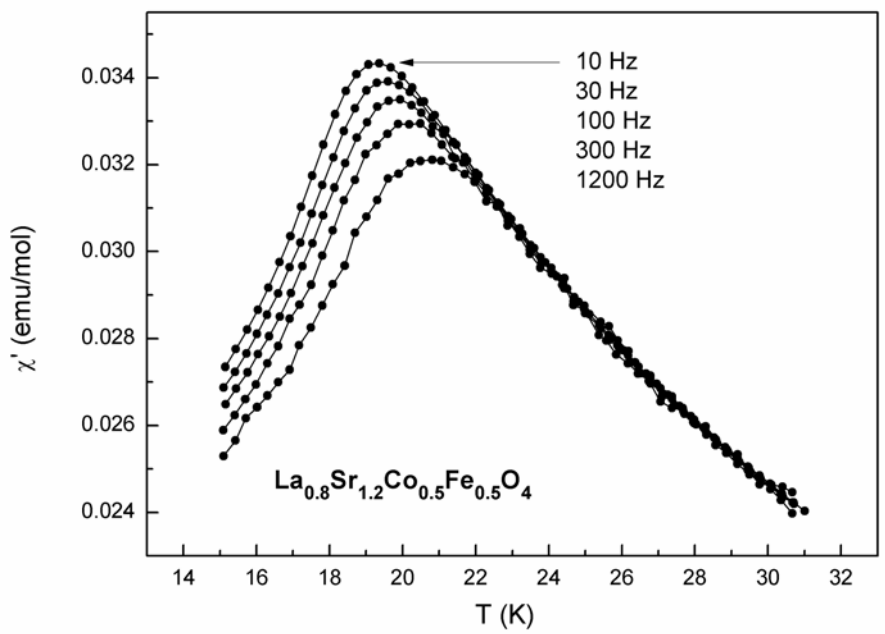

Figure 3.10 Spin glass behaviour observed in AC susceptibility at low temperature for $La_{0.8}Sr_{1.2}Co_{0.5}Fe_{0.5}O_4$.

The spin glass state in $La_{0.8}Sr_{1.2}Co_{0.5}Fe_{0.5}O_4$ is consistent with the complexity of the Mössbauer data at 16 K which is indicative of complex magnetic interactions between Fe^{3+}, Co^{3+}, Fe^{4+} and Co^{4+}. Plots of the reciprocal of the molar susceptibility against temperature for $La_{1.2}Sr_{0.8}Co_{0.5}Fe_{0.5}O_4$ and $LaSrCo_{0.5}Fe_{0.5}O_4$ (*Figure 3.11 (a,b)*) suggest a non Curie-Weiss behaviour in the given temperature range. The plots display an increased gradient at low temperature which is consistent with magnetic frustration [22]. Application of Curie-Weiss law at the end parts of the plots resulted in negative θ values and a decreasing effective moment as the temperature decreases; this is consistent with exchange interactions which are predominantly AFM. Above 250 K, the effective moments are 3.47 and 3.37 μ_B for $La_{1.2}Sr_{0.8}Co_{0.5}Fe_{0.5}O_4$ and $LaSrCo_{0.5}Fe_{0.5}O_4$, respectively; the effective moments are too small to be due to high spin Fe^{3+} and $Co^{3+}(Co^{2+})$ ions, which would provide effective magnetic moments of 5.26 and 5.43 μ_B for $La_{1.2}Sr_{0.8}Co_{0.5}Fe_{0.5}O_4$ and $LaSrCo_{0.5}Fe_{0.5}O_4$, respectively. On the other hand, the inverse susceptibility plot of $La_{0.8}Sr_{1.2}Co_{0.5}Fe_{0.5}O_4$ (*Figure 3.11 (c)*), suggests a behaviour close to Curie-Weiss in nature with similar small effective moment (μ_{eff} = 3.06 μ_B) and predominately AFM exchange interactions (θ = -23.9 K).

3.11a)

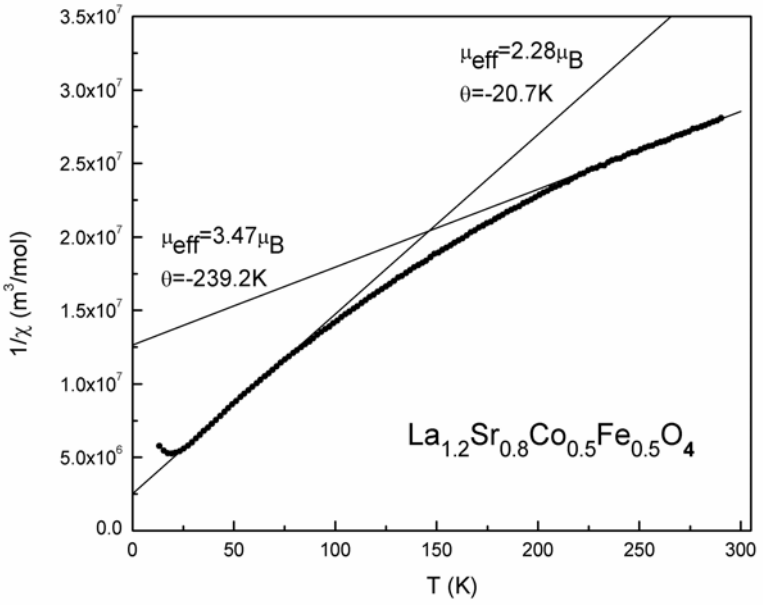

3.11b)

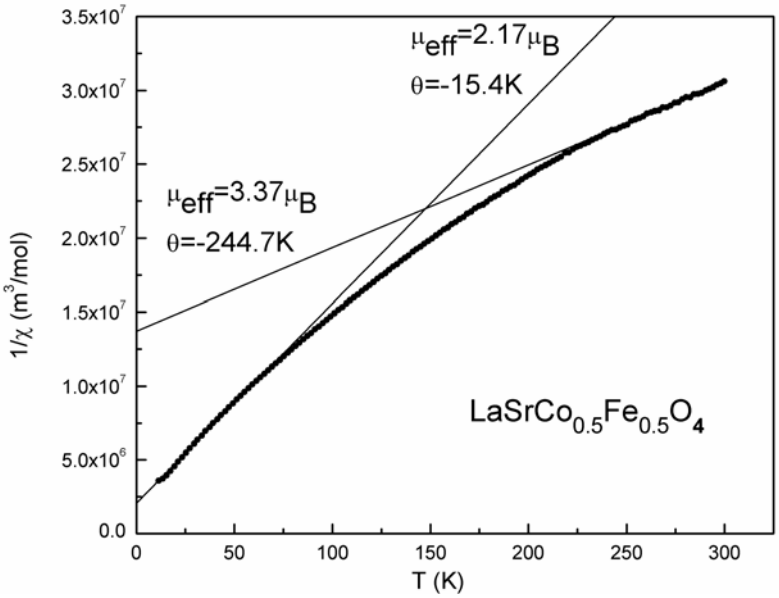

3.11c)

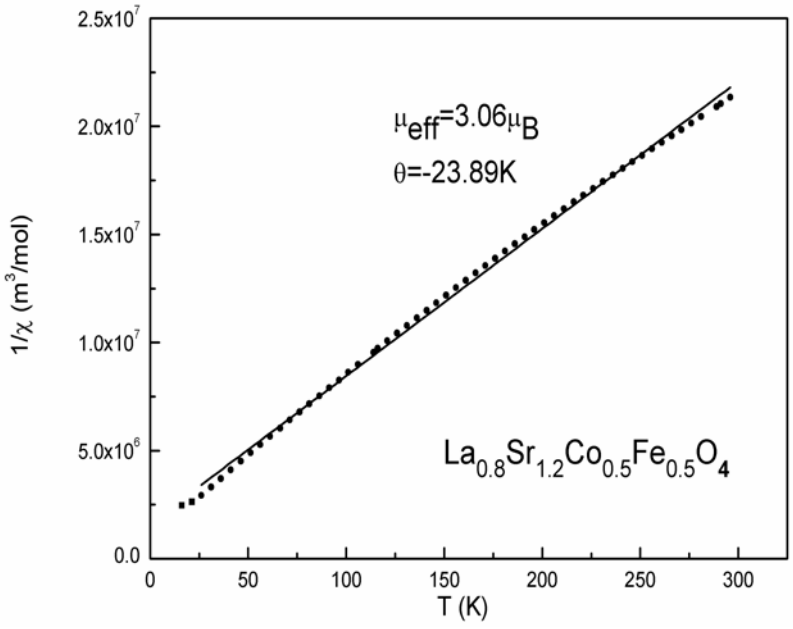

Figure 3.11 Variation of the inverse magnetic susceptibilities (ZFC) with temperature for (a) $La_{1.2}Sr_{0.8}Co_{0.5}Fe_{0.5}O_4$, (b) $LaSrCo_{0.5}Fe_{0.5}O_4$ and (c) $La_{0.8}Sr_{1.2}Co_{0.5}Fe_{0.5}O_4$.

3.7 Discussion of $La_{2-x}Sr_xCo_{0.5}Fe_{0.5}O_{4-\delta}$

The oxygenated materials $La_{1.2}Sr_{0.8}Co_{0.5}Fe_{0.5}O_4$, $LaSrCo_{0.5}Fe_{0.5}O_4$ and $La_{0.8}Sr_{1.2}Co_{0.5}Fe_{0.5}O_4$ are formed under oxidizing conditions with no evidence of oxygen nonstoichiometry. Based on oxygen stoichiometries (evidenced by TG and NPD analyses) and Mösssbauer study, the B-site oxidation states in these materials are $Co^{2+/3+}/Fe^{3+}$, Co^{3+}/Fe^{3+} and $(Co/Fe)^{3+/4+}$, respectively. 40% of Co in $La_{1.2}Sr_{0.8}Co_{0.5}Fe_{0.5}O_4$ is therefore present in the divalent state, although this presence has not induced oxygen hyperstoichiometry. The oxygen stoichiometry in $La_{0.8}Sr_{1.2}Co_{0.5}Fe_{0.5}O_4$ suggests the presence of 20% M^{4+} which is not inconsistent with Mössbauer data which implies the presence of some Fe^{4+} and Co^{4+} in this material. These materials withstand reducing conditions (10% H_2/N_2) up to 1000 °C *via* reduction of M^{4+} to M^{3+} and Co^{3+} to Co^{2+} and formation of disordered oxide ion vacancies within the equatorial planes of the K_2NiF_4-type structure. The Co^{2+}-containing materials $La_{1.2}Sr_{0.8}Co_{0.5}Fe_{0.5}O_{3.85}$, $LaSrCo_{0.5}Fe_{0.5}O_{3.75}$ and $La_{0.8}Sr_{1.2}Co_{0.5}Fe_{0.5}O_{3.65}$ are obtained at $T \geq 700$ °C, under applied reduction conditions. Unlike the K_2NiF_4 phases containing only Co^{2+} [9,15], the reduced materials are stable in air at ambient conditions. The materials show long-range AFM ordering with relatively high Néel transition temperatures (200-300 K). The strong AFM coupling in these materials is readily explained by the presence of Co^{2+} (t_{eg}^5 e_g^2) and Fe^{3+} (t_{eg}^3 e_g^2), for which AFM exchange is expected for all 180° super-exchange interactions [24,25]. The ordering scheme shown in *Figure 3.9* is used to account for the AFM coupling between Fe^{3+}/Co^{2+} spins in these materials. The ordered moments refined from the proposed model (3.46(7), 3.38(3) and 3.34(5) μ_B for $La_{1.2}Sr_{0.8}Co_{0.5}Fe_{0.5}O_{3.85}$, $LaSrCo_{0.5}Fe_{0.5}O_{3.75}$ and $La_{0.8}Sr_{1.2}Co_{0.5}Fe_{0.5}O_{3.65}$, respectively) are ~ 15% lower than the expected moments for a mixture of high spin Fe^{3+} and Co^{2+} assuming only a spin

contribution to the moment (g = 2.0). This reduction is less than might be expected from the cumulative effects of covalence, the low dimensionality of the magnetic order and quantum mechanical effects. However, Co^{2+} ions have a significant orbital contribution that enhances the moment, and an experimental moment very close to the theoretical value of 3.0 μ_B has been reported for La_2CoO_4 [23]. The higher moment for Fe^{3+} (theoretical 5.0 μ_B) rationalizes the higher moments observed for the studied materials.

The oxygenated materials (containing Co mainly in the trivalent state) showed no evidence of magnetic ordering at low temperature with magnetic behaviour consistent with AFM spin glasses. This behaviour can be attributed to competing AFM and FM interactions, which support the presence of Co^{3+} ions in the low spin state, Co^{3+} (t_{eg}^6 e_g^0). According to Goodenough-Kanamori rules for super-exchange interactions [24,25], disordered distribution of low spin Co^{3+} and high spin Fe^{3+} would result in competing FM (Co-Fe) and AFM (Co-Co and Fe-Fe) interactions. The effective magnetic moments observed in $La_{1.2}Sr_{0.8}Co_{0.5}Fe_{0.5}O_4$ and $LaSrCo_{0.5}Fe_{0.5}O_4$ near room temperature (3.47 and 3.37 μ_B, respectively) are somewhat lower than those expected from high spin Fe^{3+}/Co^{2+} and low spin Co^{3+} (4.53 and 4.18 μ_B), but the data are not in a Curie-Weiss regime. It is also likely that competing FM and AFM interactions between Fe^{3+}, Co^{3+}, Fe^{4+} and Co^{4+} ions account for the spin glass state observed in case of $La_{0.8}Sr_{1.2}Co_{0.5}Fe_{0.5}O_4$. The uncertain nature of the cation oxidation states makes it difficult to interpret the observed effective magnetic moment of 3.06 μ_B.

XRD data (*Figure 3.2*) indicate a lattice contraction through strontium doping in the stoichiometric materials $La_{2-x}Sr_xCo_{0.5}Fe_{0.5}O_4$. The NPD refined lattice parameters for $La_{1.2}Sr_{0.8}Co_{0.5}Fe_{0.5}O_4$ and $LaSrCo_{0.5}Fe_{0.5}O_4$ are a = 3.85523(6) Å; c = 12.6071(2) Å and a = 3.83900(6) Å; c = 12.5676(2) Å, respectively. This contraction results from a decrease in the B-site ionic radius owing to replacement of some high spin Co^{2+} by low spin Co^{3+}

(or some M^{3+} by M^{4+}), and this effect is larger than the expansion expected for partial replacement of La^{3+} by Sr^{2+}.

Oxide ion vacancies in the reduced phases are confined to the equatorial MO_2 planes of the K_2NiF_4 structure. Oxygen stoichiometry and the vacancy distribution in these phases suggest the formation of MO_x polyhedra of coordination lower than 6, similar to those observed in $LaSrCoO_{3.5-x}$ [9]. It can be also noted that the polyhedra exhibit a significant elongation parallel to the *c* axis in all phases, being more pronounced in the reduced phases (*Table 3.2*). These results are consistent with the large quadrupole splitting observed in the Mössbauer spectra recorded from different reduced samples.

The reduced phases are obtained *via* reduction of M^{4+} to M^{3+} and Co^{3+} to Co^{2+}, and this is associated with a significant expansion in the *c* parameter and a slight contraction in the *a* parameter (see *Figure 3.1* and *Table 3.1*). A similar effect has been observed under reduction of $LaSrCoO_4$ into $LaSrCoO_{3.5-x}$ [9]. The expansion and contraction are both proportional to the amount of Co^{3+}/M^{4+} being reduced (*i.e.* the concentration of oxygen vacancies). The expansion in the *c* parameter corresponds to a significant expansion in the M–O2 bond length (*e.g.* M–O2 is 2.086(1) Å and 2.200(1) Å in $LaSrCo_{0.5}Fe_{0.5}O_4$ and $LaSrCo_{0.5}Fe_{0.5}O_{3.75}$, respectively), while no significant contraction has been observed in the M-O1 bond (*e.g.* M–O1 is 1.91950(3) Å and 1.9218(2) Å in $LaSrCo_{0.5}Fe_{0.5}O_4$ and $LaSrCo_{0.5}Fe_{0.5}O_{3.75}$, respectively). This effect can be attributed to the rotation of the MO_6 octahedra around the *z* axis to maintain the M–O1 bond lengths whilst allowing contraction of *a*. This effect is reflected in the increase in the O1 *y* parameter with the increase of the oxygen deficiency (*Table 3.1*). An expansion in the MO_6 octahedra is generally expected under reduction of Co^{3+} to Co^{2+}, which explains the expansion in the *c* parameter. The contraction in *a*, however, is often related to the coordination requirements of the A site (La/Sr); under reduction, a contraction in the coordination sphere (achieved in the *xy* plane,

i.e. La/Sr–O_{axial} bonds) occurs due to reduction of coordination number (< 9). This effect is seen in $LaSrCoO_{3.5-x}$ *via* a small contraction in La/Sr–O_{axial} bond lengths under reduction [9], which is not significant in this study, possibly because of (i) the *a* parameter contraction in our system is significantly lower than that observed in $LaSrCoO_{3.5-x}$ since the oxygen deficiency is lower, (ii) a slight contraction in La/Sr–O_{axial} bond lengths here may be screened by the anisotropic displacement of the O2 (axial) oxygen sites. Finally, rotation of the MO_6 octahedra around *z* in the reduced samples may produce an anisotropic strain within the lattice and account for the necessity to use Finger-Cox-Jephcoat functions in refining the peak shapes for these phases.

3.8 References

[1] Y. Teraoka, H. M. Zhang, K. Okamoto, N. Yamazoe, *Mater. Res. Bull*. **23** (1988) 51.

[2] Y. Teraoka, H. M. Zhang, S. Furukawa, N. Yamazoe, *Chem. Lett*. **14** (1985) 1743.

[3] Y. Matsumoto, S. Yamada, T. Nishida, E. Sato, *J. Electrochem. Soc*. **127** (1980) 2360.

[4] S. E. Dann, M. T. Weller, D. B. Currie, *J. Solid State Chem*. **97** (1992) 179.

[5] F. Prado, T. Armstrong, A. Caneiro, A. Manthiram, *J. Electrochem. Soc*. **148** (2001) J7.

[6] Y. Bréard, C. Michel, M. Hervieu, F. Studer, A. Maignan, B.B. Raveau, *Chem. Mater*. **14** (2002) 3128.

[7] A. Bowman, M. Allix, D. Pelloquin, M. J. Rosseinsky, *J. Am. Chem. Soc*. **128** (2006) 12606.

[8] A. Tabuchi, H. Kawanaka, H. Bando, T. Sasaki, Y. Nishihara, *J. Alloy. Compd*. **424** (2006) 21.

[9] M. A. Hayward, M. J. Rosseinsky, *Chem. Mater.* **12** (2000) 2182.

[10] M. E. Leonowicz, K. R. Poeppelmeier, J. M. Longo, *J. Solid State Chem.* **59** (1985) 71.

[11] M. Crespin, J. M. Bassat, P. Odier, P. Mouron, J. Choisnet, *J. Solid State Chem.* **84** (1990) 165.

[12] P. H. Labbe, M. Ledesert, V. Caignaert, B. Raveau, *J. Solid State Chem.* **91** (1991) 362.

[13] F. Menil, *J. Phys. Chem. Solids* **46** (1985) 763.

[14] J. L. Soubeyroux, P. Courbin, L. Fournes, D. Fruchart, G. Le Flem, *J. Solid State Chem*. **31** (1980) 313.

[15] A. Nemudry, P. Rudolf, R. Schollhorn, *Solid State Ionics* **109** (1998) 213.

[16] G. Aeppli, D. J. Buttrey, *Phys. Rev. Lett*. **61** (1988) 203.

[17] G. Aeppli, D. R. Harshman, D. Buttrey, E. Ansaldo, G. P. Espinosa, A. S. Cooper, J. P. Remeika, T. Treltoft, T. M. Riseman, D. R. Noakes, B. Ellman, T. F. Rosenbaum, D. L. Williams, *Physica C* **153-155** (1988) 1111.

[18] D. E. Cox, A. I. Goldman, M. A. Subramanian, J. Gopalakrishnan, A. W. Sleight, *Phys. Rev. B* **40** (1989) 6998.

[19] A. L. Hector, C. S. Knee, A. I. MacDonald, D. J. Price, M. T. Weller, *J. Mater Chem.* **15** (2005) 3093-3103.

[20] M. M. Nguyen-Trut-Dinh, M. Vlasse, M. Perrin, G. Le Flem. *J. Solid State Chem.* **32** (1980) 1.

[21] M. H. Jung, A. M. Alsmadi, S. Chang, M. R. Fitzsimmons, Y. Zhao, A. H. Lacerda, H. Kawanaka, S. El-Khatib, H. Nakotte, *J. Appl. Phys.* **97** (2005) 10A926.

[22] K. V. Rao, M. Fahnle, E. Figueroa, O. Beckman, L. Hedman, *Phys. Rev. B* **27** (1983) 3104.

[23] K. Yamada, M. Matsuda, Y. Endoh, B. Keimer, R.J. Birgenau, S. Onedera, J. Mizusaki, T. Matsuura, G. Shirane, *Phys. Rev. B* **39** (1989) 2336.

[24] J. B. Goodenough, Magnetism and the Chemical Bond, Interscience, New York, 1963.

[25] J. Kanamori, *J. Phys. Chem. Solids* **10** (1959) 87.

CHAPTER 4

Synthesis and characterization of $La_{2-x}Sr_xCo_{0.5}Mn(Cr)_{0.5}O_{4\pm\delta}$

4.1 Background

As n = 1 members of the RP phases, the K_2NiF_4-type oxides have shown an enhanced phase stability under reducing conditions due to their ability to accommodate a wide range of coordination environments and oxidation states. Additionally, K_2NiF_4-type phases such as $La_2NiO_{4+\delta}$ have recently attracted considerable interest as alternative cathode materials for SOFCs due to their interesting transport properties [1,2]. It has been shown in chapter 3 that the $La_{2-x}Sr_xCo_{0.5}Fe_{0.5}O_4$ phases withstand reducing conditions (10% H_2/N_2) up to 1000 °C and are subject to reduction of Co^{3+} to Co^{2+} and formation of oxide ion vacancies within the equatorial planes. However, oxygen hyperstoichiometry could not be achieved in these materials. Five additional materials of this type are studied in this chapter namely, $La_{2-x}Sr_xCo_{0.5}Mn_{0.5}O_{4\pm\delta}$ (0.8, 1, 1.2) and $La_{2-x}Sr_xCo_{0.5}Cr_{0.5}O_{4-\delta}$ (0.85, 1). These materials have been suggested in an attempt to achieve (i) a wider range of oxygen nonstoichiometry including hyperstoichiometry, (ii) B-site mixed valency, and (iii) better phase-stability in different oxygen partial pressures and temperatures. These properties fundamentally characterize good mixed conducting materials for applications such as SOFCs and oxygen separation membranes.

4.2 Synthesis and characterization of $La_{2-x}Sr_xCo_{0.5}Mn_{0.5}O_{4\pm\delta}$

4.2.1 Synthesis

The materials $La_{1.2}Sr_{0.8}Co_{0.5}Mn_{0.5}O_{4.1}$ and $LaSrCo_{0.5}Mn_{0.5}O_4$ were synthesized by conventional solid state reactions using La_2O_3 (previously dried at 800 °C in air), $SrCO_3$,

Co_3O_4 and Mn_2O_3 as starting materials. A two-step synthesis procedure was employed; stoichiometric amounts of starting materials were intimately mixed, pressed into pellets and calcined at 1350 °C for 30 h under a N_2 atmosphere. The samples were then heated in air at 800 °C for 12 h in order to obtain well oxygenated materials.

The material $La_{0.8}Sr_{1.2}Co_{0.5}Mn_{0.5}O_4$ was prepared by a sol-gel method. Stoichiometric amounts of La_2O_3, $SrCO_3$, $Co(CH_3COO)_2.4H_2O$ and $Mn(CH_3COO)_2.4H_2O$ were dissolved in acetic acid and boiled under reflux for 3h. Small amounts of hydrogen peroxide and water were added and the mixture was further refluxed overnight to obtain a clear solution. This solution was evaporated to a dark violet gel. The gel was dried and decomposed in air at 400 °C and the resulting powder pressed into pellets and calcined in flowing oxygen at 1350 °C for 18 h.

4.2.2 XRD and TGA study

XRD patterns showed the synthesized materials (oxygenated materials) to be single-phase and to adopt a tetragonal K_2NiF_4-type structure (*I4/mmm* space group); however, the refinements were insensitive to oxygen nonstoichiometry and the oxide ion sites were fixed at full occupancy in all samples. *Figure 4.1* shows the profile fit of the data collected from $LaSrCo_{0.5}Mn_{0.5}O_4$ as an example. The structural data are given in *Table 4.1*. The reduction behaviour of these materials was tested by TG measurements in which the materials were heated (10 °C min^{-1}) in flowing 10% H_2/N_2 (*Figure 4.2*). The TG plots show a significant mass loss which starts at about 500 °C in all samples. A gradual decrease in the mass is also observed at higher temperature indicating further reduction or decomposition in the temperature range 700-1000 °C. However, XRD analysis of the

reduction products in this temperature range indicated that the reduced phases retain the K_2NiF_4-type structure with no evidence of phase decomposition.

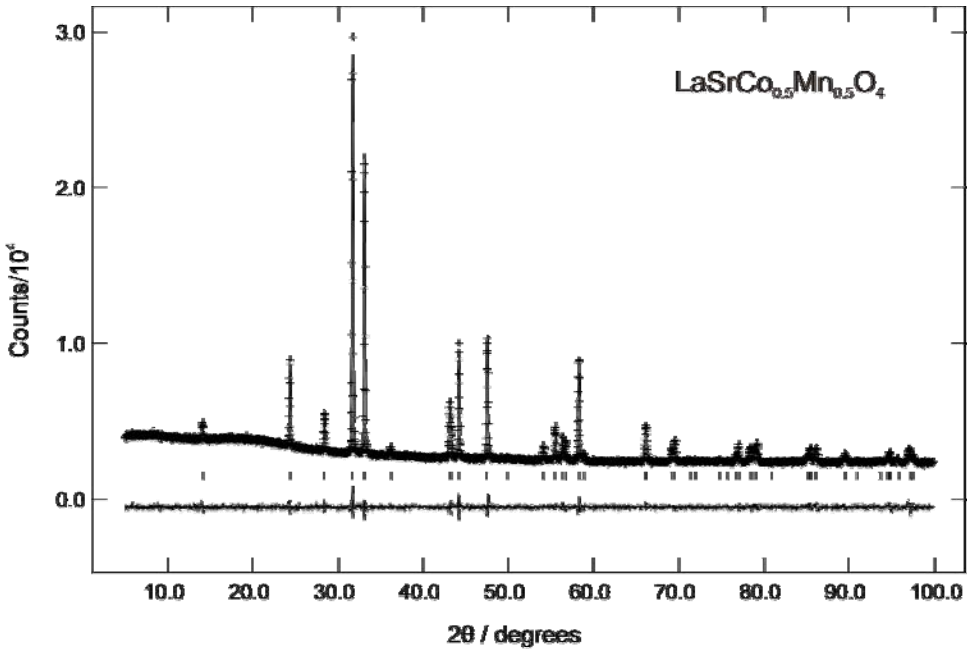

Figure 4.1 Observed, calculated and difference profiles for XRD data collected from $LaSrCo_{0.5}Mn_{0.5}O_4$.

Table 4.1 Structural results for the refinement of the XRD data collected from $LaSrCo_{0.5}Mn_{0.5}O_4$.

Atom	*x*	*y*	*z*	100 x Uiso (Å^2)	Occupancy	Site Symmetry
$LaSrCo_{0.5}Mn_{0.5}O_4$, *a* = 3.81968(5) Å; *c* = 12.5446(2) Å wRp = 0.0253; Rp = 0.0186; $\chi 2$ = 2.000						
Co/Mn	0	0	0	1.22(9)	0.5/0.5	2a
La/Sr	0	0	0.35949(9)	1.43(5)	0.5/0.5	4e
O1	0.5	0	0	1.5(3)	1	4c
O2	0	0	0.1652(6)	4.0(2)	1	4e

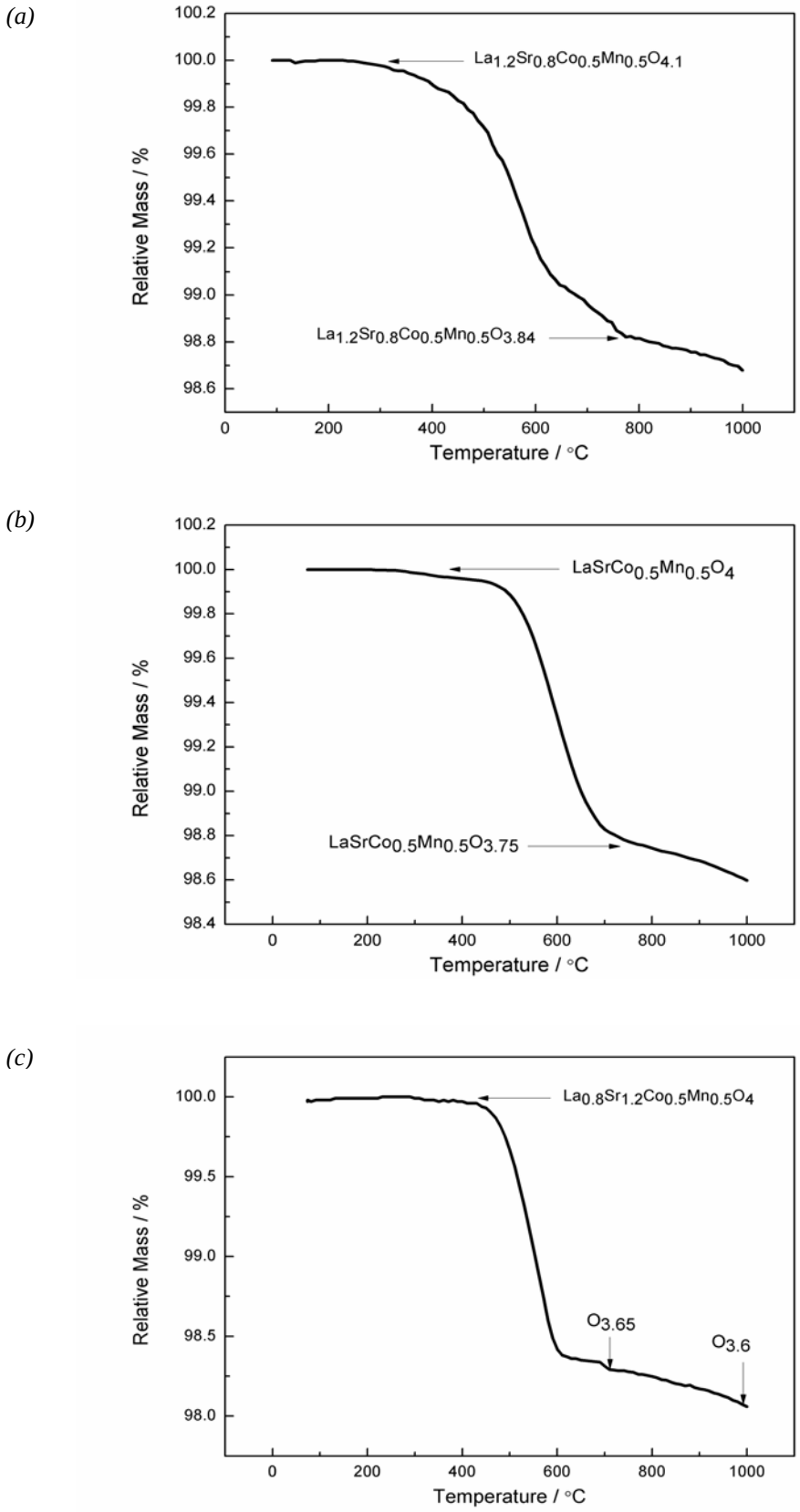

Figure 4.2 TG data for the reduction of different materials using 10% H_2 in N_2.

Assuming that the oxygenated materials are $La_{1.2}Sr_{0.8}Co_{0.5}Mn_{0.5}O_{4.1}$, $LaSrCo_{0.5}Mn_{0.5}O_4$ and $La_{0.8}Sr_{1.2}Co_{0.5}Mn_{0.5}O_4$, the reduced materials are oxygen-deficient with oxygen stoichiometries close to those indicated in *Figure 4.2*. In an attempt to investigate the oxygen deficiency in this system the reduction process was repeated on a larger scale with the oxygenated materials being heated in flowing 10% H_2/N_2 at 700 °C (in case of $La_{1.2}Sr_{0.8}Co_{0.5}Mn_{0.5}O_{4.1}$ and $LaSrCo_{0.5}Mn_{0.5}O_4$) and 1000 °C (in case of $La_{0.8}Sr_{1.2}Co_{0.5}Mn_{0.5}O_4$) for 12 h. XRD analysis indicated that the obtained materials were single-phase with the K_2NiF_4-type structure. However, the refinements were again insensitive to oxygen nonstoichiometry and the oxide ion sites were fixed at full occupancy. Similar to the iron-containing materials (section 3.3), the XRD data indicated an expansion in the *c* parameter and a contraction in the *a* parameter under reduction (*Figure 4.3*).

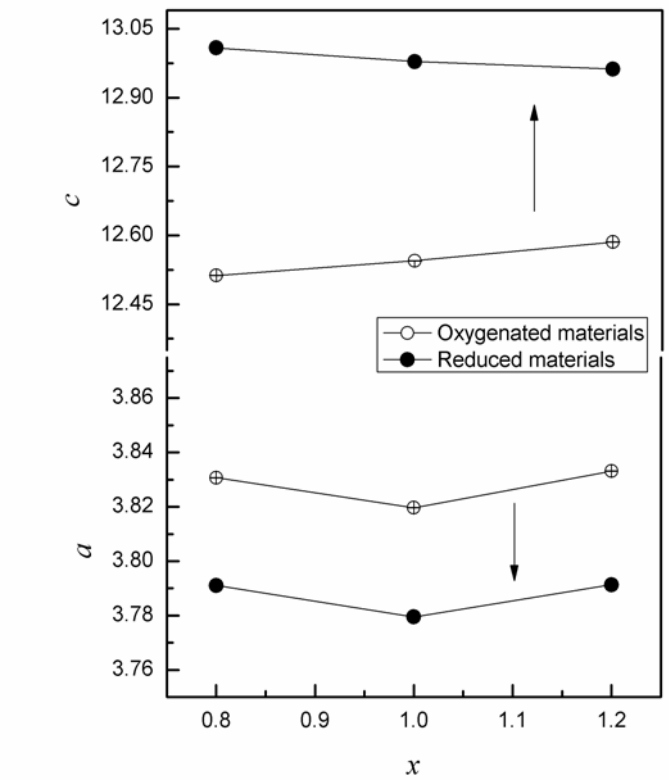

Figure 4.3 Variation of the XRD refined unit cell parameters with x in $La_{2-x}Sr_xCo_{0.5}Mn_{0.5}O_{4\pm\delta}$ (e.s.d. values are less than symbol size).

4.2.3 Room temperature NPD analysis

NPD data collected at room temperature were used to determine more reliably the oxygen content and defect structures of these materials. Refinement results from the data collected from the reduced materials at room temperature are given in *Table 4.2*. Profile fits and difference patterns from the Rietveld analysis are shown in *Figure 4.4 (a-c)*. The oxygen contents are based on formal oxidation states of Co^{2+} and Mn^{3+}(Mn^{2+}) (see section 4.2.6), which are in excellent agreement with refined data. Some selected bond lengths are given in *Table 4.3*.

Refinements were performed adopting the ideal *I4/mmm* space group; the use of lower symmetry tetragonal and orthorhombic space groups was unsuccessful and confirmed the absence of cation or defect order. It is important to note that the scattering length contrast is such that Co/Mn ordering would have been easily detectable in these experiments [3]; such B-site cation order has previously been observed in Co-Mn perovskites [4]. Analysis of the oxide ion site occupancies in these materials, in a manner similar to that used for the iron-containing samples, revealed that the vacancies are also disordered and confined to the equatorial MO_2 planes of the K_2NiF_4-type structure. An attempt to fit a model in which oxide ion vacancies are distributed between axial and equatorial oxygen sites [5] proved unstable. An associated twisting of the MO_6 octahedra around the *z* axis is also observed, that transforms the oxide ions at (0.5, 0, 0) to the split position (0.5, y, 0). Refinements gave the overall stoichiometries $La_{1.2}Sr_{0.8}Co_{0.5}Mn_{0.5}O_{3.85(1)}$, $LaSrCo_{0.5}Mn_{0.5}O_{3.75(1)}$ and $La_{0.8}Sr_{1.2}Co_{0.5}Mn_{0.5}O_{3.60(1)}$ for the reduced materials. Consideration of these results in conjunction with TGA data (*Figure 4.2*), confirms that the oxygen stoichiometries of the oxygenated materials are $La_{1.2}Sr_{0.8}Co_{0.5}Mn_{0.5}O_{4.1}$, $LaSrCo_{0.5}Mn_{0.5}O_4$ and $La_{0.8}Sr_{1.2}Co_{0.5}Mn_{0.5}O_4$.

4.4a)

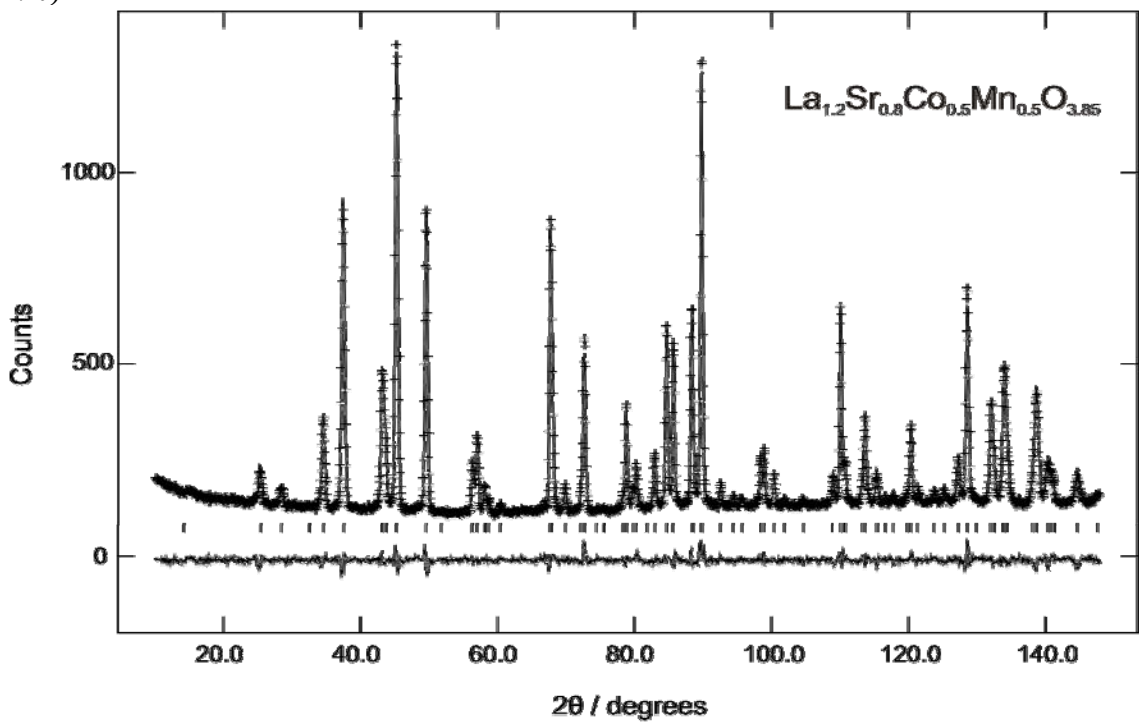
La1.2Sr0.8Co0.5Mn0.5O3.85
Counts
1000
500
0
20.0
40.0
60.0
80.0
100.0
120.0
140.0
2θ / degrees

4.4b)

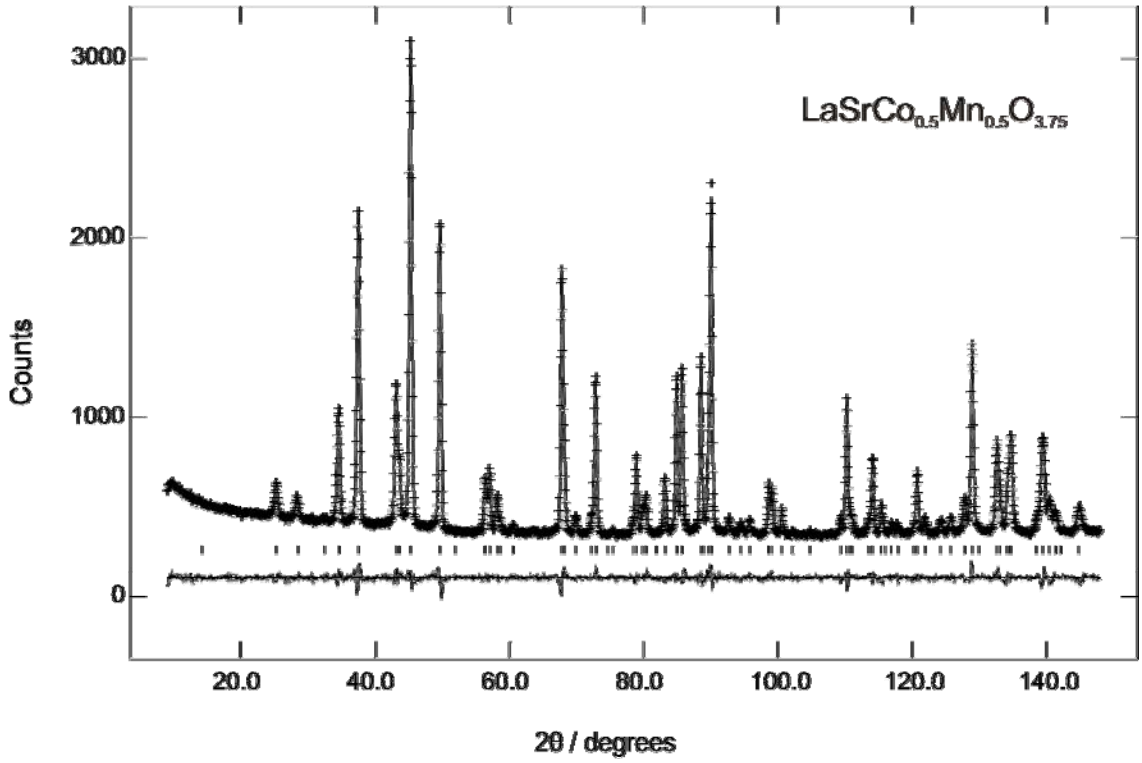
LaSrCo0.5Mn0.5O3.75
Counts
3000
2000
1000
0
20.0
40.0
60.0
80.0
100.0
120.0
140.0
2θ / degrees

4.4c)

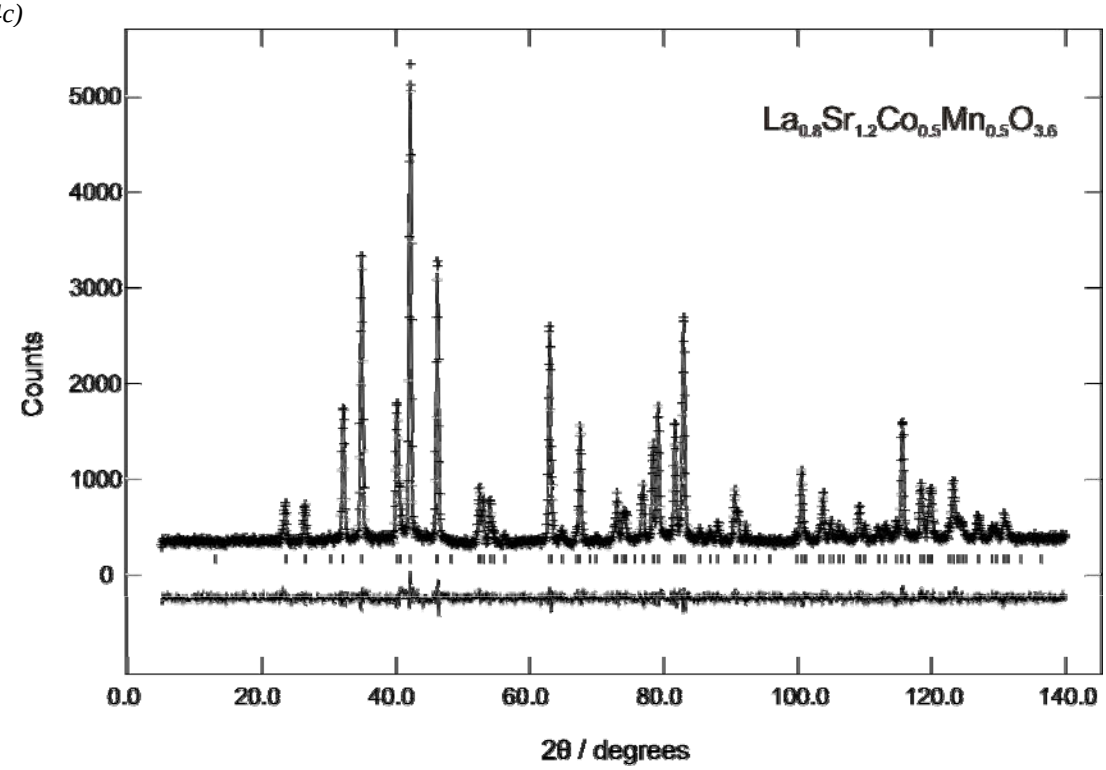

4.4d)

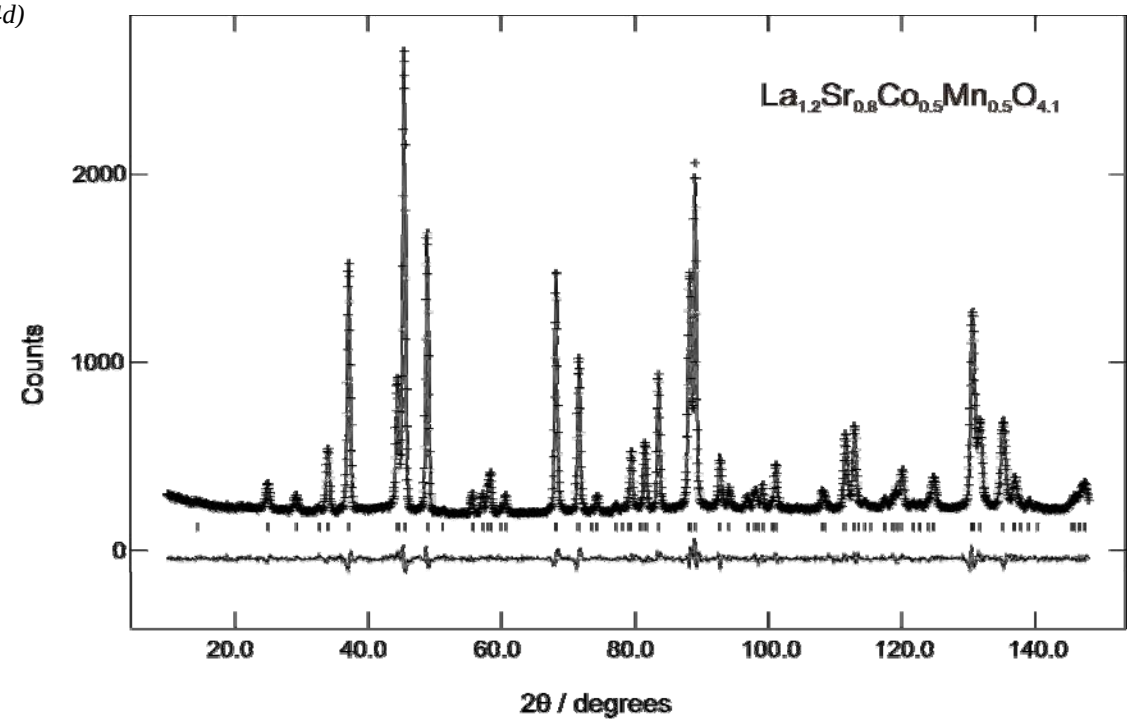

Figure 4.4 Observed, calculated and difference profiles for NPD data collected from different samples at room temperature.

Table 4.2 Structural results for the refinement of the NPD data collected from different samples at room temperature.

Atom	*x*	*y*	*z*	100 x Uiso (Å^2)	Occupancy	Site Symmetry
			$La_{1.2}Sr_{0.8}Co_{0.5}Mn_{0.5}O_{3.85}$, *a* = 3.81188(8) Å; *c* = 13.0423(3) Å wRp = 0.0357; Rp = 0.0281; χ^2 = 2.14			
Co/Mn	0	0	0	0*	0.5/0.5	2a
La/Sr	0	0	0.35772(5)	0.49(2)	0.6/0.4	4e
O1	0.5	0.0280(9)	0	0.68(5)	0.461(3)	8j
O2	0	0	0.17346(8)	1.53(3)	1	4e
*negative Uiso constrained to zero.						
			$LaSrCo_{0.5}Mn_{0.5}O_{3.75}$, *a* = 3.80329(6) Å; *c* = 13.0409(2) Å wRp = 0.0239; Rp = 0.018; χ^2 = 2.511			
Co/Mn	0	0	0	0*	0.5/0.5	2a
La/Sr	0	0	0.35687(5)	0.86(2)	0.5/0.5	4e
O1	0.5	0.0397(6)	0	0.83(5)	0.436(2)	8j
O2	0	0	0.17076(7)	2.05(3)	1	4e
*negative Uiso constrained to zero.						
			$La_{0.8}Sr_{1.2}Co_{0.5}Mn_{0.5}O_{3.6}$, *a* = 3.79614(6) Å; *c* = 13.0116(3) Å wRp = 0.052; Rp = 0.0412; χ2 = 1.39			
Co/Mn	0	0	0	0.5(3)	0.5/0.5	2a
La/Sr	0	0	0.35634(9)	1.68(3)	0.4/0.6	4e
O1	0.5	0.0543(8)	0	1.46(8)	0.400(3)	8j
O2	0	0	0.1674(1)	2.97(5)	1	4e
			$La_{1.2}Sr_{0.8}Co_{0.5}Mn_{0.5}O_{4.1}$, *a* = 3.85865(8) Å; *c* = 12.6523(3) Å wRp = 0.0307; Rp = 0.0241; χ^2 = 2.761			
Co/Mn	0	0	0	0*	0.5/0.5	2a
La/Sr	0	0	0.35905(6)	0.66(3)	0.6/0.4	4e
O1	0.5	0	0	0.92(3)	1	4c
O2	0	0.028(3)	0.1671(1)	2.04(8)	0.25	16n
O3	0	0.5	0.25	1.1(6)	0.048(4)	4d
*negative Uiso constrained to zero.						

Table 4.3 Selected bond lengths (Å) for the refined phases.

Bond	**$La_{1.2}Sr_{0.8}Co_{0.5}Mn_{0.5}O_{3.85}$**	**$LaSrCo_{0.5}Mn_{0.5}O_{3.75}$**	**$La_{0.8}Sr_{1.2}Co_{0.5}Mn_{0.5}O_{3.6}$**
Co/Mn–O1*	1.9089(2)	1.9076(2)	1.9092(3)
Co/Mn–O2	2.262(1)	2.2269(9)	2.178(2)
La/Sr–O1*	2.585(3)	2.559(2)	2.521(2)
	2.738(3)	2.774(2)	2.815(2)
La/Sr–O2	2.403(1)	2.427(1)	2.459(2)
	2.7259(2)	2.7134(2)	2.7019(2)

*Splitting of O1 sites gives twice the number of bonds compared with the ideal site

	$La_{1.2}Sr_{0.8}Co_{0.5}Mn_{0.5}O_{4.1}$
Co/Mn-O1	1.92933(4)
Co/Mn-O2**	2.117(1)
La/Sr–O1	2.6273(5)
La/Sr–O2**	2.431(2)
	2.673(7)
	2.827(7)
La/Sr–O3	2.3719(5)

**Splitting of O2 sites gives 4 times the number of bonds compared with the ideal site

In order to confirm oxygen hyperstoichiometry in $La_{1.2}Sr_{0.8}Co_{0.5}Mn_{0.5}O_{4.1}$, NPD data were collected from this sample at room temperature. The profile fit and difference pattern of the Rietveld analysis are shown in *Figure 4.4 (d)*. Structural data and some selected bond lengths are given in *Table 4.2* and *Table 4.3*, respectively. Refinement supported the presence of interstitial oxygen and was consistent with the composition $La_{1.2}Sr_{0.8}Co_{0.5}Mn_{0.5}O_{4.10(1)}$. The excess oxygen occupies the ideal interstitial sites (0, 0.5, 0.25) of the tetragonal structure. An associated displacement of the apical oxide ions, related to that of Jorgensen's interstitial defect model [6], moves apical oxygen atoms from their ideal position at (0, 0, *z*) to the split position (0, *y*, *z*). Incorporation of excess

interstitial oxygen in the K_2NiF_4-type structure with retention of tetragonal symmetry has been observed in $La_{1.2}Sr_{0.8}MnO_{4.27}$ [7].

4.2.4 Magnetic susceptibility

Figure 4.5 shows the temperature dependence of the magnetic susceptibility for different samples. The oxygenated materials generally show higher magnetization than the reduced ones. A distinct divergence between ZFC and FC susceptibilities is suggestive of spin glass behaviour. The spin glass state has been confirmed in some selected samples by AC magnetic susceptibility measurements. The frequency dependence of the AC magnetic susceptibility of $La_{0.8}Sr_{1.2}Co_{0.5}Mn_{0.5}O_4$, for example, is shown in *Figure 4.6*. The location of the cusp at the freezing temperature is dependent of the frequency of the AC susceptibility measurement which is indicative of a spin glass. The magnetic susceptibility of $La_{1.2}Sr_{0.8}Co_{0.5}Mn_{0.5}O_{3.85}$ (*Figure 4.5 (a)*) shows a broad maximum at about 70 K, which is an indication of AFM ordering in this two-dimensional system. However, no evidence of magnetic order has been found in the low temperature NPD data of this sample. The plots of the reciprocal of the molar susceptibility against temperature for $LaSrCo_{0.5}Mn_{0.5}O_{3.75}$ and $La_{0.8}Sr_{1.2}Co_{0.5}Mn_{0.5}O_{3.6}$ show departure from Curie-Weiss behaviour (*Figure 4.7*). The plots display decreasing effective moments with negative θ values on cooling which is expected for spin glasses with AFM interactions. Above 200 K, the θ values are -107.73 and -174.31 K and the effective moments are 5.01 and 5.06 μ_B for $LaSrCo_{0.5}Mn_{0.5}O_{3.75}$ and $La_{0.8}Sr_{1.2}Co_{0.5}Mn_{0.5}O_{3.6}$, respectively. On the other hand, the reciprocal susceptibility plots of the oxygenated materials (*Figure 4.8*) indicate that these materials exhibit exchange interactions which are predominantly FM with positive θ values and an increasing effective moment as the temperature decreases. Above 200 K, the θ values are 45.64, 83.41 and

80.93 K and the effective moments are 6.53, 4.76 and 4.79 μ_B for $La_{1.2}Sr_{0.8}Co_{0.5}Mn_{0.5}O_{4.1}$, $LaSrCo_{0.5}Mn_{0.5}O_4$ and $La_{0.8}Sr_{1.2}Co_{0.5}Mn_{0.5}O_4$, respectively.

4.5a)

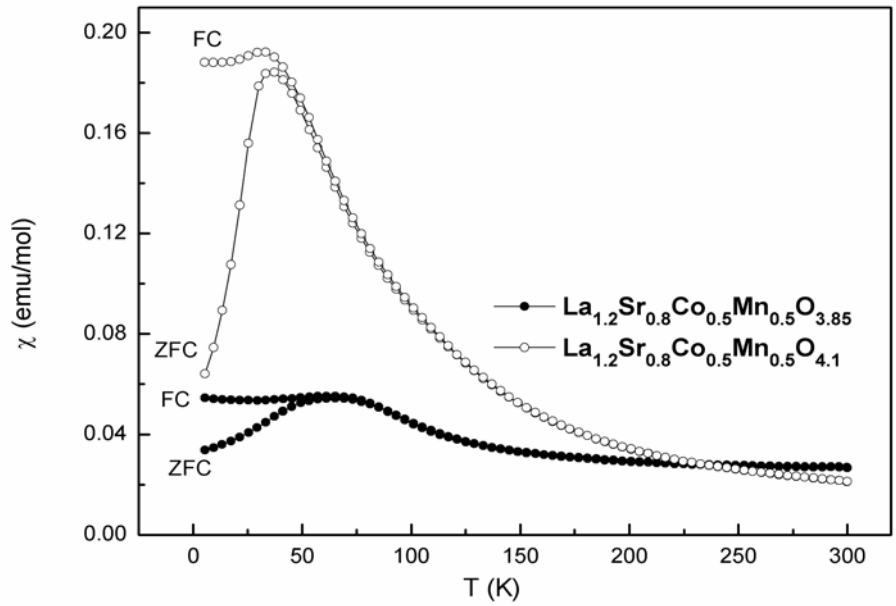

4.5b)

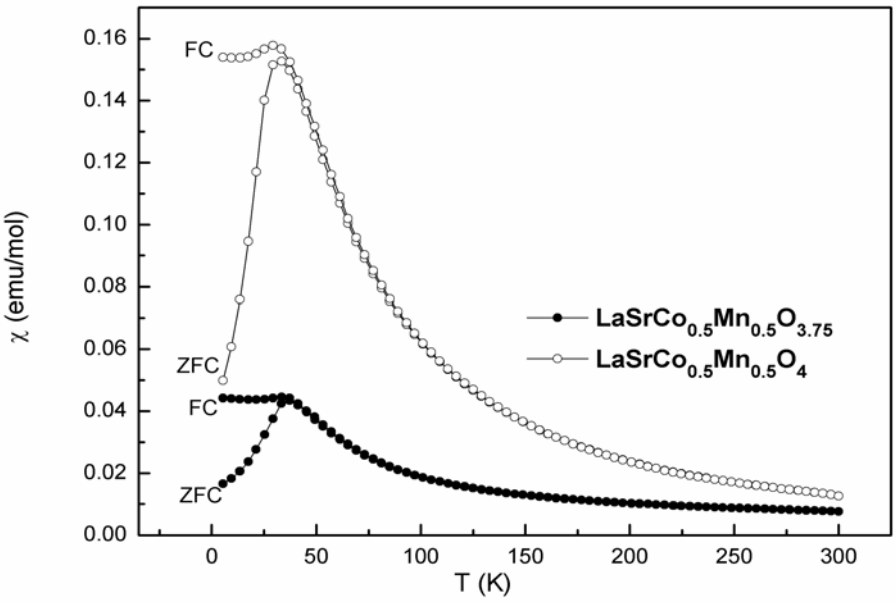

4.5c)

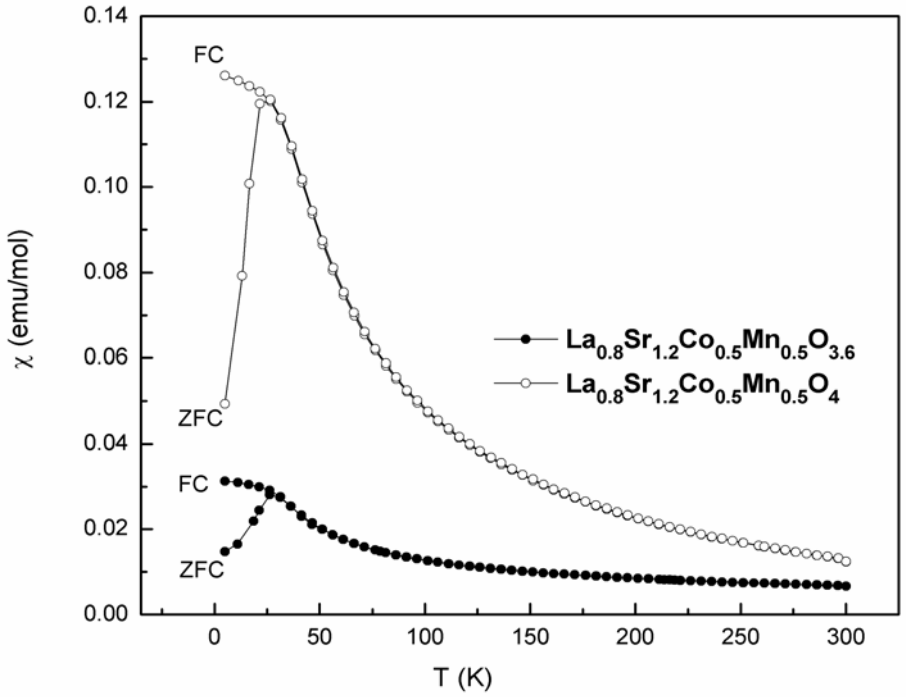

Figure 4.5 Variation of magnetic susceptibility (ZFC and FC) with temperature for (a) $La_{1.2}Sr_{0.8}Co_{0.5}Mn_{0.5}O_{4\pm\delta}$ (b) $LaSrCo_{0.5}Mn_{0.5}O_{4-\delta}$ and (c) $La_{0.8}Sr_{1.2}Co_{0.5}Mn_{0.5}O_{4-\delta}$.

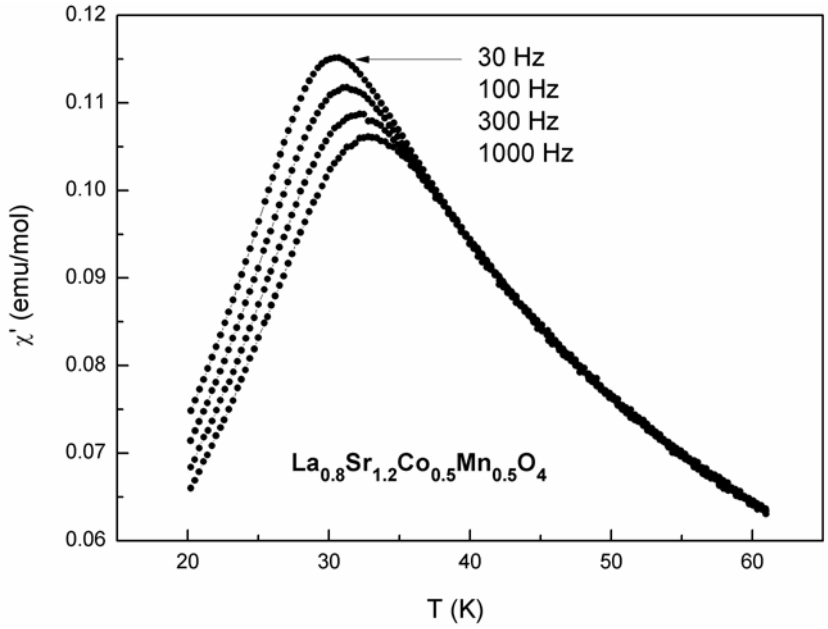

Figure 4.6 Spin glass behaviour observed in AC susceptibility at low temperature for $La_{0.8}Sr_{1.2}Co_{0.5}Mn_{0.5}O_4$.

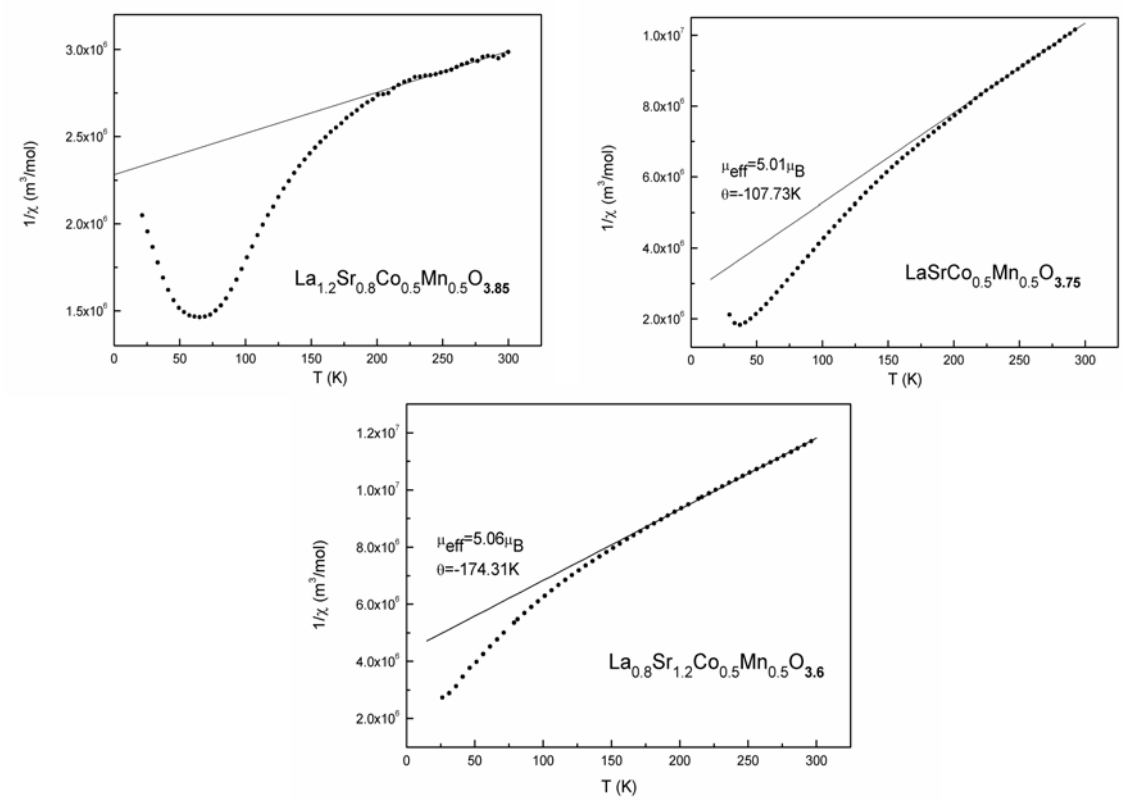

Figure 4.7 Variation of the inverse magnetic susceptibilities (ZFC) with temperature for the reduced materials.

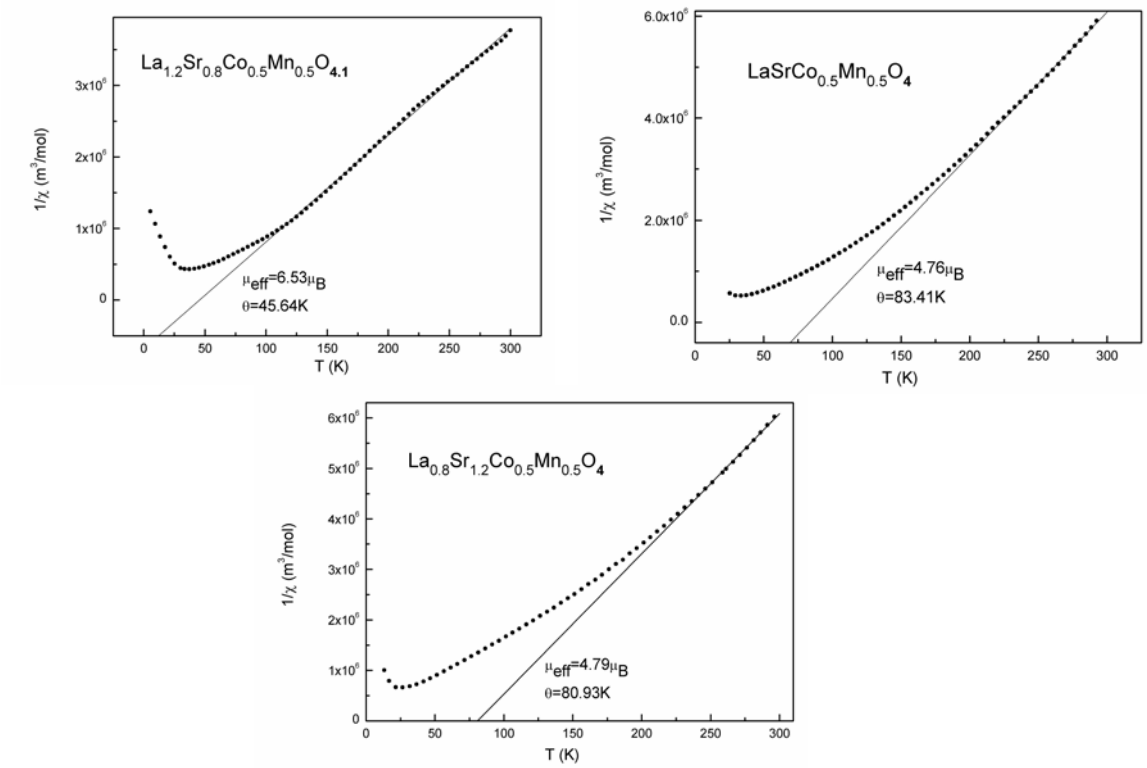

Figure 4.8 Variation of the inverse magnetic susceptibilities (ZFC) with temperature for the oxygenated materials.

4.2.5 XPS analysis

XPS measurements were used to probe the change of the B-site oxidation states in these materials after reduction. The data recorded from $LaSrCo_{0.5}Mn_{0.5}O_4$ and $LaSrCo_{0.5}Mn_{0.5}O_{3.75}$ are given as an example. No evidence of significant change could be observed in the Mn 2p region of the XPS spectrum under reduction of $LaSrCo_{0.5}Mn_{0.5}O_4$ to $LaSrCo_{0.5}Mn_{0.5}O_{3.75}$. The Co 2p spectra of the two materials were, in contrast, significantly different (*Figure 4.9*). The high spin Co^{2+} state is known to result in intense satellite structures at the higher energy side of the Co $2p_{3/2}$ and Co $2p_{1/2}$ transitions in the Co 2p XPS spectrum [8]. In contrast, the low spin Co^{3+} state shows very weak satellite structures [9,10]. The Co 2p XPS spectrum is therefore very useful to distinguish the two states in a wide range of materials [11-14]. *Figure 4.9* shows the Co 2p XPS spectra of $LaSrCo_{0.5}Mn_{0.5}O_4$ and $LaSrCo_{0.5}Mn_{0.5}O_{3.75}$, and the typical Co $2p_{3/2}$, Co $2p_{1/2}$ and satellite (S) peaks are indicated. The Co $2p_{3/2}$ binding energy values are 779.7 and 780.1 eV for $LaSrCo_{0.5}Mn_{0.5}O_4$ and $LaSrCo_{0.5}Mn_{0.5}O_{3.75}$, and are consistent with the data reported for Co-containing materials elsewhere [12,13]. The Co 2p XPS spectrum of $LaSrCo_{0.5}Mn_{0.5}O_{3.75}$ clearly shows intense satellite structures at about 787 and 803 eV which indicate presence of Co^{2+} ions in this material. On the other hand, the relatively narrow peak width and the weak satellite structures of the Co $2p_{3/2}$ and Co $2p_{1/2}$ transitions in $LaSrCo_{0.5}Mn_{0.5}O_4$ are suggestive of presence of cobalt in this material in the trivalent state. The results are therefore consistent with the presence of Co^{3+} in $LaSrCo_{0.5}Mn_{0.5}O_4$ which is reduced to Co^{2+} in $LaSrCo_{0.5}Mn_{0.5}O_{3.75}$. This is consistent with the cobalt behaviour in the related iron-containing materials $La_{2-x}Sr_xCo_{0.5}Fe_{0.5}O_{4-\delta}$ (see section 3.7).

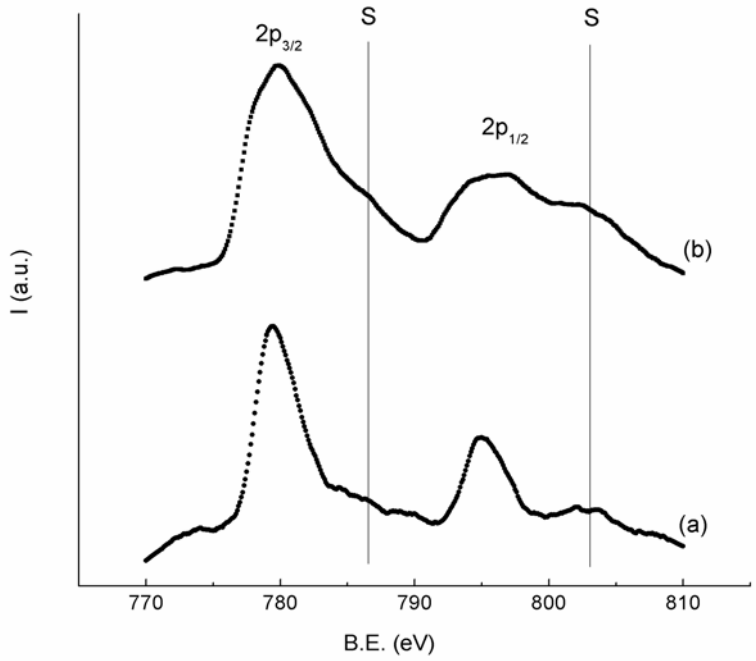

Figure 4.9 Co 2p XPS for (a) $LaSrCo_{0.5}Mn_{0.5}O_4$ and (b) $LaSrCo_{0.5}Mn_{0.5}O_{3.75}$, showing the $2p_{1/2}$, $2p_{3/2}$ and satellite (s) peaks.

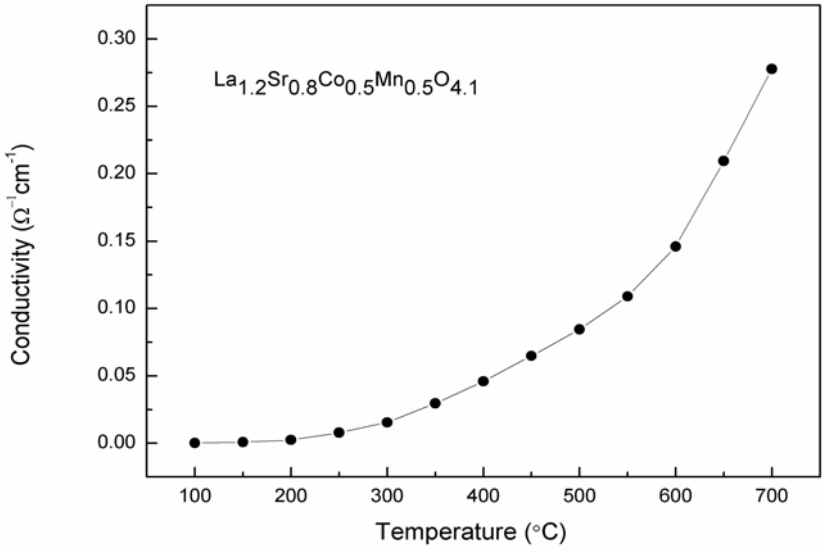

Figure 4.10 Conductivity versus temperature data for $La_{1.2}Sr_{0.8}Co_{0.5}Mn_{0.5}O_{4.1}$.

4.2.6 Conductivity of $La_{1.2}Sr_{0.8}Co_{0.5}Mn_{0.5}O_{4.1}$

The overall conductivity of $La_{1.2}Sr_{0.8}Co_{0.5}Mn_{0.5}O_{4.1}$ was measured in air in the temperature range 100-700 °C (see section 2.2.7 for experimental details). The conductivity versus temperature data (*Figure 4.10*) suggest that the material is a semiconductor in the temperature range 100-700 °C with conductivity values < 1 Ω^{-1} cm^{-1} at high temperatures.

4.2.7 Discussion of $La_{2-x}Sr_xCo_{0.5}Mn_{0.5}O_{4\pm\delta}$

The overall stoichiometries of the materials were determined by NPD and TG analyses as $La_{1.2}Sr_{0.8}Co_{0.5}Mn_{0.5}O_{4.1}$, $LaSrCo_{0.5}Mn_{0.5}O_4$, $La_{0.8}Sr_{1.2}Co_{0.5}Mn_{0.5}O_4$, and $La_{1.2}Sr_{0.8}Co_{0.5}Mn_{0.5}O_{3.85}$, $LaSrCo_{0.5}Mn_{0.5}O_{3.75}$, $La_{0.8}Sr_{1.2}Co_{0.5}Mn_{0.5}O_{3.6}$ for oxygenated and reduced materials, respectively. The oxygen stoichiometry in the oxygenated materials suggests B-site oxidation states based on Co^{3+}/Mn^{3+} or Co^{2+}/Mn^{4+}. An ordered Co^{2+}/Mn^{4+} state has been reported in the double perovskite La_2CoMnO_6 [4]. However, no cation order is observed in any of the studied materials and B-site oxidation states based on Co^{3+}/Mn^{3+} are therefore suggested in these materials. Accordingly, $LaSrCo_{0.5}Mn_{0.5}O_4$ simply contains a mixture of Co^{3+} and Mn^{3+} which is also supported by XPS measurements (section 4.2.5). On the other hand, the oxygen stoichiometry suggests 20% of the transition metal ions in $La_{0.8}Sr_{1.2}Co_{0.5}Mn_{0.5}O_4$ to be present in the tetravalent state which results in a combination of $(Co/Mn)^{3+/4+}$ in this material. The stoichiometric phase $La_{1.2}Sr_{0.8}Co_{0.5}Mn_{0.5}O_4$, however, has not been characterized in this study but it would be expected to contain a mixture of Mn^{3+}, Co^{3+} and Co^{2+} ions (a combination of Mn^{3+}, Co^{3+} and Mn^{2+} is chemically unfavoured, see below). The excess oxygen content in $La_{1.2}Sr_{0.8}Co_{0.5}Mn_{0.5}O_{4.1}$ therefore suggests instability linked to the facile oxidation of Co^{2+} into Co^{3+}. However, the absence

of oxygen hyperstoichiometry in $La_{1.2}Sr_{0.8}Co_{0.5}Fe_{0.5}O_4$ (see section 3.7) under similar oxidation conditions suggests that other factors are also involved (*e.g.* oxidation of Mn^{3+} to Mn^{4+}). The reduction behaviour of the oxygenated materials (see *Figure 4.2*) suggests reduction of M^{4+} to M^{3+} and/or Co^{3+} to Co^{2+} to reach the stoichiometries $La_{1.2}Sr_{0.8}Co_{0.5}Mn_{0.5}O_{3.85}$, $LaSrCo_{0.5}Mn_{0.5}O_{3.75}$ and $La_{0.8}Sr_{1.2}Co_{0.5}Mn_{0.5}O_{3.65}$ at 700 °C. The reduction of Co^{3+} to Co^{2+} rather than reduction of Mn^{3+} to Mn^{2+} is supported by XPS measurements. Karen *et al.* [15] have also argued that the Co^{2+}/Mn^{3+} state is more electrochemically favoured than the Co^{3+}/Mn^{2+} state in related layer-structured materials. The reduction of cobalt in these materials is consistent with its behaviour in the iron-containing materials $La_{2-x}Sr_xCo_{0.5}Fe_{0.5}O_{4-\delta}$ (section 3.7). The reduction of the B-site state Co^{3+}/Mn^{4+} to the Co^{2+}/Mn^{3+} state under similar conditions has also been suggested by X-ray absorption measurements in the related n = 2 RP system $La_{1+x}Sr_{2-x}CoMnO_{7-\delta}$ (see chapter 6). Further slow reduction as temperature increases suggests partial reduction of Mn^{3+} to Mn^{2+} in $La_{0.8}Sr_{1.2}Co_{0.5}Mn_{0.5}O_{3.6}$ (see *Figure 4.2*); the oxygen stoichiometry suggests that 20% of Mn^{3+} is reduced to Mn^{2+}. The presence of Co^{2+} and Mn^{3+} in the reduced materials rationalizes the spin glass state and absence of long-range AFM order, in $La_{1.2}Sr_{0.8}Co_{0.5}Mn_{0.5}O_{3.85}$ for example, since competing FM and AFM interactions are predicted, where the Co^{2+}-Co^{2+} interactions are AFM, Mn^{3+}-Mn^{3+} and Co^{2+}-Mn^{3+} interactions are FM/AFM, according to Goodenough-Kanamori rules for super-exchange interactions [16,17].

The predominance of Co^{3+}/Mn^{3+} oxidation state in the oxygenated materials means that a low spin state of Co^{3+} can account for the different magnetic behaviours of the oxygenated and reduced materials. The enhanced FM exchange of the oxygenated materials can be attributed to FM interactions between low spin Co^{3+} and high spin Mn^{3+};

the absence of long-range order, and hence the spin glass behaviour, at low temperature is due to competition with the AFM nature of the Mn^{3+}- Mn^{3+} interactions. Considering the presence of low concentrations of M^{4+} in the oxygenated materials (such as $La_{0.8}Sr_{1.2}Co_{0.5}Mn_{0.5}O_4$ and $La_{1.2}Sr_{0.8}Co_{0.5}Mn_{0.5}O_{4.1}$) further complicates the magnetic interactions.

The oxide ion vacancies in the reduced materials are located within the equatorial planes of the K_2NiF_4-type structure, which suggests formation of MO_x polyhedra of coordination lower than 6. Although a lattice expansion is expected under reduction, *Figure 4.3* shows significant contraction in *a* under reduction. A similar effect has been observed in the iron-containing samples and has been attributed to the coordination requirements of the A-type La/Sr ions (see section 3.7). The contraction of the La/Sr-O coordination sphere, achieved in the *xy* plane due to reduction of the coordination number, results in freezing or contraction of *a* with an associated twist of MO_x polyhedra around the *z* axis to maintain M–O1 bond lengths. The twist, as measured by the O1 *y* parameter, increases with the increase of the oxygen deficiency (*Table 4.2*).

The effect of interstitial oxygen on the lattice parameters of this type of materials can also be examined by considering the refined NPD data of $La_{1.2}Sr_{0.8}Co_{0.5}Mn_{0.5}O_{4.1}$ (*Table 4.2*) and $La_{1.2}Sr_{0.8}Co_{0.5}Fe_{0.5}O_4$ (*Table 3.1*) and their reduced forms. 3.0% contraction in *c* and 1.2% expansion in *a* in the case of $La_{1.2}Sr_{0.8}Co_{0.5}Mn_{0.5}O_{4.1}$, compared with 1.8% and 0.2% in the case of $La_{1.2}Sr_{0.8}Co_{0.5}Fe_{0.5}O_4$, occur due to insertion of oxygen in these materials (starting from $O_{3.85}$ phases). Extra contraction of *c* and expansion of *a* in $La_{1.2}Sr_{0.8}Co_{0.5}Mn_{0.5}O_{4.1}$ are therefore attributed to the interstitial oxygen; the increase of the effective charge of the transition metal ions (to compensate the excess oxygen) can account for the *c* parameter contraction, while the expansion of *a* can be attributed to an

expansion in the coordination sphere of A ions (La/Sr), achieved also in the *xy* plane, due to an increase in the coordination number (> 9).

The effect of Jahn-Teller distortion associated with the presence of Mn^{3+} in these materials can be investigated by comparing the refined NPD data for the $O_{3.75}$ and $O_{3.85}$ materials in the iron and manganese systems (see Tables 3.1, 3.2, 4.2 and 4.3). The MO_6 polyhedra generally show higher degree of distortion in the manganese-containing materials; this effect is associated with a contraction in *a* and an expansion in *c* (*e.g.* for $LaSrCo_{0.5}Fe_{0.5}O_{3.75}$: M–O2/M–O1 = 1.145, *a* = 3.82375(4) Å, *c* = 12.9635(2) Å; for $LaSrCo_{0.5}Mn_{0.5}O_{3.75}$: M–O2/M–O1 = 1.167, *a* = 3.80329(6) Å, *c* = 13.0409(2) Å).

The study indicates that the studied materials withstand reducing conditions (10% H_2/N_2) up to 1000 °C with retention of structural stability and formation of considerably higher degree of oxygen deficiency due to possible reduction of Mn^{3+} into Mn^{2+} at T > 800 °C. The presence of large oxygen nonstoichiometry along with the structural stability at high temperature in reducing environments make these materials an attractive system to be explored for use as oxygen separation membranes.

Considering the possible use of $La_{1.2}Sr_{0.8}Co_{0.5}Mn_{0.5}O_{4.1}$ as mixed conductor under oxidizing conditions (in applications such as SOFCs), The conductivity versus temperature data suggest that the material is a semiconductor in the temperature range 100-700 °C with conductivity values < 1 Ω^{-1} cm^{-1} at high temperatures. This value is very low compared with $La_2NiO_{4+\delta}$ which is a potential K_2NiF_4-type mixed conductor and exhibits conductivities of ~ 100 Ω^{-1} cm^{-1} at intermediate temperatures.

4.3 Synthesis and characterization of $La_{2-x}Sr_xCo_{0.5}Cr_{0.5}O_{4-\delta}$

4.3.1 Synthesis

The materials $La_{1.15}Sr_{0.85}Co_{0.5}Cr_{0.5}O_4$ and $LaSrCo_{0.5}Cr_{0.5}O_4$ were synthesized by solid state reactions. Stoichiometric amounts of La_2O_3 (previously dried at 800 °C in air), $SrCO_3$, Co_3O_4 and Cr_2O_3 were intimately mixed, pressed into pellets and calcined at 1350 °C for 30 h under a N_2 atmosphere. The samples were then heated in air at 800 °C for 12 h in order to obtain well oxygenated materials. Attempts to synthesize strontium-rich phases under applied oxidizing conditions (air or oxygen atmospheres) were unsuccessful.

4.3.2 XRD and TGA study

XRD analysis indicated that the synthesized materials (oxygenated materials) are single-phase and adopt a tetragonal K_2NiF_4-type structure (*I4/mmm* space group). The refined unit cell parameters (considering that the materials are stoichiometric in oxygen) are a = 3.84394(5) Å, c = 12.4974(2) Å and a = 3.83249(5) Å, c = 12.4876(2) Å for $La_{1.15}Sr_{0.85}Co_{0.5}Cr_{0.5}O_4$ and $LaSrCo_{0.5}Cr_{0.5}O_4$, respectively.

The reduction behaviour of these materials in 10% H_2/N_2 is shown in *Figure 4.11*. Assuming that the oxygenated materials are stoichiometric in oxygen, the TG measurements suggest that, under applied reduction conditions, the oxygen-deficient phases $La_{1.15}Sr_{0.85}Co_{0.5}Cr_{0.5}O_{3.83}$ and $LaSrCo_{0.5}Cr_{0.5}O_{3.76}$ are formed in the temperature range 600-1000 °C with no evidence of phase decomposition (as indicated by XRD). These reduction products are retrieved on a larger scale by heating the oxygenated materials in 10% H_2/N_2 at 700 °C for 12 h. The refined unit cell parameters of the reduced materials are a = 3.83328(7) Å, c = 12.6429(4) Å and a = 3.81822(7), Å c = 12.6682(3) Å for $La_{1.15}Sr_{0.85}Co_{0.5}Cr_{0.5}O_{3.83}$ and $LaSrCo_{0.5}Cr_{0.5}O_{3.76}$, respectively.

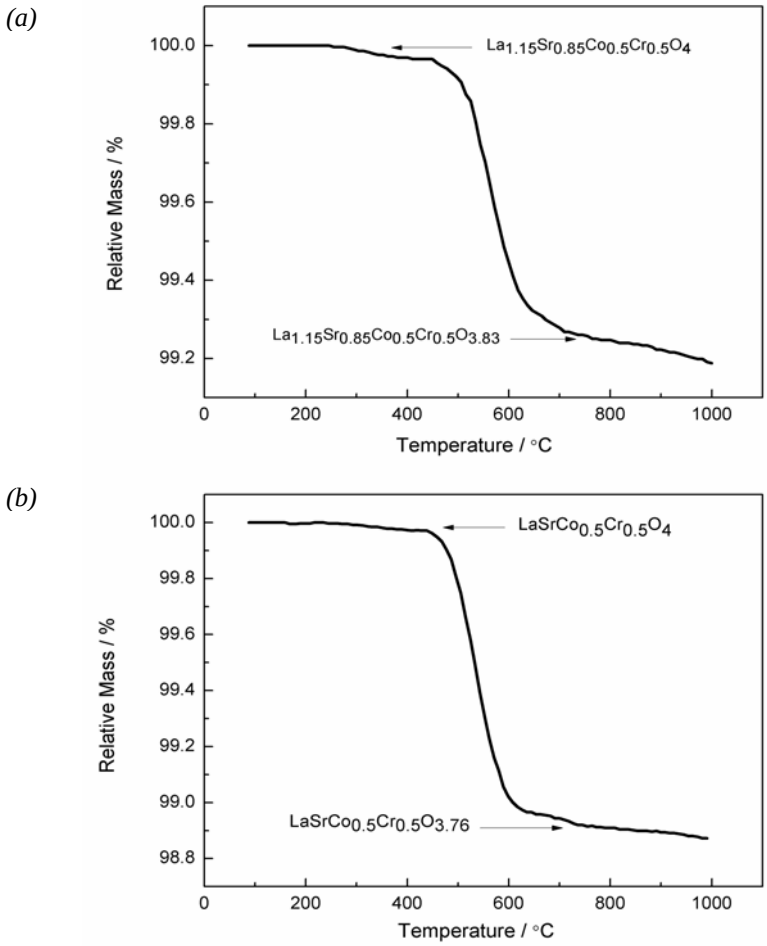

Figure 4.11 TG data for the reduction of (a) $La_{1.15}Sr_{0.85}Co_{0.5}Cr_{0.5}O_4$ and (b) $LaSrCo_{0.5}Cr_{0.5}O_4$ using 10% H_2 in N_2.

4.3.3 Room temperature NPD analysis

The oxygen content and defect structure of the reduced materials were examined by NPD. Refinement results of the data collected at room temperature are given in *Table 4.4*. Profiles and difference patterns from the Rietveld analysis are shown in *Figure 4.12*. Some selected bond lengths are given in *Table 4.5*. Analysis of the oxide ion site occupancies was carried out in the same manner as for iron- and manganese-containing phases revealing a similar disordered distribution of vacancies in the MO_2 planes of the structure. A rotation of MO_6 octahedra around the *z* axis also transforms the oxide ions at (0.5, 0, 0) to the split position (0.5, y, 0).

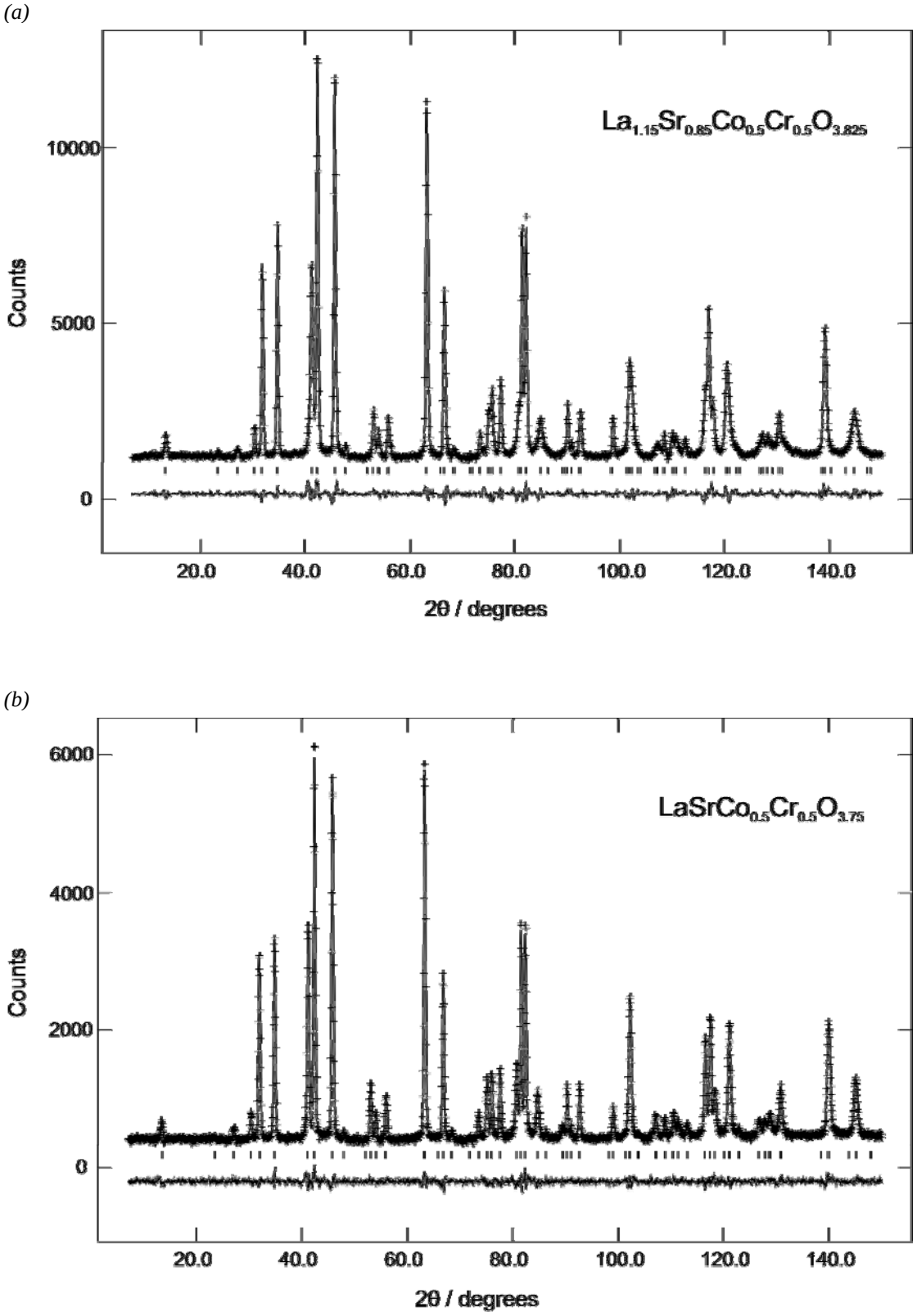

Figure 4.12 Observed, calculated and difference profiles for NPD data collected from (a) $La_{1.15}Sr_{0.85}Co_{0.5}Cr_{0.5}O_{3.825}$ and (b) $LaSrCo_{0.5}Cr_{0.5}O_{3.75}$, at room temperature.

Table 4.4 Structural results for the refinement of the NPD data collected from $La_{1.15}Sr_{0.85}Co_{0.5}Cr_{0.5}O_{3.825}$ and $LaSrCo_{0.5}Cr_{0.5}O_{3.75}$ at room temperature.

Atom	*x*	*y*	*z*	100 x Uiso (Å^2)	Occupancy	Site Symmetry
$La_{1.15}Sr_{0.85}Co_{0.5}Cr_{0.5}O_{3.825}$, *a* = 3.84641(6) Å; *c* = 12.7013(5) Å wRp = 0.0355; Rp = 0.0267; χ^2 = 2.34						
Co/Cr	0	0	0	0.76(7)	0.5/0.5	2a
La/Sr	0	0	0.3589(1)	1.12(3)	0.575/0.425	4e
O1	0.5	0.036(1)	0	0.87(8)	0.454(3)	8j
O2	0	0	0.1685(2)	2.05(5)	1	4e
$LaSrCo_{0.5}Cr_{0.5}O_{3.75}$, *a* = 3.83401(4) Å; *c* = 12.72734(25) Å wRp = 0.0468; Rp = 0.0362; χ^2 = 1.479						
Co/Cr	0	0	0	0.83(5)	0.5/0.5	2a
La/Sr	0	0	0.3582(1)	1.14(2)	0.5/0.5	4e
O1	0.5	0.036(1)	0	1.07(6)	0.439(2)	8j
O2	0	0	0.1670(1)	2.05(4)	1	4e

Table 4.5 Selected bond lengths (Å) for the refined phases.

Bond	$La_{1.15}Sr_{0.85}Co_{0.5}Cr_{0.5}O_{3.825}$	$LaSrCo_{0.5}Cr_{0.5}O_{3.75}$
Co/Cr–O1*	1.9281(4)	1.9220(3)
Co/Cr–O2	2.140(2)	2.125(2)
La/Sr–O1*	2.529(4)	2.534(3)
	2.731(4)	2.736(3)
La/Sr–O2	2.418(3)	2.434(2)
	2.7420(4)	2.7299(2)

*Splitting of O1 sites gives twice the number of bonds compared with the ideal site

Refinements indicated that the overall stoichiometries of the reduced materials are $La_{1.15}Sr_{0.85}Co_{0.5}Cr_{0.5}O_{3.82(1)}$ and $LaSrCo_{0.5}Cr_{0.5}O_{3.76(1)}$. These results are in good agreement with the TG data suggesting that the oxygenated materials are stoichiometric in oxygen. Oxygen stoichiometries given by NPD and TG data are very close to the theoretical values corresponding to Co^{2+}/Cr^{3+} in the reduced materials and $Co^{3+(2+)}/Cr^{3+}$ in the oxidized materials, *i.e.* $La_{1.15}Sr_{0.85}Co_{0.5}Cr_{0.5}O_{3.825}$, $LaSrCo_{0.5}Cr_{0.5}O_{3.75}$, $La_{1.15}Sr_{0.8}Co_{0.5}Cr_{0.5}O_4$ and $LaSrCo_{0.5}Cr_{0.5}O_4$, These nominal stoichiometries were therefore adopted.

4.3.4 Magnetic susceptibility

Figure 4.13 shows the temperature dependence of the magnetic susceptibility of different chromium-containing samples. The oxygenated materials are essentially paramagnetic, whereas a distinct divergence between ZFC and FC susceptibilities is observed in the reduced materials, which suggests spin glass behaviour.

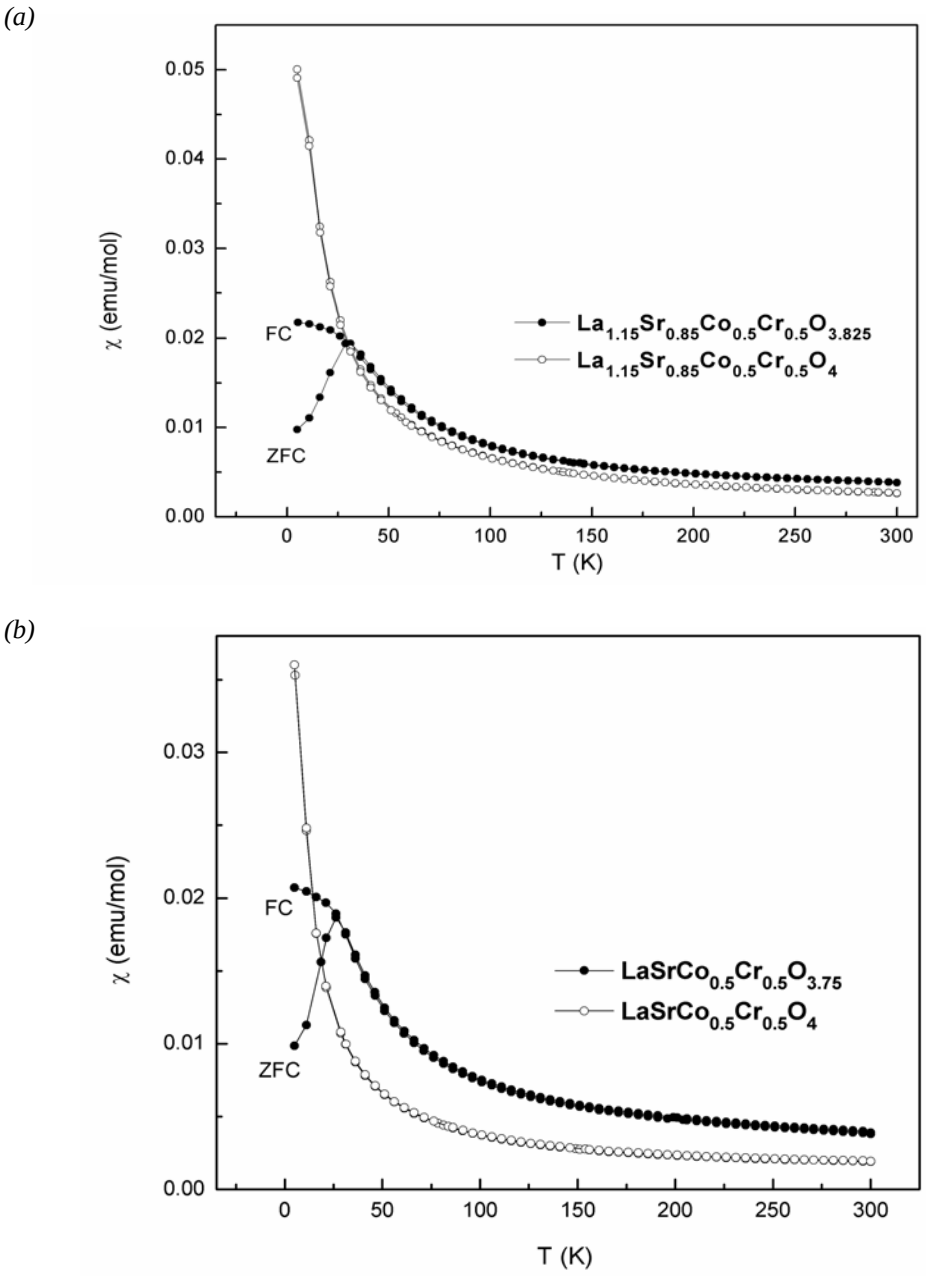

Figure 4.13 Variation of magnetic susceptibility (ZFC and FC) with temperature for (a) $La_{1.15}Sr_{0.85}Co_{0.5}Cr_{0.5}O_{4-\delta}$ and (b) $LaSrCo_{0.5}Cr_{0.5}O_{4-\delta}$.

Plots of the reciprocal of the molar susceptibility against temperature for the reduced samples (*Figure 4.14 (a)*) suggest a non Curie-Weiss behaviour in the given temperature range. However, the plots display an increase in gradient on cooling which is expected for spin glasses with AFM interactions. Application of the Curie-Weiss law at the upper and lower limits of the temperature range provides negative θ values, which confirms predominantly AFM interactions. Above 200 K, the effective moment for $La_{1.15}Sr_{0.85}Co_{0.5}Cr_{0.5}O_{3.825}$ and $LaSrCo_{0.5}Cr_{0.5}O_{3.75}$ is 3.84 μ_B. The reciprocal susceptibility plots of the oxidized materials also indicate AFM exchange interactions (*Figure 4.14 (b)*). Above 200 K, the effective moments are 2.80 and 2.88 μ_B for $La_{1.15}Sr_{0.85}Co_{0.5}Cr_{0.5}O_4$ and $LaSrCo_{0.5}Cr_{0.5}O_4$, respectively.

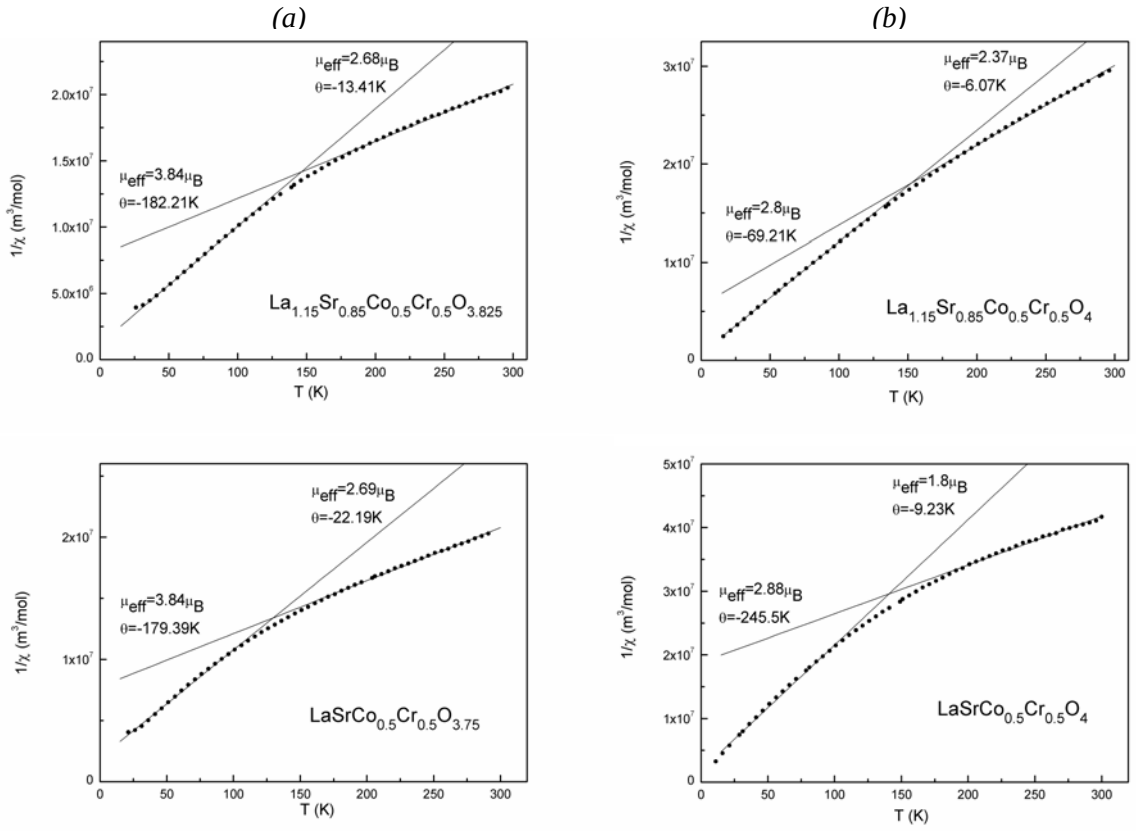

Figure 4.14 Variation of the inverse magnetic susceptibilities (ZFC) with temperature for (a) reduced samples and (b) oxygenated samples.

4.3.5 Discussion of $La_{2-x}Sr_xCo_{0.5}Cr_{0.5}O_{4-\delta}$

The phases $La_{1.15}Sr_{0.85}Co_{0.5}Cr_{0.5}O_4$, $LaSrCo_{0.5}Cr_{0.5}O_4$, $La_{1.15}Sr_{0.85}Co_{0.5}Cr_{0.5}O_{3.825}$ and $LaSrCo_{0.5}Cr_{0.5}O_{3.75}$ have been synthesized and characterized by XRD, TGA, NPD and magnetic susceptibility measurements. The reduced materials are spin glass antiferromagnets. This behaviour can be attributed to competing AFM and FM interactions between high spin Co^{2+} and Cr^{3+} ions; according to Goodenough-Kanamori rules for super-exchange interactions [16,17], a disordered Co/Cr distribution would result in competing FM (Co-Cr) and AFM (Co-Co and Cr-Cr) interactions. The effective moments for $La_{1.15}Sr_{0.85}Co_{0.5}Cr_{0.5}O_{3.825}$ and $LaSrCo_{0.5}Cr_{0.5}O_{3.75}$ near room temperature (both 3.84 μ_B) are in good agreement with the theoretical spin-only values of high spin Co^{2+} and Cr^{3+} ions (3.87 μ_B), although a higher moment may be anticipated because of the orbital contribution to the magnetic moment expected for high spin Co^{2+}. The magnetic behaviour of the oxygenated materials can be attributed to weak exchange consistent with Co^{3+} ions being in the low spin state. The effective moments of 2.80 and 2.88 μ_B for $La_{1.15}Sr_{0.85}Co_{0.5}Cr_{0.5}O_4$ and $LaSrCo_{0.5}Cr_{0.5}O_4$ are relatively close to the spin-only values based on high spin Cr^{3+}/Co^{2+} and low spin Co^{3+} ions. Spin-only moments which are predicted for $La_{1.15}Sr_{0.85}Co_{0.5}^{II/III}Cr_{0.5}O_4$ and $LaSrCo_{0.5}^{III}Cr_{0.5}O_4$ are 3.12 and 2.74 μ_B, respectively. Disappearance of the spin glass behaviour in these materials is supportive of a low spin state of Co^{3+}; presence of Co^{3+} in the high spin or intermediate spin states would produce a FM component of interactions [Co^{3+} (t_{eg}^4 e_g^2)-Cr^{3+} (t_{2g}^3 e_g^0)/ Co^{3+} (t_{eg}^5 e_g^1)-Cr^{3+} (t_{2g}^3 e_g^0)] which may result in a spin glass state at low temperatures.

Similar to iron- and manganese- containing phases (section 3.4 and 4.2.3), oxide ion vacancies in $La_{2-x}Sr_xCo_{0.5}Cr_{0.5}O_{4-\delta}$ were created within the equatorial planes of the structure *via* the reduction of Co^{3+} into Co^{2+}. This was also associated with an expansion in

c and a contraction in *a* in order to equilibrate the required expansion and contraction of (Co/Cr)-O and (La/Sr)-O coordination spheres, respectively (see section 3.7). No evidence of oxygen hyperstoichiometry could be observed in $La_{2-x}Sr_xCo_{0.5}Cr_{0.5}O_4$ under applied oxidizing conditions, and the reduced Co^{2+}/Cr^{3+} state (in $La_{1.15}Sr_{0.85}Co_{0.5}Cr_{0.5}O_{3.825}$ and $LaSrCo_{0.5}Cr_{0.5}O_{3.75}$) persists under applied reducing conditions without further reduction or phase decomposition.

4.4 References

[1] S. J. Skinner, J. A. Kilner, *Solid State Ionics* **135** (2000) 709.

[2] V. V. Vashook, H. Ullman, O. P. Olshevskaya, V. P. Kulik, V. E. Lukashevich, L. V. Kokhanovskii, *Solid State Ionics* **138** (2000) 99.

[3] V. K. Sears, *Neutron News* **3** (1992) 29.

[4] C. L. Bull, D. Gleeson, K. S. Knight, *J. Phys.: Condens. Matter* **15** (2003) 4927.

[5] P. H. Labbe, M. Ledesert, V. Caignaert, B. Raveau, *J. Solid State Chem.* **91** (1991) 362.

[6] J. D. Jorgensen, B. Dabrowski, Shiyou Pei, D. R. Richards, D. G. Hinks, *Phys. Rev. B* **40** (1989) 2187.

[7] R. K. Li, C. Greaves, *J. Solid State Chem.* **153** (2000) 34.

[8] J. van Elp, J. L. Wieland, H. Eskes, P. Kuiper, G. A. Sawatzky, F. M. F. de Groot, T. S. Turner, *Phys. Rev. B* **44** (1991) 6090.

[9] F. M. F. de Groot, M. Abbate, J. van Elp, G. A. Sawatzky, Y. J. Ma, C. T. Chen, F. Sette, *J. Phys.: Condens. Matter* **5** (1993) 2277.

[10] T. Mizokawa, L. H. Tjeng, P. G. Steeneken, N. B. Brookes, I. Tsukada, T. Yamamoto, K. Uchinokura, *Phys. Rev. B* **64** (2001) 115104.

[11] K. Takubo, T. Mizokawa, S. Hirata, J. Y. Son, A. Fujimori, D. Topwal, D. D. Sarma, S. Rayaprol, E. V. Sampathkumaran, *Phys. Rev. B* **71** (2005) 73406.

[12] I. Alvarez-Serrano, G. J. Cuello, M. L. Lopez, A. Jimenez-Lopez, C. Pico, E. Rodrıguez-Castellon, E. Rodrıguez and M. L. Veiga, *J. Phys. D: Appl. Phys.* **41** (2008) 195001.

[13] J. G. Kim, D. L. Pugmire, D. Battaglia and M. A. Langell, *Appl. Surf. Sci*. **165** (2000) 70.

[14] A. Foelske and H. H. Strehblow, *Surf. Interface Anal*. **34** (2002) 125.

[15] P. Karen, E. Suard, F. Fauth, P. M. Woodward, *Solid State Sciences* **6** (2004) 1195.

[16] J. B. Goodenough, Magnetism and the Chemical Bond, Interscience, New York, 1963.

[17] J. Kanamori, *J. Phys. Chem. Solids* **10** (1959) 87.

CHAPTER 5

Synthesis and characterization of $La_{1.5+x}Sr_{0.5-x}Co_{0.5}Ni_{0.5}O_{4\pm\delta}$ (x = 0, 0.2)

5.1 Background

Perovskite materials such as $La_{1-x}Sr_xMnO_{3-\delta}$ (LSM) and $La_{1-x}Sr_xCo_{1-y}Fe_yO_{3-\delta}$ (LSCF) have been very widely studied as potential mixed conducting materials. The need for more stable phases under reducing conditions has stimulated the study of intergrowth oxides belonging to the RP series [1]. The K_2NiF_4-type phases (n =1 RP phases) are of particular interest because of their flexibility: they can withstand reducing conditions *via* loss of oxygen, usually from equatorial planes, and also accommodate excess interstitial oxygen under oxidizing conditions. It has been shown in chapter 3 and 4 that $La_{2-x}Sr_xCo_{0.5}Fe(Cr)_{0.5}O_4$ phases withstand reducing conditions (10% H_2/N_2) up to 1000 °C and are subject to reduction of Co^{3+} to Co^{2+} and formation of oxide ion vacancies within the equatorial planes. However, oxygen hyperstoichiometry could not be achieved in these materials. On the other hand, the manganese-containing materials ($La_{2-x}Sr_xCo_{0.5}Mn_{0.5}O_{4\pm\delta}$) have shown a wider range of oxygen nonstoichiometry. $La_{1.2}Sr_{0.8}Co_{0.5}Mn_{0.5}O_{4.1}$ is hyperstoichiometric in oxygen under oxidizing conditions and also withstands reducing conditions *via* formation of oxygen deficiency. However, the overall conductivity of this material in air at high temperature is very low (see section 4.2.6) which limits its application as a mixed conductor under oxidizing conditions (*e.g.* as a cathode material in SOFCs).

$La_2NiO_{4+\delta}$, on the other hand, is known to exhibit oxygen hyperstoichiometry accompanied by mixed valency and shows relatively large oxide-ion and electronic conductivities. $La_2NiO_{4+\delta}$ exhibits a broad semiconductor-metal transition in the

temperature range 250-450 °C [2-8] with a maximum conductivity of 100 Ω^{-1} cm^{-1}, which is reasonable for use as a cathode in SOFCs. The oxide-ion conductivity is also an order of magnitude larger than the conventional perovskites in the intermediate-temperature range [9] and has been assigned to complex mechanisms involving interstitial migration in the intergrowth region and vacancy migration in the perovskite planes [10,11]. $La_2NiO_{4+\delta}$ is therefore the parent of an important family of mixed conductors for intermediate-temperature applications. A wide range of La_2NiO_4-based materials have been studied in an attempt to optimize novel stoichiometries for improved mixed conducting behaviour and electrode performance [11-17]. Despite the promising mixed ionic-electronic conducting characteristics, these materials have shown less promising electrode performance compared to conventional perovskites due to problems of phase stability and electrolyte incompatibility [18-20]. It has been suggested that the cobalt-doped phases, $La_2Ni_{1-x}Co_xO_{4+\delta}$ for example, have improved catalytic properties for the oxygen reduction at the cathode, and enhanced low-temperature diffusion properties compared with $La_2NiO_{4+\delta}$ [13,14]; however, less promising phase-stability characteristics were observed after prolonged heating in air [19] or under reduced oxygen pressures [21].

Based on previous studies on mixed B-site K_2NiF_4-type phases (chapter 3 and 4), it has been suggested that the possible introduction of some M^{3+} ions into the B-site of the $La_2Ni_{1-x}Co_xO_{4+\delta}$ system (*via* strontium doping) may improve the phase stability of these materials *via* the formation of stable B-site cations in oxidizing conditions, and the formation of relatively stable oxygen-deficient phases under reducing conditions (due to reduction of Co^{3+} to Co^{2+}). The materials $La_{1.5+x}Sr_{0.5-x}Co_{0.5}Ni_{0.5}O_{4\pm\delta}$ (x = 0, 0.2) were therefore synthesized and studied and the results are reported in this chapter. Particular interest was focused on three materials: the oxygen stoichiometric $La_{1.5}Sr_{0.5}Co_{0.5}Ni_{0.5}O_4$,

the oxygen-deficient phase $La_{1.5}Sr_{0.5}Co_{0.5}Ni_{0.5}O_{3.70}$ and the oxygen-excess phase $La_{1.7}Sr_{0.3}Co_{0.5}Ni_{0.5}O_{4.08}$.

5.2 Synthesis

The materials $La_{1.7}Sr_{0.3}Co_{0.5}Ni_{0.5}O_{4(+\delta)}$ and $La_{1.5}Sr_{0.5}Co_{0.5}Ni_{0.5}O_{4(+\delta)}$ were synthesized by direct solid state reactions using $SrCO_3$, La_2O_3, Co_3O_4 and NiO as the starting materials (La_2O_3 was previously dried at 800 °C). Stoichiometric amounts of starting materials were intimately mixed, pressed into pellets and fired at 1300 °C in air for 30 h; the materials were then allowed to cool slowly (1 °C min^{-1}) to room temperature to obtain well-oxygenated materials.

5.3 XRD and TGA study

XRD data indicated that the as-prepared materials were single-phase with tetragonal *I4/mmm* space group consistent with the K_2NiF_4-type structure. Considering the expected poor sensitivity of X-ray scattering to locate oxygen in this system, oxide ion sites were fixed at full occupancy in simple XRD refinements which resulted in the lattice parameters a = 3.85305(3) Å, c = 12.5268(1) Å and a = 3.83355(2) Å, c = 12.5199(1) Å for $La_{1.7}Sr_{0.3}Co_{0.5}Ni_{0.5}O_{4(+\delta)}$ and $La_{1.5}Sr_{0.5}Co_{0.5}Ni_{0.5}O_{4(+\delta)}$, respectively. The reduction behaviour of these materials was followed by TG measurements in which the materials were heated (10 °C min^{-1}) in flowing 10% H_2/N_2 (*Figure 5.1*). The measurements suggested that, under the applied conditions, the materials lose oxygen either gradually ($La_{1.7}Sr_{0.3}Co_{0.5}Ni_{0.5}O_{4(+\delta)}$) or in a stepwise fashion ($La_{1.5}Sr_{0.5}Co_{0.5}Ni_{0.5}O_{4(+\delta)}$) with retention of structure in the temperature range 400-800 °C, followed by rapid decomposition to the constituent phases La_2O_3, SrO, Co, and Ni, as evidenced by XRD, at T > 800 °C.

Accordingly, the stoichiometries $La_{1.7}Sr_{0.3}Co_{0.5}Ni_{0.5}O_{4.08}$ and $La_{1.5}Sr_{0.5}Co_{0.5}Ni_{0.5}O_4$ were suggested for the as-prepared materials, and the oxygen deficient compound $La_{1.5}Sr_{0.5}Co_{0.5}Ni_{0.5}O_{3.74}$ is suggested for the intermediate composition observed as a plateau in the mass loss curve of $La_{1.5}Sr_{0.5}Co_{0.5}Ni_{0.5}O_4$.

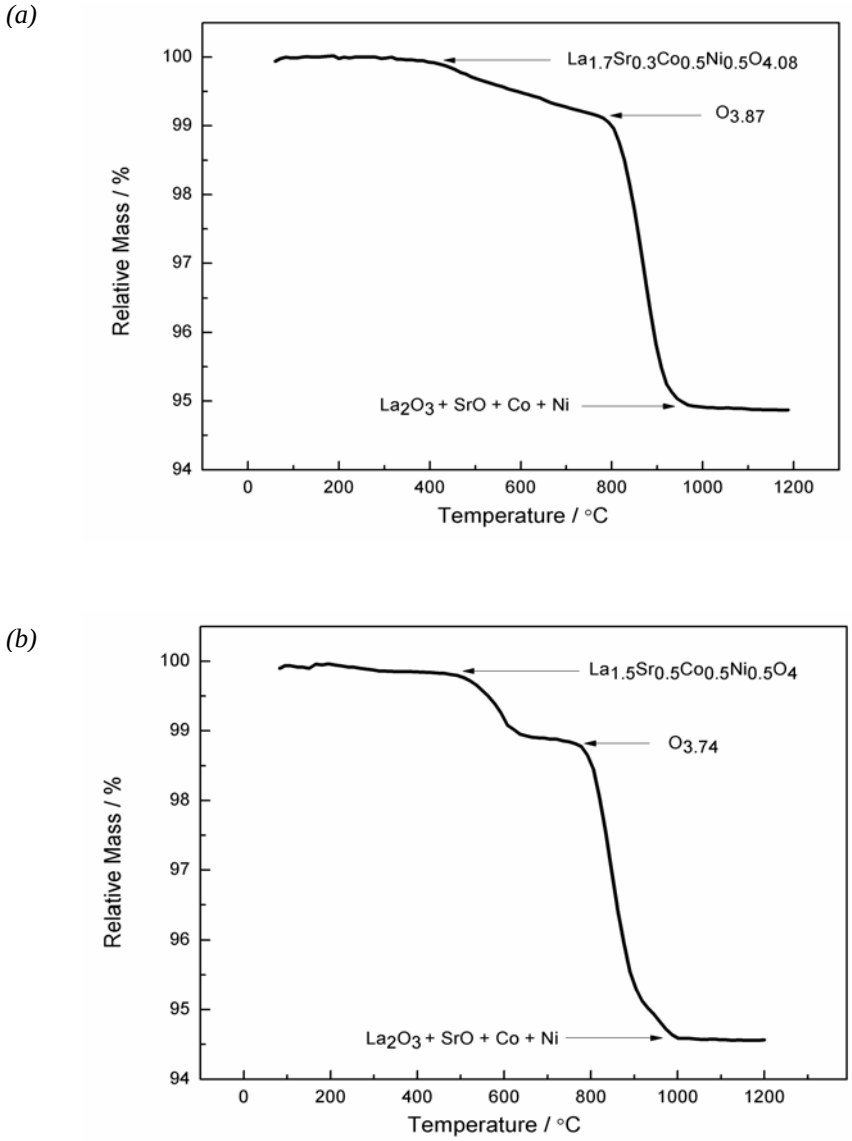

Figure 5.1 TG data for the reduction of the as-prepared materials using 10% H_2 in N_2.

Repeating the reduction of $La_{1.5}Sr_{0.5}Co_{0.5}Ni_{0.5}O_4$ on a large scale (in 10% H_2/N_2 at 750 °C for 12 h) yielded a phase retaining the crystal structure and symmetry with lattice parameters a = 3.81863(5) Å, c = 12.7918(2) Å. The reduced phase showed good stability in air at ambient conditions with no evidence of significant re-oxidation.

5.4 Room temperature NPD analysis

NPD was used to probe more reliably the oxygen content and defect structure of these materials. Rietveld profile refinements, based on ambient temperature data, were performed using the ideal *I4/mmm* space group, and the results are shown in *Table 5.1*. Profile fits and difference patterns of the Rietveld analysis are shown in *Figure 5.2*. Some selected bond lengths are given in *Table 5.2*. NPD analysis showed the overall stoichiometries of the studied materials as $La_{1.7}Sr_{0.3}Co_{0.5}Ni_{0.5}O_{4.08(1)}$, $La_{1.5}Sr_{0.5}Co_{0.5}Ni_{0.5}O_4$ and $La_{1.5}Sr_{0.5}Co_{0.5}Ni_{0.5}O_{3.70(2)}$. These results are in good agreement with the TGA results. Estimated standard deviation values of oxygen stoichiometry are avoided in discussion for simplicity. Oxide ion vacancies in $La_{1.5}Sr_{0.5}Co_{0.5}Ni_{0.5}O_{3.70}$ were disordered and confined to the equatorial MO_2 planes of the K_2NiF_4-type structure, thereby retaining overall tetragonal symmetry. No evidence of symmetry lowering due to vacancy order was observed in the NPD data, which indicates the absence of the differential occupancy of the (0, 0.5, 0) and (0.5, 0, 0) sites observed in $La_{1.6}Sr_{0.4}NiO_{3.47}$ and $LaSrNiO_{3.1}$ [22,23]. An attempt to fit the data to a model in which oxide ion vacancies are distributed between axial and equatorial oxygen sites in a manner similar to $NdSrCuO_{3.56}$ [24] proved unsuccessful. The refinement of $La_{1.5}Sr_{0.5}Co_{0.5}Ni_{0.5}O_{3.70}$ implied a rotation of the $(Co/Ni)O_6$ octahedra around the z axis which converts the oxide ions at (0.5, 0, 0) to the split position (0.5, y, 0); a similar effect has been observed in $LaSrCoO_{3.5-x}$ [25] and $La_{2-x}Sr_xCo_{0.5}M_{0.5}O_{4-\delta}$ (chapters 3 and 4). The

Table 5.1 Structural results for the refinement of the NPD data collected from different samples at room temperature.

Atom	*x*	*y*	*z*	100 x Uiso (Å^2)	Occupancy	Site Symmetry
			$La_{1.7}Sr_{0.3}Co_{0.5}Ni_{0.5}O_{4.08}$, *a* = 3.85498(4) Å; *c* = 12.5346(2) Å wRp = 0.0504; Rp = 0.0387; χ^2 = 1.742			
Co/Ni	0	0	0	0.48(4)	0.5/0.5	2a
La/Sr	0	0	0.36168(9)	0.44(3)	0.85/0.15	4e
O1	0.5	0	0	0.79(3)	1	4c
O2	0	0.042(2)	0.1696(2)	1.25(8)	0.25	16n
O3	0	0.5	0.25	2.63(3)	0.041(5)	4d
			$La_{1.5}Sr_{0.5}Co_{0.5}Ni_{0.5}O_4$, *a* = 3.83636(7) Å; *c* = 12.5305(3) Å wRp = 0.0477; Rp = 0.0362; χ^2 = 1.474			
Co/Ni	0	0	0	0.59(4)	0.5	2a
La/Sr	0	0	0.36235(9)	0.49(3)	0.75/0.25	4e
O1	0.5	0	0	0.81(3)	1	4c
O2	0	0	0.1693(1)	1.38*	1	4e
*U_{11}=1.52(4) Å^2; U_{22}=1.52(4) Å^2; U_{33}=1.11(7) Å^2						
			$La_{1.5}Sr_{0.5}Co_{0.5}Ni_{0.5}O_{3.70}$, *a* = 3.8189(2) Å; *c* = 12.7943(6) Å wRp = 0.0481; Rp = 0.0371; χ^2 = 2.324			
Co/Ni	0	0	0	0.85(8)	0.5/0.5	2a
La/Sr	0	0	0.3595(2)	1.51(7)	0.75/0.25	4e
O1	0.5	0.040(2)	0	0.8(2)	0.423(4)	8j
O2	0	0	0.1724(2)	2.32*	1	4e
*U_{11}=1.9(1) Å^2; U_{22}=1.9(1) Å^2; U_{33}=3.3(3) Å^2						

Table 5.2 Selected bond lengths (Å) for the refined phases.

Bond	$La_{1.7}Sr_{0.3}Co_{0.5}Ni_{0.5}O_{4.08}$	$La_{1.5}Sr_{0.5}Co_{0.5}Ni_{0.5}O_4$	$La_{1.5}Sr_{0.5}Co_{0.5}Ni_{0.5}O_{3.70}$
Co/Ni-O1	1.92749(2)	1.91818(4)	1.9157(6)**
Co/Ni-O2	2.132(2)*	2.122(2)	2.205(3)
La/Sr–O1	2.5925(7)	2.5602(7)	2.512(6)**
	-	-	2.737(6)**
La/Sr–O2	2.413(2)*	2.419(2)	2.395(4)
	2.644(4)*	2.7416(3)	2.7310(6)
	2.868(4)*	-	-
La/Sr–O3	2.3822(6)	-	-

*Splitting of O2 sites gives 4 times the number of bonds compared with the ideal site.

**Splitting of O1 sites gives twice the number of bonds compared with the ideal site

5.2a)

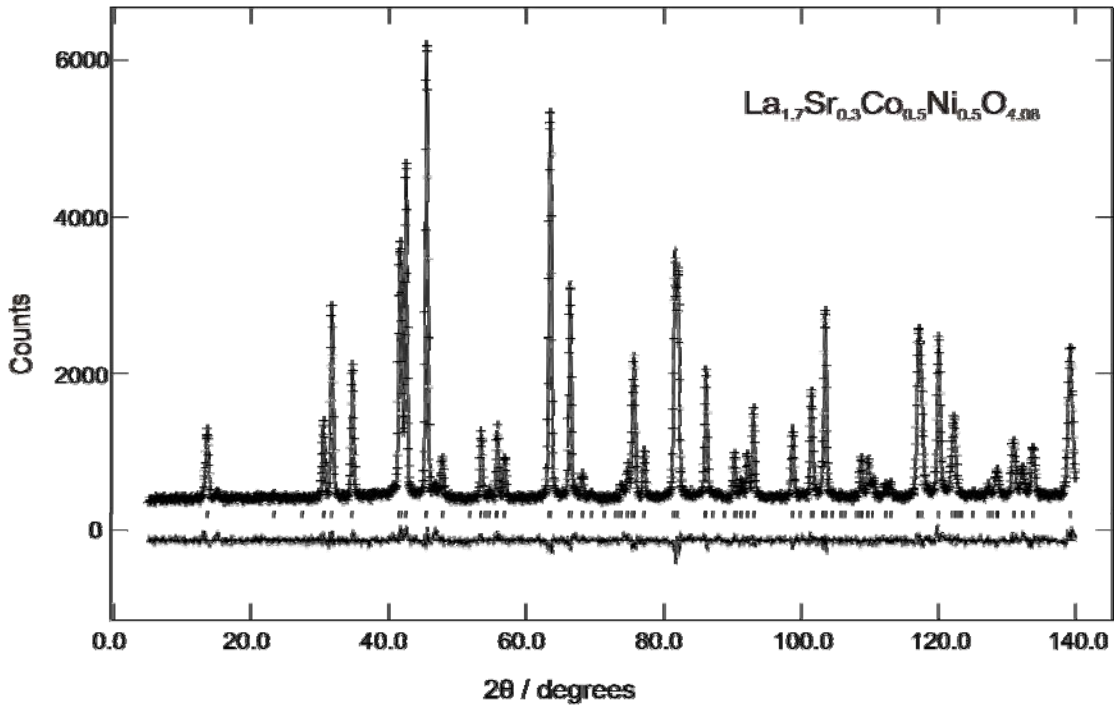
La1.7Sr0.3Co0.5Ni0.5O4.08
Counts
2θ / degrees
6000
4000
2000
0
0.0
20.0
40.0
60.0
80.0
100.0
120.0
140.0

5.2b)

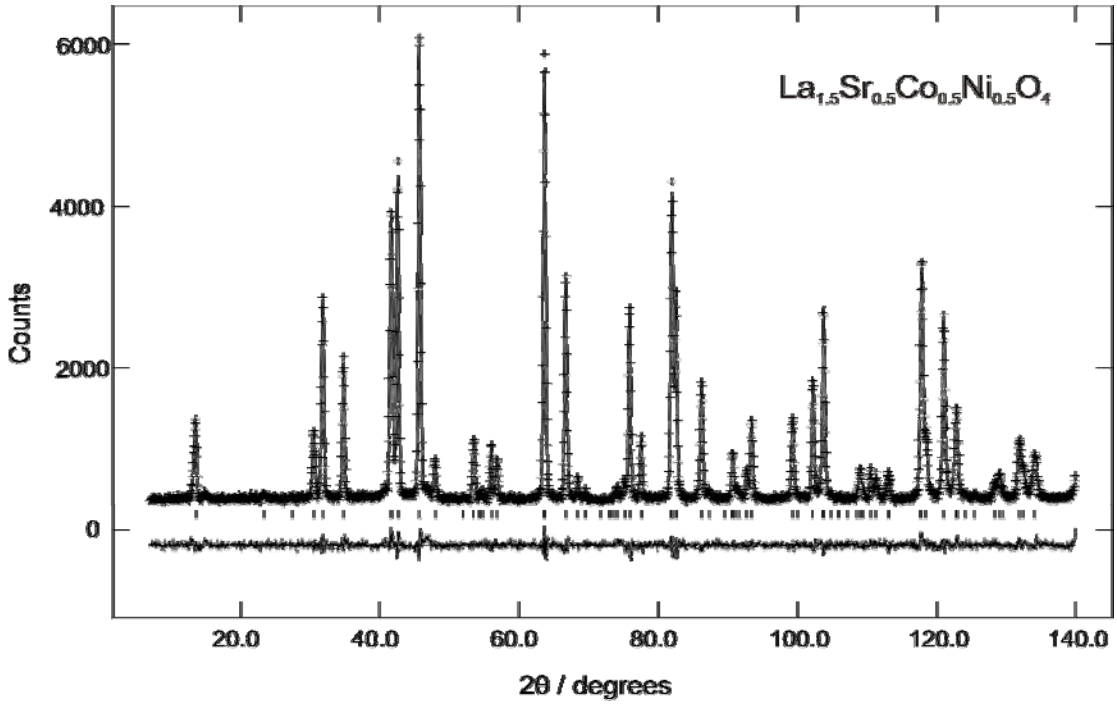
La1.5Sr0.5Co0.5Ni0.5O4
Counts
2θ / degrees
6000
4000
2000
0
20.0
40.0
60.0
80.0
100.0
120.0
140.0

5.2c)

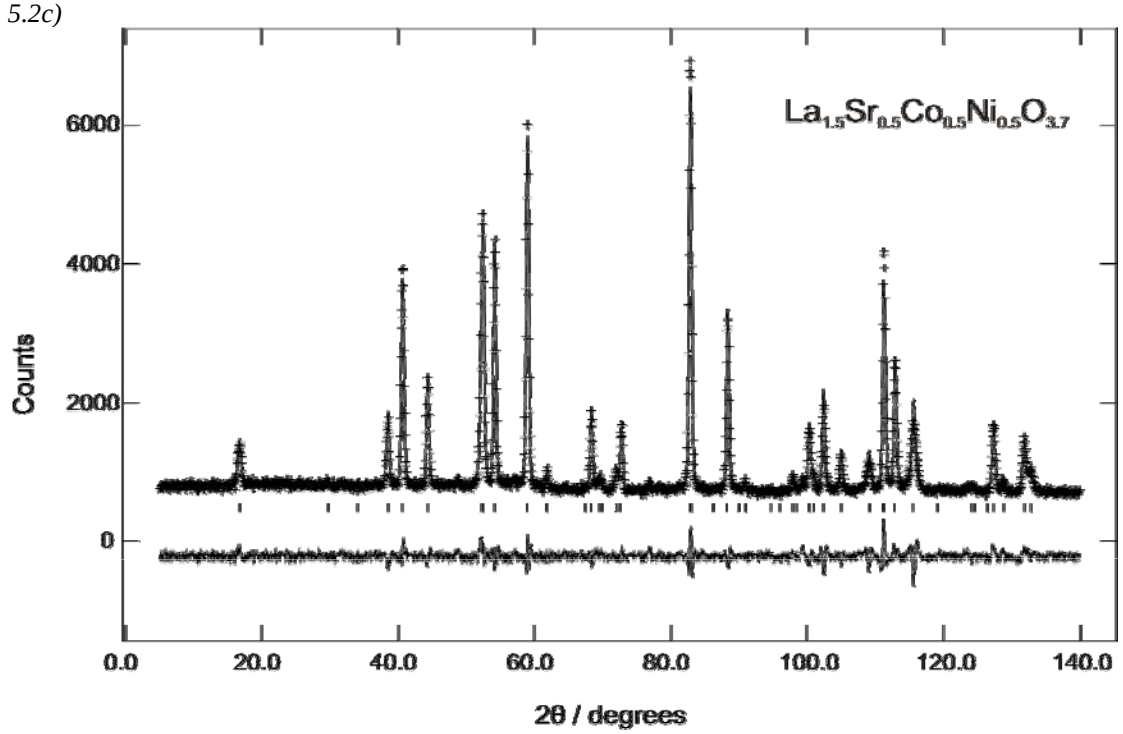

Figure 5.2 Observed, calculated and difference profiles for NPD data collected from different samples at room temperature.

O2 apical oxygen sites (0, 0, z) were allowed to vibrate anisotropically in this model and indicated a higher displacement along the (Co/Ni)–O bond (*Table 5.1*). This may indicate the presence of some Ni^{1+} in this material as discussed later. NPD data showed no evidence of oxygen nonstoichiometry in $La_{1.5}Sr_{0.5}Co_{0.5}Ni_{0.5}O_4$ and the anisotropic vibration of the axial oxygen now showed higher displacement perpendicular to the (Co/Ni)–O bond. The reduced value of U_{33} is consistent with oxidation of Ni^{+} to Ni^{2+}. In contrast to $La_{1.5}Sr_{0.5}Co_{0.5}Ni_{0.5}O_4$, NPD refinement data confirmed oxygen hyperstoichiometry in $La_{1.7}Sr_{0.3}Co_{0.5}Ni_{0.5}O_{4.08}$. The excess oxygen occupies the ideal interstitial sites (0, 0.5, 0.25) of the tetragonal structure. An associated displacement of the apical oxide ions, related to that of Jorgensen's interstitial defect model [26], moves apical oxygens from their ideal position at (0 ,0, z) to the split position (0, y, z). No evidence of magnetic order was observed in the NPD data for any sample.

5.5 Magnetic susceptibility

Figure 5.3 shows the temperature dependence of the magnetic susceptibility, χ, of different materials in the temperature range 5-300 K. Plots of $1/\chi$ against temperature for the as-prepared materials (see insets in *Figure 5.3 (a,b)*) suggest a non Curie-Weiss behaviour in the given temperature range. However, the plots display an increased gradient on cooling which is consistent with predominantly AFM interactions. Application of the Curie-Weiss law at the upper and lower limits of the temperature range provides negative θ values, confirming the AFM interactions. Above 200 K, the effective moments are 2.42 and 2.48 μ_B for $La_{1.7}Sr_{0.3}Co_{0.5}Ni_{0.5}O_{4.08}$ and $La_{1.5}Sr_{0.5}Co_{0.5}Ni_{0.5}O_4$, respectively. $La_2CoO_{4+\delta}$ and $La_2NiO_{4.00}$, in comparison, are antiferromagnetically ordered at room temperature [27-29]. The three-dimensional AFM order in $La_2NiO_{4.00}$ is suppressed [28-30] by introduction of interstitial oxygen and/or strontium doping which is consistent with the observed behaviour of $La_{1.7}Sr_{0.3}Co_{0.5}Ni_{0.5}O_{4.08}$ and $La_{1.5}Sr_{0.5}Co_{0.5}Ni_{0.5}O_4$.

5.3a)

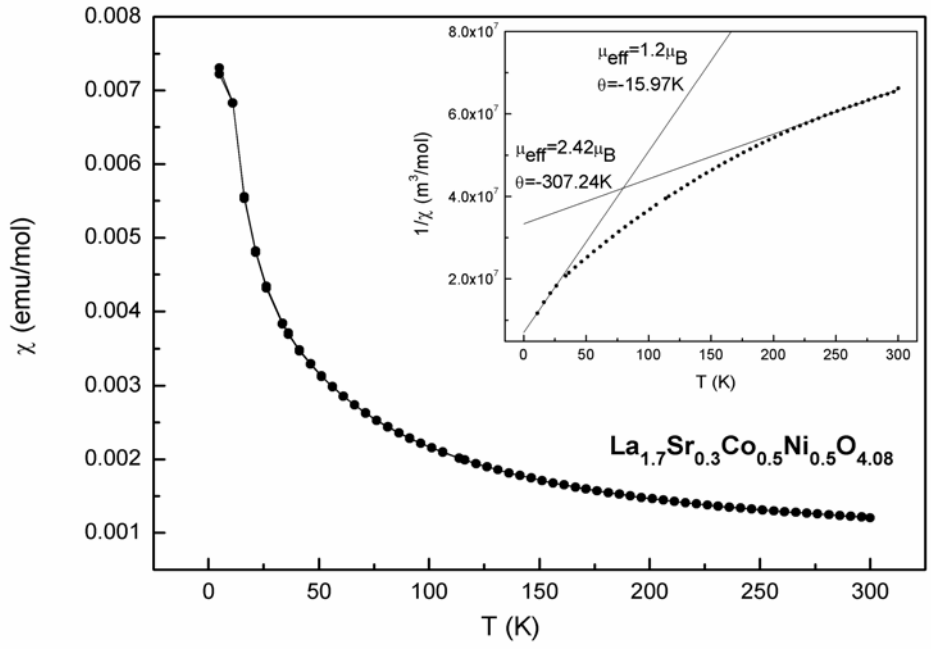

5.3b)

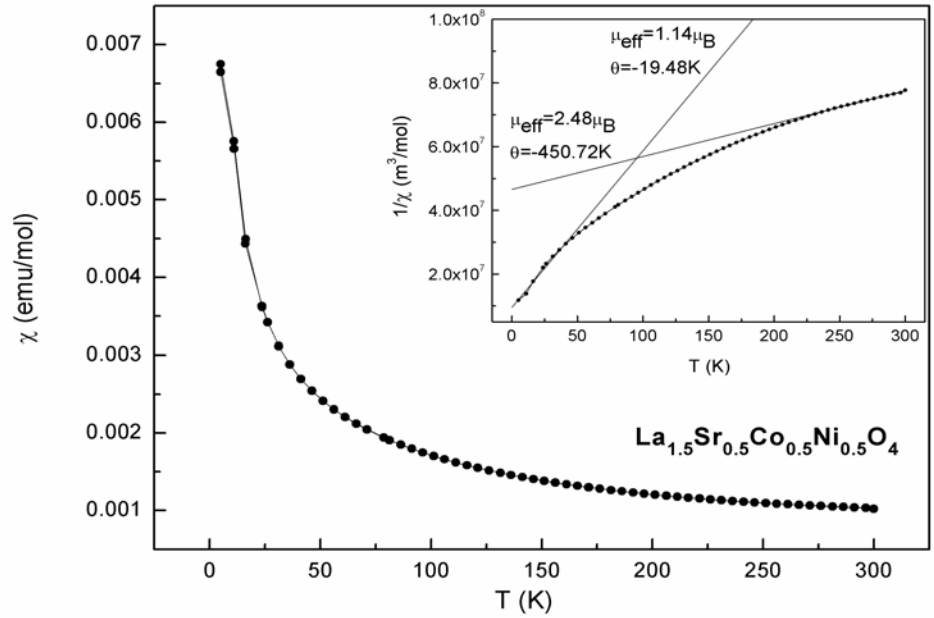

5.3c)

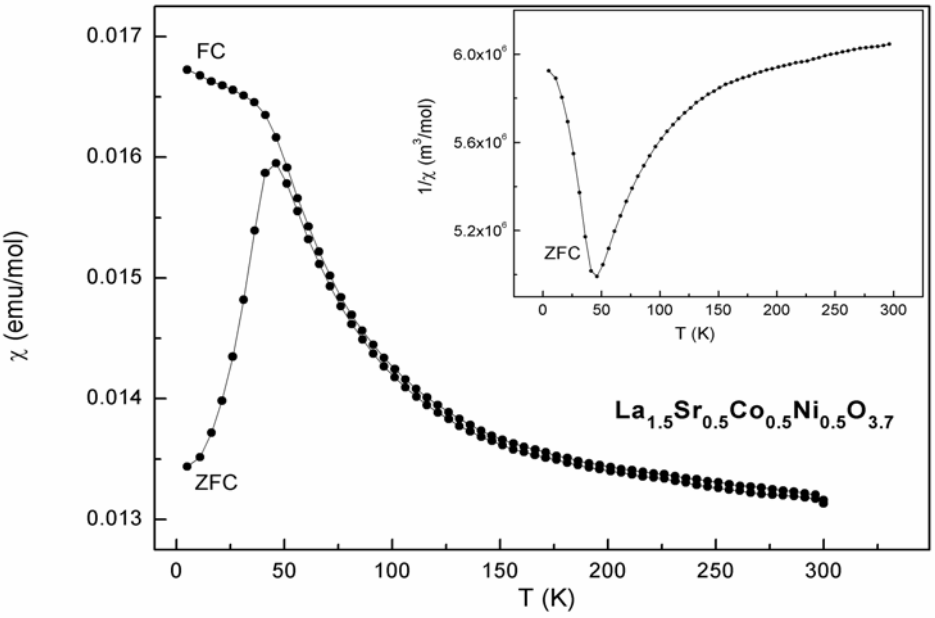

Figure 5.3 Variation of magnetic susceptibility (ZFC and FC) with temperature for (a) $La_{1.7}Sr_{0.3}Co_{0.5}Ni_{0.5}O_{4.08}$ (b) $La_{1.5}Sr_{0.5}Co_{0.5}Ni_{0.5}O_4$ and (c) $La_{1.5}Sr_{0.5}Co_{0.5}Ni_{0.5}O_{3.7}$.

The reduced material $La_{1.5}Sr_{0.5}Co_{0.5}Ni_{0.5}O_{3.70}$ shows a maximum in the ZFC susceptibility at about 50 K, with a marked divergence between ZFC and FC susceptibilities at lower temperatures (*Figure 5.3 (c)*) which is characteristic of spin glass behaviour. The plot of $1/\chi$ against temperature cannot be considered in terms of Curie-Weiss behaviour. No evidence of magnetic order was found in the low temperature NPD data of this sample.

5.6 Transport properties

Measurement of electrical resistivity versus temperature in air for $La_{1.7}Sr_{0.3}Co_{0.5}Ni_{0.5}O_{4.08}$ and $La_{1.5}Sr_{0.5}Co_{0.5}Ni_{0.5}O_4$ in the temperature range 100-900 °C (see section 2.2.7) indicated that the resistivity decreases with increasing temperature in the whole temperature range (*Figure 5.4 (a)*). The data are well fitted with the general law:

$$\rho(\mathrm{T}) = \rho_0 \exp(E_g / k_B \mathrm{T}) \qquad (5.1)$$

(*Figure 5.4 (b)*) which represents simple thermally activated electrical conductivity [31] in which an electron or hole (as the charge carrier) hops between localized states; in equation 5.1 ρ_0 is the electrical resistivity at extremely high temperatures, E_g is the thermal activation energy of the electron or hole and k_B is the Boltzmann constant. The thermal activation energy for $La_{1.7}Sr_{0.3}Co_{0.5}Ni_{0.5}O_{4.08}$ and $La_{1.5}Sr_{0.5}Co_{0.5}Ni_{0.5}O_4$ are 296 and 338 meV, respectively. The electrical conduction of the parent $La_2NiO_{4+\delta}$ in the low temperature range (T < 350 °C) has been interpreted in terms of a thermally activated hopping of small polarons [6]. A semiconductor-metal transition is observed in $La_2NiO_{4+\delta}$ between 250 and 450 °C, and the material behaves as a metal at T > 350 °C. This effect has been linked to a possible orthorhombic-tetragonal transition [6,28] and/or reduction of hole-concentration linked to loss of excess oxygen above 350 °C [7,8]. Such a transition is

(a)

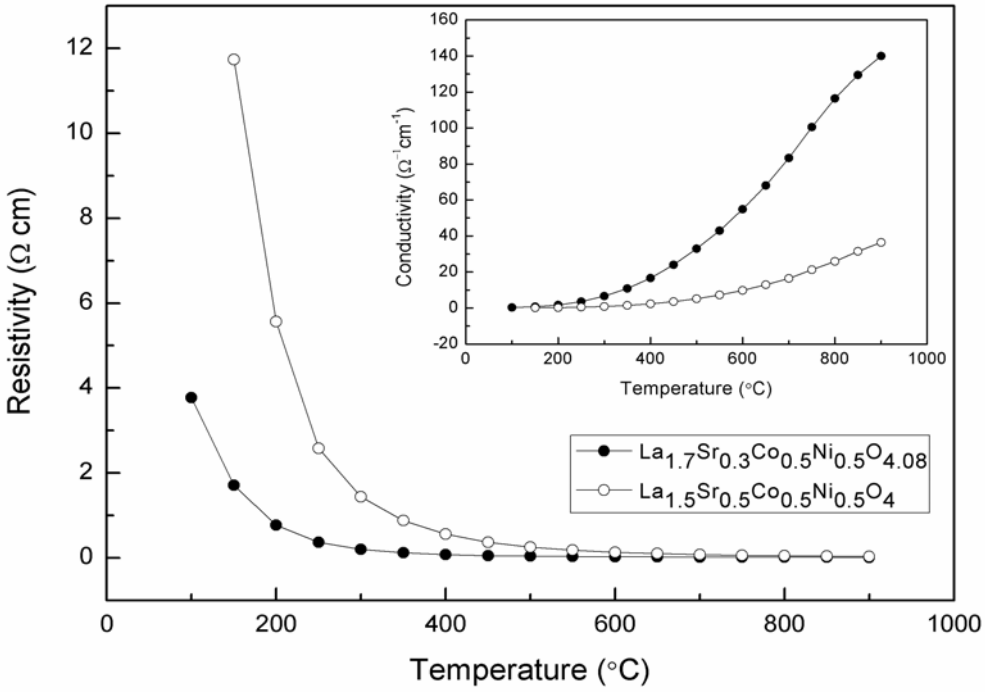

(b)

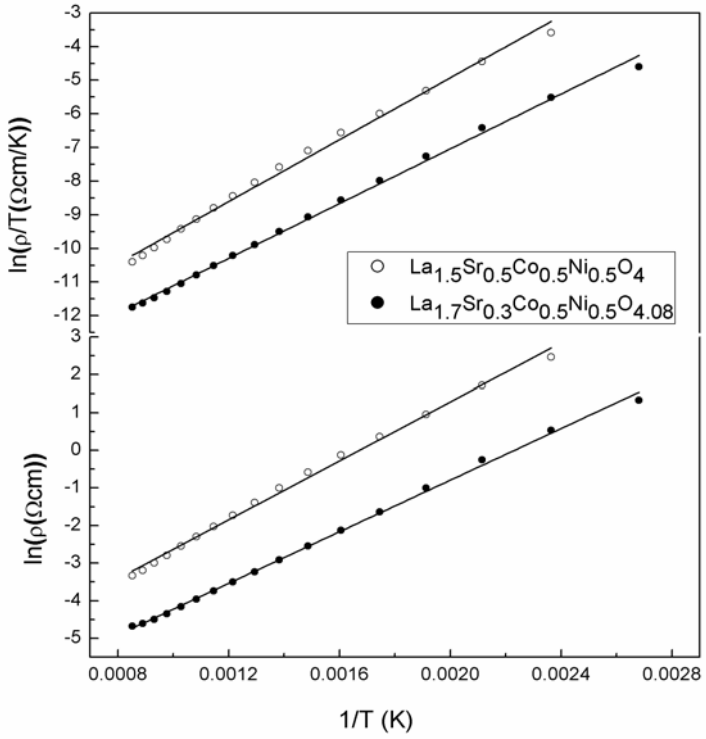

Figure 5.4 (a) Resistivity (ρ) and conductivity (inset) data for $La_{1.7}Sr_{0.3}Co_{0.5}Ni_{0.5}O_{4.08}$ and $La_{1.5}Sr_{0.5}Co_{0.5}Ni_{0.5}O_4$; (b) ln($\rho$)-T and ln($\rho$/T)-T plots for $La_{1.7}Sr_{0.3}Co_{0.5}Ni_{0.5}O_{4.08}$ and $La_{1.5}Sr_{0.5}Co_{0.5}Ni_{0.5}O_4$.

not observed for the materials studied here, and the semiconductive behaviour covers the whole temperature range (100-900 °C). Considering polaron conduction in $La_{1.5+x}Sr_{0.5-x}Co_{0.5}Ni_{0.5}O_{4\pm\delta}$, the polaron hopping energy can be estimated using the formula for thermally activated small polaron hopping by the Emin-Holstein theory [32], given by

$$\rho(T) = \rho_0 T \exp(E_A / k_B T) \qquad (5.2)$$

Plotting the natural logarithm of ρ / T as a function of $1/T$ (*Figure 5.4 (b)*) gives the E_A values 351 and 397 meV for $La_{1.7}Sr_{0.3}Co_{0.5}Ni_{0.5}O_{4.08}$ and $La_{1.5}Sr_{0.5}Co_{0.5}Ni_{0.5}O_4$ respectively, compared with 84 meV for $La_2NiO_{4.16}$ (T < 400°C) [8].

It should be noted that a semiconductor-metal transition occurs in strontium-doped nickelates with the transition-temperature decreasing with increasing x in $La_{2-x}Sr_xNiO_{4+\delta}$, and $LaSrNiO_4$ is metallic at room temperature [33,34]. The transition also occurs in $La_2Ni_{1-x}Co_xO_{4+\delta}$ phases with small x values [35]; however, a disappearance of such transition is claimed for highly doped phases prepared under inert atmospheres [14,20], but the materials are not stable in air at elevated temperatures.

5.7 XPS analysis

XPS data were recorded from $La_{1.5}Sr_{0.5}Co_{0.5}Ni_{0.5}O_4$ and $La_{1.5}Sr_{0.5}Co_{0.5}Ni_{0.5}O_{3.70}$ in order to investigate the change of the B-site oxidation state under reduction. The Ni 2p XPS spectra of the two materials were very similar with no evidence of significant change under reduction. The Co 2p spectra, in contrast, were significantly different. The Co 2p spectra of $La_{1.5}Sr_{0.5}Co_{0.5}Ni_{0.5}O_4$ and $La_{1.5}Sr_{0.5}Co_{0.5}Ni_{0.5}O_{3.70}$ are shown in *Figure 5.5*, and the typical Co $2p_{3/2}$, Co $2p_{1/2}$ and satellite (S) peaks are indicated. The Co $2p_{3/2}$ binding energy values of 780.2 and 780.5 eV for $La_{1.5}Sr_{0.5}Co_{0.5}Ni_{0.5}O_4$ and $La_{1.5}Sr_{0.5}Co_{0.5}Ni_{0.5}O_{3.70}$, are in good agreement with the data recently reported for related Co-containing materials

[36]. The shoulders observed at the higher energy side of the $2p_{3/2}$ and Co $2p_{1/2}$ transitions for $La_{1.5}Sr_{0.5}Co_{0.5}Ni_{0.5}O_{3.70}$ are believed to be due to satellite structures characterizing high spin Co^{2+} in this material. These peaks are less intense in $La_{1.5}Sr_{0.5}Co_{0.5}Ni_{0.5}O_4$. The significant shift of the Co $2p_{1/2}$ peak to lower energies in this material gives lower Co $2p_{3/2}$ and Co $2p_{1/2}$ separation than that observed in $La_{1.5}Sr_{0.5}Co_{0.5}Ni_{0.5}O_{3.70}$. These results are consistent with presence of Co^{2+} and Co^{3+} in $La_{1.5}Sr_{0.5}Co_{0.5}Ni_{0.5}O_{3.70}$ and $La_{1.5}Sr_{0.5}Co_{0.5}Ni_{0.5}O_4$, respectively [37-40]. However, for $La_{1.5}Sr_{0.5}Co_{0.5}Ni_{0.5}O_4$, the Co $2p_{3/2}$ peak is relatively broad and the intensity of the Co $2p_{1/2}$ peak is significantly decreased with a slight diffusion in the higher energy side. This can be attributed to peak shift associated with presence of some Co^{2+} in this material [41-43].

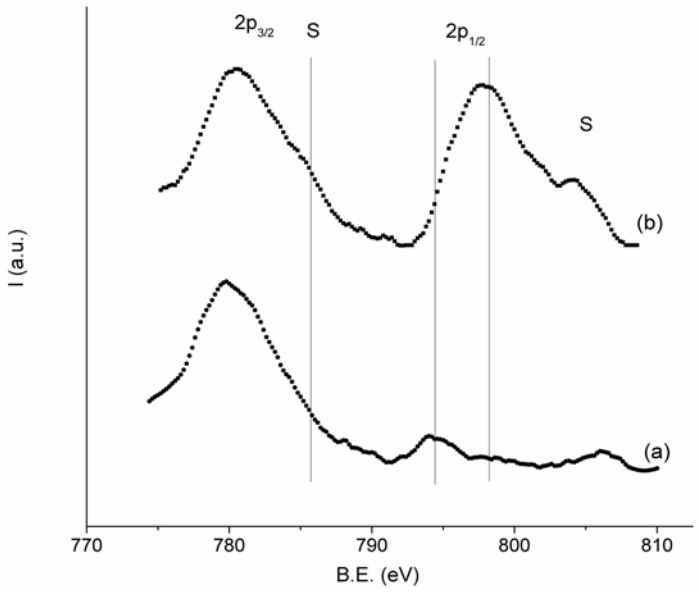

Figure 5.5 Cobalt 2p XPS for (a) $La_{1.5}Sr_{0.5}Co_{0.5}Ni_{0.5}O_4$ and (b) $La_{1.5}Sr_{0.5}Co_{0.5}Ni_{0.5}O_{3.7}$, showing the $2p_{1/2}$, $2p_{3/2}$ and satellite (s) peaks.

5.8 Discussion of $La_{1.5+x}Sr_{0.5-x}Co_{0.5}Ni_{0.5}O_{4\pm\delta}$

The overall stoichiometries of the studied materials were determined by NPD as $La_{1.7}Sr_{0.3}Co_{0.5}Ni_{0.5}O_{4.08}$, $La_{1.5}Sr_{0.5}Co_{0.5}Ni_{0.5}O_4$ and $La_{1.5}Sr_{0.5}Co_{0.5}Ni_{0.5}O_{3.70}$. Oxygen stoichiometry suggests the mixed B-site oxidation state $(Co/Ni)^{2+/3+}$ for $La_{1.5}Sr_{0.5}Co_{0.5}Ni_{0.5}O_4$. The XPS data are consistent with the predominance of Co^{3+} (and Ni^{2+}) in this material. The material is stoichiometric in oxygen. $La_2NiO_{4+\delta}$, in contrast, has been shown to exhibit a wide range of oxygen hyperstoichiometry associated with partial oxidation of Ni^{2+} to Ni^{3+} [44,45]. The trend to incorporate interstitial oxygen in $La_2NiO_{4+\delta}$ is generally reduced by strontium doping and the preferential oxidation of Ni^{2+} to Ni^{3+} [46,47]. Absence of oxygen hyperstoichiometry in $La_{1.5}Sr_{0.5}Co_{0.5}Ni_{0.5}O_4$ is therefore consistent with this trend. Reduction of the strontium content, however, allows hyperstoichiometry to be achieved in $La_{1.7}Sr_{0.3}Co_{0.5}Ni_{0.5}O_{4.08}$. Compared with $La_{1.5}Sr_{0.5}Co_{0.5}Ni_{0.5}O_4$, the hypothetical composition $La_{1.7}Sr_{0.3}Co_{0.5}Ni_{0.5}O_4$ contains more M^{2+} ions and the excess oxygen content in $La_{1.7}Sr_{0.3}Co_{0.5}Ni_{0.5}O_{4.08}$ suggests oxidation of some M^{2+} to M^{3+} to provide charge balance for the excess oxygen. Despite the presence of some Co^{2+} in the stoichiometric forms of the related materials $La_{1.2}Sr_{0.8}Co_{0.5}M_{0.5}O_{4+\delta}$ (M = Fe, Mn), it has been found that the excess-oxygen insertion is induced by the tendency of the non-cobalt ions (Fe^{3+} and Mn^{3+}) to be oxidized under applied conditions (*e.g.* Mn^{3+} to Mn^{4+}) (chapters 3 and 4). These observations may indicate a role of Ni^{2+}/Ni^{3+} states to induce hyperstoichiometry in this material.

Regarding the presence of $(Co/Ni)^{2+/3+}$ state in $La_{1.5}Sr_{0.5}Co_{0.5}Ni_{0.5}O_4$, the reduction behaviour of this material then suggests the total reduction of the trivalent ions to the divalent state (*i.e.*, Ni^{2+} and Co^{2+}) followed by formation of some M^{1+} ions in order to reach the nominal oxygen stoichiometry in $La_{1.5}Sr_{0.5}Co_{0.5}Ni_{0.5}O_{3.70}$. The formation of Co^{2+}

in this material is supported by XPS measurements. Ni^{1+} has been previously obtained in related systems under controlled reduction in H_2 atmosphere [22,23]; however, there is no evidence of formation of Co^{1+}, for example in $LaSrCo_{0.5}Fe_{0.5}O_{4-\delta}$ (chapter 3), under similar reduction conditions. Ni^{1+} is therefore assumed to be formed in $La_{1.5}Sr_{0.5}Co_{0.5}Ni_{0.5}O_{3.70}$. The oxygen stoichiometry suggests reduction of 20% of Ni^{2+} into Ni^{1+} in this material. The anisotropic displacement of axial oxygen in $La_{1.5}Sr_{0.5}Co_{0.5}Ni_{0.5}O_{3.70}$ is consistent with formation of Ni^{1+}, a known d^9 Jahn-Teller ion. According to Goodenough-Kanamori rules for super-exchange interactions [48,49], a combination of high spin Co^{2+} and Ni^{2+} ions would result in AFM interactions, and $La_{1.5}Sr_{0.5}Co_{0.5}Ni_{0.5}O_{3.70}$ therefore shows a broad antiferromagnetic-like peak at about 50 K. However, no evidence of long-range order was observed in the low temperature NPD data of this material, which can be attributed to the presence of Ni^{1+} species. Ni^{1+} ions introduce a FM component of interactions to the system resulting in competing FM and AFM interactions which may participate to the observed spin-glass-like state.

Oxide ion vacancies in $La_{1.5}Sr_{0.5}Co_{0.5}Ni_{0.5}O_{3.70}$ are located within the equatorial planes of the K_2NiF_4-type structure with an associated twist of MO_x polyhedra around the *z* axis to equilibrate the required expansion and contraction of (Co/Ni)-O and (La/Sr)-O coordination spheres, respectively (see section 3.7). The effect of interstitial oxygen on the lattice parameters can also be examined by considering the refined structural data of $La_{1.7}Sr_{0.3}Co_{0.5}Ni_{0.5}O_{4.08}$ and $La_{1.5}Sr_{0.5}Co_{0.5}Ni_{0.5}O_4$. These materials provide a useful comparison since the B-site has approximately the same oxidation state. Two competing effects therefore influence the (La/Sr)-O coordination sphere in $La_{1.7}Sr_{0.3}Co_{0.5}Ni_{0.5}O_{4.08}$, compared with that in $La_{1.5}Sr_{0.5}Co_{0.5}Ni_{0.5}O_4$: a contraction due to the higher La/Sr ratio and an expansion due to the increased coordination number related to the interstitial oxygen.

The latter effect seems to dominate with a more pronounced effect in the *xy* plane, leading to expansion in *a* but an almost negligible change in *c* (*Table 5.1*).

Conductivity data show that the materials are semiconductors with no evidence of a semiconductor-metal transition in the studied temperature range. Goodenough *et al.* suggested a localized-electron to itinerant-electron transition among the antibonding σ* electrons to account for the semiconductor-metal transition observed in $La_2NiO_{4+\delta}$ [5,6]. They showed that the thermal activation energy $E_g = 53$ meV$\approx kT_{Transition}$ found for the conductivity of $La_2NiO_{4+\delta}$ phases [3] is characteristic of the localized-electron to itinerant-electron transition. At lower temperature, the electron hopping is reduced further by small polaron formation; at higher temperatures, a *k*T greater than E_g puts the mobile electrons or holes in the threshold of itinerant character [6]. The significantly higher activation energies (296 and 338 meV) observed here for $La_{1.5+x}Sr_{0.5-x}Co_{0.5}Ni_{0.5}O_{4\pm\delta}$ may account for the absence of such transitions in these materials, and can be related to the heterogeneous nature of the M-O-M interactions in the basal plane (M = Co, Ni). An increase in the thermal activation energy is observed on cobalt doping in $La_2Ni_{1-x}Co_xO_{4+\delta}$ [35] and has been attributed to increasing the hopping length due to an increase of Co/Ni–O_{Basal} bond length on doping. A similar interpretation is used to account for the predominance of the semiconductive behaviour in highly doped $La_2Ni_{1-x}Co_xO_{4+\delta}$ phases [20]. The study here showed no evidence of M–O_{Basal} bond length elongation, compared with Ni–O_{Basal} in $La_2NiO_{4+\delta}$ (recently reported value is 1.9303(1) Å [47]), possibly because of strontium doping and having cobalt mainly in the trivalent state; the relatively higher activation energies can then be attributed to weaker M-O-M hopping interactions due to B-site doping with low spin Co^{3+}. The M–O_{Basal} bond lengths in $La_{1.5+x}Sr_{0.5-x}Co_{0.5}Ni_{0.5}O_{4\pm\delta}$ are,

however, slightly larger than those in $La_{2-x}Sr_xNiO_{4+\delta}$ (M-O_{Basal} is 1.91818(4) and 1.9095(1) Å for $La_{1.5}Sr_{0.5}Co_{0.5}Ni_{0.5}O_4$ and $La_{1.5}Sr_{0.5}NiO_4$ [47], respectively).

The lower resistivity values observed for $La_{1.7}Sr_{0.3}Co_{0.5}Ni_{0.5}O_{4.08}$, compared with $La_{1.5}Sr_{0.5}Co_{0.5}Ni_{0.5}O_4$, can be attributed to the higher concentration of charge carriers in the former. Due to strontium doping, $La_{1.7}Sr_{0.3}Co_{0.5}Ni_{0.5}O_{4.08}$ may also bond excess oxygen more strongly than $La_2NiO_{4+\delta}$ [46]. The material reaches a SOFC-applicable conductivity level ($> 100\ \Omega^{-1}\ cm^{-1}$) *via* semiconductive behaviour and shows enhanced structural stability at elevated temperatures. These properties suggest good cathode behaviour of this material in SOFC applications.

The reduction behaviour of these materials is also interesting and suggests that relatively stable oxygen-deficient phases can be formed in this system with the introduction of oxide ion vacancies into the basal planes. This is not known for $La_2NiO_{4+\delta}$ or cobalt-doped phases which are normally reduced in two steps, where one step corresponds to loss of excess-oxygen and the second step is the complete decomposition into the constituent La_2O_3 and Ni/Co phases [13]. The materials studied here withstand reducing conditions (10% H_2/N_2) up to 800 °C with formation of Ni^{1+}-containing phases *e.g.* $La_{1.5}Sr_{0.5}Co_{0.5}Ni_{0.5}O_{3.70}$.

5.9 Preliminary tests for SOFC applications

The oxygen-rich phase $La_{1.7}Sr_{0.3}Co_{0.5}Ni_{0.5}O_{4.08}$ has promising structural, electronic and phase-stability properties to act as a cathode material in SOFCs. The material was therefore re-synthesized using a sol-gel method (see section 2.1.2) and tested for reactivity toward yttria-stabilized zirconia (YSZ), as one of the commonest SOFC electrolytes. Stevens *et al.* have recently studied the electrode properties and phase stability of $Ln_2NiO_{4+\delta}$ using YSZ as the electrolyte [17]. However, Skinner *et al.* have suggested better phase stability and electrode performance of $La_2NiO_{4+\delta}$-based materials with intermediate-temperature electrolytes such as gadolinia-doped ceria (GDC) and lanthanum-strontium-magnesium gallates (LSGM) [19,20]. Xia *et al.* have reported recently good cathode behaviour for composites consisting of $La_{1.2}Sr_{0.8}Co_{0.8}Ni_{0.2}O_{4+\delta}$ and GDC at 600 °C [50]. Mao *et al.* have also very recently studied the cathode behaviour of $La_2Ni_{0.8}Co_{0.2}O_{4+\delta}$ using SDC as electrolyte [51].

5.9.1 Sol-gel synthesis of $La_{1.7}Sr_{0.3}Co_{0.5}Ni_{0.5}O_{4+\delta}$

Powders of very fine microstructure or even nanostructure are often required in SOFC applications in order to provide a larger surface area for catalytic reactions at the electrodes. The oxygen-rich phase $La_{1.7}Sr_{0.3}Co_{0.5}Ni_{0.5}O_{4.08}$ was therefore re-synthesized using a sol-gel procedure in an attempt to improve its microstructure. Stoichiometric amounts of La_2O_3, $SrCO_3$, $Co(CH_3COO)_2.4H_2O$ and $Ni(CH_3COO)_2.4H_2O$ were dissolved in very dilute nitric acid. EDTA, dissolved in NH_3 solution, was then added to the mixture and followed by the addition of solid citric acid under stirring (mole ratio of total metal ions to EDTA and to citrate = 1 : 1 : 2). NH_4OH was used to adjust the pH value of the solution to a value > 7. With the evaporation of water at 90 °C, a transparent gel was

produced which was then heated in an electrical oven at 250 °C to convert to a solid precursor. Then the solidified precursor was calcined in air at 1100 °C for 18 h and slowly cooled to room temperature. The XRD pattern of the produced material was identical to be that of $La_{1.7}Sr_{0.3}Co_{0.5}Ni_{0.5}O_{4.08}$ previously prepared by solid state reactions, with no evidence of significant peak broadening. *Figure 5.6* shows the morphology of the two materials from SEM measurements. The material prepared by sol-gel method shows significant reduction in particle-size with mean particle size of less than 1μm.

5.9.2 Phase reactivity with YSZ powders

Lanthanum-based perovskite cathode materials such as LSM are known to react with YSZ at high temperatures to form the insulating phase $La_2Zr_2O_7$, which acts as blocking interface between LSM and YSZ, leading to the increase of the polarization resistance. It is important therefore to test the chemical reactivity of the electrode materials with electrolyte with respect to long-term performance. In order to test the long-term reactivity of $La_{1.7}Sr_{0.3}Co_{0.5}Ni_{0.5}O_{4+\delta}$ with YSZ, powders of the materials were intimately mixed together (1 : 1 molar ratio) and heated at different temperatures (500-800 °C) for prolonged times (up to two weeks). *Figure 5.7* shows the XRD pattern of the mixture after heating at 800 ºC for 12 days. No evidence of reaction between phases is observed which reflects good stability of the compound at these conditions. However, sintering at temperatures higher than 1000 ºC for a few hours resulted in the formation of traces of $La_2Zr_2O_7$ (see inset in *Figure 5.7*). A sintering temperature not greater than 1000 ºC and an operating temperature up to 800 ºC are therefore suggested for the $La_{1.7}Sr_{0.3}Co_{0.5}Ni_{0.5}O_{4+\delta}$-YSZ system.

(a)

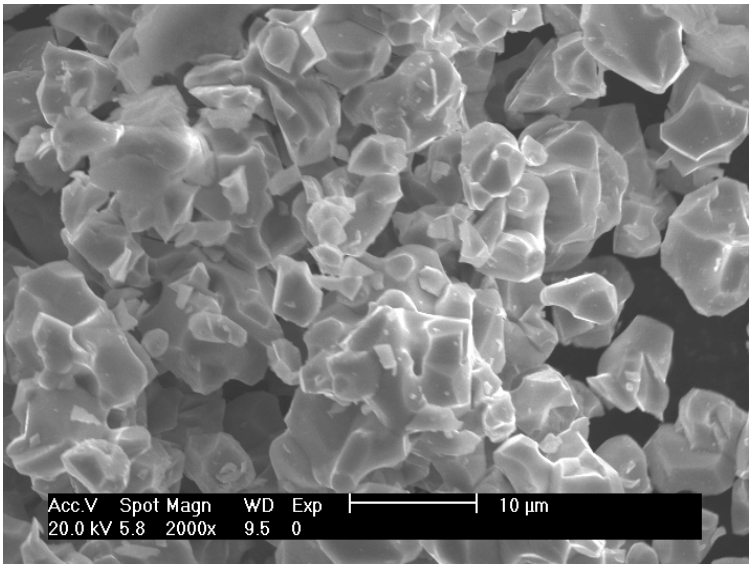

(b)

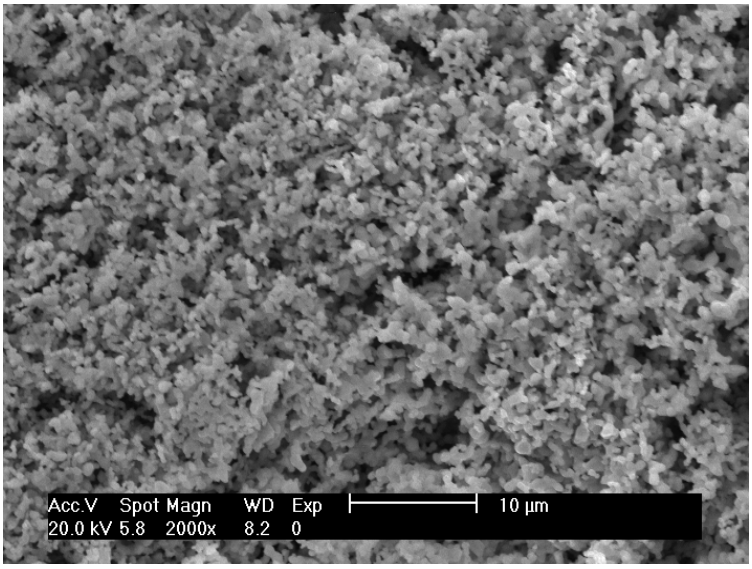

Figure 5.6 Morphology of $La_{1.7}Sr_{0.3}Co_{0.5}Ni_{0.5}O_{4+\delta}$ synthesized by (a) solid state reactions, and by (b) sol-gel method.

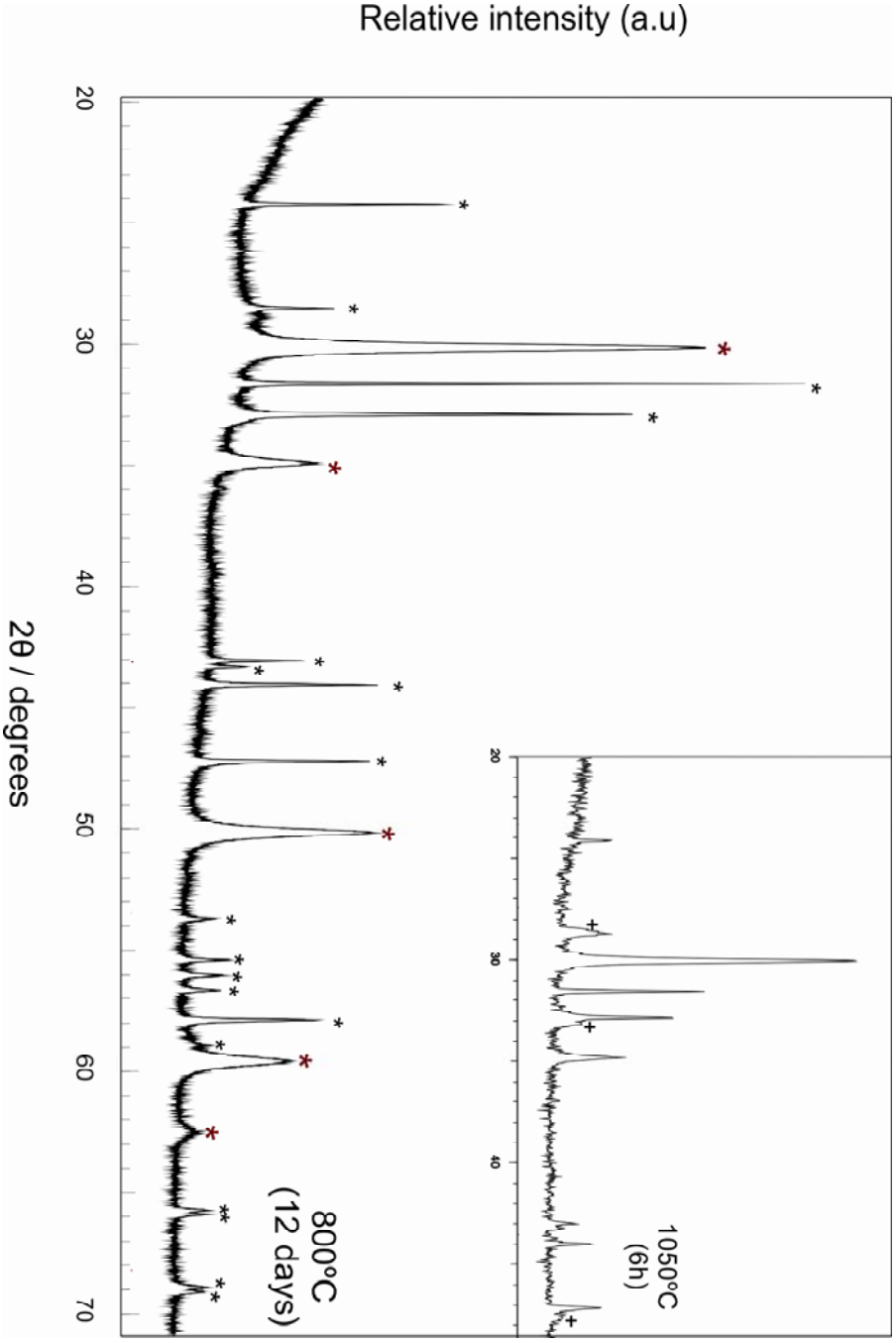

Figure 5.7 XRD results of $La_{1.7}Sr_{0.3}Co_{0.5}Ni_{0.5}O_{4+\delta}$/YSZ mixture (1:1) sintered in air at 800ºC for 12 days and at 1050ºC for 6h (inset): (*) $La_{1.7}Sr_{0.3}Co_{0.5}Ni_{0.5}O_{4+\delta}$ (black); (*) YSZ (red); (+) $La_2Zr_2O_7$.

5.10 References

[1] F. Prado, T. Armstrong, A. Caneiro, A. Manthiram, *J. Electrochem. Soc*. **148** (2001) J7.

[2] P. Ganguly, C. N. R. Rao, *Mater. Res. Bull*. **8** (1973) 405.

[3] K. K. Singh, P. Ganguly, J. B. Goodenough, *J. Solid State Chem*. **52 (**1984) 254.

[4] C. N. R. Rao, D. J. Buttrey, N. Otsuka, P. Ganguly, H. R. Harrison, C. J. Sandberg, J. M. Honig, *J. Solid State Chem.* **51** (1984) 266.

[5] J. B. Goodenough, S. Ramasesha, *Mater. Res. Bull*. **17** (1982) 383.

[6] J. B. Goodenough, *J. Less-common Met.* **116** (1986) 83.

[7] P. Odier, J. M. Bassat, J. C. Rifflet, J. P. Loup, *Solid State Commun*. **85** (1993) 561.

[8] J. M. Bassat, P. Odier, J. P. Loup, *J. Solid State Chem.* **110** (1994) 124.

[9] S. J. Skinner, J. A. Kilner, *Solid State Ionics* **135** (2000) 709.

[10] L. Minervini, R. W. Grimes, J. Kilner, K. E. Sickafus, *J. Mater. Chem*. **10** (2000) 2349.

[11] V. V. Kharton, A. P. Viskup, E. N. Naumovich, F. M. B. Marques, *J. Mater. Chem.* **9** (1999) 2623.

[12] V. V. Vashook, I. I. Yushkevich, L. V. Kokhanovsky, L. V. Makhnach, S. P. Tolochko, I. F. Kononyuk, H. Ullmann, H. Altenburg, *Solid State Ionics* **119** (1999) 23.

[13] C. K. M. Shaw, J. A. Kilner, *Solid State Ionics* **154-155** (2002) 523.

[14] C. N. Munnings, S. J. Skinner, G. Amow, P. S. Whitfield, I. J. Davidson, *Solid State Ionics* **176** (2005) 1895.

[15] E. Boehm, J. M. Bassat, P. Dordor, F. Mauvy, J. C. Grenier, P. H. Stevens, *Solid State Ionics* **176** (2005) 2717.

[16] V. Vashook, J. Zosel, T. Wen, U. Guth, *Solid State Ionics* **177** (2006) 1827.

[17] F. Mauvy, C. Lalanne, J. M. Bassat, J. C. Grenier, H. Zhao, L. Huo, P. Stevens, *J. Electrochem. Soc.* **153** (2006) A1547.

[18] G. Amow and I. J. Davidson (2005) In: Singhal SC, Misuzaki J (eds) SOFC-IX, vol 2005–007. Electrochemical Society, Quebec City, Quebec, Canada, p 1745.

[19] G. Amow, P. S. Whitfield, I. J. Davidson, R. P. Hammond, C. N. Munnings, S. J. Skinner, *Ceramic international* **30 (**2004) 1635.

[20] G. Amow, S. J. Skinner, *J. Solid State Electrochem*. **10** (2006) 538.

[21] A. A. Yaremchenko, V. V. Kharton, M. V. Patrakeev, J. R. Frade, *J. Mater. Chem.* **13 (**2003) 1136.

[22] M. Crespin, J. M. Bassat, P. Odier, P. Mouron, J. Choisnet, *J. Solid State Chem*. **84** (1990) 165.

[23] M. Crespin, C. Landron, P. Odier, J. M. Bassat, P. Mouron, J. Choisnet, *J. Solid State Chem*. **100** (1992) 281.

[24] P. H. Labbe, M. Ledesert, V. Caignaert, B. Raveau, *J. Solid State Chem*. **91** (1991) 362.

[25] M. A. Hayward, M. J. Rosseinsky, *Chem. Mater.* **12** (2000) 2182.

[26] J. D. Jorgensen, B. Dabrowski, Shiyou Pei, D. R. Richards, D. G. Hinks, *Phys. Rev. B* **40** (1989) 2187.

[27] R. A. Mohan Ram, P. Ganguly, C. N. R. Rao, *Mater. Res. Bull*. **23** (1988) 501.

[28] J. Rodriguez-Carvajal, M. T. Fernandez-Diaz, J. L. Martinez, *J. Phys.:Condens. Matter* **3** (1991) 3215.

[29] T. Freltoft, D. J. Buttrey, G. Aeppli, D. Vaknin, G. Shirane, *Phys. Rev. B* **44** (1991) 5046.

[30] K. Sreedhar, C. N. R. Rao, *Mater. Res. Bull*. **25** (1990) 1235.

[31] N. F. Mott and E. A. Davis, Electronic Processes in Noncrystalline Materials, Oxford University Press, 1979.

[32] D. Emin, T. Holstein, *Ann. Phys. (NY)* **53** (1969) 439.

[33] Y. Takeda, R. Kanno, M. Sakano, O. Yamamoto, M. Takano, Y. Bando, H. Akinaga, K. Takita, J. B. Goodenough, *Mat. Res. Bull.* **25** (1990) 293.

[34] K. Sreedhar, J. M. Honig, *J. Solid State Chem*. **111** (1994) 147.

[35] S. Nishiyama, D. Sakaguchi, T. Hattori, *Solid State Commun*. **94** (1995) 279.

[36] I. Alvarez-Serrano, G. J. Cuello, M. L. Lopez, A. Jimenez-Lopez, C. Pico, E. Rodrıguez-Castellon, E. Rodrıguez, M. L. Veiga, *J. Phys. D: Appl. Phys.* **41** (2008) 195001.

[37] J. van Elp, J. L. Wieland, H. Eskes, P. Kuiper, G. A. Sawatzky, F. M. F. de Groot, T. S. Turner, *Phys. Rev. B* **44** (1991) 6090.

[38] T. Mizokawa, L. H. Tjeng, P. G. Steeneken, N. B. Brookes, I. Tsukada, T. Yamamoto, K. Uchinokura, *Phys. Rev. B* **64** (2001) 115104.

[39] J. G. Kim, D. L. Pugmire, D. Battaglia, M. A. Langell, *Appl. Surf. Sci*. **165** (2000) 70.

[40] A. Foelske, H. H. Strehblow, *Surf. Interface Anal*. **34** (2002) 125.

[41] D. Briggs and M. P. Seah, Practical Surface Analysis, Wiley, New York, 1990.

[42] G. A. Carson, M. H. Nassir, M. A. Langell, *J. Vac. Sci. Techol*. **14** (1996) 9006.

[43] C. R. Brundle, T. J. Chuang, D.W. Rice, *Surf. Sci*. **60** (1976) 286.

[44] D. E. Rice, D. J. Buttrey, *J. Solid State Chem*., **105** (1993) 197.

[45] H. Tamura, A. Hayashi, Y. Ueda, *Physica C*, **216** (1993) 83.

[46] V. V. Vashook, S. P. Tolochko, I. I. Yushkevich, L. V. Makhnach, I. F. Kononyuk, H. Altenburg, J. Hauck, H. Ullmann, *Solid State Ionics* **110** (1998) 245.

[47] A. Aguadero, M. J. Escudero, M. Perez, J. A. Alonso, V. Pomjakushim, L. Daza, *Dalton Trans*. **36** (2006) 4377.

[48] J. B. Goodenough, Magnetism and the Chemical Bond, Interscience, New York, 1963.

[49] J. Kanamori, *J. Phys. Chem. Solids* **10** (1959) 87.

[50] F. Zhao, X. Wang, Z. Wang, R. Peng, C. Xia, *Solid State Ionics* **179** (2008) 1450.

[51] J. Huang, R. Gao, Z. Mao, J. Feng, *Int. J. Hydrogen Energy*, doi:10.1016/j.ijhydene.2009.04.022.

CHAPTER 6

Synthesis and characterization of $La_{1+x}Sr_{2-x}CoMnO_{7-\delta}$ (x = 0, 0.2)

6.1 Background

The variable oxidation state and coordination flexibility of cobalt in mixed B-site K_2NiF_4-type oxides have been shown to stimulate oxygen nonstoichiometry in these materials (chapters 3-5). With the B-site in these materials being half-doped with cobalt in the 3+/2+ state, *i.e.* $Co_{0.5}^{II/III}$-$M_{0.5}$, the materials have shown a wide range of oxygen nonstoichiometry under oxidizing and reducing conditions due to oxidation or reduction of cobalt ions (and the co-ion M). The structural features of oxygen nonstoichiometry, the magnetic and the electronic properties of these materials have been studied. The materials studied in this chapter have similar B-site states (half-doped with $Co^{3+(/2+)}$) but in a different structure, namely the n = 2 RP structure. The materials $La_{1+x}Sr_{2-x}CoMnO_{7-\delta}$ (x = 0, 0.2) have been synthesised and reduced in 10% H_2/N_2 in an attempt to induce oxygen deficiency in this double-layered system. The defect structure and the magnetic properties of these materials have been examined.

In the n = 1 RP phases, the oxide ion vacancies preferentially distribute within the MO_2 planes of the perovskite layers where the vacancies may be ordered [1-3] or disordered [4]. The oxygen-deficient materials characterized in chapters 3, 4 and 5 are examples of the latter case. A disordered distribution of vacancies within the equatorial MO_2 planes has also been reported for the n = 2 RP phase $Sr_3Mn_2O_{6.55}$ [5]. The O6 variant of this material ($Sr_3Mn_2O_6$) has been shown by Greaves *et al.* [6] to exhibit vacancy order within the MO_2 planes. Unlike the manganese-containing phases, the n = 2 RP phases containing cobalt and iron ($Sr_3M_2O_{7-\delta}$, M = Co, Fe [7-11]) systematically lose oxygen from

the apical sites linking the MO_6 octahedra giving rise to a square pyramidal coordination around the transition metal ions in the O6 phase [7,8]. The synthesis of $LaSr_2CoMnO_7$ by a standard ceramic method has recently been reported [12] and the structural and magnetic properties described. The O7 phases $LaSr_2CoMnO_7$ and $La_{1.2}Sr_{1.8}CoMnO_7$ are prepared here by a sol-gel technique and then reduced in H_2/N_2 atmosphere to the O6-like phases. The synthesis, structural and magnetic characterization of the O7-type phases $LaSr_2CoMnO_7$ and $La_{1.2}Sr_{1.8}CoMnO_7$, and of the O6-type materials $LaSr_2CoMnO_{6.18}$ and $La_{1.2}Sr_{1.8}CoMnO_{6.14}$ are discussed in this chapter.

6.2 Synthesis

The materials $LaSr_2CoMnO_7$ and $La_{1.2}Sr_{1.8}CoMnO_7$ were synthesized by a sol-gel procedure using La_2O_3 (previously dried at 800 °C), $SrCO_3$, $Co(CH_3COO)_2.4H_2O$ and $Mn(CH_3COO)_2.4H_2O$ as starting materials. Stoichiometric amounts of the starting materials were dissolved in acetic acid and boiled under reflux for 3 h. Small amounts of hydrogen peroxide and water were added and the mixture was further refluxed overnight to obtain a clear solution. This solution was evaporated to a dark violet gel which was then dried and heated in air at 400 °C. The resulting powder was pressed into pellets and calcined in flowing oxygen at 1350 °C for 18 h.

6.3 XRD and TGA study

XRD showed the as-prepared materials to be single-phase and to crystallize in the tetragonal *I4/mmm* space group with a structure related to that of $Sr_3Ti_2O_7$ [13] (*Figure 6.1 (a)*). No evidence of oxygen nonstoichiometry could be obtained from the XRD structural refinements and the oxide ion sites were therefore fixed at full occupancy

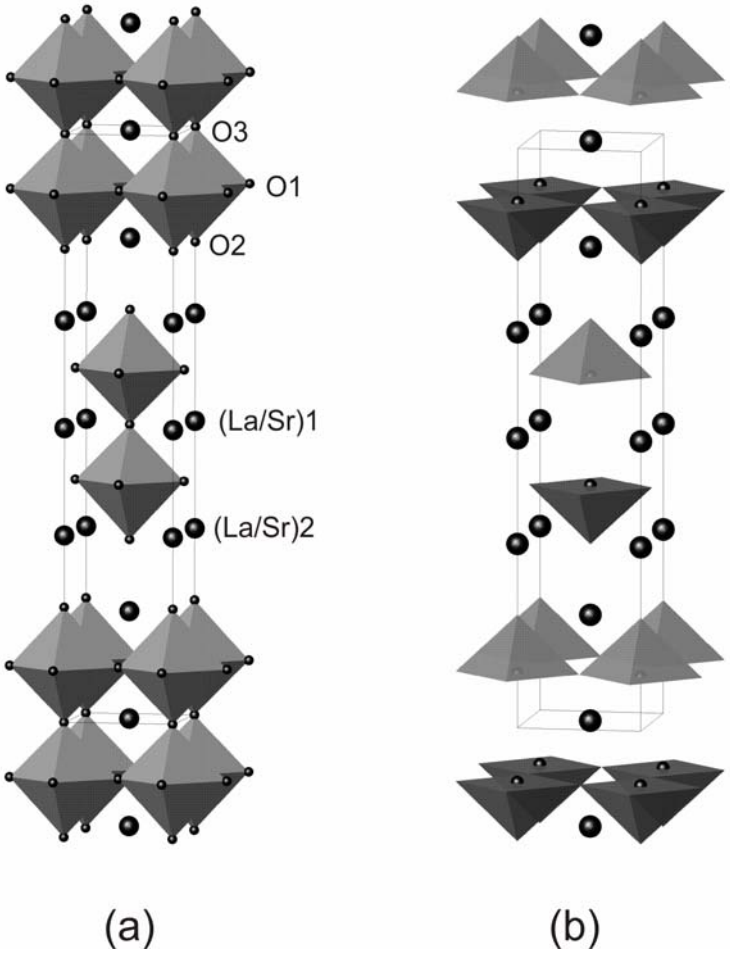

Figure 6.1 The n = 2 RP phases: (a) $La_{1+x}Sr_{2-x}CoMnO_7$, (b) $La_{1+x}Sr_{2-x}CoMnO_6$.

corresponding to the stoichiometries $LaSr_2CoMnO_7$ and $La_{1.2}Sr_{1.8}CoMnO_7$. The reduction behaviour of these materials was followed by TG measurements in which the materials were heated in flowing 10% H_2/N_2 (*Figure 6.2*). The measurements suggest that the materials loss oxygen in a stepwise fashion with retention of structure (as indicated by XRD) in the temperature range T ≈ 400-800 °C, followed by rapid decomposition to a n = 1 RP and other decomposition phases at T > 800 °C. The TG data suggest (assuming the as-prepared materials to be $LaSr_2CoMnO_7$ and $La_{1.2}Sr_{1.8}CoMnO_7$) the first-stage

reduction products to be $LaSr_2CoMnO_6$ and $La_{1.2}Sr_{1.8}CoMnO_6$. These phases were prepared on a large scale by heating the as-prepared materials in 10% H_2/N_2 at 700 °C for 12 h. The reduced phases have shown good stability in air at ambient temperature with no evidence of re-oxidation.

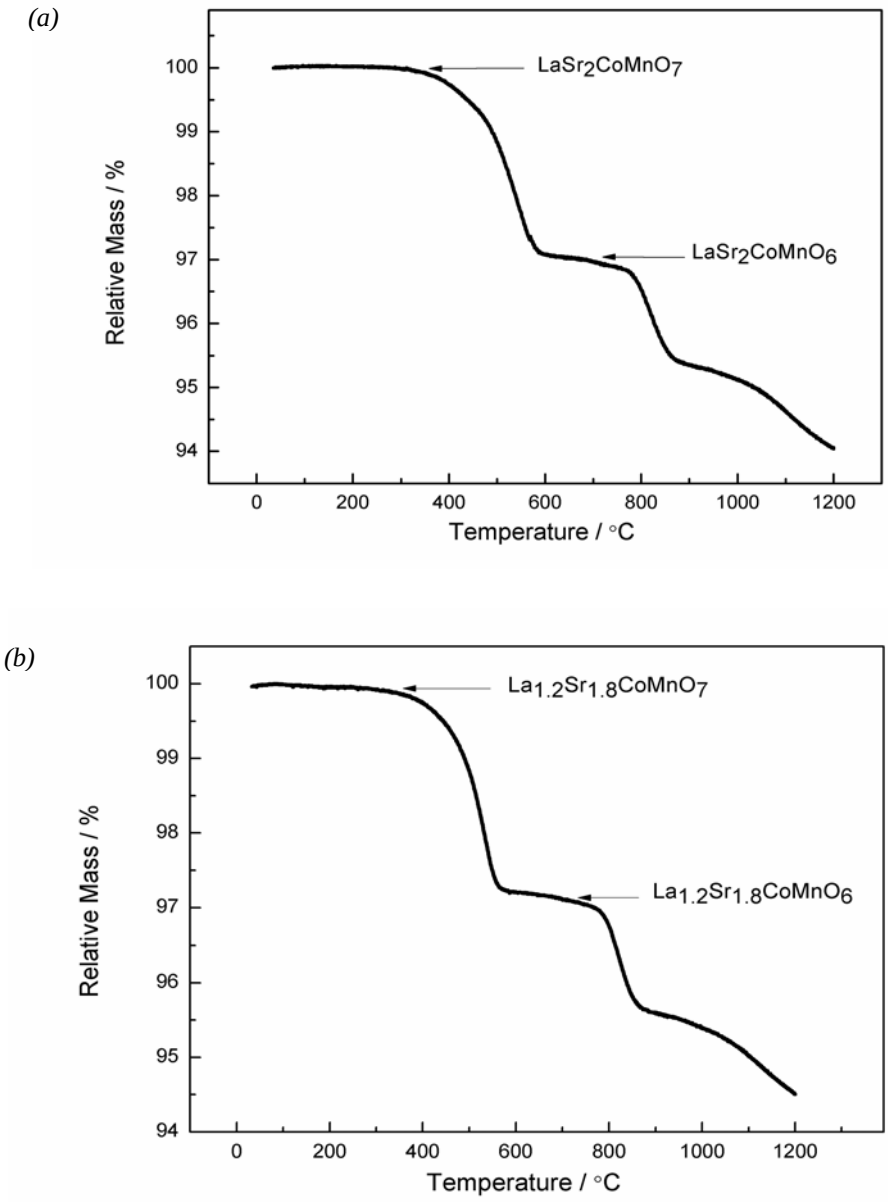

Figure 6.2 TG data for the reduction of the as-prepared materials using 10% H_2 in N_2.

6.4 Electron microscopy

ED data were recorded from the reduced materials in order to investigate the defect structure in these materials. The ED data recorded from the two reduced samples were identical. The data from one material ($LaSr_2CoMnO_6$) are given in *Figure 6.3*. The ED data from the reduced materials can be indexed using cell parameters of approximately a ≈ 3.9 Å and c ≈ 20.0 Å and show the reflection condition *hkl: h + k + l = 2n.* The very fine spots that are present on the [001] ED patterns at *h00: h = 2n+1* and

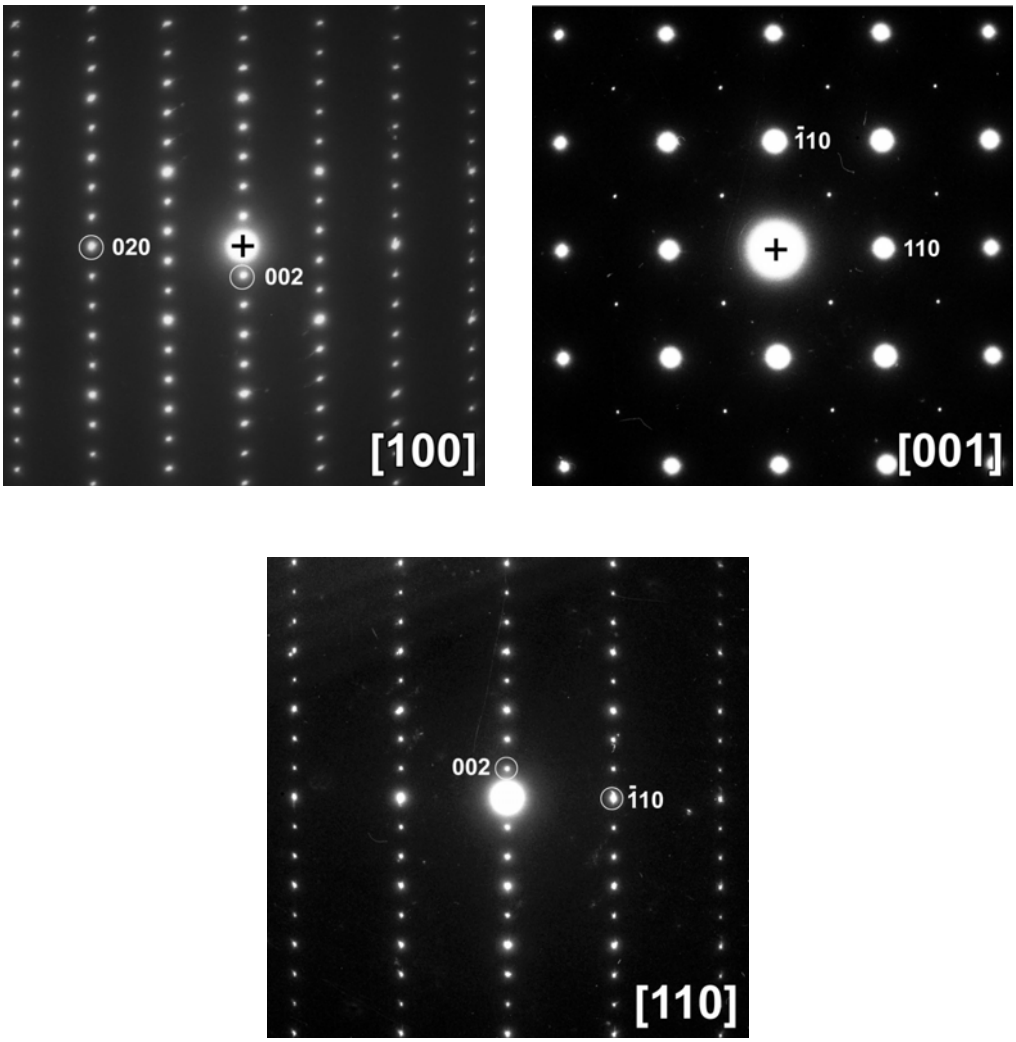

Figure 6.3 ED data recorded along the main zone axes of $LaSr_2CoMnO_6$.

0k0: k = 2n + 1 are due to the intersection of this pattern with weak streaks along the *c** axis at these positions. The streaks were present on only some of the [uv0] ED patterns and are due to an occasional local difference in *c* parameter that was also observed on the HREM images, probably due to small local changes in the oxygen stoichiometry. The cell parameters and the reflection condition are consistent with n = 2 RP-type structure (*I4/mmm* space group). The patterns clearly show that there is no superstructure. *Figure 6.4* shows a HRTEM image of the [100] zone of $LaSr_2CoMnO_6$. The HREM study confirmed the absence of long-range oxygen-vacancy order in these materials. On this image the projected atom columns correspond to the black dots. The block with zigzag contrast is the rock salt type block. The outline of one unit cell is indicated by a black rectangle.

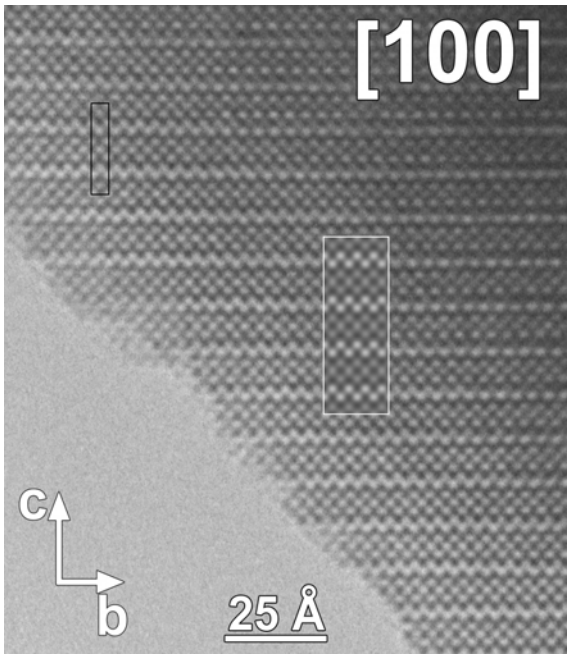

Figure 6.4 HRTEM image along [100] of $LaSr_2CoMnO_6$. The outline of one unit cell is indicated by a black rectangle. The white border shows the calculated HRTEM image using the refined model from NPD.

6.5 NPD and XANES studies

NPD data collected from the as-prepared and reduced samples at room temperature are shown in *Figure 6.5* (profile fits) and *Tables 6.1 and 6.2* (structural results). Rietveld profile refinements were performed using the ideal *I4/mmm* space group and the structural parameters of $Sr_3Ti_2O_7$ as a starting model. The refinement of oxygen sites occupancies in the oxygen-deficient materials located the vacancies on the O3 site (*Figure 6.1*) and showed that all other oxide ion sites were fully occupied. Variable occupancy of O3 and full occupancy of other oxide ion sites were therefore maintained throughout the refinement. NPD analysis confirmed the formulation of the studied materials as $LaSr_2CoMnO_7$, $La_{1.2}Sr_{1.8}CoMnO_7$, $LaSr_2CoMnO_{6.18(1)}$ and $La_{1.2}Sr_{1.8}CoMnO_{6.14(1)}$. The results therefore validate the thermogravimetric analysis. Unlike the situation in $Sr_3Mn_2O_6$ [6], oxide ion vacancies in $LaSr_2CoMnO_{6.18}$ and $La_{1.2}Sr_{1.8}CoMnO_{6.14}$ were confined to the apical O3 sites with no evidence of symmetry lowering due to vacancy order. The result is therefore consistent with the ED results. The calculated HRTEM image using the refined model from NPD is shown as an inset to *Figure 6.4* (white border) and shows an excellent agreement with the experimental image at focus value f = -100 Å and thickness t = 50 Å. The vacancy distribution in $LaSr_2CoMnO_{6.18}$ and $La_{1.2}Sr_{1.8}CoMnO_{6.14}$ is similar to that found in the O6 phases containing cobalt and iron [7,8] and suggests a square pyramidal coordination around cobalt and manganese ions (*Figure 6.1 (b)*). A square pyramidal coordination for cobalt and manganese ions has been observed in the oxygen-deficient perovskite $YBaCoMnO_5$ [14]. No evidence of cation order is observed in the NPD data of any sample. In contrast, cation order was observed in the NPD study of the double perovskite La_2CoMnO_6 [15].

6.5a)

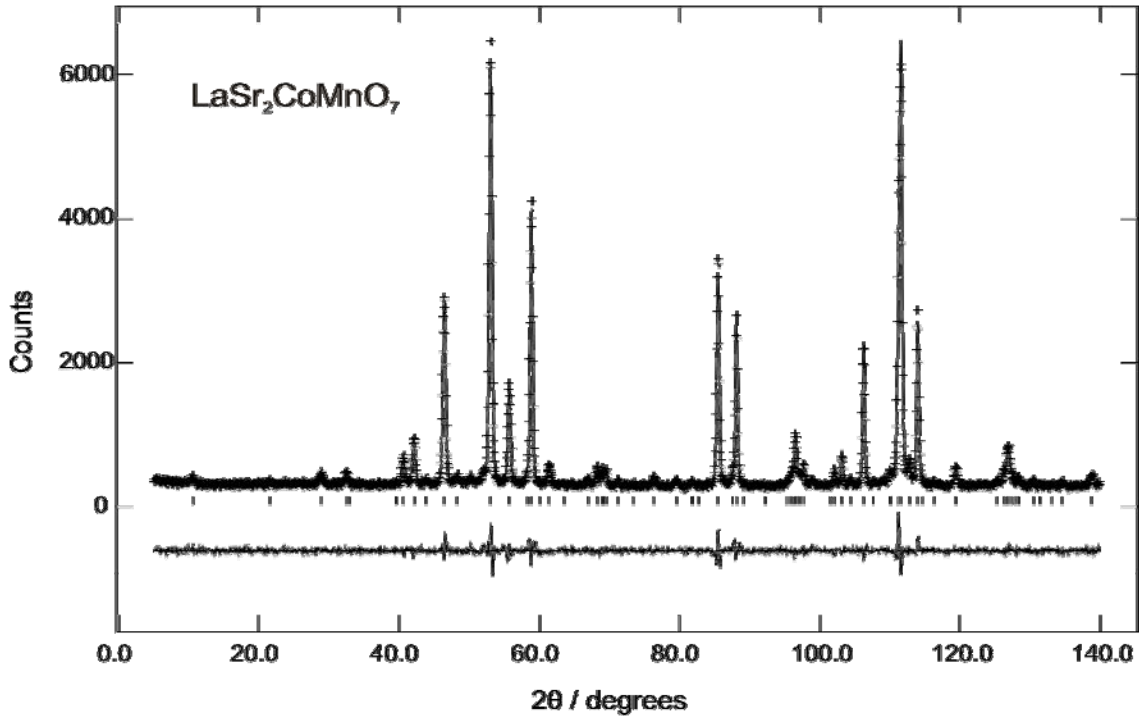
LaSr2CoMnO7
Counts
6000
4000
2000
0
0.0
20.0
40.0
60.0
80.0
100.0
120.0
140.0
2θ / degrees

6.5b)

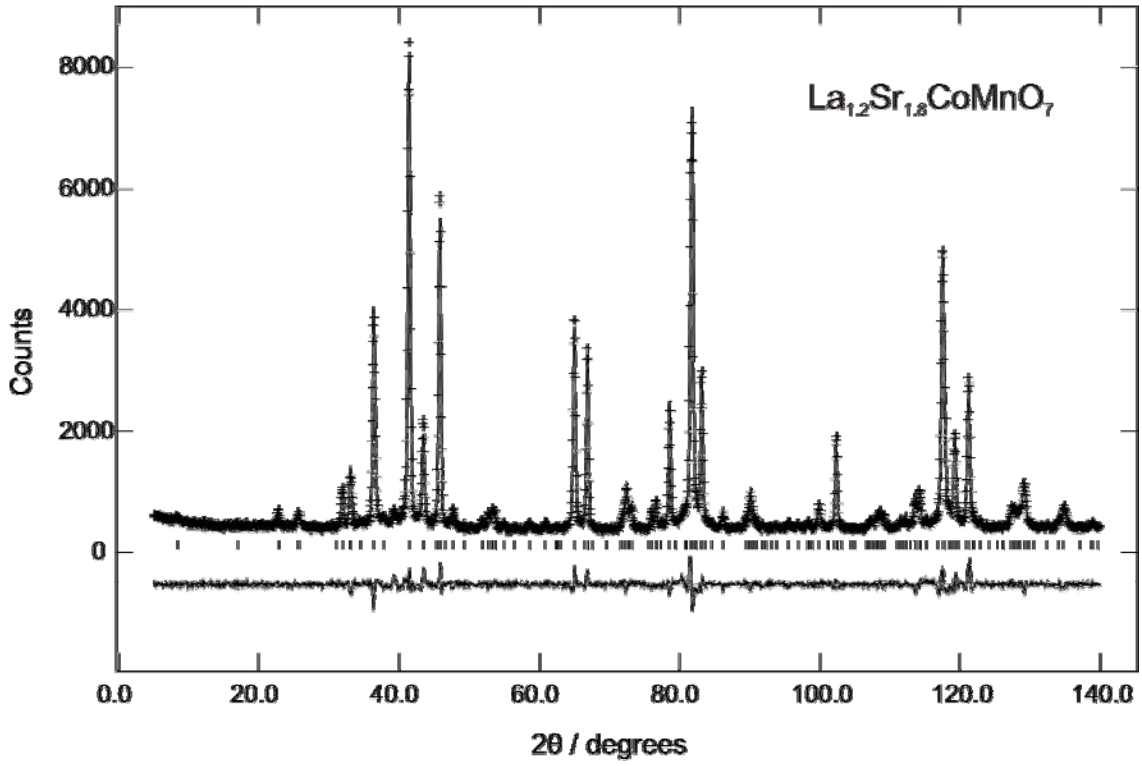
La1.2Sr1.8CoMnO7
Counts
8000
6000
4000
2000
0
0.0
20.0
40.0
60.0
80.0
100.0
120.0
140.0
2θ / degrees

6.5c)

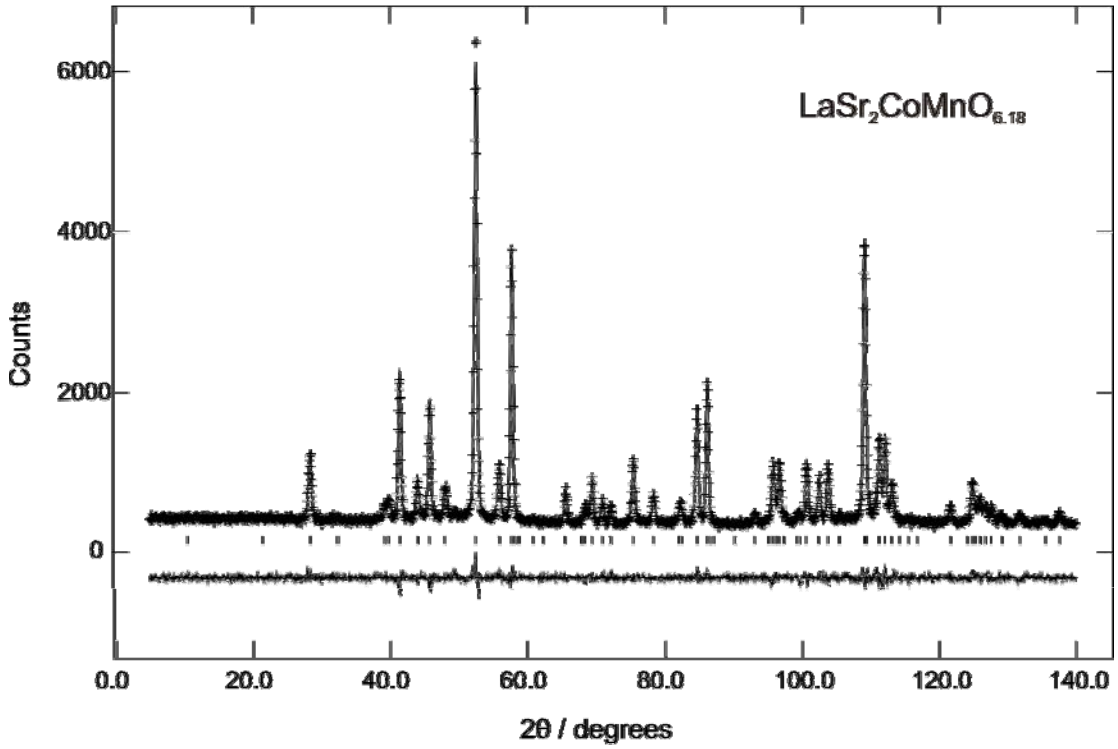

6.5d)

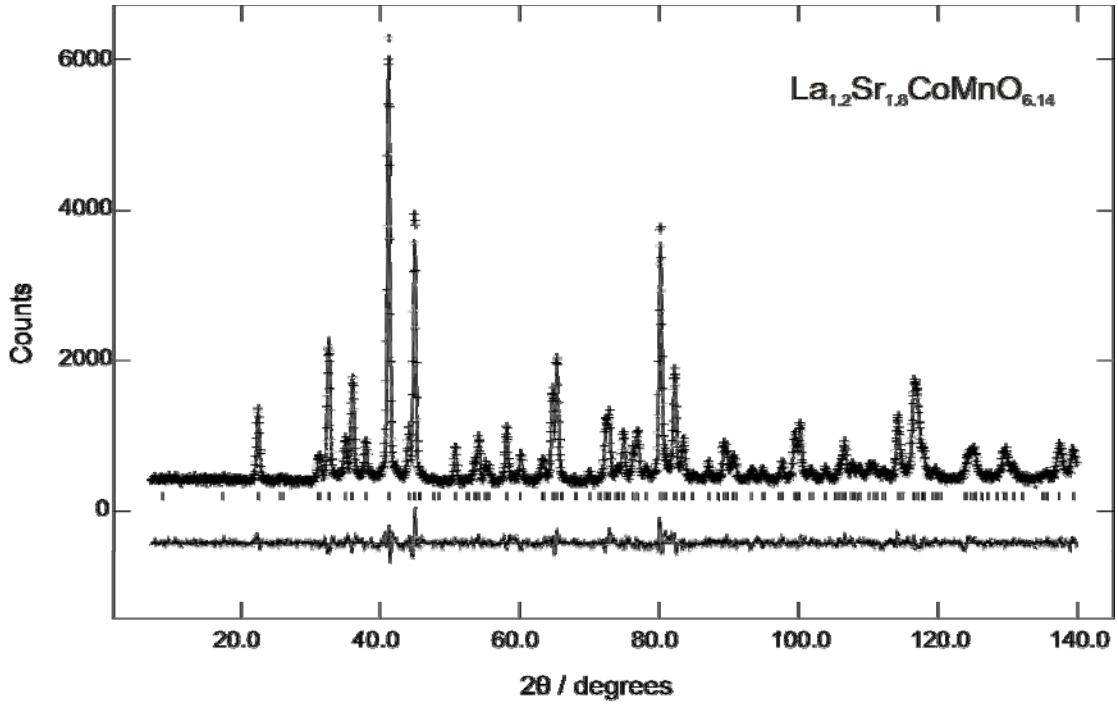

Figure 6.5 Observed, calculated and difference profiles for NPD data collected from different samples at room temperature.

Table 6.1 Structural results for the refinement of the NPD data collected from different samples at room temperature.

Atom	*x*	*y*	*z*	100 x Uiso (Å^2)	Occupancy	Site Symmetry
			$LaSr_2CoMnO_7$, *a* = 3.82785(5) Å; *c* = 20.1266(4) Å wRp = 0.0616; Rp = 0.0477; χ^2 = 1.819			
(La/Sr)1	0	0	0.5	0.67(8)	0.333/0.667	2b
(La/Sr)2	0	0	0.3176(1)	0.80(6)	0.333/0.667	4e
Co/Mn	0	0	0.091(1)	0.7(5)	0.5/0.5	4e
O1	0	0.5	0.0948(1)	0.82(4)*	1	8g
O2	0	0	0.1956(1)	0.82(4)*	1	4e
O3	0	0	0	0.82(4)*	1	2a
* U_{iso} constrained to be equal						
			$La_{1.2}Sr_{1.8}CoMnO_7$, *a* = 3.83262(5) Å; *c* = 20.1618(4) Å wRp = 0.0594; Rp = 0.0467; χ^2 = 2.449			
(La/Sr)1	0	0	0.5	0.27(6)	0.4/0.6	2b
(La/Sr)2	0	0	0.3172(1)	0.46(4)	0.4/0.6	4e
Co/Mn	0	0	0.093(1)	0.3(3)	0.5/0.5	4e
O1	0	0.5	0.0951(1)	0.73(3)*	1	8g
O2	0	0	0.1950(1)	0.73(3)*	1	4e
O3	0	0	0	0.73(3)*	1	2a
* U_{iso} constrained to be equal						
			$LaSr_2CoMnO_{6.18}$, *a* = 3.8948(2) Å; *c* = 20.042(1) Å wRp = 0.0518; Rp = 0.0405; χ^2 = 1.516			
(La/Sr)1	0	0	0.5	0.91(9)	0.333/0.667	2b
(La/Sr)2	0	0	0.31834(8)	0.82(8)	0.333/0.667	4e
Co/Mn	0	0	0.089(1)	0.0**	0.5/0.5	4e
O1	0	0.5	0.0841(1)	2.32(7)*	1	8g
O2	0	0	0.1986(1)	2.32(7)*	1	4e
O3	0	0	0	2.32(7)*	0.175(8)	2a
** negative U_{iso} constrained to zero						
* U_{iso} constrained to be equal						
			$La_{1.2}Sr_{1.8}CoMnO_{6.14}$, *a* = 3.9157(1) Å; *c* = 19.9139(8) Å wRp = 0.0604; Rp = 0.0475; χ^2 = 2.246			
(La/Sr)1	0	0	0.5	0.38(7)	0.4/0.6	2b
(La/Sr)2	0	0	0.3199(1)	0.93(5)	0.4/0.6	4e
Co/Mn	0	0	0.084(1)	0.0**	0.5/0.5	4e
O1	0	0.5	0.0832(1)	2.12(4)*	1	8g
O2	0	0	0.1994(2)	2.12(4)*	1	4e
O3	0	0	0	2.12(4)*	0.14(1)	2a
** negative U_{iso} constrained to zero						
* U_{iso} constrained to be equal						

Table 6.2 Selected bond lengths (Å) for the refined phases.

Bond	$LaSr_2CoMnO_7$	$La_{1.2}Sr_{1.8}CoMnO_7$	$LaSr_2CoMnO_{6.18}$	$La_{1.2}Sr_{1.8}CoMnO_{6.14}$
Co/Mn-O1	1.915(1)	1.9168(6)	1.950(1)	1.9579(2)
Co/Mn-O2	2.10(3)	2.06(2)	2.20(2)	2.30(2)
Co/Mn-O3	1.83(3)	1.87(2)	1.78(2)	1.67(2)
(La/Sr)1–O1	2.703(1)	2.711(1)	2.576(1)	2.565(2)
(La/Sr)1–O3	2.70670(3)	2.71007(4)	2.7540(2)	2.76881(7)

The Co- and Mn- K-edge XANES recorded from $LaSr_2CoMnO_7$ and $LaSr_2CoMnO_{6.18}$ are shown in *Figure 6.6*. The edge positions are collected in *Table 6.3*. The difficulty in ascertaining an edge position for the Co_2O_3 standard should be noted. The Co K- and Mn K- edge positions of $LaSr_2CoMnO_7$ both appear at higher energy than those of $LaSr_2CoMnO_{6.18}$. By comparison with the edge positions of the reference materials (*Table 6.3*) it would appear that cobalt and manganese in $LaSr_2CoMnO_7$ are present as Co^{3+} and Mn^{4+} (although the edge positions are at higher energy than those of the standards) and in $LaSr_2CoMnO_{6.18}$ as Co^{2+} and Mn^{4+}/Mn^{3+}. The data therefore provide an evidence of reduction of both cobalt and manganese, although comparison with the standards is relatively poor.

Table 6.3 X-ray absorption edge positions recorded from the X-ray absorption near-edge structure.

Compound	Co K-edge position (± 0.2)(eV)	Mn K-edge position (± 0.2)(eV)
CoO	7721.5	-
Co_2O_3	7722.0*	-
MnO	-	6543.4
Mn_2O_3	-	6547.2
MnO_2	-	6551.5
$LaSr_2CoMnO_7$	7724.3	6554.3
$LaSr_2CoMnO_{6.18}$	7721.5	6550.4

*plus two other maxima of almost equal intensity at 7718.2 and 7728.3 eV.

(a)

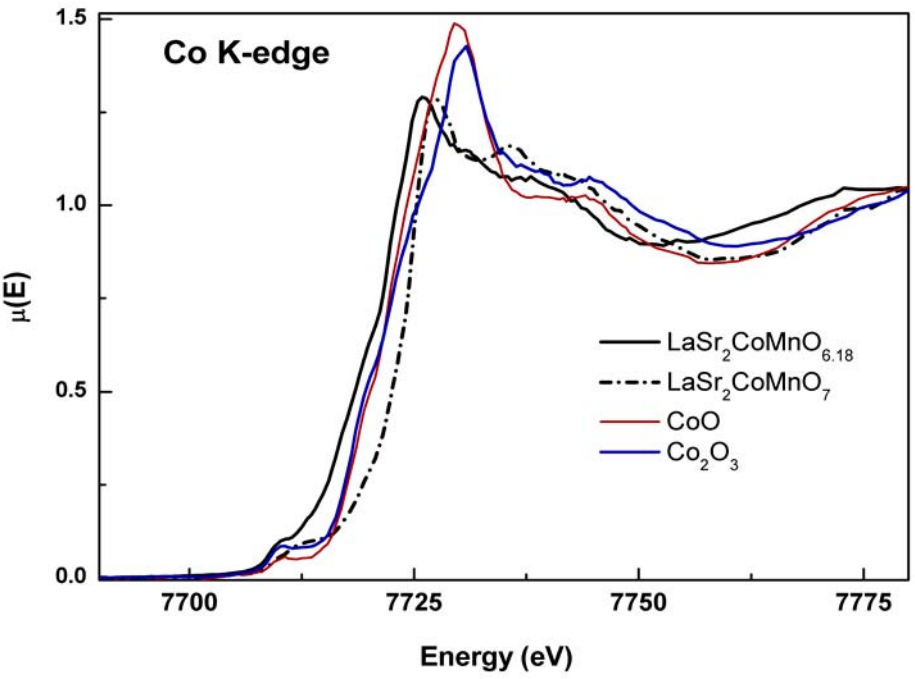

(b)

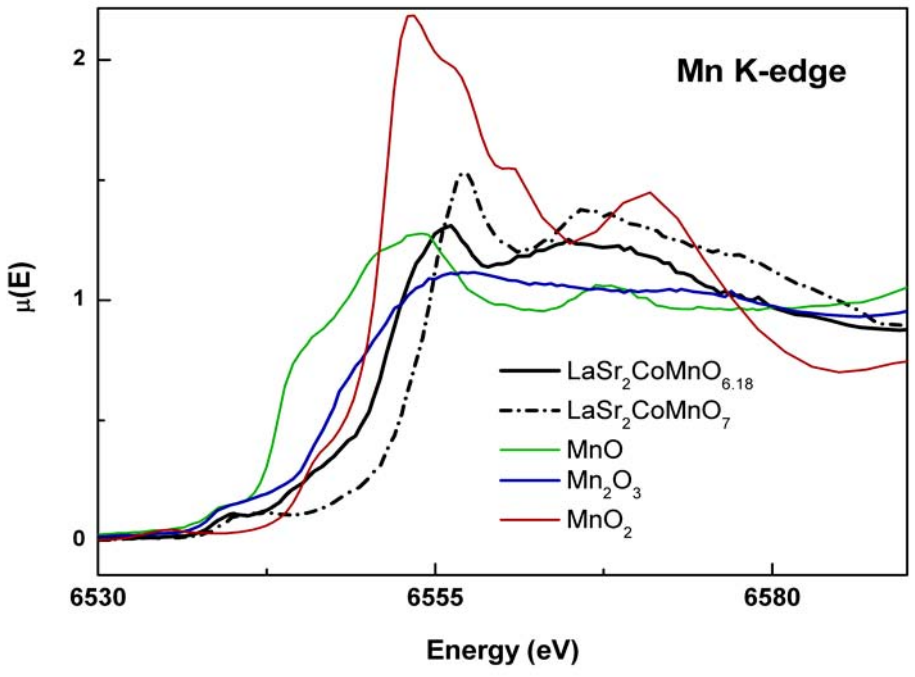

Figure 6.6 XANES recorded from $LaSr_2CoMnO_7$ and $LaSr_2CoMnO_{6.18}$: (a) Co K-edge and (b) Mn K-edge.

The oxygen stoichiometry suggests the B-site oxidation state $(Co/Mn)^{3+/4+}$ in $LaSr_2CoMnO_7$. In contrast to the B-site state $(Co/Mn)^{3+}$ in La_2CoMnO_6, the $(Co/Mn)^{3+/4+}$ state failed to give any evidence of cation order in the NPD or ED study of $LaSr_2CoMnO_7$. It has been reported that the B-site state $(Co/Mn)^{3+}$ exhibits order in the form of Co^{2+} and Mn^{4+} in La_2CoMnO_6. However, this order disappeared in the single-layered material $LaSrCo_{0.5}Mn_{0.5}O_4$ (chapter 4). The two-dimensional nature of $LaSr_2CoMnO_7$ and $La_{1.2}Sr_{1.8}CoMnO_7$ seems to inhibit a three-dimensional cation order in these materials. The XANES study indicates that $LaSr_2CoMnO_7$ contains a mixture of Mn^{4+} and Co^{3+}. The O7 to O6 reduction in this material suggests that Mn^{4+} and Co^3 ions are reduced to Mn^{3+} and Co^{2+}. The formation of a mixture of Mn^{2+} and Co^{3+} is chemically unfavoured [14] and is inconsistent with the XANES data. The Co^{2+}/Mn^{3+} state has been suggested for $YBaCoMnO_5$ [14] and $La_{2-x}Sr_xCo_{0.5}Mn_{0.5}O_{4-\delta}$ (chapter 4). The excess oxygen in the O6-type phase $LaSr_2CoMnO_{6.18}$ suggests that the reduction of Mn^{4+}-Co^{3+} to Mn^{3+}-Co^{2+} is not complete in this material. XANES data are consistent with presence of some Mn^{4+} in the reduced material. No evidence of local cation order could be observed in the ED study of $LaSr_2CoMnO_{6.18}$ which suggests that a Co^{2+}/Mn^{4+} state in this material is either disordered or ordered in the form of clusters containing few metal ions. $La_{1.2}Sr_{1.8}CoMnO_7$ may contain a mixture of $Mn^{4+}/Co^{3+}(Co^{2+})$ or $Mn^{4+}(Mn^{3+})/Co^{3+}$. However, the excess oxygen in the O6-type phase $La_{1.2}Sr_{1.8}CoMnO_{6.14}$ suggests that the reduction of Mn^{4+}-Co^{3+} to Mn^{3+}-Co^{2+} is approximately complete in this material.

The predominant reduction of Mn^{4+} and Co^{3+} to Mn^{3+} and Co^{2+} in the O6-type materials suggests an expansion in the M–O bonds. The NPD data show a general expansion of M–O1 and M–O2 bonds while the M–O3 bonds undergo significant contraction (*Table 6.2*). However, it should be noted that the O3 site has an occupancy of

only ~ 15% (*Table 6.1*) such that the M–O3 distance mainly reflects half the separation between M sites when the O3 site is empty. The true M–O3 distance is therefore uncertain. The reduction process was associated with an expansion in the *a* parameter and a contraction in the *c* parameter (*e.g.* $La_{1.2}Sr_{1.8}CoMnO_7$: *a* = 3.83262(5) Å, *c* = 20.1618(4) Å; $La_{1.2}Sr_{1.8}CoMnO_{6.14}$: *a* = 3.9157(1) Å; *c* = 19.9139(8) Å). Similar effects have been observed on the reduction of $Sr_3Fe_2O_7$ to $Sr_3Fe_2O_6$ [7]. This can be related to the coordination requirements of (La/Sr)1. Under reduction, a contraction in (La/Sr)1-O coordination sphere (achieved in the *z* direction, *i.e. c*) occurs due to removal of in-plane oxygen atoms (O3) and reduction of the coordination number from 12 to ~ 8. The apical contraction of the (La/Sr)1-O coordination sphere can be observed through the significant reduction of (La/Sr)1–O1 bond lengths (from 2.703(1) to 2.576(1) Å, for example, in $LaSr_2CoMnO_7$ and $LaSr_2CoMnO_{6.18}$, respectively).

6.6 Magnetic susceptibility

Figure 6.7 shows the temperature dependence of the magnetic susceptibilities of $LaSr_2CoMnO_7$ and $La_{1.2}Sr_{1.8}CoMnO_7$ in the temperature range 5-300 K. Plots of the reciprocal of the molar susceptibility against temperature for these materials (insets in *Figure 6.7*) suggest a non Curie-Weiss behaviour within this temperature range. However, the plots display a decreased gradient on cooling which suggests the predominance of FM interactions. The application of the Curie-Weiss law to the high temperature magnetic susceptibility data gives positive values of θ which is consistent with FM interactions. Above 200 K, the θ values are 33.06 and 46.23 K for $LaSr_2CoMnO_7$ and $La_{1.2}Sr_{1.8}CoMnO_7$, and the effective moments are 6.21 and 6.50 μ_B, respectively. The relatively high effective moments suggest a high spin state of Co^{3+} in these materials; the

effective moments are in good agreement with the theoretical spin-only values for high-spin Mn^{4+} and $Co^{3+}(Co^{2+})$ ions (6.24 and 6.10 μ_B for $LaSr_2CoMnO_7$ and $La_{1.2}Sr_{1.8}CoMnO_7$, respectively).

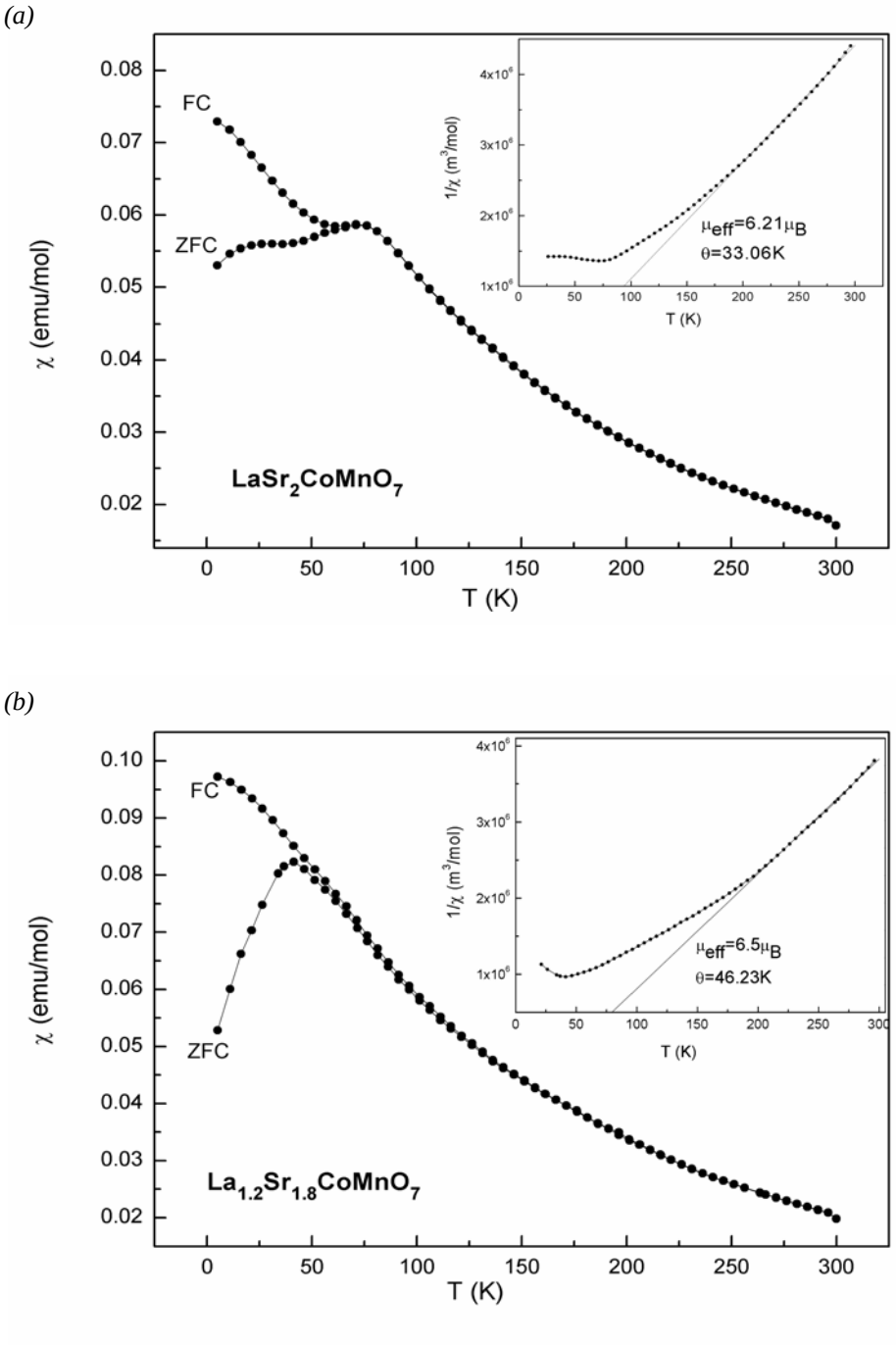

Figure 6.7 Variation of magnetic susceptibility (ZFC and FC) and the inverse magnetic susceptibilities (ZFC) with temperature for (a) $LaSr_2CoMnO_7$, (b) $La_{1.2}Sr_{1.8}CoMnO_7$.

A distinct divergence between ZFC and FC susceptibilities is indicative of spin glass transition in these materials with freezing temperatures of 50-70 K (see *Figure 6.7*). The spin glass state can be attributed to competitive FM and AFM interactions between disordered Mn^{4+} and Co^{3+} ions. The second cusp observed at lower temperature (~ 25 K) for $LaSr_2CoMnO_7$ can be related to a possible change in the spin state of Co^{3+} (to low or intermediate spin) [12]. This peak is, under applied conditions, invisible in case of $La_{1.2}Sr_{1.8}CoMnO_7$ probably because it contains a lower content of Co^{3+} ions (*i.e.* Co^{3+}/Co^{2+}). The spin glass behaviour in these materials has been confirmed by AC magnetic susceptibility measurements. The frequency dependence of the AC magnetic susceptibility of $La_{1.2}Sr_{1.8}CoMnO_7$ is shown in *Figure 6.8*. It is clearly seen that the location of the cusp at the freezing temperature is dependent on the frequency of the AC susceptibility measurement which is a characteristic feature of spin glasses. Moreover, the low temperature cusp is observed in this material under the AC conditions.

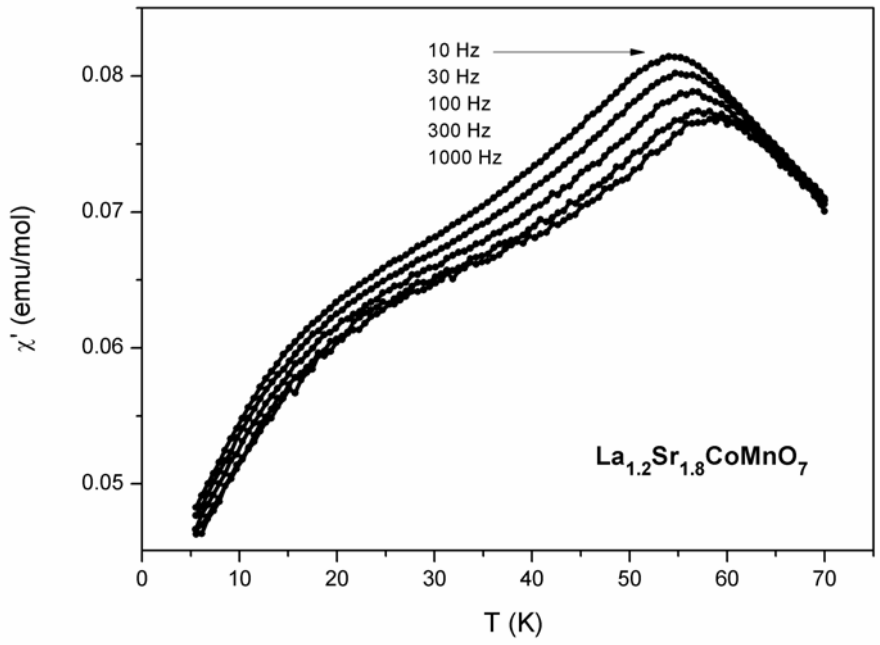

Figure 6.8 AC susceptibility data recorded from $La_{1.2}Sr_{1.8}CoMnO_7$.

The reduced materials $LaSr_2CoMnO_{6.18}$ and $La_{1.2}Sr_{1.8}CoMnO_{6.14}$ also show spin glass behaviour at low temperatures (*Figure 6.9*). This can be attributed to competitive FM and AFM interactions between high spin Mn^{3+} and Co^{2+} ions. The inverse susceptibility plots (see insets in *Figure 6.9*) show that the magnetic interactions are predominately AFM; however, no evidence of long-range magnetic order is observed in the low temperature NPD data. This is consistent with the magnetic behaviour of Mn^{3+} and Co^{2+} in related n = 1 RP phases (chapter 4). Above 200 K, the effective moments are 13.79 and 8.35 μ_B for $LaSr_2CoMnO_{6.18}$ and $La_{1.2}Sr_{1.8}CoMnO_{6.14}$, respectively. The significantly high effective moments (compared with the spin-only values, *e.g.* 6.24 μ_B per unit formula containing Co^{2+} and Mn^{3+}) are possibly due to presence of ferromagnetic clusters of ordered Co^{2+} and $Mn^{3+}(Mn^{4+})$ ions in these materials. Similar effect has been observed in the single-layered material $La_{1.2}Sr_{0.8}MnO_{4.27}$ [16].

6.9a)

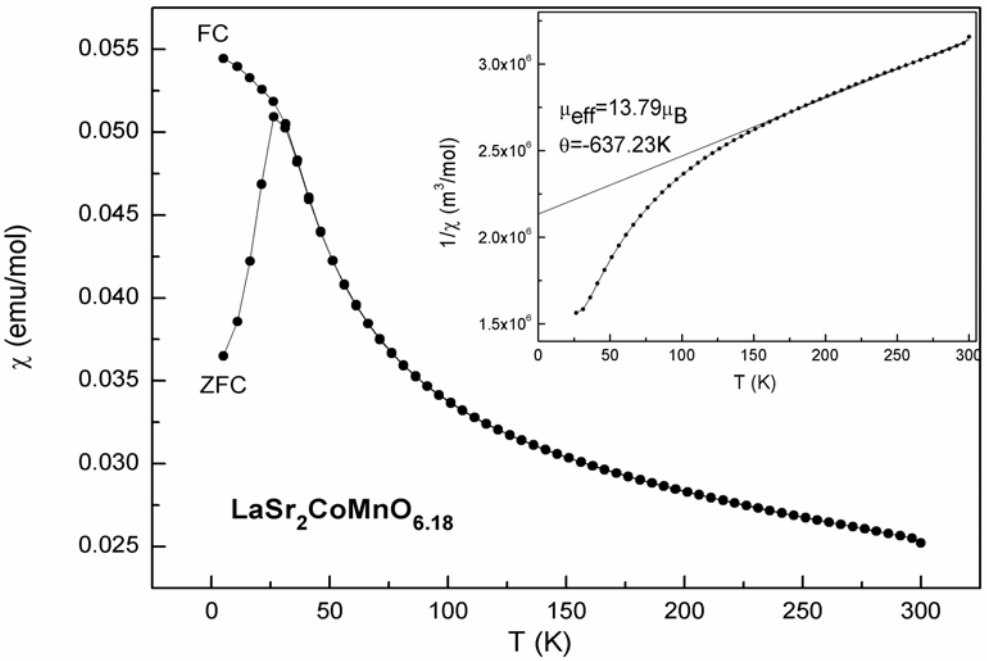

6.9b)

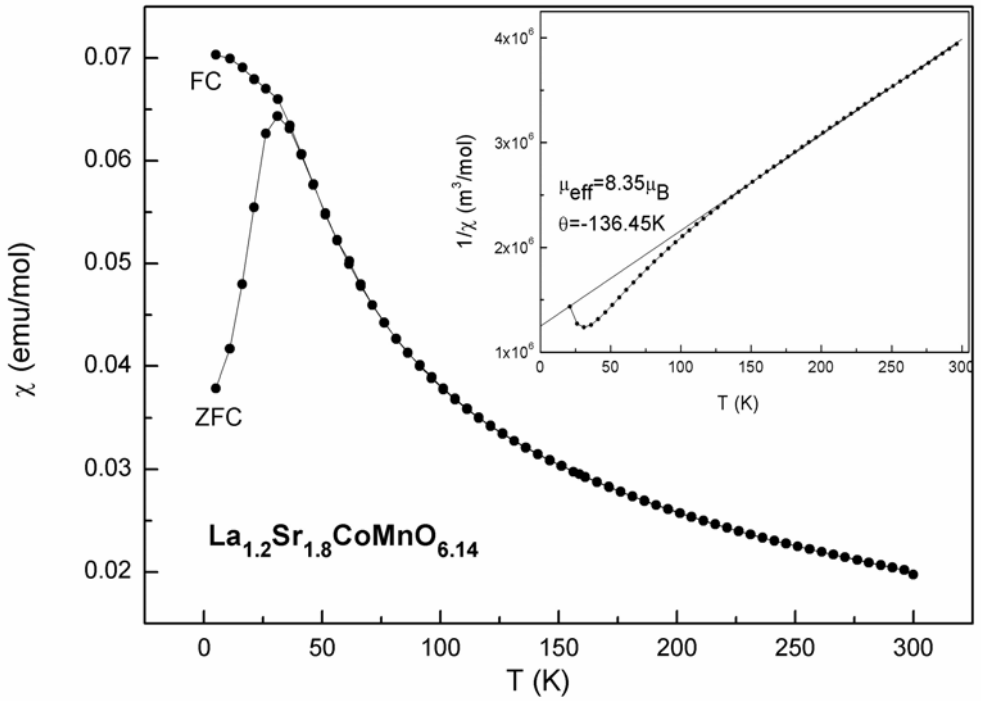

Figure 6.9 Variation of magnetic susceptibility (ZFC and FC) and the inverse magnetic susceptibilities (ZFC) with temperature for (a) $LaSr_2CoMnO_{6.18}$, (b) $La_{1.2}Sr_{1.8}CoMnO_{6.14}$.

6.7 References

[1] M. Crespin, J. M. Bassat, P. Odier, P. Mouron, J. Choisnet, *J. Solid State Chem.* **84** (1990) 165.

[2] M. Crespin, C. Landron, P. Odier, J. M. Bassat, P. Mouron, J. Choisnet, *J. Solid State Chem*. **100** (1992) 281.

[3] M. E. Leonowicz, K. R. Poeppelmeier, J. M. Longo, *J. Solid State Chem.* **59** (1985) 71.

[4] M. A. Hayward, M. J. Rosseinsky, *Chem. Mater.* **12** (2000) 2182.

[5] J. F. Mitchell, J. E. Millburn, M. Medarde, S. Short, J. D. Jorgensen, *J. Solid State Chem.* **141** (1998) 599.

[6] L. J. Gillie, A. J. Wright, J. Hadermann, G. Van Tendeloo, C. Greaves, *J. Solid State Chem.* **175** (2003) 188.

[7] S. E. Dann, M. T. Weller, D. B. Currie, *J. Solid State Chem*. **97** (1992) 179.

[8] S. E. Dann, M. T. Weller, *J. Solid State Chem*. **115** (1995) 499.

[9] J. M. Hill, B. Dabrowski, J. F. Mitchell, J. D. Jorgensen, *Phys. Rev. B* **74** (2006) 174417.

[10] L. Viciu, H.W. Zandbergen, Q. Xu, Q. Huang, M. Lee, R.J. Cava, *J. Solid State Chem*. **179** (2006) 500.

[11] Y. Bréard, C. Michel, M. Hervieu, F. Studer, A. Maignan, B. B. Raveau, *Chem. Mater.* **14** (2002) 3128.

[12] T. I. Chupakhina, G. V. Bazuev, *Russ. J. Inorg. Chem*. **53** (2008) 681.

[13] S. R. Ruddlesden, P. Popper, *Acta Crystallogr*. **10** (1957) 538; **11** (1958) 54.

[14] P. Karen, E. Suard, F. Fauth, P. M. Woodward, *Solid State Sciences* **6** (2004) 1195.

[15] C. L. Bull, D. Gleeson, K. S. Knight, *J. Phys.: Condens. Matter* **15** (2003) 4927.

[16] R. K. Li, C. Greaves, *J. Solid State Chem.* **153** (2000) 34.

CHAPTER 7

Synthesis and characterization of $LaSrCoFeO_6$, $LaSrCoFeO_5$, $LaSrCoFeO_5F$ and $LaSrCoFeO_{5.5}$

7.1 Background

The reduction of Co^{3+} to Co^{2+} in the mixed B-site materials $La_{2-x}Sr_xCo_{0.5}M_{0.5}O_{4-\delta}$ has been shown to stimulate different degrees of oxygen deficiency in these single-layered materials (chapters 3-5); oxygen vacancies were found to be disordered and confined to the equatorial planes of the structure. In the double-layered materials $La_{1+x}Sr_{2-x}CoMnO_{7-\delta}$, the reduction of Co^{3+}/Mn^{4+} to Co^{2+}/Mn^{3+} located the vacancy in the common apex of the double-layered structure giving a square pyramidal coordination around cobalt and manganese ions (chapter 6). Regarding a simple perovskite structure, it has been reported that the reduction of Co^{3+} to Co^{2+} in $LaCoO_3$ gives the metastable phase $La_3Co_3O_8$ as an intermediate on the pathway to the brownmillerite phase $La_2Co_2O_5$ [1,2]. The objective of study in this chapter was to investigate the nature of oxygen deficiency resulting from reduction of the mixed B-site perovskite $LaSrCoFeO_6$. The $(Co/Fe)^{3+}$ and $(Co/Fe)^{3+/4+}$ B-site electronic states are common in perovskite-type oxides and induce interesting structural, electronic and magnetic properties. The link between the latter and oxygen nonstoichiometry in $La_{1-x}Sr_xCo_{l-y}Fe_yO_{3-\delta}$ has attracted recent interest because of the potential to manipulate the mixed ionic-electronic conduction in these materials [3,4]. The $(Co/Fe)^{3+}$ state occurs in oxygen-stoichiometric perovskites such as $LaCo_{0.5}Fe_{0.5}O_3$. Unlike the Co-Mn phase (La_2CoMnO_6) [5], B cations do not order in $LaCo_{0.5}Fe_{0.5}O_3$. Furthermore, Co^{3+} in $LaCo_{0.5}Fe_{0.5}O_3$ is assumed to be in the low spin state and the AFM order claimed for this material at low temperature has been attributed to the dominant interaction between

Fe^{3+} ions [6]. It has been shown that Co^{3+} also exists in the low spin state in layered Co-Fe materials (chapter 3); however, the $(Co/Fe)^{3+}$ state in these materials failed to give evidence of magnetic order at low temperatures probably because of the low dimensionality of the structure. The B-site $(Co/Fe)^{3+}$ electronic state also occurs in oxygen-deficient perovskites such as Sr_2CoFeO_5. This material crystallizes with a brownmillerite structure. Like the ternary phases $Sr_2Co_2O_5$ [7] and $Sr_2Fe_2O_5$ [8], Sr_2CoFeO_5 is AFM at room temperature and crystallizes in the disordered *Icmm* space group [9]. The high Néel temperatures in these materials have been attributed to strong AFM exchange interactions due to presence of Co^{3+} in the high spin state. Unlike the oxidized combination $(Co/Fe)^{3+/4+}$, the reduced $(Co/Fe)^{2+/3+}$ B-site electronic state has not been characterized often in perovskite oxides. However, this state has been observed in layered perovskites such as $La_{2-x}Sr_xCo_{0.5}Fe_{0.5}O_{4-\delta}$ (chapter 3) and $Sr_3LaFe_{1.5}Co_{1.5}O_{10-\delta}$ [10] and has induced a high degree of oxygen deficiency in these materials. In this chapter, the brownmillerite phase $LaSrCoFeO_5$, in which the electronic state $(Co/Fe)^{2+/3+}$ predominates, is synthesized and characterized . The related perovskite-type phases $LaSrCoFeO_5F$ and $LaSrCoFeO_{5.5}$, which mainly contain a $(Co/Fe)^{3+}$ state, are also characterized.

7.2 Synthesis and characterization of $LaSrCoFeO_6$ and $LaSrCoFeO_5$

7.2.1 Synthesis of $LaSrCoFeO_6$

The starting material $LaSrCoFeO_6$ was prepared by a conventional solid state reaction. Stoichiometric amounts of La_2O_3 (previously dried at 800 °C in air), $SrCO_3$, Co_3O_4 and Fe_2O_3 were intimately mixed, pressed into pellet and calcined in air at 1300 °C for 48 h with intermediate grinding. The product was allowed to cool slowly to room temperature.

7.2.2 Characterization of $LaSrCoFeO_6$

XRD revealed $LaSrCoFeO_6$ to be single-phase and to adopt a distorted perovskite structure which could be refined with either a rhombohedral or orthorhombic lattice. The NPD data recorded from this material at room temperature were best fitted in the rhombohedral $R\bar{3}c$ space group with unit cell parameters $a = 5.4519(2)$ Å and $c = 13.2963(4)$ Å (see *Figure 7.1* for the fitted profile and *Table 7.1* for structural data). A similar distortion has been observed in the related perovskite $LaCo_{0.5}Fe_{0.5}O_3$ [6]. The data also suggest that the material is stoichiometric in oxygen with no evidence of cation/magnetic order.

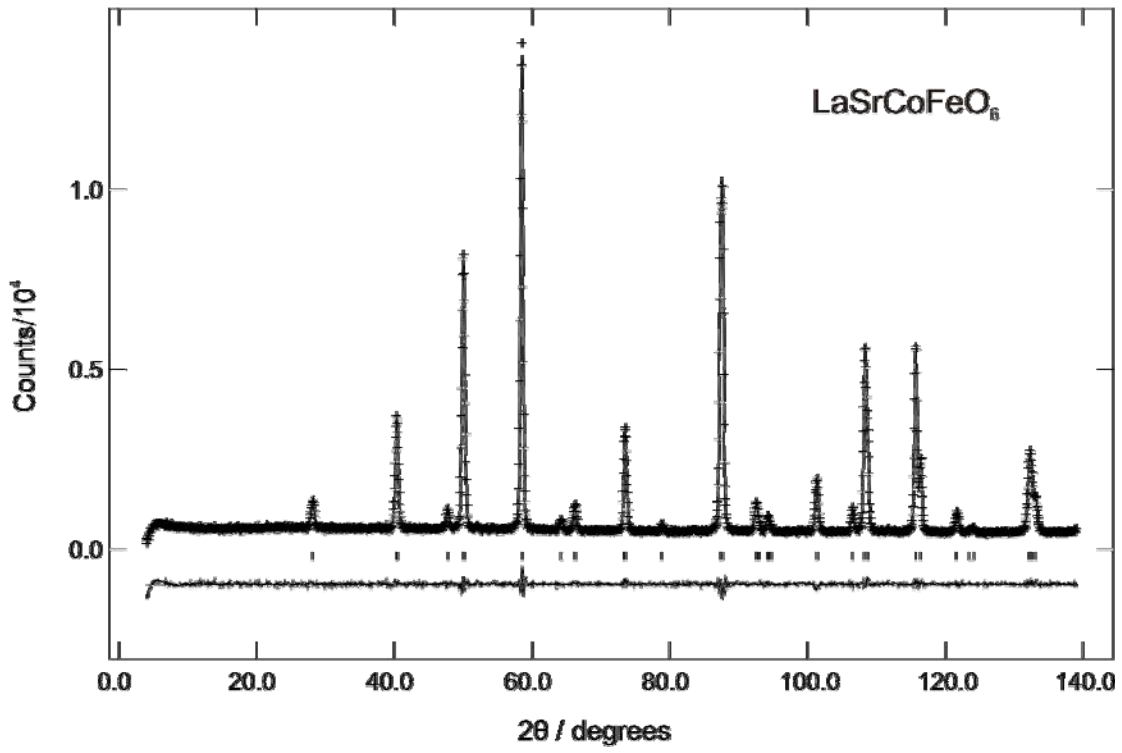

Figure 7.1 Observed, calculated and difference profiles for NPD data collected from $LaSrCoFeO_6$ at room temperature.

Table 7.1 Structural results for the refinement of the NPD data collected from $LaSrCoFeO_6$ at room temperature.

Atom	***x***	***y***	***z***	**100 x Uiso (Å^2)**	**Occupancy**	**Site Symmetry**
La/Sr	0	0	0.25	0.78(3)	0.5/0.5	6a
Co/Fe	0	0	0	0.44(3)	0.5/0.5	6b
O	0	0.4742(1)	0.25	1.20(3)	1	18e
			a = 5.4519(2) Å; c = 13.2963(4) Å			
			Space group $R\bar{3}c$; wRp = 0.0400; Rp = 0.0311; χ^2 = 1.385			
Some selected bond lengths (Å) and angles (°)						
Co/Fe–O	1.92987(7)					
Co/Fe–O–Co/Fe	171.64(4)					

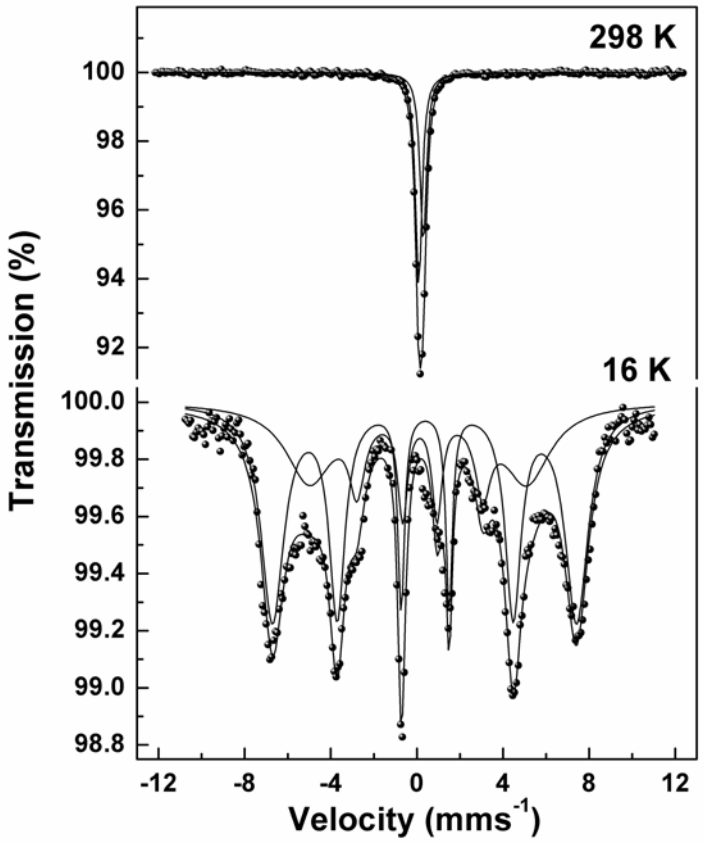

Figure 7.2 ^{57}Fe Mössbauer spectra recorded from $LaSrCoFeO_6$ at 298 and 16 K.

Table 7.2 ^{57}Fe Mössbauer parameters (isomer shift, δ; quadrupole splitting, Δ; hyperfine field, H) for $LaSrCoFeO_6$.

T (K)	δ ± 0.04 (mm s^{-1})	Δ or $e^2Q_q/2$ ± 0.02 (mm s^{-1})	H ± 0.05 (T)	Area ± 3%
298	0.30			47
	0.09			53
16	0.37	-0.02	43.8	62
	0.10	-0.08	31.3	38

Oxygen stoichiometry suggests an average B-site oxidation state of 3.5+ in $LaSrCoFeO_6$ (*i.e.* $(Co/Fe)^{3+/4+}$). It has been suggested from X-ray absorption and Mössbauer studies [11] that both Co^{4+} and Fe^{4+} may contribute to the 4+ state in this material. The ^{57}Fe Mössbauer spectra recorded at 298 and 16 K from this material are shown in *Figure 7.2*, and parameters are given in *Table 7.2*. The spectrum recorded at 298 K was best fitted to two single absorptions. The absorption at $\delta = 0.30$ mm s^{-1} is typical of Fe^{3+} in octahedral oxygen coordination whilst that at $\delta = 0.09$ mm s^{-1} is characteristic of Fe^{4+}. The relative spectral areas indicate approximately equal concentrations of Fe^{3+} and Fe^{4+}. The spectrum recorded at 16 K had a complex structure. Close inspection of the spectrum shows the existence of broad outer lines suggesting the presence of several contributions. The spectrum was amenable to fitting in several ways but the simplest approach, involving two broad sextet patterns in which the areas and linewidths of the individual sextet patterns were not constrained, is presented here. The main contribution to the spectrum accounting for 62% of the spectral area with chemical isomer shift $\delta = 0.37$ mm s^{-1} is characteristic of Fe^{3+} whilst the other sextet, $\delta = 0.10$ mm s^{-1} corresponding to 38% of the spectral area is consistent with the presence of Fe^{4+}. Whilst this fit of the data does represent the simplest approach it should be noted that different models using a larger number of sextet components gave results in which the

components with magnitudes of chemical isomer shifts and magnetic hyperfine fields corresponding to Fe^{3+} consistently approximated to *ca* 60% of the spectral area whilst components which could be assigned to Fe^{4+} accounted for *ca* 40% of the spectral area. Given the presence of Fe^{3+} and Fe^{4+}, and presumably Co^{3+} and Co^{4+}, the broadened spectral lines and overall complexity of the spectrum reflects the complex interactions between these ions.

Figure 7.3 shows the temperature dependence of the magnetic susceptibility of $LaSrCoFeO_6$. The material shows a weak ferromagnetic-like transition at about 200 K with a strong divergence between ZFC and FC susceptibilities below ~ 25 K. Low temperature NPD data of this material show no evidence of long-range magnetic order, which suggests that there exists magnetic frustration (consistent with the mixed cation oxidation states), certainly for T < ~ 25 K.

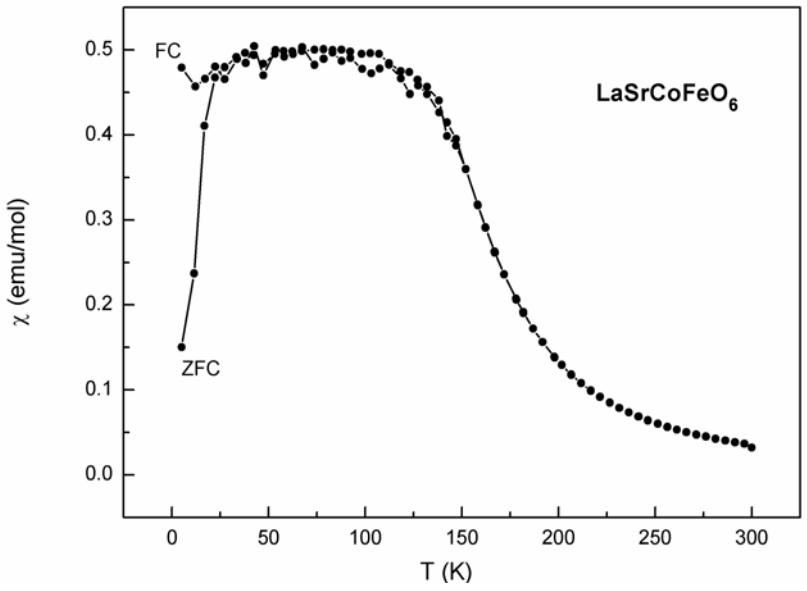

Figure 7.3 Variation of magnetic susceptibility (ZFC and FC) with temperature for $LaSrCoFeO_6$.

7.2.3 Reduction of $LaSrCoFeO_6$

The reduction behaviour was first examined by TGA where a sample of $LaSrCoFeO_6$ was heated (10 °C min^{-1}) in flowing 10% H_2/N_2 (*Figure 7.4*). The TG study suggested that, under the applied conditions, the material is reduced in two steps. The first reduction step at T ≈ 300-500 °C corresponds to formation of a compound with the composition $LaSrCoFeO_5$. The second step (T ≈ 800 °C) corresponds to partial decomposition to the n = 1 RP and other phases (as indicated by XRD). *In situ* VT-XRD measurements were then used to investigate the structure of the reduction products. A sample of $LaSrCoFeO_6$ was heated in flowing 10% H_2/N_2 and XRD data were recorded at different temperatures. As shown in *Figure 7.5*, a significant peak-shift to lower angles is observed in the temperature range T ≈ 25-300 °C which suggests an expansion in the unit cell probably due to reduction of cobalt and iron ions to lower oxidation states; however, the effect of thermal expansion should be considered. In the temperature range T ≈ 500-600 °C, a pattern which is characteristic of a brownmillerite structure is observed.

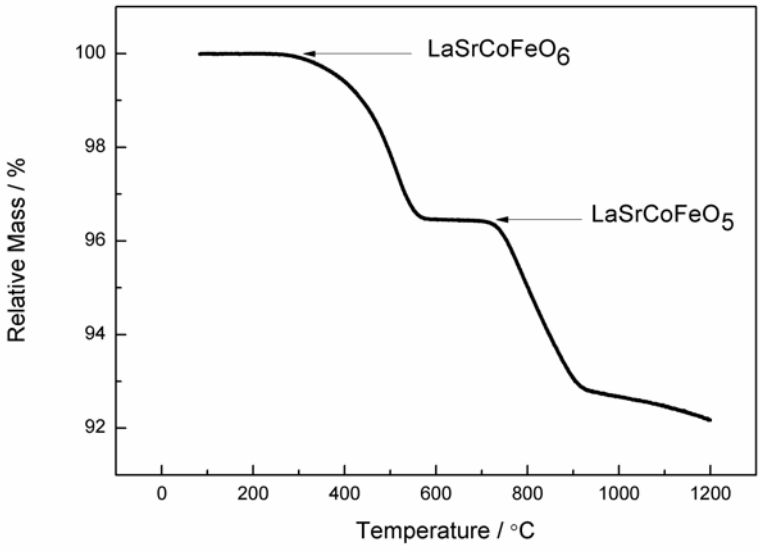

Figure 7.4 TG data for the reduction of $LaSrCoFeO_6$ using 10% H_2 in N_2.

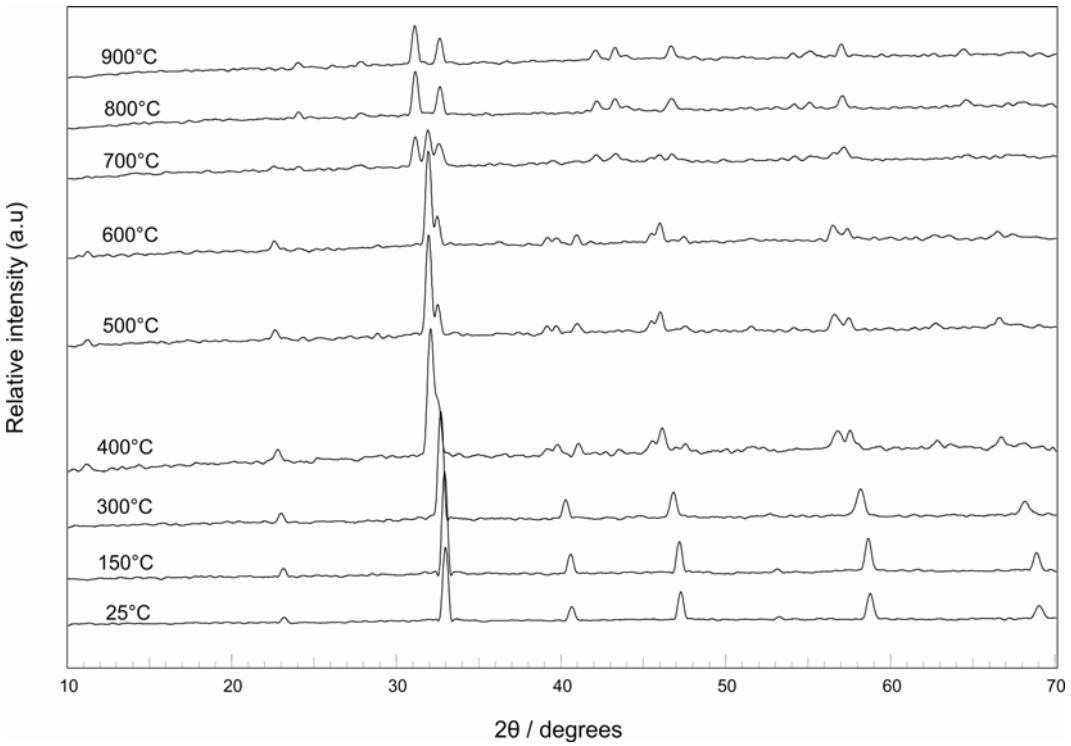

Figure 7.5 VT-XRD data for the reduction of $LaSrCoFeO_6$ using 10% H_2 in N_2.

At $T \geq 700$ ºC, this brownmillerite phase is decomposed to a K_2NiF_4-type phase ($LaSrFeO_4$) and other phases. TG and VT-XRD data therefore suggest that, at $T \approx$ 500-600 °C, $LaSrCoFeO_6$ is reduced to a brownmillerite phase with the composition $LaSrCoFeO_5$.

7.2.4 Synthesis of $LaSrCoFeO_5$

Attempts to repeat the reduction process, to obtain $LaSrCoFeO_5$, on a larger scale showed that the reduction product is sensitive to variables such as temperature, time and the gas-mixture flow rate. A pure single-phase material could be obtained when ~ 3 gm sample of the O6 phase was placed in alumina boat and heated at 525 °C for 12 h in 10% H_2/N_2 (20 ml min^{-1}) followed by slow cooling to room temperature. The reduced material showed relatively good stability in air for 1-2 days, but partial oxidation was observed after

longer exposure times. The material was therefore removed from the furnace immediately after reduction and stored under an argon atmosphere. XRD and magnetic susceptibility data were recorded from fresh samples and samples in sealed containers were used to record the NPD data.

7.2.5 Characterization of $LaSrCoFeO_5$

The XRD pattern of the reduced material confirmed the brownmillerite structure and was successfully refined in the high symmetry space group *Icmm* with the unit cell parameters a = 5.6341(1) Å, b = 15.8950(3) Å and c = 5.5028(1) Å (see *Figure 7.6* for the fitted profile and *Table 7.3* for structural data). The temperature dependence of the magnetic susceptibility of this material, in the temperature range 5-300 K, (see *Figure 7.7*) suggested that the material is antiferromagnetically ordered at room temperature. This behaviour is similar to that of the parent brownmillerite phases $Sr_2Co_2O_5$ (T_N = 570 K) [7] and $Sr_2Fe_2O_5$ (T_N = 700 K) [12] and suggests that the Néel temperature of this material is similarly high.

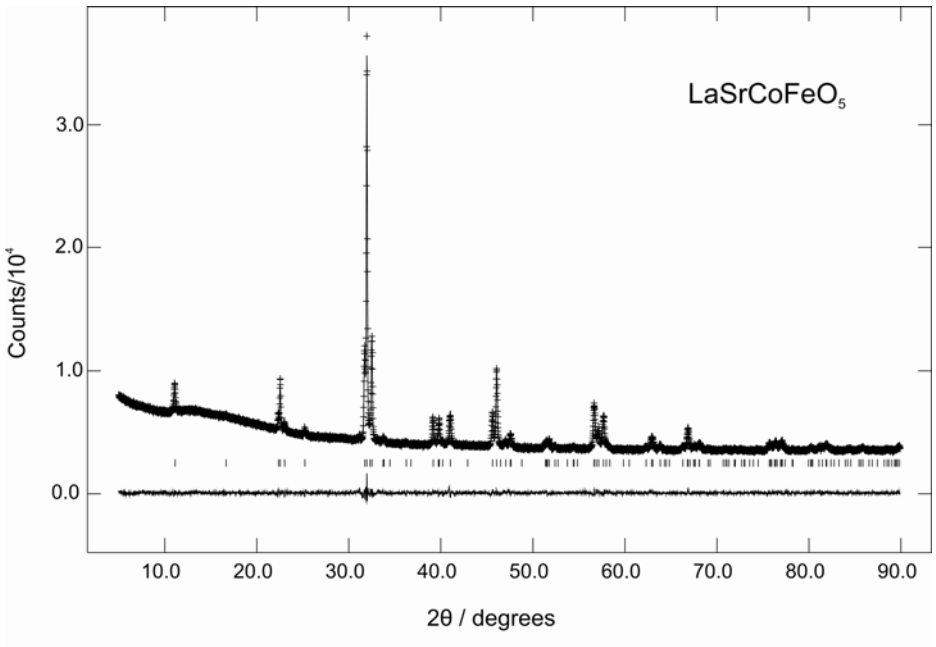

Figure 7.6 Observed, calculated and difference profiles for XRD data collected from $LaSrCoFeO_5$.

Table 7.3 Structural results for the refinement of the XRD data collected from $LaSrCoFeO_5$.

Atom	*x*	*y*	*z*	100 x Uiso (Å^2)	Occupancy	Site Symmetry
$LaSrCoFeO_5$, *a* = 5.6341(1) Å; *b* = 15.8950(3) Å; *c* = 5.5028(1) Å wRp = 0.0179; Rp = 0.0138; $\chi 2$ = 1.53						
La/Sr	0.51315(6)	0.61115(6)	0	1.11(6)	0.5/0.5	8h
(Co/Fe)1	0	0	0	0.88(9)	0.5/0.5	4a
(Co/Fe)2	0.5620(7)	0.25	0.4570(7)	0.88(9)	0.25/0.25	8i
O1	0.25	0.9898(8)	0.25	0.7(3)	1	8g
O2	0.050(2)	0.1375(5)	0	2.0(3)	1	8h
O3	0.636(3)	0.25	0.098(4)	6(1)	0.5	8i

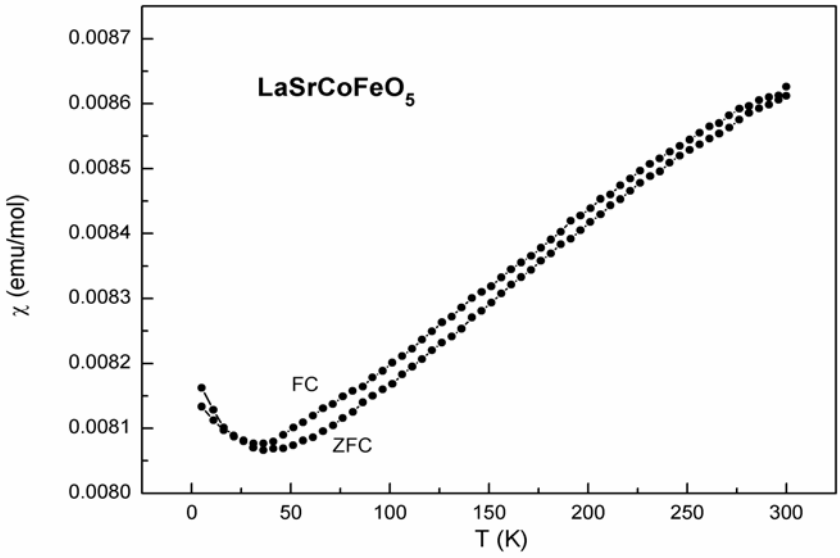

Figure 7.7 Variation of magnetic susceptibility (ZFC and FC) with temperature for $LaSrCoFeO_5$.

NPD data collected from this material confirmed the brownmillerite structure and magnetic order at room- and low- temperature (20 K) (*Figure 7.8*). The magnetic reflections showed enhanced intensity at low temperature indicating enhancement of the spin order. The analysis of the data collected at 20 K was therefore considered in detail since they better describe the magnetic order. The data were best fitted to a nuclear model consistent with a disorder of atomic displacements in adjacent tetrahedral layers, *i.e*. *Icmm* space group, and a G-type AFM model in which the magnetic moments were constrained to lie along the *z* axis (*Figure 7.9*). This is consistent with the nuclear and magnetic structures observed for the parent materials $Sr_2Fe_2O_5$, $Sr_2Co_2O_5$ and Sr_2CoFeO_5 [7-9]. The NPD refinements have shown a preference of the *Icmm* space group (wRp = 0.0335, Rp = 0.0261, χ^2 = 3.731) over the ordered *Ibm2* space group (wRp = 0.0440, Rp = 0.0342, χ^2 = 6.460), while the absence of any additional peaks eliminated primitive symmetry, *Pcmn*, and enlarged cells for the lengthscale appropriate to NPD. The use of the *Icmm* space group reflects the disorder in the layers of tetrahedra through the half occupation of (Co/Fe)2 and O3 to produce the 8i sites, where the atoms are located on two symmetry-related positions (see section 1.2.1). O2 links the tetrahedral cations to the octahedrally coordinated (Co/Fe)1 site, which is bonded to four equatorial O1 sites. The refinement also indicated that the cobalt and iron atoms are randomly distributed over the octahedral and tetrahedral sites of the structure. In comparison, a small preferential occupation of Co^{3+} of the tetrahedral sites was suggested for Sr_2CoFeO_5 [9]. The profile fits and difference patterns of the Rietveld analysis of $LaSrCoFeO_5$ are shown in *Figure 7.8*. Structural results for the analysis of the 20 K data are given in *Table 7.4*. *P1* symmetry was used in modelling the magnetic structure and an average of Fe^{3+} and Co^{2+} form factors was used in the refinement. The magnetic structure is shown in *Figure 7.9*.

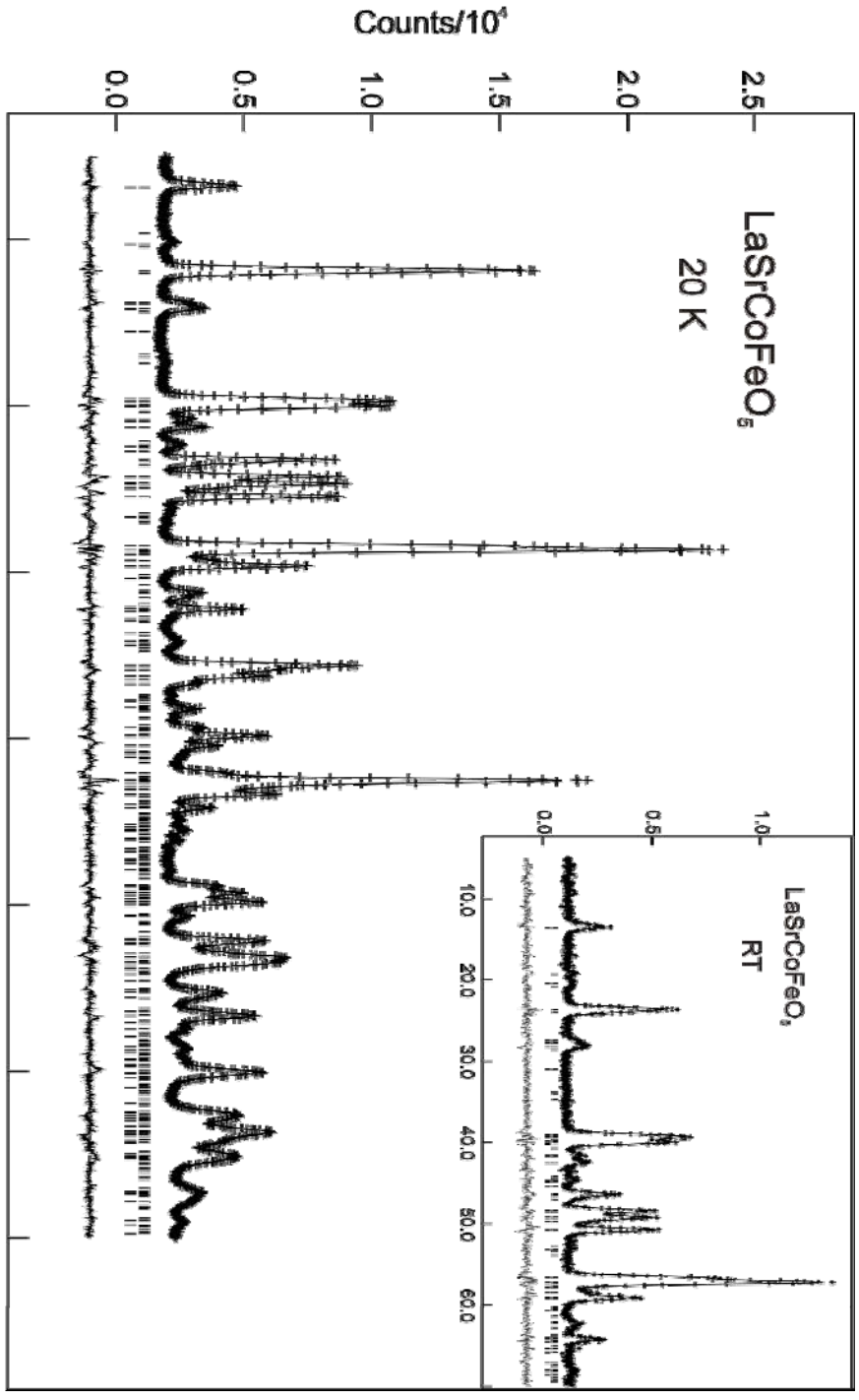

Figure 7.8 Observed, calculated and difference profiles for NPD data collected from $LaSrCoFeO_5$ at 20 K and room temperature (inset), showing nuclear (lower tick marks) and magnetic (upper tick marks) reflections.

Table 7.4 Structural results for the refinement of the NPD data collected from $LaSrCoFeO_5$ at 20 K.

Atom	*x*	*y*	*z*	100 x Uiso (Å^2)	Occupancy	Site Symmetry
La/Sr	0.5126(3)	0.61008(7)	0	0.16(5)	0.5/0.5	8h
(Co/Fe)1	0	0	0	0.05(6)	0.5/0.5	4a
(Co/Fe)2	0.5640(5)	0.25	0.4590(7)	0.05(6)	0.25/0.25	8i
O1	0.25	0.9916(2)	0.25	0.57(6)	1	8g
O2	0.0492(5)	0.1380(1)	0	1.83(6)	1	8h
O3	0.6171(8)	0.25	0.1094(6)	0.7(1)	0.5	8i

A = 5.6287(2) Å; *b* = 15.8481(5) Å; *c* = 5.4923(2) Å
Space group *Icmm*; wRp = 0.0334; Rp = 0.0261; χ^2 = 3.731

Some selected bond lengths (Å) and angles (°)

(Co/Fe)1—O1	1.9706(2) x 4	**La/Sr—O1**	2.582(2) x 2
(Co/Fe)1—O2	2.205(2) x 2	**La/Sr—O1**	2.683(2) x 2
(Co/Fe)2—O2	1.899(2) x 2	**La/Sr—O2**	2.7893(4) x 2
(Co/Fe)2—O3	1.943(5), 1.976(4)	**La/Sr—O2**	2.506(3), 3.193(3)
		La/Sr—O3	2.411(2)

O1—(Co/Fe)1—O1	88.34(1), 91,66(1), 180.0
O2—(Co/Fe)1—O2	138.3(2)
O2—(Co/Fe)2—O3	99.7(1), 104.8(1)
O3—(Co/Fe)2—O3	105.9(2)

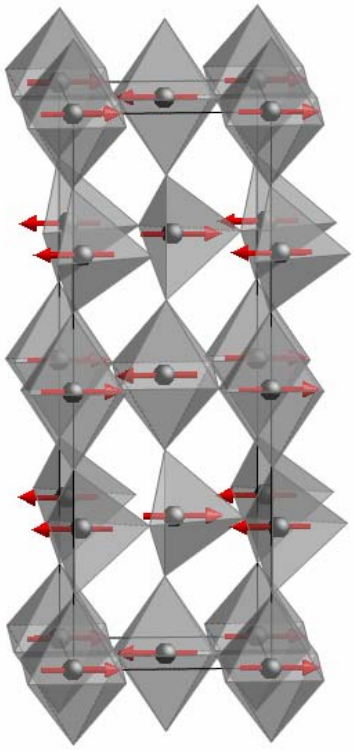

Figure 7.9 Magnetic structure of $LaSrCoFeO_5$. The arrows indicate the direction of Co/Fe magnetic moments (*Ibm2* symmetry was used to aid clarity).

The refined magnetic moments of the octahedral and tetrahedral site cations at 20 K were found to be 3.93(4) and 3.26(4) μ_B, respectively. The high Néel temperature observed in $LaSrCoFeO_5$ suggests very strong AFM interactions and is consistent with the presence of predominantly Co^{2+}/Fe^{3+} in this material. The Co^{2+}/Fe^{3+} state has shown strong AFM interactions at low temperatures in the layered system $La_{2-x}Sr_xCo_{0.5}Fe_{0.5}O_{4-\delta}$ (chapter 3). Considering the higher dimensionality of $LaSrCoFeO_5$, a higher Néel temperature is expected and the material is therefore magnetically ordered at room temperature. The refined magnetic moments of the octahedral and tetrahedral site cations (3.93(4) and 3.26(4) μ_B at 20 K) can be compared with the expected spin-only moment of 4.0 μ_B for Fe^{3+}/Co^{2+} in these sites. Given the moment reduction that can be attributed to covalence, low dimensionality of the magnetic order and quantum mechanical effects, the octahedral site moment is very high. This provides further support for the presence of a large percentage of Co^{2+}, which is known to have a substantial orbital contribution to its moment in octahedral coordination, resulting from the $^4T_{1g}$ ground state.

7.3 Synthesis and characterization of $LaSrCoFeO_5F$ and $LaSrCoFeO_{5.5}$

The $(Co/Fe)^{3+}$ B-site electronic state was achieved in the equimolar La-Sr-Co-Fe perovskite system through preparation of $LaSrCoFeO_5F$ and $LaSrCoFeO_{5.5}$. The two phases adopt a distorted perovskite structure; $LaSrCoFeO_5F$ was prepared by fluorination of $LaSrCoFeO_5$, while $LaSrCoFeO_{5.5}$ could be obtained by two different approaches: first, by quenching the O6 phase ($LaSrCoFeO_6$) from 1300 ºC into liquid nitrogen and, second, by room temperature air oxidation of $LaSrCoFeO_5$.

7.3.1 Fluorination of $LaSrCoFeO_5$

Fluorine was successfully incorporated within the brownmillerite phase by heating $LaSrCoFeO_5$ at 250 °C in flowing 10% F_2/N_2 gas (~ 20 ml min^{-1}) for 3h.

7.3.2 Characterization of the fluorinated phase ($LaSrCoFeO_5F$)

XRD showed that the fluorinated material crystallizes in a rhombohedrally distorted lattice ($R\bar{3}c$ space group) consistent with that of the parent $LaSrCoFeO_6$ phase (see *Figure 7.10* for the fitted profiles).

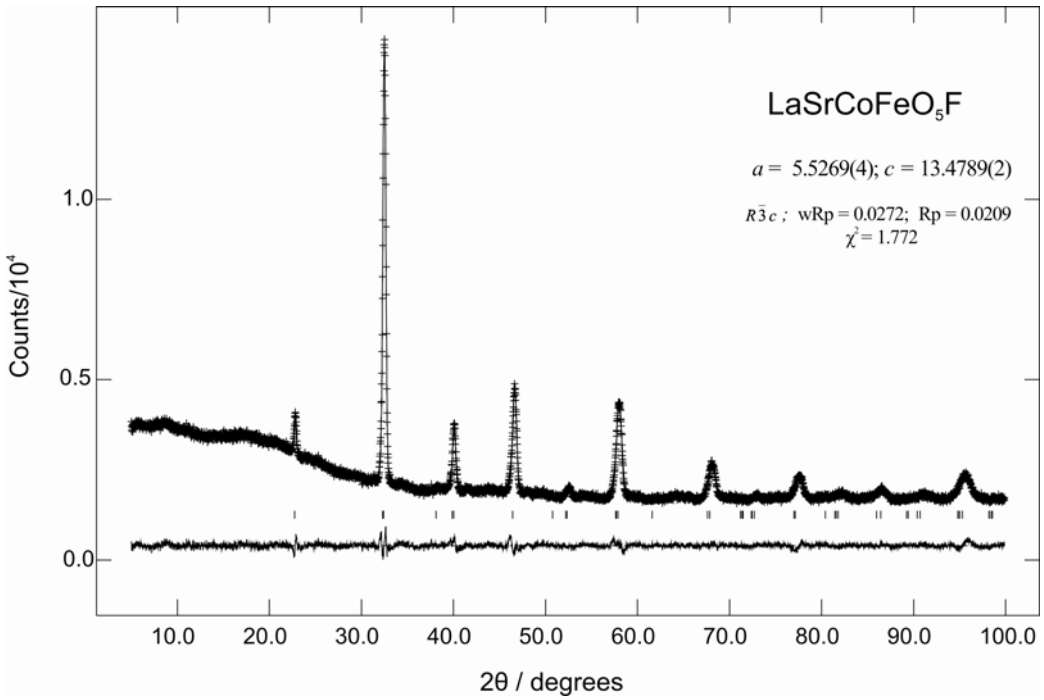

Figure 7.10 Observed, calculated and difference profiles for XRD data collected from the fluorinated material.

The NPD data recorded from this material, however, showed a pattern typical of a distorted perovskite structure but also with additional peaks inconsistent with $R\bar{3}c$ symmetry, in particular the (101/003) reflections at 2θ ~ 24° which corresponds to (½ ½ ½)

for the cubic perovskite subcell (see *Figure 7.11*). Reflections of this type were observed in neither the XRD pattern of this material (*Figure 7.10*), nor the NPD pattern of the starting $LaSrCoFeO_6$ material (*Figure 7.1*), and had a relatively increased intensity at low temperature (see *Figure 7.11*). This pattern is characteristic of superstructure in the perovskite lattice usually resulting from either B-site cation order (see, for example, ref. 13) or G-type antiferromagnetism [6,14,15], although the latter is less common. Given that no cation order has been observed in the starting materials $LaSrCoFeO_6$ and $LaSrCoFeO_5$, achievement of cation order as a result of fluorine insertion (at 250 ºC) is not expected. The ^{57}Fe Mössbauer spectra recorded from the fluorinated material at 298 at 16 K are shown in *Figure 7.12* with parameters in *Table 7.6*. The room temperature spectrum showed two sextet patterns corresponding to *ca* 77% of iron experiencing a static magnetic field. An additional quadrupole split absorption is attributed to small particle paramagnetic Fe^{3+} (to which a small amount of Fe^{4+} could contribute). The spectrum recorded at 16 K showed a simpler pattern with a single sextet and *ca* 93% of the Fe^{3+} being magnetically ordered. The additional NPD reflections were therefore assigned to a magnetic model, and the data were well fitted to a distorted perovskite nuclear structure ($R\bar{3}c$ space group) with G-type antiferromagnetism in which moments at Co/Fe are antiparallel to the moment on all six neighbours (see *Figure 7.11* for the fitted profiles and *Table 7.5* for structural data). The Co/Fe moments were aligned parallel to the hexagonal *c* axis (which is equivalent to the [111] direction in the rhombohedral setting). *P1* symmetry was used in modelling the magnetic structure and an average of Fe^{3+} and Co^{3+} form factors was used in the refinement. Refinement of the fractional occupation of oxygen/fluorine sites showed that these sites are fully occupied. The suggested overall stoichiometry is therefore $LaSrCoFeO_5F$ with no evidence for O/F order and a $(Co/Fe)^{3+}$ B-site oxidation state.

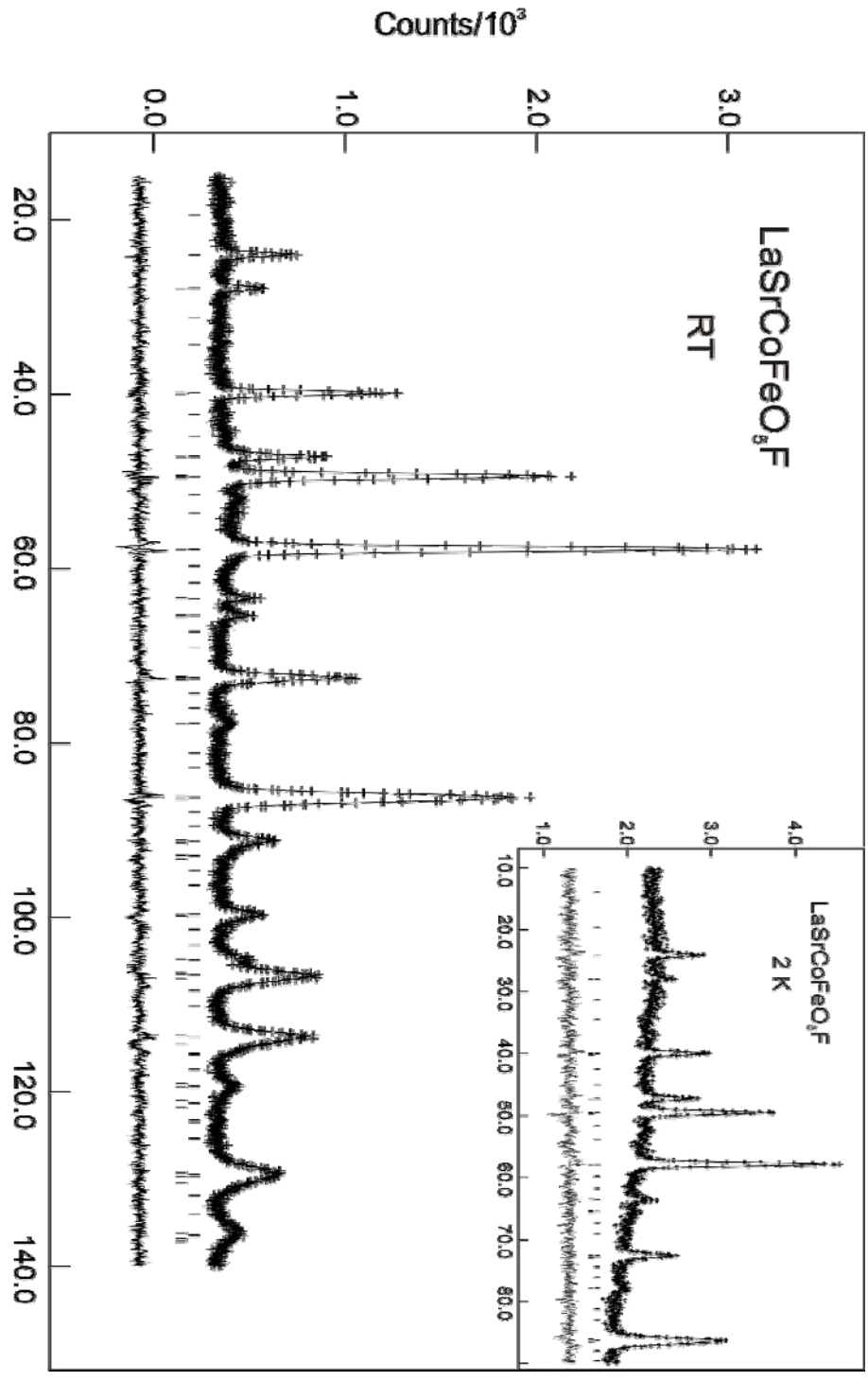

Figure 7.11 Observed, calculated and difference profiles for NPD data collected from LaSrCoFeO$_5$F at room temperature and 2K (inset), showing nuclear (lower tick marks) and magnetic (upper tick marks) reflections.

Table 7.5 Structural results for the refinement of the NPD data collected from $LaSrCoFeO_5F$ at room temperature.

Atom	***x***	***y***	***z***	**100 x Uiso (Å^2)**	**Occupancy**	**Site Symmetry**
La/Sr	0	0	0.25	1.54(9)	0.5/0.5	6a
Co/Fe	0	0	0	1.09(9)	0.5/0.5	6b
O/F	0	0.4602(4)	0.25	2.23(7)	1	18e
			a = 5.5193(3) Å; c = 13.438(1) Å			
			Space group $R\bar{3}c$; wRp = 0.0507; Rp = 0.0400; χ^2 = 1.208			
Some selected bond lengths (Å) and angles (°)						
Co/Fe-O/F	1.9598(3)					
Co/Fe-O-Co/Fe	167.1(1)					

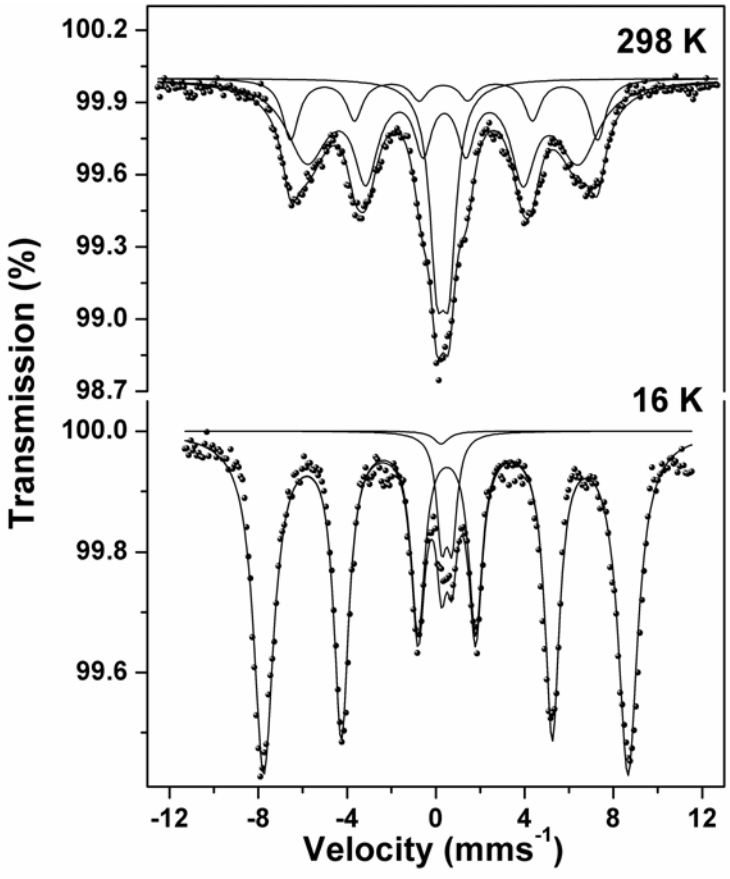

Figure 7.12 ^{57}Fe Mössbauer spectra recorded from $LaSrCoFeO_5F$ at 298 and 16 K.

Table 7.6 ^{57}Fe Mössbauer parameters (isomer shift, δ; quadrupole splitting, Δ; hyperfine field, H) for $LaSrCoFeO_5F$.

T (K)	δ ± 0.04 (mm s^{-1})	Δ or $e^2Q_q/2$ ± 0.02 (mm s^{-1})	H ± 0.05 (T)	Area ± 3%
298	0.35	-0.08	37.9	59
	0.36	0.02	42.9	18
	0.32	0.47		23
16	0.47	-0.04	50.9	93
	0.50	0.47		7

Oxygen replacement by fluorine in this material resulted in a significant expansion of MO_6 octahedra (Co/Fe–O/F bond-lengths are 1.92987(7) and 1.9598(3) Å for $LaSrCoFeO_6$ and $LaSrCoFeO_5F$, respectively) due to reduction of $(Co/Fe)^{3+/4+}$ to $(Co/Fe)^{3+}$. This was associated with a general expansion of the unit cell (for $LaSrCoFeO_6$: a = 5.4519(2) Å; c = 13.2963(4) Å, and for $LaSrCoFeO_5F$: a = 5.5193(3) Å; c = 13.438(1) Å). Observation of G-type antiferromagnetism at room temperature in $LaSrCoFeO_5F$ suggests that the M-O-M (M = Fe^{3+}, Co^{3+}) interactions are predominately AFM. This supports a high spin state for Co^{3+} in this material, since a low spin configuration would result in competing AFM (Fe-Fe) and FM (Co-Fe) interactions and magnetic frustration. A high spin state of Co^{3+} has been suggested to account for the high Néel temperatures in the brownmillerite materials $Sr_2Co_2O_5$ and Sr_2CoFeO_5 [7,9], but is unusual in perovskite oxides [16,17]. It is worth noting that a charge transfer model in the Ru^{4+}/Cr^{4+} system has been suggested to produce pure AFM M-O-M interactions and account for a similar type of magnetic order [14,15].

The variation of magnetic susceptibility with temperature (*Figure 7.13*) showed a gradually increasing divergence between ZFC and FC measurements. However, it can be observed that $LaSrCoFeO_5F$ shows much lower magnetization than $LaSrCoFeO_6$, and is comparable to that of $LaSrCoFeO_5$. The data are consistent with AFM order in the

temperature range 5-300 K, and in accordance with the NPD and Mössbauer data. The divergence between ZFC and FC measurements in this case may indicate a small ferromagnetic component due to canting of the moments or result from termination effects in small magnetic domains. The refined magnetic moment for Co/Fe in $LaSrCoFeO_5F$ is 2.19(4) and 3.07(8) μ_B at room temperature and 2 K, respectively. The reduction of the 2 K moment from that expected for a mixture of high spin Co^{3+} and Fe^{3+} (ideally 4.5 μ_B for spin-only contributions) is attributed to covalence and quantum mechanical effects.

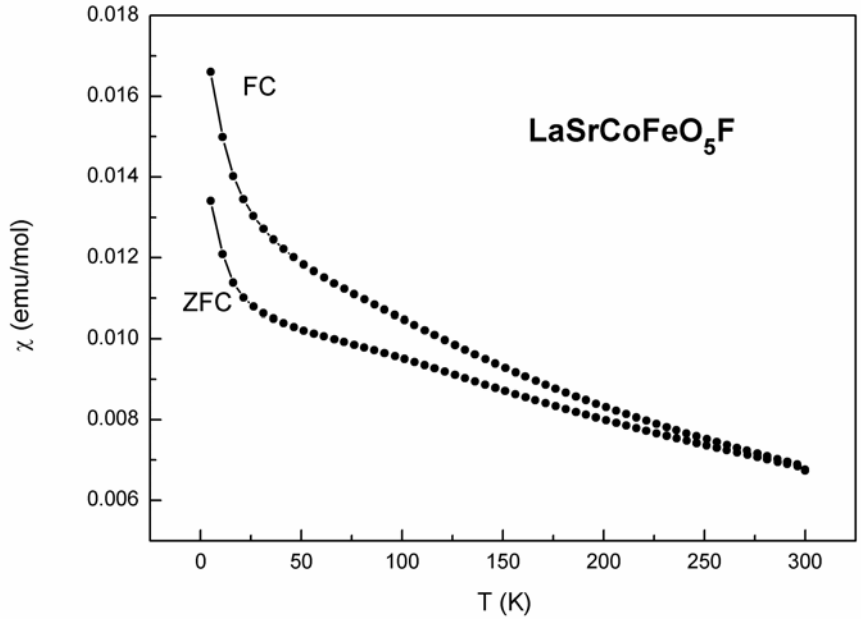

Figure 7.13 Variation of magnetic susceptibility (ZFC and FC) with temperature for $LaSrCoFeO_5F$.

7.3.3 Synthesis and characterization of $LaSrCoFeO_{5.5}$

An attempt to reach the $(Co/Fe)^{3+}$ B-site electronic state in the La-Sr-Co-Fe-O perovskite system (*i.e.* $LaSrCoFeO_{5.5}$) was successful through quenching a sample of $LaSrCoFeO_6$ from 1300 ºC into liquid nitrogen. XRD revealed that the product showed significant shifts in all reflection peaks to lower 2θ values (see *Figure 7.14*). A similar shift is observed in the VT-XRD data under reduction of $LaSrCoFeO_6$ in 10% H_2/N_2

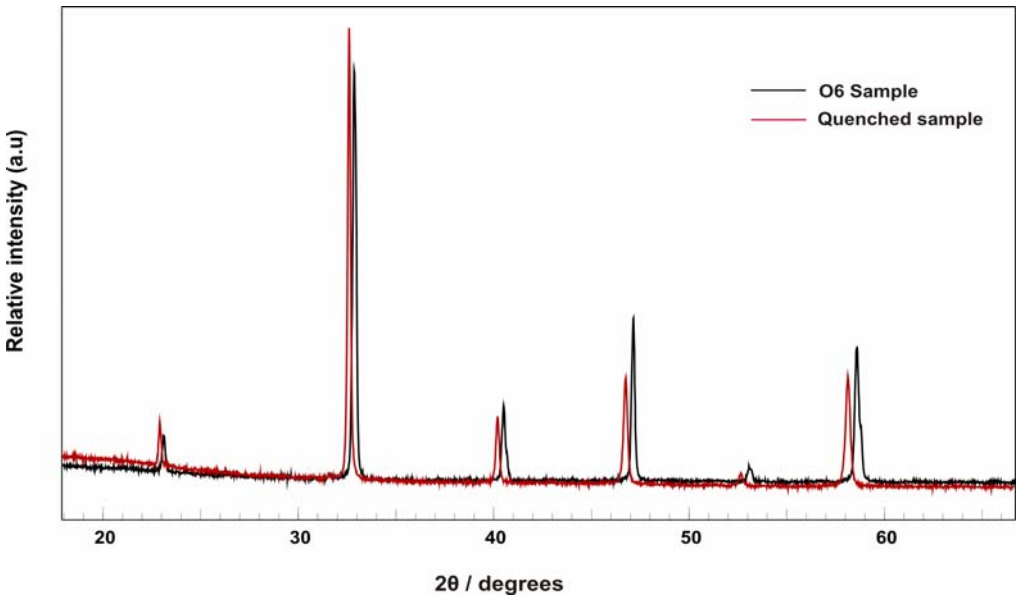

Figure 7.14 XRD data collected from $LaSrCoFeO_6$ (black) and the quenched sample (red).

(*Figure 7.5*) which indicated that the material is oxygen-deficient; however, refinements based on XRD data were relatively insensitive to oxygen site occupancy. NPD data recorded from this sample confirmed that the material is oxygen-deficient with an overall stoichiometry of $LaSrCoFeO_{5.56}$. The NPD pattern was very similar to that of $LaSrCoFeO_5F$ with significant intensity for the (101/003) reflections resulting from magnetic order. The data were fitted using similar structural and magnetic models (see *Figure 7.15* for the fitted profile and *Table 7.7* for structural data). The data therefore suggest similar B-site oxidation state ($(Co/Fe)^{3+}$) in the two materials. Given that cation order is very unlikely to be achieved under quenching conditions, the data confirm the magnetic nature of the (101/003) peak in these materials. The Co/Fe refined moment in $LaSrCoFeO_{5.56}$ at room temperature was 1.40(4) μ_B. This is significantly lower than that for $LaSrCoFeO_5F$ at room temperature, and probably reflects a lower Néel temperature, which probably relates to the anion deficiency and consequential reduction in M-O-M

super-exchange interactions. The oxygen stoichiometry in $LaSrCoFeO_{5.56}$ also suggests the presence of traces of M^{4+} ions in this material.

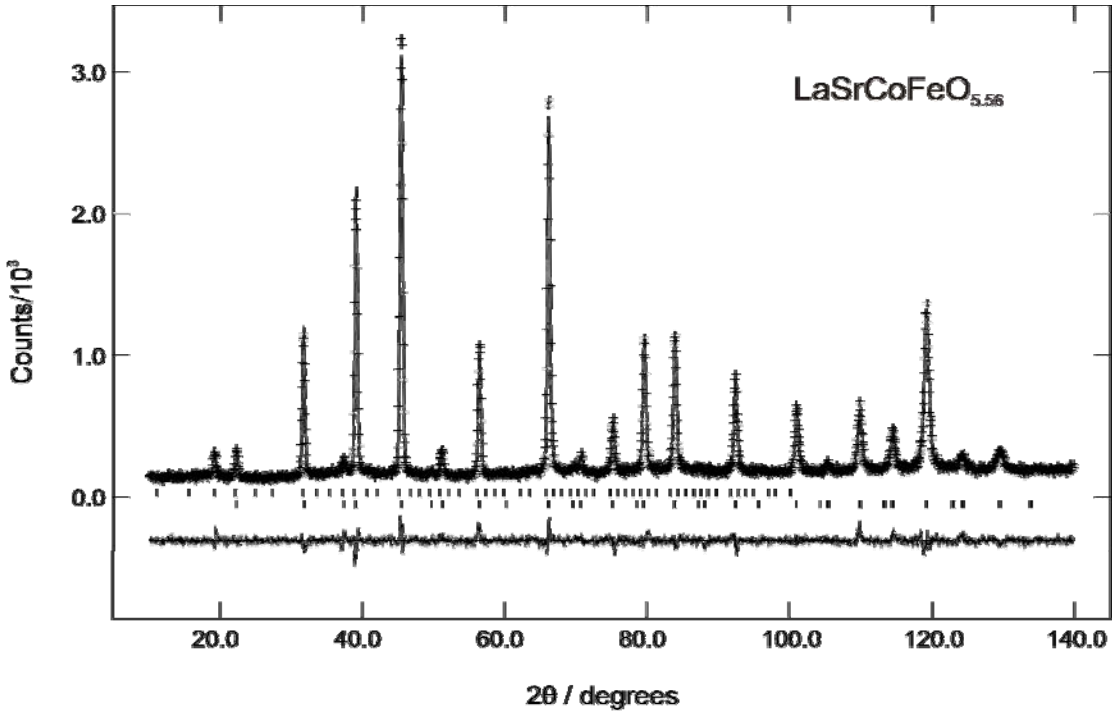

Figure 7.15 Observed, calculated and difference profiles for NPD data collected from $LaSrCoFeO_{5.56}$ at room temperature, showing nuclear (lower tick marks) and magnetic (upper tick marks) reflections

Table 7.7 Structural results for the refinement of the NPD data collected from $LaSrCoFeO_{6-\delta}$ phases at room temperature.

Atom	*x*	*y*	*z*	100 x Uiso (Å^2)	Occupancy	Site Symmetry
		$LaSrCoFeO_{5.56}$, space group $R\bar{3}c$, a = 5.4751(5) Å; c = 13.429(2) Å wRp = 0.0770; Rp = 0.0603; χ^2 = 1.485				
La/Sr	0	0	0.25	1.21(5)	0.5/0.5	6a
Co/Fe	0	0	0	0.22(4)	0.5/0.5	6b
O	0	0.4881(7)	0.25	2.29(5)	0.927(6)	18e
		$LaSrCoFeO_{5.58}$, space group $R\bar{3}c$, a = 5.463(1) Å; c = 13.372(6) Å wRp = 0.0800; Rp = 0.0621; χ^2 = 2.316				
La/Sr	0	0	0.25	1.13(7)	0.5/0.5	6a
Co/Fe	0	0	0	0.79(8)	0.5/0.5	6b
O	0	0.4820(6)	0.25	2.16(7)	0.930(6)	18e

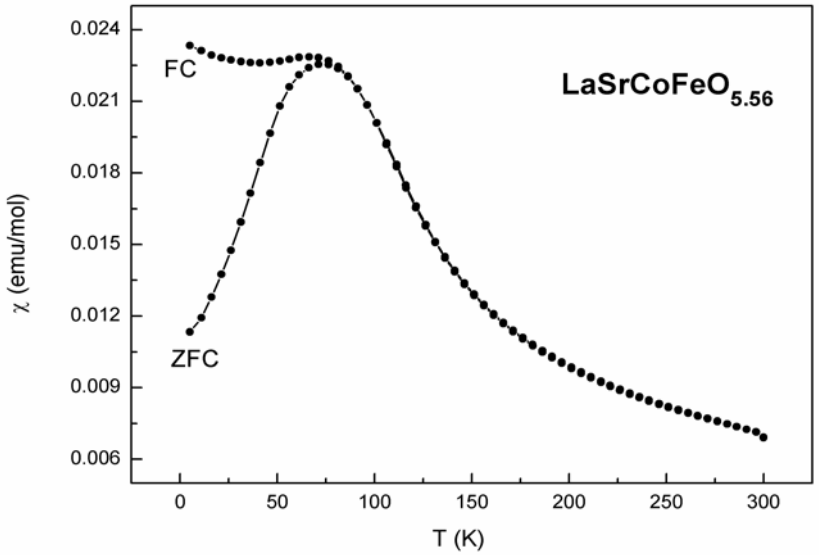

Figure 7.16 Variation of magnetic susceptibility (ZFC and FC) with temperature for $LaSrCoFeO_{5.56}$.

The magnetization of this material (*Figure 7.16*) is again significantly lower than that for $LaSrCoFeO_6$, as expected for AFM order within this temperature range. FC and ZFC susceptibilities, however, show divergence below ~ 100 K. The nature of this effect remains unclear but could involve an enhanced canting contribution, which may relate to the presence of a small amount of M^{4+} in this material.

The ^{57}Fe Mössbauer spectrum recorded from $LaSrCoFeO_{5.56}$ at 298 K was best fitted to two sextets and a doublet (*Figure 7.17*). The sextet with the highest magnetic hyperfine field (H = 43 T) has a chemical isomer shift (δ = 0.34 mm s^{-1}) characteristic of Fe^{3+} in octahedral coordination whilst that of lower magnetic hyperfine field and smaller chemical isomer shift (δ = 0.29 mm s^{-1}) is indicative of Fe^{3+} in lower oxygen coordination. The quadrupole split absorption at δ = 0.26 mm s^{-1} is consistent with the presence of a paramagnetic Fe^{3+} species but a contribution to this component from Fe^{4+} cannot be excluded.

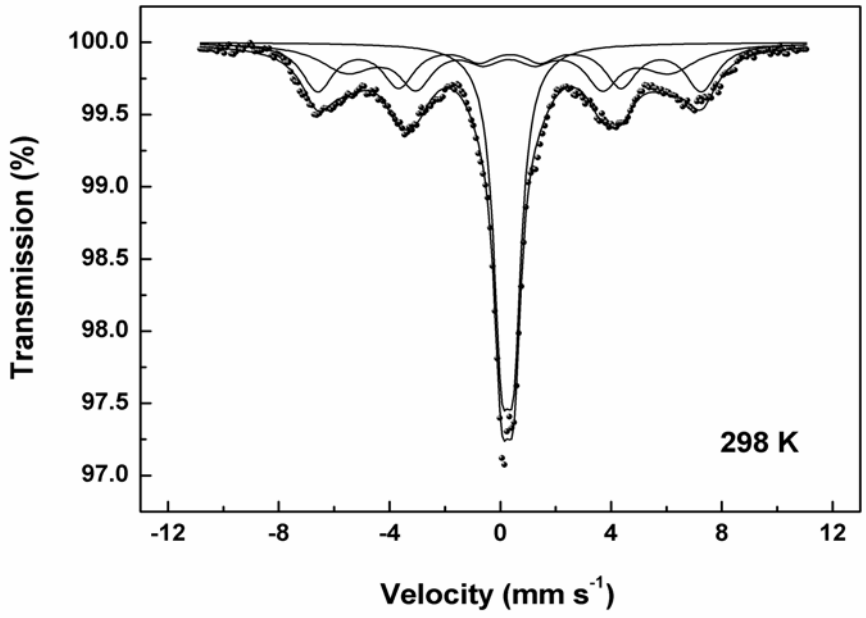

Figure 7.17 ^{57}Fe Mössbauer spectra recorded from $LaSrCoFeO_{5.56}$ at 298 K.

The O5.5 phase could also be obtained by room temperature air oxidation of $LaSrCoFeO_5$; the sample was periodically examined by XRD until the brownmillerite phase completely changed to the perovskite phase. The material showed very similar XRD and NPD patterns to that of the quenched sample ($LaSrCoFeO_{5.56}$). NPD data were fitted using similar structural and magnetic models (see *Figure 7.18* for the fitted profile and *Table 7.7* for structural data) showing a composition of $LaSrCoFeO_{5.58}$. The room temperature moment, 1.41(4) μ_B, is the same as that determined from the quenched sample. When the sample is heated in air (at 300 ºC for one week), the starting O6 phase was retrieved (see *Figure 7.19*) indicating the full reversibility of the $LaSrCoFeO_5$-$LaSrCoFeO_6$ oxidation-reduction process.

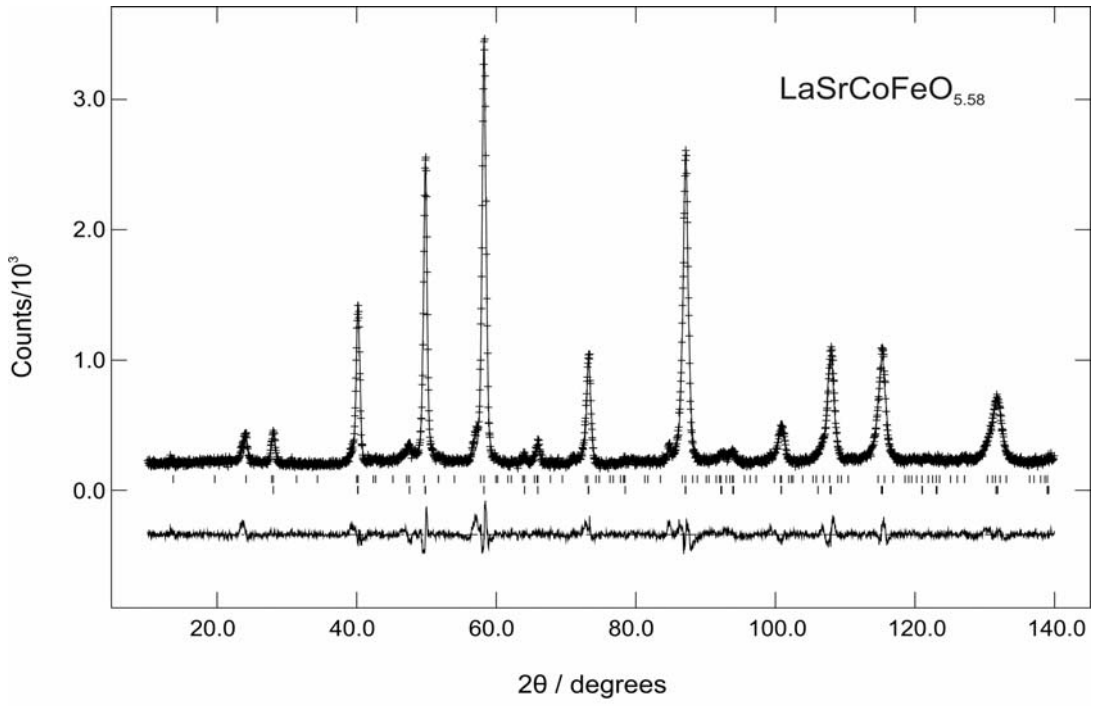

Figure 7.18 Observed, calculated and difference profiles for NPD data collected from $LaSrCoFeO_{5.58}$ at room temperature, showing nuclear (lower tick marks) and magnetic (upper tick marks) reflections.

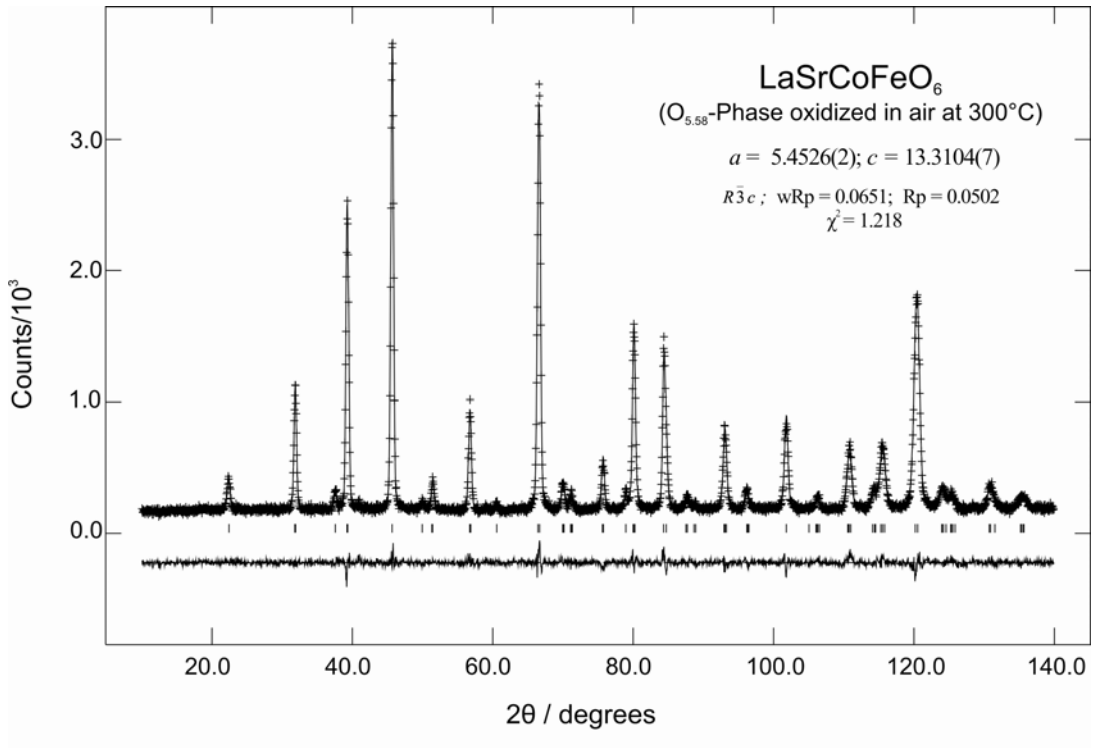

Figure 7.19 Observed, calculated and difference profiles for NPD data collected at room temperature from $LaSrCoFeO_{5.58}$ after oxidation in air at 300ºC.

7.4 References

[1] O. H. Hansteen, H. Fjellvag, B. C. Hauback, *J. Mater. Chem.* **8** (1998) 2081

[2] O. H. Hansteen, H. Fjellvag, B. C. Hauback, *J. Solid State Chem*. **141** (1998) 411

[3] Y. Teraoka, H. M. Zhang, K. Okamoto, N. Yamazoe, *Mater. Res. Bull*. **23** (1988) 51.

[4] A. Mineshige, J. Abe, M. Kobune, Y. Uchimoto, T. Yazawa, *solid State Ionics* **177** (2006) 1803.

[5] C. L. Bull1, D. Gleeson, K. S. Knight, *J. Phys.: Condens. Matter* **15** (2003) 4927.

[6] D. V. Karpinsky, I. O. Troyanchuk, K. Bärner, H. Szymczak, M. Tovar *J. Phys.: Condens. Matter* **17** (2005) 7219.

[7] T. Takeda, Y. Yamaguchi, H. Watanabe, *J. Phys. Soc. Japan.* **33** (1972) 970.

[8] C. Greaves, A. J. Jacobson, B. C. Tofield, B. E. F. Fender, *Acta Crystallogr. Sect. B* **31** (1975) 641.

[9] P. D. Battle, T. C. Gibb, P. Lightfoot, *J. Solid State Chem*. **76** (1988) 334.

[10] A. Bowman, M. Allix, D. Pelloquin, M. J. Rosseinsky, *J. Am. Chem. Soc.* **128** (2006) 12606.

[11] F. J. Berry, J. R. Gancedo, J. F. Marco, X. Ren, *Hyperfine Interact.* **166** (2005) 449.

[12] T. Takeda, Y. Yamaguchi, S. Tomiyoshi, M. Fukase, M. Sugimoto, H. Watanabe, *J. Phys. Soc. Japan* **24** (1968) 446.

[13] H. Sakuma, T. Taniyama, Y. Kitamoto, Y. Yamazaki, *J. Appl. Phys*. **93** (2003) 2816.

[14] A. J. Williams, A. Gillies, J. P. Attfield, G. Heymann, H. Huppertz, M. J. Martinez-Lope, J. A. Alonso. *Phys. Rev. B* **73** (2006) 104409.

[15] J. A. Rodgers, A. J. Williams, M. J. Martinez-Lope, J. A. Alonso, J. P. Attfield, *Chem. Mater.* **20** (2008) 4797.

[16] G. Blasse, *J. Appl. Phys*. **36** (1965) 879.

[17] M. A. Senaris-Rodriguez, J. B. Goodenough, *J. Solid State Chem.* **116** (1995) 224.

CHAPTER 8

Conclusions and further work

8.1 Conclusions

A number of cobalt-containing perovskite-type oxides were synthesized and characterized in this study. All materials were half-doped with cobalt in their B-sites, *i.e.* contain the $Co_{0.5}M_{0.5}$ B-site state where M = Fe, Mn, Cr, Ni; the materials adopted single-layered, double-layered and simple perovskite-type structures. The single-layered materials $La_{2-x}Sr_xCo_{0.5}M_{0.5}O_4$ (M = Fe, Cr) have shown enhanced stability with respect to structural breakdown under oxidizing and reducing conditions. Under oxidizing conditions, the materials are stoichiometric in oxygen with no evidence of oxygen hyperstoichiometry. The oxidized materials contain mixtures of $Fe^{3+(4+)}$, Cr^{3+} and $Co^{3+(2+)}$ ions, with Co^{3+} being in the low spin state; this inhibits long-range AFM order to give a spin glass state in $La_{2-x}Sr_xCo_{0.5}Fe_{0.5}O_4$. In $La_{2-x}Sr_xCo_{0.5}Cr_{0.5}O_4$, there are no signs of spin glass behaviour and the materials are simply paramagnetic. A mixture of Co^{2+} and Co^{3+} in $La_{1.2}Sr_{0.8}Co_{0.5}Fe_{0.5}O_4$ and $La_{1.15}Sr_{0.85}Co_{0.5}Cr_{0.5}O_4$ failed to induce oxygen hyperstoichiometry in these materials (*via* oxidation of Co^{2+} to Co^{3+}). Under reduction in 10% H_2/N_2, Co^{3+} is reduced to Co^{2+} with the formation of oxygen deficiency. The oxygen-deficient materials $La_{2-x}Sr_xCo_{0.5}Fe_{0.5}O_{4-\delta}$ and $La_{2-x}Sr_xCo_{0.5}Cr_{0.5}O_{4-\delta}$ ($\delta \leq 0.25$) were formed at $T \geq 500$ ºC and withstand reducing conditions (10% H_2/N_2) up to 1000 ºC with no evidence of phase decomposition. Oxygen vacancies in these materials were disordered and confined to the equatorial planes of the K_2NiF_4 structure. The formation of these vacancies provides lower coordination around the transition metal ions (< 6) and results in a significant expansion in the *c* parameter and a contraction in the *a* parameter in order to equilibrate the expansion in

the MO_x polyhedra (due to reduction of the transition metal ions) and the contraction of $(La/Sr)O_x$ polyhedra (due to reduction of the coordination number). An associated rotation of MO_x polyhedra around the *z* axis is also observed in these materials. The formation of Co^{2+} in the reduced materials results in long-range AFM order and a spin glass state in $La_{2-x}Sr_xCo_{0.5}Fe_{0.5}O_{4-\delta}$ and $La_{2-x}Sr_xCo_{0.5}Cr_{0.5}O_{4-\delta}$ respectively, at low temperatures. No evidence of symmetry lowering is observed under reduction and a tetragonal noncollinear magnetic model was used to account for the magnetic order in $La_{2-x}Sr_xCo_{0.5}Fe_{0.5}O_{4-\delta}$.

Unlike the iron- and chromium- containing materials, oxygen hyperstoichiometry could be achieved in $La_{1.2}Sr_{0.8}Co_{0.5}Mn_{0.5}O_{4.1}$ and $La_{1.7}Sr_{0.3}Co_{0.5}Ni_{0.5}O_{4.08}$. On the other hand, the materials $LaSrCo_{0.5}Mn_{0.5}O_4$ and $La_{1.5}Sr_{0.5}Co_{0.5}Ni_{0.5}O_4$ are stoichiometric in oxygen with no evidence of oxygen hyperstoichiometry under similar oxidation conditions. This may indicate a role of the Co^{2+}/Co^{3+} state, which is present in stoichiometric $La_{1.2}Sr_{0.8}Co_{0.5}Mn_{0.5}O_4$ and $La_{1.7}Sr_{0.3}Co_{0.5}Ni_{0.5}O_4$, to induce oxygen hyperstoichiometry in these materials *via* oxidation of Co^{2+} to Co^{3+}; however, this effect is not observed in the iron- and chromium- containing materials which suggests that the effect of oxidation of some Mn^{3+}/Ni^{2+} to Mn^{4+}/Ni^{3+} in $La_{1.2}Sr_{0.8}Co_{0.5}Mn_{0.5}O_{4.1}$ and $La_{1.7}Sr_{0.3}Co_{0.5}Ni_{0.5}O_{4.08}$, to induce excess-oxygen insertion, can not be excluded. XPS measurements indicated the presence of Ni^{3+} in $La_{1.7}Sr_{0.3}Co_{0.5}Ni_{0.5}O_{4.08}$. Oxygen hyperstoichiometry in these materials was accommodated in the interstitial (0, 0.5, 0.25) sites of the tetragonal K_2NiF_4-type structure with no evidence of symmetry alteration. An associated displacement of the apical oxide ions is observed in these materials and moves the apical oxygens from their ideal position at $(0, 0, z)$ to the split position $(0, y, z)$. The overall conductivity of the oxygen-rich phases $La_{1.2}Sr_{0.8}Co_{0.5}Mn_{0.5}O_{4.1}$ and $La_{1.7}Sr_{0.3}Co_{0.5}Ni_{0.5}O_{4.08}$, in air at different temperatures, was also examined. $La_{1.7}Sr_{0.3}Co_{0.5}Ni_{0.5}O_{4.08}$ exhibited much higher conductivity which was comparable to that of $La_2NiO_{4+\delta}$. However,

$La_{1.7}Sr_{0.3}Co_{0.5}Ni_{0.5}O_{4.08}$ showed a semiconductive behaviour in the temperature range 100-900 ºC, with no evidence of a semiconductor-to-metal transition. The material is therefore attractive to be explored as a cathode material in SOFCs (see section 8.2). Preliminary tests of $La_{1.7}Sr_{0.3}Co_{0.5}Ni_{0.5}O_{4.08}$-compatibility with YSZ indicated good stability of the system up to 1000 ºC. The nickel-containing materials $La_{1.5+x}Sr_{0.5-x}Co_{0.5}Ni_{0.5}O_{4(+\delta)}$ also withstand reducing conditions (10% H_2/N_2) up to 800 ºC *via* reduction of Co^{3+}(Ni^{3+}) to the divalent states and formation of oxygen deficiency. The formation of Ni^{1+} is also observed in $La_{1.5}Sr_{0.5}Co_{0.5}Ni_{0.5}O_{3.7}$. The manganese-containing materials, on the other hand, withstand applied reduction conditions up to 1000 ºC with no evidence of phase decomposition. In these materials, Co^{3+} is reduced to Co^{2+} with a further reduction of Mn^{3+} to Mn^{2+} at T > 800 ºC, as evidenced for $La_{0.8}Sr_{1.2}Co_{0.5}Mn_{0.5}O_{3.6}$. Oxygen deficiency in $La_{2-x}Sr_xCo_{0.5}Mn_{0.5}O_{4-\delta}$ and $La_{1.5+x}Sr_{0.5-x}Co_{0.5}Ni_{0.5}O_{4-\delta}$ is structurally similar to that observed in iron- and chromium- containing phases. The reduced materials are spin glasses due to competitive FM and AFM interactions between Co^{2+} and $Mn^{3+/2+}$ / $Ni^{2+/1+}$ ions.

An important feature of the oxygen-deficient K_2NiF_4-type materials studied in this thesis is that they all show good stability in air at ambient temperature which is not known for most of the Co^{2+}-containing compounds. Regarding oxygen nonstoichiometry in the single-layered materials $La_{2-x}Sr_xCo_{0.5}M_{0.5}O_{4\pm\delta}$ (M = Fe, Mn, Cr, Ni), it can be concluded that (i) the manganese- and nickel- containing materials show a wider range of oxygen nonstoichiometry, and (ii) the oxygen deficiency is structurally similar in all materials.

The reduction behaviour of the B-site state $Co_{0.5}M_{0.5}$ was also examined in perovskite materials with higher dimensionality, namely the manganese-containing n = 2 RP phases $La_{1+x}Sr_{2-x}CoMnO_7$ and the iron-containing perovskite material $LaSrCoFeO_6$. In contrast to the single-layered materials, Co^{3+} in these materials is shown to be in the high

spin state. The Co^{3+}/Mn^{4+} state in $LaSr_2CoMnO_7$ and $La_{1.2}Sr_{1.8}CoMnO_7$ results in spin glass behaviour of the materials at low temperatures, with predominant FM exchange interactions. This state is reduced mainly to Co^{2+}/Mn^{3+} in $LaSr_2CoMnO_{6.18}$ and $La_{1.2}Sr_{1.8}CoMnO_{6.14}$. In these materials the crystal symmetry is retained (*I4/mmm* space group) and oxygen is removed from the apical sites linking the MO_6 octahedra giving rise to a square pyramidal coordination around cobalt and manganese ions. The reduced materials are spin glasses with predominant AFM interactions.

Controlled reduction of the perovskite material $LaSrCoFeO_6$ resulted in the formation of the brownmillerite phase $LaSrCoFeO_5$. The material crystallizes in the *Icmm* space group with the transition metal ions randomly distributed over the octahedral and tetrahedral sites of the structure. The material shows G-type AFM order at room temperature which is consistent with the presence of high spin Co^{2+} and Fe^{3+}. The perovskite phases $LaSrCoFeO_5F$ and $LaSrCoFeO_{5.58}$ were synthesized by fluorination and room temperature air oxidation of $LaSrCoFeO_5$, respectively. $LaSrCoFeO_{5.56}$ could be prepared by quenching a sample of $LaSrCoFeO_6$ from 1300 °C into liquid nitrogen. The materials show G-type antiferromagnetism at room temperature consistent with the presence of Co^{3+} in the high spin state.

8.2 Further work

The current study indicated that the single-layered materials $La_{2-x}Sr_xCo_{0.5}Mn_{0.5}O_{4\pm\delta}$ and $La_{1.5+x}Sr_{0.5-x}Co_{0.5}Ni_{0.5}O_{4\pm\delta}$ exhibit interesting structural, electronic and phase-stability properties making them attractive to be explored as electrode materials in SOFCs. The manganese-containing materials $La_{2-x}Sr_xCo_{0.5}Mn_{0.5}O_{4\pm\delta}$ have shown enhanced stability under reducing conditions with the formation of oxygen vacancies and B-site mixed valency (Mn^{3+}/Mn^{2+}), which suggests good mixed-conducting characteristics under

reducing conditions. The materials are therefore considered as possible anode materials in SOFCs and preliminary tests are now under consideration. The nickel-containing materials $La_{1.5+x}Sr_{0.5-x}Co_{0.5}Ni_{0.5}O_{4\pm\delta}$, on the other hand, have shown interesting characteristics to act as a cathode in SOFCs. In an attempt to characterize the cathode behaviour of these materials in SOFCs, $La_{1.7}Sr_{0.3}Co_{0.5}Ni_{0.5}O_{4+\delta}$ was employed as a cathode material in anode-supported micro-tubular SOFCs. The microtubes were based on YSZ electrolyte coated on top of a NiO-YSZ anode. The sintering and operating conditions suggested in this thesis (section 5.10.2) were employed in the measurements. The cells have shown interesting I-V characteristics which were comparable to that of LSM-based cells. Durability tests have also shown that the performance is significantly stable. Careful measurements involving both $La_{1.7}Sr_{0.3}Co_{0.5}Ni_{0.5}O_{4.08}$ and LSM, for comparison, are now under consideration. The material is also being tested in cells based on GDC and LSGM as electrolytes, employing both fuel cell and electrolysis modes. Another aspect of the future work is the study of the reduction behaviour of $LaSrCoMnO_6$. The material has been synthesized by a sol-gel method and structurally characterized. The reduction to the brownmillerite phase $LaSrCoMnO_5$ is now being examined.

List of publications resulting from this thesis

1. **Synthesis and characterization of the K_2NiF_4 phases $La_{1+x}Sr_{1-x}Co_{0.5}Fe_{0.5}O_{4-\delta}$ (x = 0, 0.2)**

   H. El Shinawi and C. Greaves,

   J. Solid State Chem. **181** (2008) 2705.

2. **Structural and magnetic characterization of $La_{1+x}Sr_{1-x}Co_{0.5}M_{0.5}O_{4\pm\delta}$ (M = Cr, Mn)**

   H. El Shinawi and C. Greaves,

   Z. Anorg. Allg. Chem. **635** (2009) 1856.

3. **Synthesis and characterization of $La_{0.8}Sr_{1.2}Co_{0.5}M_{0.5}O_{4-\delta}$ (M = Fe, Mn)**

   H. El Shinawi, J. F. Marco, F. J. Berry and C. Greaves,

   J. Solid State Chem. **182** (2009) 2261.

4. **Synthesis and characterization of $La_{1.5+x}Sr_{0.5-x}Co_{0.5}Ni_{0.5}O_{4\pm\delta}$ (x = 0, 0.2)**,

   H. El Shinawi and C. Greaves,

   J. Mater. Chem. **20** (2010) 504.

5. **$LaSrCoFeO_5$, $LaSrCoFeO_5F$ and $LaSrCoFeO_{5.5}$: new La-Sr-Co-Fe perovskites**

   H. El Shinawi, J. F. Marco, F. J. Berry and C. Greaves,

   J. Mater. Chem. (2010) DOI: 10.1039/b927141d

6. **Synthesis and characterization of $La_{1+x}Sr_{2-x}CoMnO_{7-\delta}$ (x = 0, 0.2)**

   H. El Shinawi, A. Bertha, J. Hadermann, T. Herrranz, B. Santos, J. F. Marco, F. J. Berry and C. Greaves,

   Submitted to J. Solid State Chem.

7. **K_2NiF_4-type $La_{1.7}Sr_{0.3}Co_{0.5}Ni_{0.5}O_{4+\delta}$ as cathode material in SOFCs**

   R. Sayers, M. A. Laguna-Bercero, S. J. Skinner, H. El Shinawi and C. Greaves,

   In Preparation.